MRI TO PREDICT CARTILAGE FUNCTION

USE OF MAGNETIC RESONANCE IMAGING TO ASSESS TIBIOFEMORAL CARTILAGE BEHAVIOUR FOLLOWING LOADING: A MULTI-DISCIPLINARY EVALUATION OF CARTILAGE MECHANICS

BY
ELORA C. BRENNEMAN WILSON, MSc

A THESIS
SUBMITTED TO THE DEPARTMENT OF KINESIOLOGY
OF MCMASTER UNIVERSITY
IN PARTIAL FULFILMENT OF THE REQUIREMENTS
FOR THE DEGREE OF
DOCTOR OF PHILOSOPHY

Doctor of Philosophy (2020)
Kinesiology

McMaster University
Hamilton, Ontario, Canada

TITLE:	Use of magnetic resonance imaging to assess tibiofemoral cartilage behaviour following loading: a multi-disciplinary evaluation of cartilage mechanics
AUTHOR:	Elora C. Brenneman Wilson, MSc
SUPERVISOR(S):	Dr. Monica Maly PT, PhD Dr. Peter Keir, PhD
NUMBER OF PAGES:	xviii, 192

Lay Abstract

This thesis used a multi-disciplinary approach to characterize articular cartilage mechanics in the knee joint. First, the deformation of knee cartilage following running was quantified using magnetic resonance imaging (MRI), and the effects of 1) running; 2) biological sex; and 3) their interaction were explored using a statistical mapping procedure. Second, daily cumulative knee load (or total load incurred by the knee joint over a day) was related to knee cartilage deformation (via MRI) following running in women. Third, a pig knee model was used to develop a 3D statistical model predicting cartilage mechanical properties from MRI-derived cartilage metrics. This thesis integrated elements of engineering, biomechanics, and medical imaging to derive novel evaluation techniques for the cartilage of the knee joint. This work builds a critical foundation for future development of statistical models that can assist with the assessment of cartilage health and disease management.

Abstract

Understanding articular cartilage mechanics is imperative to gain insight into tissue tolerances and loads, and how these may change with disease. This thesis used a multi-disciplinary approach to quantify cartilage mechanics using magnetic resonance imaging (MRI), a non-invasive tool for the evaluation of soft tissues. Study 1 (Chapter 2) outlined an *in vivo* study that aimed to identify the effect of 1) running; 2) biological sex; and 3) their interaction on tibial and femoral cartilage thickness changes following running using Statistical Parametric Mapping (SPM). Running caused deformation in all knee compartments, and especially in the lateral tibia ($p < 0.0001$). Females had thinner cartilage than males ($p \leq 0.009$). Finally, clusters indicating an interaction of Running×Sex were identified on the posterior lateral tibia, suggesting females experienced greater cartilage deformation than males ($p \leq 0.012$). Studies 2 and 3 (Chapters 3 and 4) integrated MRI and biomechanical datasets to explore the loading environment at the knee. Study 2 investigated the effect of daily cumulative knee load (measured using musculoskeletal modeling and accelerometry) on cartilage response (change in morphology, composition) following running in women. This cumulative loading metric was related to tibial volume change ($F(4, 14) = 4.68$, $p = 0.013$, $R^2 = 0.50$), suggesting a potential cartilage conditioning effect. Study 3 outlined the use of an *ex vivo* porcine stifle model to build a 3D voxelwise statistical map exploring the relationship between cartilage mechanical properties (measured via automated indentation mapping) and cartilage outcomes from MRI (cartilage thickness, T2 change) following static loading. No significant relationships were identified; however, this novel integration of indentation mapping and MRI cartilage outcomes shows utility moving forward. Overall, this thesis characterizes cartilage response to biomechanical load using novel tools derived by integrating engineering, biomechanics, and imaging. Together this work provides an exciting opportunity to explore and quantify spatial relationships between mechanical properties and cartilage MRI outcomes.

Acknowledgements

This journey would not have been possible without the help of a few incredible people. First, I wish to extend my deepest gratitude to my supervisor Dr. Monica Maly. The last seven years have been a monumental period of growth, both personally and professionally. I consider myself extremely lucky to learn from a strong woman in science. I thank you for your patience, guidance, and support. I would also like to extend special thanks to my supervisory committee members, Drs Peter Keir, Mike Noseworthy, and Cheryl Quenneville. This thesis would not be possible without the use of your lab spaces (Drs. Keir and Quenneville), guidance, and expertise.

A number of people played a key role in the construction and testing of the MRI-compatible loading apparatus used in this thesis. Thank you to Monica and Cheryl for collaborating on this excellent project. You both were instrumental in bringing my initial (and crazy) research vision to fruition! As well, a huge thank you to Guillaume Hesketh and Kevin Perera for your help in kick-starting the project. Thank you to Dan Wright, Rob Sluban, and John Colenbrander at the JHE machine shop, and to Jeff at the University of Waterloo for your help with various design and construction projects. Thank you to Cooper Gluek and Ariana Fraschetti for your help with the specimen potting cups and load cell. Thank you to Greg Noseworthy for help with conception of the static loading design. Finally, thank you to Norm Konyer for all your help at the Imaging Research Centre.

I would like to give a sincere thank you to my labmates. First and foremost, a most special thank you to Anthony Gatti. Sharing this PhD journey with you has been a pleasure. I have learned so much from you. Thank you for being a collaborator and most importantly, a friend. Thank you to all the others that I have had the pleasure of getting to know: Emily, Alex, Nick, Damjana, Sarah, Jackie, Kendall, Emma, and Natasha. Thank you for creating an exciting and inclusive work environment. I genuinely enjoyed coming into work everyday!

I would like to thank some excellent graduate students. Thank you to Cooper, Fatemah, Julia, Marisa, and Noah who always made me feel welcome at ETB. Thank you for also fielding all my annoying engineering-based questions! Secondly, thank you to Amanda, Andrew, Colin, Dan, Kevin, Kumar, and Riley who accepted me as part of their own lab group. You all created a wonderful work environment. It was a pleasure learning alongside all of you.

I would like to extend a special thanks to my family. Thank you to my parents and sisters for your abiding support of my academic endeavours. A final, and special, thank you to my husband Aaron. You have been my greatest teacher, and biggest fan. Thank you for helping me strive to be better every day. I love you!

Table of Contents

List of Figures

List of Tables

Notation and Abbreviations

AI	Analog Input
ANOVA	Analysis of Variance
AO	Analog Output
B_0	External Magnetic Field
B_1	Net Magnetization
BMI	Body Mass Index
CAD	Computer-aided Design
cDAQ	Compact Data Acquisition Unit
CDF	Cumulative Distribution Function
COM	Common Ground
COMAK	Concurrent Optimization of Muscle Activations and Secondary Kinematics
CPD	Coherent Point Drift
CT	Computed Tomography
DC	Direct Current
dGEMRIC	Delayed Gadolineum-Enhanced MRI of Cartilage
ECM	Extracellular Matrix
fMRI	Functional Magnetic Resonance Imaging
FS	Fat Saturated
FSPGR	Fast Spoiled Gradient Recalled
FWER	Family-wise Error Rate
GAG	Glycosaminoglycan
GRE	Gradient Echo
GMM	Gaussian Mixture Model
HL	High-Loading group
ICP	Iterative Closest Point

ICRS	International Cartilage Repair Scores
ID	Inner Diameter
IM	Instantaneous Modulus
IPAQ	International Physical Activity Questionnaire
JRF	Joint Reaction Force
JRFI	Joint Reaction Force Impulse
LEFS	Lower Extremity Function Scale
LL	Low-Loading group
LM	Lvenberg-Marquardt
MESE	Multi-Echo Spin Echo
MET	Metabolic Equivalent
MRI	Magnetic Resonance Imaging
NPT	National Pipe Tapered Thread
OA	Osteoarthritis
OBB	Oriented Bounding Box
OD	Outer Diameter
PBS	Phosphate Buffer Solution
PD	Proton Density
PG	Proteoglycan
QP	Quantitative Parameter
RF	Radiofrequency
RFT	Random Field Theory
RR	Risk Ratio
SE	Spin Echo
SEM	Standard Error of Measurement
SIMM	Software for Interactive Musculoskeletal Model
SPM	Statistical Parametric Mapping
T1	Spin-lattice relaxation
T1ρ	Spin-lattice relaxation in the rotating frame
TKA	Total Knee Arthroplasty
T2	Spin-spin relaxation
TE	Echo Time
TR	Relaxation Time

UNC	Unified National Coarse Thread
UNF	Unified National Fine Thread
VTK	Visualization Toolkit
WB	Weight-Bearing

Declaration of Academic Achievement

This thesis is the primary work of Doctor of Philosophy candidate Elora C. Brenneman Wilson. This thesis is composed of five chapters. The first chapter contains a general introduction to articular cartilage structure and function, measurement of biological tissue with magnetic resonance imaging (MRI), and estimation of cartilage mechanical properties. The following three chapters contain manuscripts that explore knee articular cartilage mechanics.

Chapter 2 contains the following prepared manuscript: Brenneman Wilson EC, Gatti AA, Maly MR. A New Technique to Evaluate the Impact of Running on Knee Cartilage Deformation by Region. *Submitted to Magnetic Resonance Materials in Physics, Biology, and Medicine on 3 July 2020.* Submission # MRMP-D-20-00119. This study investigated the effect of biological sex on tibial and femoral articular cartilage deformation patterns following running using Statistical Parametric Mapping. This study was conceived by Elora C. Brenneman Wilson, Anthony A. Gatti, and Monica R. Maly. Data for the sample of men was collected as part of Mr. Gatti's Master's thesis (where Elora Brenneman Wilson assisted with collection as an RA), and data for the sample of women were collected by Elora C. Brenneman Wilson. Anthony Gatti also assisted with statistical analyses. Data analysis, interpretation, and preparation of the manuscript were all led by Elora Brenneman Wilson. All co-authors contributed substantially to the final manuscript submitted to *Magnetic Resonance Materials in Physics, Biology, and Medicine.*

Chapter 3 contains the following manuscript: Brenneman Wilson EC, Gatti AA, Keir PJ, Maly MR. Daily Cumulative Load and Body Mass Index Alter Knee Cartilage Response to Running in Women. *Submitted to Gait & Posture 2 July 2020.* Submission # GAIPOS-S-20-00953. This study used accelerometry and biomechanical gait analyses to calculate a representative measure of daily cumulative knee load (joint reaction force impulse × average number of steps per day), and determined the relationship of this daily knee load on cartilage response to running in young women.

This study was conceived by Elora C. Brenneman Wilson and Monica R. Maly. Data were collected by Elora C. Brenneman Wilson. Data analysis, interpretation, and preparation of the manuscript were all led by Elora Brenneman Wilson. Anthony A. Gatti and Peter J. Keir made substantial contributions to statistical analyses and interpretation, respectively. All co-authors made considerable contributions to the final manuscript submitted to *Gait & Posture*.

Chapter 4 contains the following manuscript: Brenneman Wilson EC, Quenneville CE, Maly MR. Integrating MR Imaging with Full-Surface Indentation Mapping of Femoral Cartilage in an Ex Vivo Porcine Stifle. *Submitted to Annals of Biomedical Engineering 7 October 2020.* Submission # ABME-D-20-01025. This study used a multi-disciplinary approach to investigate the relationship between cartilage deformation (measured via magnetic resonance imaging) and cartilage mechanical properties (via indentation) in an *ex vivo* porcine stifle model. This study was conceived by Elora C. Brenneman Wilson, Cheryl E. Quenneville, and Monica R. Maly. Data was collected by Elora C. Brenneman Wilson. Data analysis, interpretation, and manuscript preparation was led by Elora C. Brenneman Wilson.

The work presented in Chapter 4 required the build of an MRI-compatible loading apparatus for porcine stifle joints. To preserve flow in a 'sandwich'-style thesis, design and testing of this apparatus are included in Thesis Appendices A and B. There are a number of important people who made substantial contributions to this project. Monica R. Maly and Cheryl E. Quenneville share project lead (with Elora C. Brenneman Wilson), and were responsible for fund acquisition. Guillaume Hesketh was an Engineering summer student responsible for hardware design (May-Aug 2017). Kevin Perera was an Engineering summer student responsible for control system implementation and design of a custom Delrin load cell (May-Aug 2017). John Colenbrander, Dan Wright, and Robert Sluban from the John Hodgins Engineering machine shop assisted with design and LabVIEW coding. Jeff Rice, technical manager at the University of Waterloo, assisted with physical construction of individual apparatus components. Cooper Gluek assisted with design updates, physical construction, and load cell calibration. Greg Noseworthy, kinesiology lab technician at McMaster University assisted with troubleshooting pneumatics and design considerations for the static loading components.

Finally, Chapter 5 contains the discussion, conclusions, and future directions of the work presented in this thesis.

1 — Literature Review

This literature review starts with a discussion on articular cartilage structure and function. Next, factors affecting cartilage structure and function are introduced, with special attention to the roles of biological sex and cumulative load. Then, two methods to quantify articular cartilage function are introduced: magnetic resonance imaging (MRI) and cartilage indentation. Finally, a discussion on the prediction of cartilage mechanical properties from MRI is presented, along with an identification of gaps in the literature that this thesis has directly addressed. This section ends with the specific objectives of this thesis.

1.1 Articular Cartilage Structure

Hyaline articular cartilage is an avascular, multi-phasic material. Within this complex material are chondrocytes, structural macromolecules (collagen and proteoglycans), and fluid. Articular cartilage is commonly considered bi-phasic, with 1) a solid phase, consisting of the chondrocytes, collagen, and proteoglycans (PGs); and 2) a fluid phase, consisting of free, mobile, unbounded water molecules interspersed with ions (Mow et al. 1984).

Chondrocytes are highly specialized, differentiated cells found only in hyaline articular cartilage. Their primary responsibility is cartilage development and maintenance of the structural matrix (Buckwalter and Mankin 1997). Chondrocytes react to external stimuli such as joint loading, changes in the extracellular matrix (ECM), and growth factors to preserve homeostasis by controlling the formation of Type II collagen, hyaluronan[1], and other ECM components (Muir 1995). Chondrocyte activity and health are therefore pertinent to the overall structural integrity of the articular

---

[1] A central component of aggrecans as well as a "gel" acting to support the chondrocyte.

cartilage.

Type II collagen and proteoglycans, the major structural components of articular cartilage, create a resilient environment for the transmission of loads at the joint. Type II collagen is known for its torsional stability and high tensile strength (Cohen et al. 1998; Von der Mark 1999; Williamson et al. 2003). Proteoglycans in articular cartilage fall into two main categories 1) large PG macromolecules comprised of many aggrecan monomers of a long protein core and negatively-charged sulphated glycosaminoglycan (GAG) side chains (Cohen et al. 1998; Muir 1978); and 2) smaller non-aggregating PGs (Buckwalter and Mankin 1997; Roughley and Lee 1994). The large, aggregating PGs are in greater concentrations within the articular cartilage than small PGs. The aggregate structure serves to anchor PGs within the matrix, providing stability during tissue deformation (Buckwalter and Mankin 1997). The smaller PGs are involved in other accessory processes within the ECM (Roughley and Lee 1994).

The solid components of articular cartilage are arranged anisotropically throughout the tissue (Minns and Steven 1977). From this organization, three distinct zones have been established 1) deep zone: thick collagen fibrils are arranged radially in a low concentration; 2) transitional zone: collagen fibrils start to exhibit anisotropic orientation; and 3) superficial zone: finer collagen fibrils are densely packed (higher concentration) and arranged parallel to the articular surface (Minns and Steven 1977; Muir et al. 1970). The pattern of dispersion of proteoglycans is the opposite of that of collagen, with a higher concentration in the deep zone moving toward a lower concentration at the surface (Muir 1978; Muir et al. 1970). Together, the solid matrix and fluid constituents provide a framework for cartilage form and function (Mow et al. 1984).

1.2 Articular Cartilage Function

The anisotropically oriented Type II collagen fibrils along with the interactions of other collagen types create a structurally stable “mesh”. This mesh contributes to the overall strength of the tissue (Buckwalter and Mankin 1997). Entrapped within the mesh are PGs and mobile water ions. The negatively charged sulphated GAG side-chains on the PGs attract cations (mainly sodium) which increases the osmotic gradient in the tissue (Mosher and Dardzinski 2004). Free water ions are then attracted to the solid matrix, creating a swelling pressure within the tissue (this is also known as the Donnan Effect). In healthy tissue, physical swelling is restricted by the high tensile strength of the Type II collagen fibrils in the collagen mesh (Maroudas 1976). The swelling pressure increases tensile forces in the collagen mesh, resulting in overall compressive stiffness of the tissue (Maroudas 1976).

During loading, cartilage will deform (a volumetric change or pressure gradient (Lu and Mow 2008)) as fluid re-distributes within the tissue (Mow et al. 1984). During deformation, healthy tissue will have a high resistance to interstitial fluid-flow, resulting in increased drag forces (Maroudas 1976). Further, this high resistance to fluid flow results in high interstitial fluid pressure, and consequently protects the solid matrix (collagen, proteoglycans, chondrocytes) from high strains (Lu and Mow 2008). In fact, Soltz and Ateshian (1998) demonstrated in bovine cartilage explants that interstitial fluid pressure supported over 90% of the total load during the first 6.5 and 12 minutes of creep and stress-relaxation tests, respectively. This work highlights the importance of the fluid phase in healthy cartilage function.

A comprehensive understanding of articular cartilage function in healthy states is important for applications to tissue degeneration and disease. Osteoarthritis (OA) is a common degenerative joint disease hallmarked by the loss of hyaline articular cartilage. OA is a leading cause of disability for older adults (Guccione 1994). An estimated 1 in 8 (13.0%) Canadian adults over the age of 20 have OA, with an increased prevalence with increasing age (Kopec et al. 2007; Kopec et al. 2008). Projected estimates of OA in the Canadian population suggest that older adults ≥ 60 years will represent 53% of incident cases, and OA will be present in 25.6% of the population by the year 2040 (Bombardier et al. 2011). Both direct (joint replacement, post-surgical care; \$546.4 billion[2]) and indirect (work-loss, disability; \$909.1 billion) costs are projected to substantially increase through the year 2040 due to the aging population (Bombardier et al. 2011). From these estimates, it is evident that OA is a major healthcare issue in Canada.

Changes in the structure of the articular cartilage are evident with OA. Osteoarthritis involves the progressive loss and damage of chondrocytes, collagen, and

---

[2] Cumulative estimates from 2010 to 2040.

PGs, accompanied by an ill-attempt to repair and remodel the lost or damaged constituents (Buckwalter et al. 2005). Some of the hallmark structural alterations include 1) altered activity of the chondrocytes (Aigner et al. 2007) including a decreased capacity for chondrogenesis from mesenchymal stem cells (Murphy et al. 2002); 2) disorganization of the collagen structural matrix which is most pronounced in the superficial zone (Panula et al. 1998; Saarakkala et al. 2010); 3) reduction in PG content (Bi et al. 2006); and 4) increases in tissue hydration (Armstrong and Mow 1982; Guilak et al. 1994). By compromising the organization, integrity, function, or number of these constituents, the ability of the tissue to function is diminished. Specifically, if the solid matrix is disrupted, in concert with a reduced ability to adequately counteract swelling pressure (i.e., fewer negatively-charged GAG side-chains (Bi et al. 2006), decreased frictional forces and drag with fluid flux (Mow et al. 1984)), it would be expected that OA-degenerated cartilage would undergo greater deformation when loaded, and have a greater proportion of that force supported by the solid matrix. *In vivo*, there have been conflicting results with regards to cartilage deformation as measured by magnetic resonance imaging. Cotofana et al. (2011) showed females with knee OA had greater (though not statistically significant) deformation in the medial tibial and central weight-bearing medial femoral cartilage following loading in an MR-compatible static loader (to 50% body weight for 30 minutes) when compared to females presenting with no radiographic OA. Alternatively, others have demonstrated less deformation in the patellar (Hudelmaier et al. 2001) and tibiofemoral (Mosher et al. 2010) cartilage of older adults compared to young. Further work is required to understand these discrepancies.

1.2.1 Risk Factors for Osteoarthritis

The Osteoarthritis Research Society International defines OA as a joint disorder characterized by cell stress and ECM degradation (*Standardization of Osteoarthritis Definitions* 2015). OA is has a multi-factorial etiology, and is "initiated by micro- and macro-injury that activates maladaptive repair responses including pro-inflammatory pathways of innate immunity". (*Standardization of Osteoarthritis Definitions* 2015). Some common risk factors for OA have been identified. For example, sex is a key risk factor for knee OA, where females are more susceptible and experience worse disease severity than males (Felson et al. 1995; Hawker et al. 2000; Srikanth et al. 2005). Secondly, a growing body of literature suggests that cumulative exposure to loading may influence disease outcomes. Cumulative load is defined in the literature as the impulse of a knee loading curve during one step (e.g., knee adduction moment (Maly et al. 2013), axial knee joint contact force (Miller et al. 2015; Miller et al. 2014)), multiplied by a finite number of steps (e.g., steps per day as measured by accelerometry (Maly et al. 2013), number of steps during a run or walk (Miller et al. 2015)). For this thesis, the tibial compressive joint reaction force[3] (calculated via Static Optimization and Joint Reaction Analyses in OpenSim) was used with accelerometry to quantify cumulative load at the knee joint. *The in vivo portion of my thesis sought to provide novel data to explore the mechanisms underlying the risk factors of sex and cumulative load.*

1.2.1.1 Sex-Differences

It is well established that prevalence of knee OA is higher in females (Hawker et al. 2000; Srikanth et al. 2005), and females experience greater severity of symptoms than males (Felson et al. 1995; Srikanth et al. 2005). A comprehensive meta-analysis by Srikanth et al. (2005) showed females had a 0.63 (95 % CI 0.53-0.75) pooled risk ratio (males:females) for prevalent knee OA (12 studies; n=22,359). Further, symptoms were more severe for females, with a female versus male pooled standardized mean difference of 0.20 (95 % CI 0.11-0.28; $p < 0.001$) (Srikanth et al. 2005). Males also had a significant reduction in incident knee OA, with an incidence rate ratio of 0.55 (95 % CI 0.32-0.94; $p = 0.03$) (Srikanth et al. 2005).

The cause of this sex disparity in knee OA is not clearly understood. This thesis was interested in cartilage loading patterns between males and females, and ultimately provide insight into underlying mechanical factors contributing to disease in females. Studies have explored sex differences in static lower-limb alignment, cartilage composition, and cartilage morphology. First, females tend to have greater valgus knee alignment (Wise et al. 2012) and a greater quadriceps angle (Horton and Hall 1989) than males. Consequently, females have an increased prevalence of lateral knee OA compared to males (Wise et al. 2012). Second, while differences in lateral femoral and patellar proteoglycan content (via MRI) have been demonstrated between males

---

[3] OpenSim defines the Joint Reaction Force as "the resultant forces and moments the joint structure carrie(d) in response to all motions and forces in the model, including muscles, motors, and all other actuators".

and females with radiographic knee OA (Kumar et al. 2015), these compositional differences have not been corroborated in young or middle-aged adults without OA (Kumar et al. 2015; Mosher et al. 2004; Wirth et al. 2017)[4]. Third, females have thinner tibial and femoral cartilage (Cicuttini et al. 2002; Otterness and Eckstein 2007) and less cartilage volume (Cicuttini et al. 1999; Ding et al. 2003) than males, even when adjusted for age, body size, and bone size. A combination of mechanical factors (static alignment) and anatomical factors (cartilage morphology, composition) may contribute to differences in cartilage deformation 1. magnitudes; or 2. patterns across the joint compared to males. If present, these could have long-term effect on cartilage health. *The first manuscript of my thesis directly addressed this question by assessing regional cartilage thickness maps before and after running in healthy males and females.*

1.2.1.2 Cumulative Joint Load and Cartilage Conditioning

There are opposing relationships between exposures and cartilage degradation. Evidence from *in vitro* studies suggests that high magnitude loads on cartilage explants result in decreased cell viability (Torzilli et al. 1994), an increased presence of pro-inflammatory cytokines (Houard et al. 2013), and reductions in tensile strength of the collagen network (McCormack and Mansour 1997). Decreased cell viability and increased concentrations of pro-inflammatory cytokines would have a negative effect on ECM homeostasis. Along with reduced tensile strength of collagen, these changes would result in reduced swelling pressure, and the ability of the cartilage to transmit load (Cohen et al. 1998). Indirectly, cartilage damage via high-magnitude loads has been implicated *in vivo* as those that experience higher magnitude loads at the knee joint via the knee adduction moment have a greater cartilage loss over 1 - 5 years (Bennell et al. 2011; Brisson et al. 2017; Chang et al. 2015; Chehab et al. 2014) and increased radiographic evidence of OA over two years (Miyazaki et al. 2002). However, some cross-sectional data suggest the opposite can be true. First, there is a lack of evidence relating recreational long-distance running (10-20 miles/week)

---

[4] It is worth noting that a few studies have demonstrated a 'trend' toward increased T2 relaxation times in males (Wirth et al. 2014; Wirth et al. 2017). T2 values tend to increase with worsening OA status (Dunn et al. 2004). Males demonstrating longer T2 times, but females presenting with greater incidence and severity of OA symptoms, is an interesting paradox.

with the development of OA, an activity with high joint load magnitude and high frequency (Miller 2017). In fact, there is a reported protective effect (OR 0.46, 95% CI 0.30 – 0.71) of recreational levels of running or orienteering from knee replacement surgery due to OA (Timmins et al. 2017). As well, in a sample of healthy older adults (no history of knee pain or presentation of knee OA), self-reported frequency and duration of vigourous activity positively correlated with tibial cartilage volume, suggesting vigourous physical activity was protective of cartilage (Racunica et al. 2007). A proposed theory for the disconnect in evidence is *cartilage conditioning* whereby healthy cartilage will undergo mechanically-driven re-modeling to support areas of higher stress (Seedhom 2005). Cartilage conditioning theory has been indirectly supported by early work from Yao and Seedhom (1993), who used cadaveric ankle and knee joints from the same donor to show cartilage areas that bear greater stresses strongly correlate with greater compressive modulus. So far, only indirect evidence has supported this theory *in vivo*.

The mechanism for cartilage conditioning is not well understood. In can be speculated that, like other biological tissues, gene expression and protein synthesis in articular cartilage may by activated by micro-injury leading to repair and adaptation (anabolism) (Goldring and Marcu 2009). However, this tightly-regulated process can instead shift into a catabolic state (Goldring and Marcu 2009; Mazor et al. 2019). This tightly-controlled homeostasis model for cartilage health was adopted by Andriacchi et al. (2009), suggesting that a disruption in cartilage homeostasis (i.e., injury, abnormal joint mechanics, aging, obesity) is the initiating factor in a cascade of events leading to the breakdown of joint tissues (Figure 1.2.1). Two recent modeling studies investigated mechanisms related to anabolism (Miller and Krupenevich 2020) and catabolism (Mononen et al. 2016) of articular cartilage. Miller and Krupenevich (2020) proposed a combined musculoskeletal (discrete element) and probabilistic fatigue modeling approach to quantify the potential effect of walking loads on medial knee cartilage adaptation over the lifespan. Mononen et al. (2016) used a cartilage overloading algorithm[5] to model collagen fibril degeneration in the medial tibial and femoral cartilage surfaces of low BMI versus high BMI participants from the Osteoarthritis Initiative. These two models investigating cartilage homeostasis (Miller

---

[5] Cartilage overloading was defined as cumulative excessive stresses above the failure limit that altered tissue properties with time (Mononen et al. 2016).

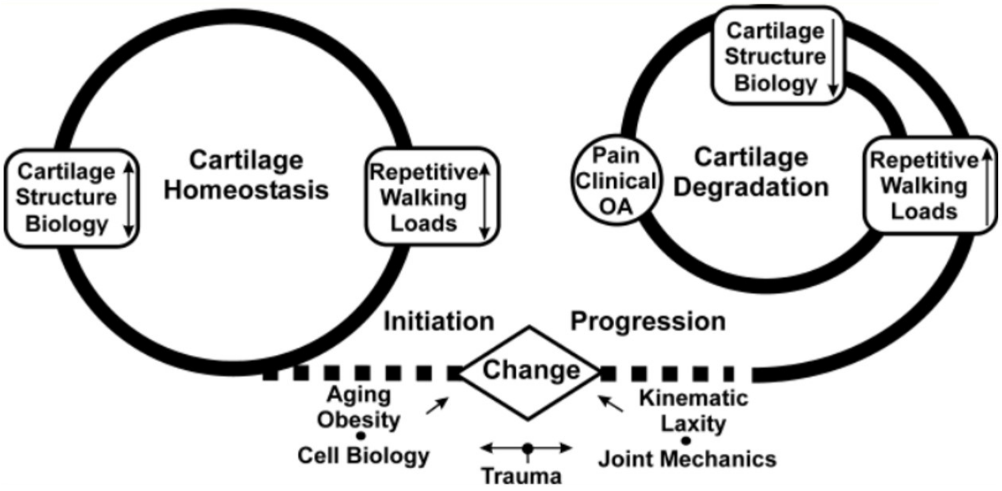

Figure 1.2.1: Proposed pathogenesis of cartilage in osteoarthritis (from Andriacchi et al. 2009). A joint is in a healthy state of breakdown/repair until perturbed by an instigating event (i.e., injury, abnormal joint mechanics, aging, obesity). Then, the biological and mechanical environment is in a state of imbalance, leading to breakdown and degeneration often seen in OA.

and Krupenevich 2020) and imbalance (Mononen et al. 2016) highlight the sensitivity of articular cartilage to mechanical factors, both in the maintenance and breakdown pathways. Understanding the role of cumulative load at the knee in cartilage deformation mechanics (following physical activity) may provide insight into initiating mechanical factors related to anabolic (conditioning) or catabolic (breakdown) states.

Few studies have investigated the *in vivo* relationship between physical activity history and cartilage response to acute loading. Using four distinct groups of participants divided by age (young: <45, old: ≥ 46) and activity level (sedentary, marathon runners), Mosher et al. (2010) found no main effects of age or physical activity level on tibiofemoral T2 relaxation changes (water content via MRI[6]) following 30-minutes of running. Alternatively, in a secondary analysis, young healthy men who reported

---

[6] See Section 1.3.1.2 for a detailed overview.

higher levels of physical activity had smaller changes in tibial and femoral T2 relaxation following running and bicycling activities (Gatti et al. 2017). As well, GAG content in knee cartilage improved in women who underwent a 10-week Start-to-Run program (Van Ginckel et al. 2010). These studies underline a pivotal role of habitual exercise on overall cartilage health. Further, the magnitude and frequency of loads at the knee joint may not be sole determinants of tissue turnover, but instead may be heavily influenced by duration and accumulation of the experienced loads.

Body mass index (BMI) may influence cartilage mechanics. Larger BMI was associated with greater diurnal knee cartilage strains (Widmyer et al. 2013). Those with high BMI ($> 31.6kg/m^2$) who walked a moderate (6,000 - 7,900) or high (>7,900) number of steps per day were at a greater risk of medial tibiofemoral damage on MRI 2 years later (RR 2.61 and 2.83 respectively) (Voinier et al. 2020). *The second manuscript of my thesis directly explored the associations of daily cumulative knee load and BMI on tibiofemoral cartilage response to running in young healthy women.*

1.3 Assessment of Articular Cartilage Function

The two major assessment techniques for articular cartilage function outlined in this thesis are MRI, a non-invasive method able to obtain information on cartilage composition and mechanics *in vivo*; and cartilage indentation, an *ex vivo* method used to quantify mechanical properties of articular cartilage. MRI was chosen for its ability to clearly delineate biological tissues. Cartilage indentation was chosen over and above other methods (confined compression, unconfined compression) due to its theoretical derivations of mechanical behaviour including the subchondral bone tissue. Therefore, indentation could be employed at multiple sites over a whole articulating surface using proprietary automated indentation mapping technology (Sim et al. 2017a).

1.3.1 Magnetic Resonance Imaging

MRI is a non-invasive imaging modality able to provide quantitative information on cartilage morphology (i.e., thickness, volume), molecular composition, and physiological processes in biological tissue (Guermazi et al. 2013; Roemer et al. 2014). The theory of MRI is based on the theory of nuclear magnetic resonance. A proton, the positively charged subatomic particle that is a main constituent of an atom's nucleus, naturally spins around its axis. This results in a proton exhibiting electromagnetic properties. In biological tissues, one of the main constituents is hydrogen (from a high water content) which contains one proton and zero neutrons in the nucleus. When a biological tissue is exposed to an external magnetic field (B_0), like in an MRI scanner, the proton spins of the hydrogen atoms align in the direction of B_0. Using radiofrequency (RF) waves, the spins tip the net magnetization into the X-Y plane (B_1) at a flip angle α. Cessation of the RF wave results in the relaxation of the proton spins back to B_0 and two relaxation parameters are acquired:

1. Spin-lattice ($T1$) relaxation, where the proton spins dissipate excess energy to the surroundings while returning to the ground state. This relaxation is representative of the recovery of the main (longitudinal) magnetization; and
2. Spin-spin ($T2$) relaxation, where the transverse (B_1) magnetization shrinks due to the dephasing of the proton spins.

Altering parameters like echo time (TE; time between an RF pulse and the resulting signal) and repetition time (TR; time between successive pulse sequences) will result in contrast of different tissues dependent on their inherent T1 and T2 properties.

1.3.1.1 Cartilage Thickness and Volume Changes

Quantitative measurements of cartilage morphology include thickness and volume. To assess cartilage tissue, high-resolution 3D scans using a fast spin echo[7], or a variant of the gradient echo[8] are common (Crema et al. 2011). Though, gradient echo scans (e.g., spoiled gradient, double-echo steady-state) have been recommended if possible (Li et al. 2016a). From these scans, articular cartilage can be segmented from surrounding tissue using either manual, semi-automated, or automated techniques.

---

[7] A spin echo (SE) sequence can capture "true" T2 (Hahn 1950). Briefly, an RF pulse tips the net magnetization 90^o into the X-Y plane. Upon cessation of the RF pulse, precessing proton spins will start to relax back to the external electromagnetic field, B_0. However, due to field inhomogeneities, proton spin relaxation will occur at different rates. To overcome this, a second 180^o refocusing RF pulse reverses the spins, allowing the slower spins to "catch-up" to the faster spins. This captures true T2 relaxation properties of the tissue, independent of inhomogeneities in the main magnetic field (Hahn 1950).

[8] A gradient echo (GRE) sequence involves a single RF pulse at an angle α, typically $\leq 30^o$ (Ridgway 2015). This allows for a reduction in TR, and ultimately a reduction in imaging time compared to SE. It is useful to note that decay of transverse magnetization is dependent on T2*, not true T2 like the SE approach (Ridgway 2015).

Changes in thickness (mm) and volume (mm^3) measures following activity are typically an indication of the changes in water content (Blumenkrantz and Majumdar 2007). When the articular cartilage is subjected to compressive forces, interstitial fluid pressure counteracts the applied stresses to protect the structural matrix (Ateshian et al. 1994). Following a bout of weight-bearing activity — running for example — fluid re-distributes over the contact area, resulting in overall tissue deformation and bearing of the load by the structural matrix (Armstrong and Mow 1982; Blumenkrantz and Majumdar 2007; Mow et al. 1984). Therefore, *in vivo* studies of articular cartilage have used physiological bouts of loading to investigate changes in thickness and volume (e.g., Eckstein et al. 2000; Eckstein et al. 2005; Farrokhi et al. 2011; Gatti et al. 2017; Kessler et al. 2006; Liu et al. 2017), and act as a non-invasive model of cartilage deformation mechanics. These studies clearly indicate that cartilage deformations in knee articular cartilage vary dependent on magnitude (Eckstein et al. 2005), type (Eckstein et al. 2000; Gatti et al. 2017), and duration (Kessler et al. 2006) of loading. An understanding of cartilage deformation following a physiological bout of loading, and what factors may influence this response (e.g., biological sex, physical activity history), is integral to advance our knowledge of cartilage mechanics in healthy and diseased states.

There are a few challenges to the assessment of cartilage morphology changes following physical activity. First, there is a relatively large range of deformation values presented in the literature. Cartilage volume changes are fairly consistent, with studies reporting small non-significant changes in the medial tibia, and decreases in the lateral tibia (-4.0 to -6.1%) (Boocock et al. 2009; Kersting et al. 2005; Niehoff et al. 2011), whole tibia (-2.6 to -3.6%) (Kersting et al. 2005; Kessler et al. 2006), and whole femur (-3.0 to -3.2%) (Kersting et al. 2005; Niehoff et al. 2011) following running[9]. However, cartilage thickness changes following running are more variable, with reported estimates ranging from -2.2 to -13.6% in the tibial cartilage (Mosher et al. 2005; Niehoff et al. 2011; Subburaj et al. 2012). These differences may stem from methodological differences in thickness measurements, therefore caution is recommended when interpreting results. Second, articular cartilage is sensitive to loading.

---

[9] These studies employed different running parameters (duration, terrain) and MRI scanners (1.0, 1.5, 3.0 T). Despite these differences, cartilage volume changes remained fairly consistent between studies.

Therefore, strict pre-imaging protocols are imperative to minimize the impact of prior loading on cartilage deformation. It has been recommended to perform imaging in the morning as there is a diurnal effect on measurements of cartilage thickness (Coleman et al. 2013).

1.3.1.2 T2 Relaxation Mapping

T2 relaxation mapping (T2) is a parametric mapping technique that is sensitive to tissue water content (Liess et al. 2002) and collagen fibre orientation (Henkelman et al. 1994). No contrast agents are required and is therefore a non-invasive imaging tool *in vivo*. Changes in T2 in articular cartilage may reflect one or a combination of 1) changes in free water content and/or collagen fibre orientation over time (Souza et al. 2012); or 2) acute changes in free water distribution and/or collagen fibre orientation following a bout of mechanical loading (Gatti et al. 2017; Mosher et al. 2005; Souza et al. 2014). To obtain images appropriate for the estimation of T2, an SE sequence with a consistent TR and varying TE is required (Multi-Echo Spin Echo [MESE]) (Blumenkrantz and Majumdar 2007). Using multiple TE's, multiple echoes can be acquired and the mono-exponential T2 signal decay can be estimated voxel-by-voxel using the Levenberg-Marquardt (LM) algorithm (Gatti et al. 2017; Subburaj et al. 2012):

$$SI_{TE} = SI_0 \cdot e^{-TE/T2} \tag{1}$$

where SI_{TE} is the signal intensity at echo time TE, SI_0 is the y-intercept, and $T2$ is a parameter of the line fit that corresponds to the T2 time (ms) for the signal to decay by 37%. Alternatively, the natural logarithm of the signal intensity can be used to calculated relaxation time using a linear least squared approach:

$$b = (X^T X)^{-1} X^T Y \tag{2}$$

where b is a $2-by-n$ matrix containing data to calculate PD values in the first row and data to calculate T2 relaxation in the bottom row; X is an $m-by-2$ matrix with the first column containing ones and the second column containing the m echo times, and; Y is an $m-by-n$ flattened matrix of the voxel signal intensities at each of m echo times.

Cartilage T2 is sensitive to mechanical loading, as compressive forces will act to re-distribute the interstitial fluid (Gatti et al. 2017; Mosher et al. 2005; Souza et al.

2014). T2 also demonstrates spatial variability. Dardzinski et al. (1997) was the first group to show that T2 in the patellar cartilage of healthy asymptomatic adults *in vivo* increased moving from the subchondral bone (deep zone) and were subsequently the first to provide normative values for T2 *in vivo* in a 3.0T scanner dependent on location: 32 ± 1 *ms* in the deep zone, 48 ± 1 *ms* in the deep transitional zone, and 67 ± 2 *ms* in the superficial transitional zone (p <0.001). This pattern of T2 spatial distribution matched those proposed by previous *in vitro* studies (Chalkias et al. 1994; Mlynárik et al. 1996) and matches the spatial distribution of water content throughout the cartilage tissue (Lüssea et al. 2000). Other authors were able to quantify differences in the spatial distribution of cartilage T2 based on age (Mosher et al. 2000) and OA-status (Carballido-Gamio et al. 2009; Dunn et al. 2004; Li et al. 2009) with T2 relaxation times increasing with age and disease severity. The sensitivity of T2 to collagen matrix structure and water content make it a useful non-invasive imaging metric to estimate mechanical properties.

There are inherent limitations with the estimation and application of cartilage T2. First, relaxation values will depend on the strength of the magnet used leading to difficulty in comparison of results between studies (Jordan et al. 2013). Second, a lack of standardization in post-imaging analysis protocols will induce error, also leading to a difficulty in comparison of results between studies. Koff et al. (2008) demonstrated different estimations of T2 (p <0.0001) and R^2 values (p <0.0001) between three different fitting methods (linearized least squares, weighted linearized least squares, and non-linear least squares). It has also been suggested that the first echo be removed from the fit to reduce systematic error (Milford et al. 2015), a technique that has not been consistently implemented.

1.4 Quantifying Articular Cartilage Mechanical Properties

Mechanical properties are quantitative metrics that provide insight into the mechanical behaviour of a material that cannot be gleaned *in vivo*. In the literature, common properties used to describe articular cartilage include Aggregate (elastic) modulus, Young's modulus, permeability[10], and Poisson's ratio. These properties are outlined

---

[10] Permeability is considered a magnetic property rather than a mechanical property. However, articular cartilage has electromagnetic properties due to the interaction of the negatively charged

in Table 1.4.1. As well, a great summary of the direct (and indirect) calculation of each property is presented in Korhonen et al. (2002).

The mechanical properties of articular cartilage are obtained using specific testing protocols and modeling techniques. The first testing protocol involves compressing cartilage explants with a rigid permeable plate in a confined compression configuration, where the lateral expansion of the tissue is restricted by chamber walls in a loading chamber. This configuration forces the interstitial fluid to flow in one direction, exerting experimental control over fluid exudation. This method is used to directly measure aggregate (equilibrium) modulus and permeability (Mow et al. 1980). The second testing protocol involves compressing cartilage explants with a rigid impermeable plate in an unconfined compression configuration, where fluid extrudes the tissue laterally. Unconfined compression allows for the direct measurement of Young's modulus (Armstrong et al. 1984). The final testing protocol involves indenting osteochondral explants (i.e., cartilage still mounted on its underlying subchondral bone) with an indenter instrument with controlled displacement (or force) and porous tip. Mathematical models enable the indirect estimation of aggregate modulus, Young's modulus, and permeability. The indentation technique was used in this thesis, and is described in detail below.

1.4.1 Indentation of Articular Cartilage

The indentation method is one of the most common approaches to study the mechanical properties of articular cartilage due to ease of experimentation and the existence of well-established classical mathematical models of elastic contact between two bodies (e.g., Hertzian contact theory) (Mak et al. 1987). Hayes et al. (1972) were the first group to derive a mathematical relationship for the indentation mechanics of articular cartilage. The solution considered an infinite elastic layer (cartilage) bonded to a rigid half-space (subchondral bone) in contact with a cylindrical indenter (fixed contact area) or a spherical indenter (variable contact area directly influenced by displacement) (Hayes et al. 1972). The two unitless parameters (χ and κ) required to determine the relationship between the applied force (F) and the displacement of the

---

sulphated GAGs sidechains of the PGs with cations, creating an osmotic gradient within the tissue.

Table 1.4.1: List of mechanical properties of articular cartilage.

Mechanical Property	**Definition**	**Units**	**Methods of Derivation**
Aggregate (elastic) modulus	Stiffness of the solid matrix (measured in equilibrium, when all fluid flow has ceased in articular cartilage)	MPa	1. Direct measurement from confined compression 2. Indirect calculation from indentation or unconfined compression
Young's modulus	Ratio of the stress applied and its resultant strain in the same axis (usually measured in the elastic range [10-20% strain])	MPa	1. Direct measurement from unconfined compression 2. Indirect estimation from confined compression or indentation
Permeability	Ability of cartilage to hold a charge	m^4/Ns	1. Direct measurement from confined compression 2. Indirect measurement from unconfined compression or indentation
Poisson's ratio	Ratio of shear strain to axial strain	Unitless	1. Direct measurement from optical imaging 2. Indirect measurement from comparison of (a) unconfined compression and confined compression (b) unconfined compression and indentation

cartilage (ω_0) during indentation are:

$$\chi = \frac{a^2}{\omega_0 R} \tag{3}$$

$$\kappa = \frac{F(1-v)}{4aG\omega_0} \int_0^1 \omega_1(\tau) d\tau \tag{4}$$

where a is the radius of the contact region; R is the radius of the spherical indenter in contact with the cartilage; v is Poisson's ratio; G is the elastic shear modulus; and numerical values from the term $\int_0^1 \omega_1(\tau) d\tau$ allows for the computation of κ at given values of the contact area to height of specimen ratio (aspect ratio, $\frac{a}{h}$) and v.

The indentation approach offers advantages that were attractive for use in this thesis. Mainly, the theoretical derivations of mechanical properties include subchondral bone material. This enables indentation for full-surface mapping of mechanical properties over a finite number of indentation sites (Athanasiou et al. 1991; Manzano et al. 2016; Sim et al. 2017a). For the *ex vivo*[11] portion of this thesis, I collaborated with Biomomentum, Inc. to utilize their proprietary technology to compute full-surface maps of 1. instantaneous modulus; and 2. Quantitative Parameter (QP), a unitless parameter providing information on surface electromechanical properties. Instantaneous modulus reflects the compressive resistance in response to an instantaneous application of load. In healthy tissue, the instantaneously increased interstitial fluid pressure combined with low permeability would result in an increased stiffness (or higher instantaneous modulus) (Hayes et al. 1972; Mow et al. 1984; Patel et al. 2019). Cartilage experiencing degeneration would not generate the same resistance due to greater permeability (Armstrong and Mow 1982) and a compromised collagen network (Saarakkala et al. 2010). Therefore, instantaneous modulus of degenerated cartilage would be expected to be relatively lower than that of healthy cartilage. QP provides insight into electromechanical properties by measuring surface streaming potential with 37 micro-electrodes on the surface of a 6.36 mm indenter (Sim et al. 2014). The QP reflects the number of micro-electrodes whose streaming potential hits a minimum threshold; lower values indicate fewer micro-electrodes in contact, and stiffer cartilage (Sim et al. 2014). The unique automated indentation mapping technology

---

[11] An entire excised tibiofemoral joint with all intra-capsular tissues intact.

in combination with MR imaging and loading in an *ex vivo* porcine stifle model enabled a novel exploration of the relationships between MR-derived cartilage metrics and mechanical properties. *The third manuscript of my thesis explored these relationships and built a 3D voxel-by-voxel statistical map predicting mechanical properties in a porcine model.*

1.4.2 Changes in Mechanical Properties with OA

Structural changes in articular cartilage with OA (see Section 1.2) result in quantifiable changes in the mechanical properties of the tissue. Changes in cartilage mechanical properties with OA are observed at different macroscopic levels. For example, Alexopoulos et al. (2005) used a micro-pipette aspiration technique to calculate the force deflection profile of healthy versus OA human femoral head chondrocytes embedded within their pericellular matrix (chondrons). They observed that OA chondrons had lower Young's modulus than normal chondrons (Alexopoulos et al. 2005). Additionally, using a modified biphasic model to quantify the transient creep response, they found that OA chondrons had increased permeability (Alexopoulos et al. 2005). In a study of full-thickness articular cartilage explants from humans undergoing total knee arthroplasty (TKA; OA) or human cadavers (healthy), Robinson et al. (2016) found that explants from the tibia of OA patients had lower shear modulus than healthy controls. Further, compared to healthy cartilage, osteoarthritic cartilage had increased water content (Mankin and Thrasher 1975), increased permeability (Boschetti and Peretti 2008), decreased Young's modulus (Alexopoulos et al. 2003), decreased equilibrium shear modulus (Robinson et al. 2016), and decreased equilibrium elastic modulus (Boschetti and Peretti 2008). As discussed in Section 1.2, these changes in properties result in an altered loading environment via reduced ability to adequately counteract swelling pressure with a disorganized solid matrix. The ability to glean insightful information regarding cartilage mechanical properties (or structural integrity) from non-invasive imaging methods such as MRI will vastly improve our ability to monitor joint health *in vivo*.

1.5 Relating MRI Parameters to Cartilage Mechanical Properties

The estimation of tissue mechanical properties from MRI, a non-invasive modality able to provide comprehensive information on composition and morphology *in vivo*, is an excellent endeavour for scientific research. This work could dramatically advance our ability to detect OA and monitor disease progression; model and predict tissue loading tolerances; and track response to interventions such as exercise or pharmacology. Currently, much of the work relating MRI parameters to mechanical properties of the articular cartilage is driven by research with explants (Hatcher et al. 2017; Juras et al. 2009; Kurkijärvi et al. 2004; Lammentausta et al. 2006; Nebelung et al. 2018; Nebelung et al. 2017b; Nieminen et al. 2004; Nissi et al. 2007; Nissi et al. 2004; Rautiainen et al. 2015; Wheaton et al. 2005) using several imaging protocols (T1, T2, T1ρ, delayed gadolinium-enhanced MRI of cartilage (dGEMRIC)) and mechanical testing procedures (unconfined compression, confined compression). These studies have provided fundamental information regarding relationships between parametric mapping techniques and mechanical properties. A summary of studies that have related MR parametric mapping to mechanical properties of the articular cartilage is provided in Table 1.5.1.

To complete a comprehensive table, additional parametric mapping techniques outside the scope of this thesis were included (T1ρ, dGEMRIC). Briefly, T1ρ — or spin-lattice relaxation in the rotating frame — is a surrogate measure of PG content (Akella et al. 2001; Duvvuri et al. 1997) as well as fixed charge density (Wheaton et al. 2004). dGEMRIC also provides indirect information on PG content (by quantifying GAG concentration); however, it requires intravenous administration of a contrast agent (Burstein et al. 2001; Tiderius et al. 2006; Young et al. 2005), and lengthy pre-imaging protocols (Burstein et al. 2001). T1ρ has gained popularity over dGEMRIC because it is non-invasive, though this technique is not available on all scanners.

A few studies have aimed to quantify a relationship between mechanical properties and parametric mapping techniques on an excised joint surface (Table 1.5.1). Samosky et al. (2005) obtained dGEMRIC scans of tibial plateaus from human patients undergoing TKA. Indentation tests were completed at pre-determined grid locations across the tibial surface and registered to the dGEMRIC images to obtain site-specific estimates of GAG concentration (Samosky et al. 2005). Similarly, Keenan et al. (2015) utilized a surface indentation technique (Athanasiou et al. 1991; Keenan et al. 2009) to perform creep indentation tests at 7 specified sites along the surface of human cadaveric patellas. T1ρ and T2 images were obtained, however, data were pooled for analysis (i.e., spatial relationships were not investigated) (Keenan et al. 2015).

Table 1.5.1: Relationships between MR parametric mapping and mechanical properties of articular cartilage. With the exception of Samosky et al (2005) and Keenan et al (2015), all studies were completed on cartilage explants from either the patella, femur, or tibia. Bulk (mean) results are presented for brevity. Pearson correlation coefficients (r) with statistical significance (p) are displayed. Agg. Mod. = Aggregate modulus; Perm. = Permeability; Young's Mod. = Young's modulus; Dynamic Mod. = Dynamic modulus; Inst. Mod. = Instantaneous modulus; IM/YM = Instantaneous modulus/Young's modulus ratio.

Study	**Specimen**	**Parameter**	**Mechanical Property**						
			Agg. Mod. (MPa)	*Perm. (m^4/Ns)*	*Young's Mod. (MPa)*	*Dynamic Mod. (MPa)*	*Inst. Mod. (MPa)*	*IM/YM*	*Peak Indenter Load (N)*
Hatcher et al (2017)	Porcine (n=37)	*T1ρ*	-0.75 (< 0.001)	0.93 (< 0.001)	-	-	-	-	-
Juras et al (2009)	Human (n=13)	*T2*	-	-	0.47 (*N/A*)	-	0.12 (*N/A*)	-0.46 (*N/A*)	-
		dGEMRIC	-	-	-0.87 (*N/A*)	-	0.16 (*N/A*)	0.93 (*N/A*)	-
		Apparent Diffusion Constant	-	-	-0.52 (*N/A*)	-	0.38 (*N/A*)	0.30 (*N/A*)	-
Kurkijärvi et al (2004)	Human (n=77)	*T2*	-	-	-0.27 (< 0.05)	-0.10 (*N.S*)	-	-	-
		dGEMRIC	-	-	-0.49 (< 0.01)	-0.47 (< 0.01)	-	-	-

Table 1.5.1 – *Continued from previous page*

Lammentausta et al (2006)[*]	Human (n=75)	*T2*	-	-	-0.40 (< 0.01)	-0.45 (< 0.01)	-	-	-
		dGEMRIC	-	-	0.43 (< 0.01)	0.42 (< 0.01)	-	-	-
Nebelung et al (2017)[†]	Human (n=20)	*T2*	-	-	-	-	-0.27 to -0.24 (*N.S*)	-	-
		$T1\rho$	-	-	-	-	0.17 to 0.25 (*N.S*)	-	-
Nebelung et al (2018)[‡]	Human (n=18)	$T1\rho$ *(500 Hz)*	-	-	-0.05 to -0.40 (0.10 - 0.85)	-	-	-	-
Nieminen et al (2004)	Bovine (n=12)	*T2*	-0.33 (*N/A*)	-	-0.31 (*N/A*)	0.20 (*N/A*)	-	-	-
		dGEMRIC	-0.85 (*N/A*)	-	-0.84 (*N/A*)	-0.47 (*N/A*)	-	-	-
Nissi et al (2004)	Bovine (n=20)	*T2*	-	-	-0.25 (*N.S*)	0.02 (*N.S*)	-	-	-
		dGEMRIC	-	-	-0.61 (< 0.05)	-0.45 (< 0.05)	-	-	-

[*] Lammentausta et al (2006) compared results from imaging in a research-dedicated 9.4T scanner and a clinical grade 1.5T scanner. The results presented are for the 9.4T scanner.

[†] Nebelung et al (2017) performed a neat study where human patellar explants were loaded with an MRI-compatible device able to perform quasi-static uniaxial compression on the sample. T2 and T1ρ maps were obtained at baseline, during loading, and during unloading. They collected 'Instantaneous Young's Modulus', which I assume (based on the experimental parameters) is the estimation of elastic response when the sample is not yet in equilibrium.

[‡] Nebelung et al (2018) used the same loading apparatus as their 2017 paper, with minor adjustments. Spearman correlation coefficients were used to determine the relationship between Young's modulus and relative change in T1ρ between loading scenarios.

Table 1.5.1 – *Continued from previous page*

Nissi et al (2007)	Human (n=12)	*T2*	-	-	-0.71 (< 0.01)	-0.48 (*N.S*)	-	-	-	
		dGEMRIC	-	-	-0.47 (*N.S*)	-0.52 (*N.S*)	-	-	-	
	Porcine (n=11)	*T2*	-	-	0.16 (*N.S*)	-0.13 (*N.S*)	-	-	-	
		dGEMRIC	-	-	-0.29 (*N.S*)	-0.15 (*N.S*)	-	-	-	
	Bovine (n=12)	*T2*	-	-	0.51 (*N.S*)	0.88 (< 0.01)	-	-	-	
		dGEMRIC	-	-	-0.32 (*N.S*)	0.12 (*N.S*)	-	-	-	
Rautiainen et al (2015)	Human (n=14)	*T2*	-	-	-0.65 (< 0.05)	-0.49 (*N.S*)	-	-	-	
		dGEMRIC	-	-	0.48 (*N.S*)	0.52 (*N.S*)	-	-	-	
		T1ρ (125 Hz)	-	-	-0.67 (< 0.01)	-0.62 (< 0.05)	-	-	-	
		T1ρ (250 Hz)	-	-	-0.80 (< 0.01)	-0.72 (< 0.01)	-	-	-	
		T1ρ (500 Hz)	-	-	-0.81 (< 0.01)	-0.76 (< 0.01)	-	-	-	
		T1ρ (1000 Hz)	-	-	-0.64 (< 0.05)	-0.68 (< 0.01)	-	-	-	
Wheaton et al (2005)	Bovine (n=42)	*1/T1ρ (500 Hz)*	0.91 (*N/A*)	0.93 (*N/A*)	-	-	-	-	-	

Table 1.5.1 – *Continued from previous page*

Keenan et al (2015)	Human (n=79)	*T2*	-	-	-	-	-0.09 (0.490)	-	-
		T1ρ (500 Hz)	-	-	-	-	0.12 (0.340)	-	-
		T1ρ (1000 Hz)	-	-	-	-	0.17 (0.194)	-	-
Samosky et al (2005)	Human (n=119)	*dGEMRIC*	-	-	-	-	-	-	0.56 (< 0.0001)

Unfortunately, design challenges and critical limitations exist with the estimation of mechanical properties across a whole joint surface with MRI. Cartilage explant studies neglect the interaction of multiple tissues in a whole-joint model. These limitations potentially reduce the fidelity of applying these MR-derived mechanical properties in mathematical models of articular cartilage mechanics. *My third manuscript aimed to directly address this issue.*

1.6 *Ex Vivo* Models - Bridging the Gap Between *In Vitro* and *In Vivo*

The use of an *ex vivo* knee model has been scarcely investigated in the estimation of cartilage response to loading. In a pair of studies, human cadaveric femoro-patellar joints were loaded in an MRI-compatible static loading device to simultaneously image the joint in a loaded state (static loading at 150% body weight) and an unloaded state (Herberhold et al. 1999; Herberhold et al. 1998). While these studies were interested in quantifying global deformation of the articular cartilage, the *ex vivo* approach can enable the 3D quantification and visualization of cartilage deformation following physiologic articulation of the whole joint. Recently, Nebelung et al. (2017) placed cartilage explants within a polyvinyl-siloxane-covered bone mold for loading and imaging in an MR suite. This work was able to investigate cartilage mechanics in an explant model while mimicking an *in situ* loading environment (Nebelung et al. 2019; Nebelung et al. 2017a). Following theory derivation and testing in explant configurations (Neu and Hull 2003; Neu et al. 2005), a series of studies (Butz et al. 2011; Chan et al. 2009a; Chan et al. 2009b; Martin et al. 2009; Neu and Walton 2008) adapted a simultaneous cyclic loading and imaging protocol from work in cardiac imaging (displacement encoding with stimulated echoes) (Aletras et al. 1999) to capture cartilage deformation of *ex vivo* tibiofemoral joints. In fact, the group has demonstrated the utility of the approach *in vivo* in a clinical-grade MRI scanner (Chan et al. 2016). However, severe time constraints (approximately 35 minutes to obtain a single 2D slice, following a period of pre-loading) preclude the use of this approach in a clinical setting, at this time. Ideally, a practical alternative would be to create a statistical model able to identify relationships between commonly acquired MR metrics (i.e., cartilage deformation, T2) and mechanical properties of the articular cartilage (i.e., instantaneous modulus) to 1) improve mathematical models of knee joint tissues; and 2) build models to quantify cartilage responses to load, and monitor changes in response with disease. *This thesis will work toward the development of these statistical models.* This will enable the use of imaging, a non-invasive modality, to provide physiological estimates of mechanical properties obtained via *ex vivo* methods that would otherwise be captured using invasive procedures.

1.7 Comparative Anatomy - Use of a Porcine Stifle Model as a Proxy for Human Knee Joints

The porcine stifle is located on the hindlimb between the articulations of the hip and the tarsal (hock). The stifle joint has a different operational range of motion compared to the human due solely to the differences in mechanics between bipeds and quadrupeds (Proffen et al. 2012). Most notably, porcine stifle joints are unable to reach full extension (Proffen et al. 2012). There are also morphological differences in intracapsular structures. First, the anteromedial and posterolateral bundles of the ACL in the porcine stifle are physically separated by the anterior root of the lateral meniscus (Proffen et al. 2012; Tantisricharoenkul et al. 2014). As well, the ACL:Tibial Plateau ratio for the length of the ACL was found to be significantly longer in porcine specimens compared to humans (Proffen et al. 2012). Using this normalization process, porcine specimens had a significantly longer posterior cruciate ligament, significantly smaller intercondylar notch, and significantly wider medial meniscus than human cadaveric knee specimens (Proffen et al. 2012). These morphological differences in porcine specimens, however, had no significant effect on *in situ* forces in the whole intact ACL in comparison to human specimens (Xerogeanes et al. 1998). In fact, in comparison to goat and sheep specimens, the pig was determined to be the closest correlate to the human ACL for animal modeling research (Xerogeanes et al. 1998). Morphological differences between porcine and human specimens are apparent. However, these differences appear to have minimal effect on the function of important intracapsular soft tissues.

Differences in cartilage-specific structure and properties are also important to consider. In a study of cultured chondrocytes from different species, Schulze-Tanzil et al. (2009) determined that in terms of proliferation rate and cartilage-specific ECM expression, chondrocytes from porcine specimens were closest to those extracted from human cartilage. Using T2 relaxation and polar light microscopy, Nissi et al. (2006) showed a tri-laminar orientation of the cartilage collagen in most porcine specimens (like humans); those showing a quin-laminar appearance could arguably be skeletally immature as vigourous remodeling of the collagen network occurs during maturation (Rieppo et al. 2009). In a study that compared cartilage mechanical properties in three quadruped mammals (ovine, bovine, porcine), it was determined that explants from the tibial and femoral surfaces of porcine specimens had an equilibrium modulus of $0.74 \pm 0.15 MPa$ and permeability of $8.1 \pm 2.5 \times 10^{-16} m^4/N \cdot s$ (McLure et al. 2012). For comparison, Armstrong and Mow (1982) estimated an equilibrium modulus of $0.79 \pm 0.36 MPa$ and permeability of $0.47 \pm 0.36 \times 10^{-14} m^4/N \cdot s$ for explants from the human patella. These values were different from Athanasiou et al. (1991) who showed a range of 0.530–$0.701 MPa$ and 1.137–$2.173 \times 10^{-15} m^4/N \cdot s$ for equilibrium modulus and permeability respectively on different sites of the femoral cartilage in humans. In a direct comparison of human and porcine cartilage, Nissi et al. (2007) estimated equilibrium modulus to be $0.53 \pm 0.25 MPa$ in human patellar cartilage and $0.85 \pm 0.25 MPa$ in porcine patellar cartilage; this difference was significant ($p < 0.05$). Both inter- and intra-species variation in material properties is apparent, and are likely a factor of 1. specimen age and disease severity; 2. sampling location; and 3. testing methods. Therefore, initial testing and building of a statistical model between MR parametric mapping parameters and articular cartilage mechanical properties in a porcine model is fiscally feasible, but future replication of the project in human cadaveric models is recommended.

1.8 Gaps in the Literature

Several gaps in the literature were addressed with this thesis. Specifically:

1) The influence of biological sex on the deformation of tibial and femoral articular cartilage following running in asymptomatic adults;

2) The effect of daily cumulative knee load and BMI on tibial and femoral articular cartilage response to running in young healthy women; and

3) The estimation of instantaneous modulus and electromechanical properties of femoral cartilage from thickness and T2 relaxation maps following static loading in an *ex vivo* porcine stifle model.

1.8.1 Sex-Differences in Cartilage Deformation

The prevalence of painful knee OA is higher in females (Hawker et al. 2000; Srikanth et al. 2005), and the cause of this sex-disparity is not well understood. It is reported that females have thinner tibiofemoral cartilage (Cicuttini et al. 2002; Otterness and Eckstein 2007) and less tibiofemoral cartilage volume (Cicuttini et al. 1999; Ding et al. 2003) than males, even when adjusted for common covariates. These morphological and compositional differences may manifest in concomitant, systematic differences in loading patterns in the tibiofemoral compartment. *Chapter 2 contains the first manuscript of my thesis, where advanced statistical techniques were employed to evaluate cartilage thickness changes following running in males and females, and investigate the role of biological sex.*

1.8.2 Role of Daily Cumulative Knee Load in Cartilage Conditioning

Cartilage conditioning is a theory that describes the phenomenon whereby healthy cartilage will undergo mechanically-driven re-modelling to support areas of higher stress (Seedhom 2005). The few studies that have investigated the *in vivo* relationship between physical activity history and cartilage response to loading have highlighted a link between habitual physical activity and cartilage conditioning (Gatti et al. 2017; Van Ginckel et al. 2010). What is unknown is whether a general accumulation of knee joint load over a day is related to the magnitude of tibiofemoral cartilage change (thickness, volume, T2 relaxation) following an acute running stimulus. *Chapter 3 contains the second manuscript of my thesis, where musculoskeletal modelling, accelerometry, and MRI were used to quantify the relationship between daily cumulative knee load and tibiofemoral cartilage response to running in healthy women.*

1.8.3 *Ex Vivo* Porcine Stifle Model for the Estimation of Cartilage Mechanical Properties from MRI-Metrics

Many studies to date have explored the interaction of MR-derived metrics with mechanical properties of the articular cartilage using explant-based models (Hatcher et al. 2017; Juras et al. 2009; Kurkijärvi et al. 2004; Lammentausta et al. 2006; Nebelung et al. 2018; Nebelung et al. 2017b; Nieminen et al. 2004; Nissi et al. 2007; Nissi et al. 2004; Rautiainen et al. 2015; Wheaton et al. 2005). However, limited work using whole-joint *ex vivo* models confirm that estimates from explant models do not account for the complex tissue interactions that occur in the joint (Narmoneva et al. 1999; Schinagl et al. 1997; Schinagl et al. 1996). *Chapter 4 contains the third manuscript of my thesis, where two datasets (full-surface automated indentation mapping and MRI) were uniquely combined to provide the data necessary to predict articular cartilage mechanical properties from MRI in a porcine stifle model.* A diagram of the central themes in this thesis is presented in Figure 1.9.1.

1.9 Specific Thesis Objectives

The specific objectives of this thesis were:

Chapter 2

1) quantify the specific, regional changes in tibial and weight-bearing femoral cartilage deformation following an acute bout of running in young healthy adults using Statistical Parametric Mapping;
2) identify regional differences in tibiofemoral cartilage thickness between males and females; and
3) explore the influence of biological sex on the deformational response of tibiofemoral cartilage.

Chapter 3

1) determine the relationship of the number of steps per day, Joint Reaction Force impulse, and their interaction (i.e., daily cumulative knee load) on tibial and femoral thickness, volume, and T2 relaxation change following an acute bout of running in healthy women; and
2) investigate the associations of BMI, steps per day, and their interaction on tibial and femoral thickness, volume, and T2 relaxation change.

Chapter 4

1) calculate voxelwise relationships between mechanical properties (Instantaneous Modulus, QP) and femoral cartilage response to static loading via MRI (thickness, T2 relaxation) in an intact porcine stifle model, and determine spatial clusters of significant relationships using a random permutation method.

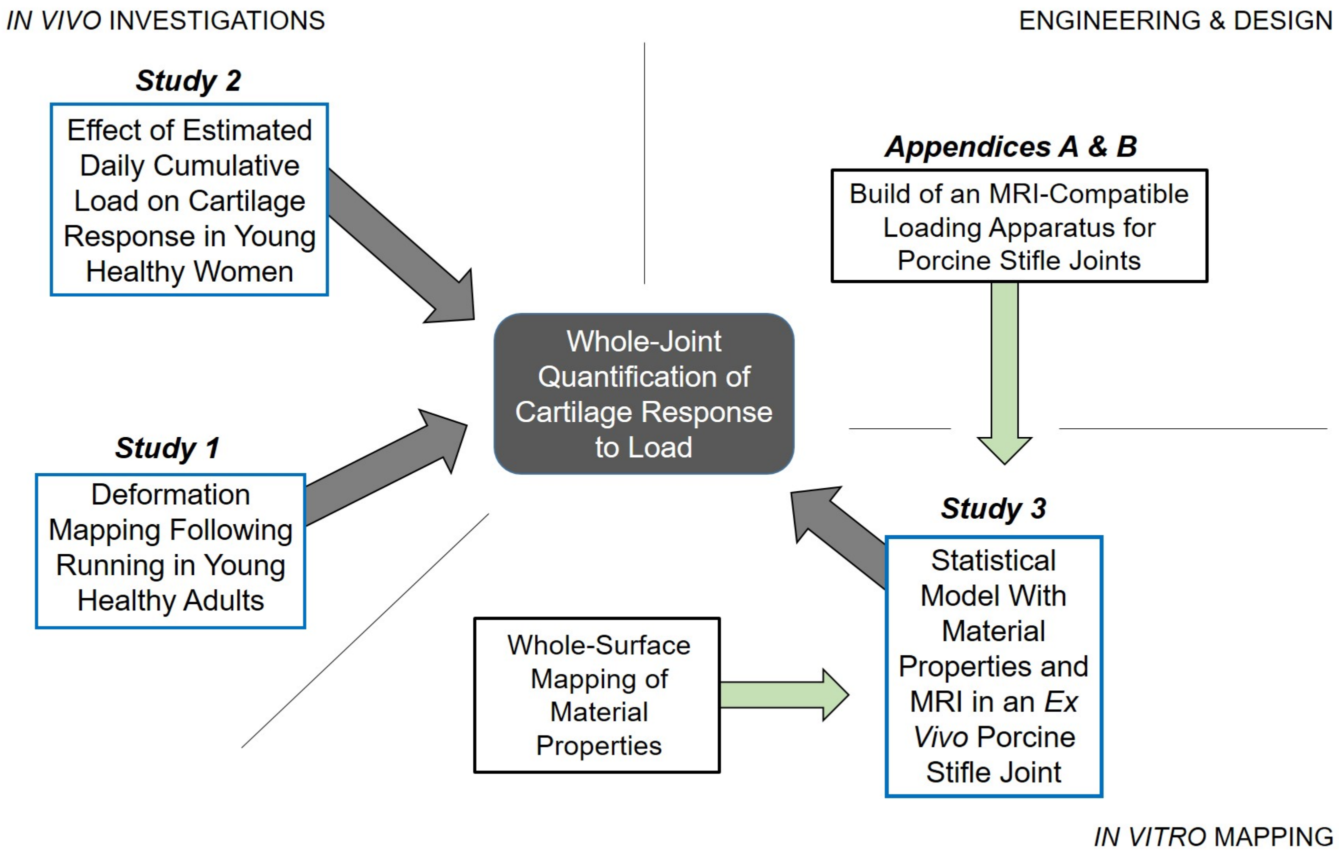

Figure 1.9.1: Schematic organization of the central themes in this thesis. Studies 1 and 2 took an *in vivo* approach to the investigation of cartilage response to acute activity. Study 3 was a multi-disciplinary approach where a combined imaging and indentation protocol were used to create a 3D statistical model of relationship between imaging parameters and cartilage material properties in an *ex vivo* model.

2 — Modeling Regional Knee Cartilage Deformation Following Running in Healthy Adults Using Statistical Parametric Mapping

This paper was submitted to Magnetic Resonance Materials in Physics, Biology, and Medicine on 3 July 2020, and is currently in revision (Submission # MRMP-D-20-00119-R1). This manuscript was transcribed to LaTeX and follows the formatting guidelines required by McMaster University's School of Graduate Studies.

A NEW TECHNIQUE TO EVALUATE THE IMPACT OF RUNNING ON KNEE CARTILAGE DEFORMATION BY REGION

Elora C. Brenneman Wilson[a], Anthony A. Gatti[b,c], Monica R. Maly[a,c,d]*

[a]Department of Kinesiology, McMaster University, Hamilton, ON Canada
[b]NeuralSeg Ltd., Hamilton, ON Canada
[c]School of Rehabilitation Science, McMaster University, Hamilton, ON Canada
[d]Department of Kinesiology, University of Waterloo, Waterloo, ON Canada

*Corresponding Author:
Monica R. Maly
Burt Matthews Hall, Rm 1036
Department of Kinesiology
University of Waterloo
200 University Avenue West
Waterloo, ON N2L 3G1
Phone: (519) 888-4567 ext. 37916
E-mail: mrmaly@uwaterloo.ca

Acknowledgements

Thank-you to Imaging Research Centre director Norm Konyer, as well as technicians Julie Lecomte, Carol Awde, Cheryl Contant, and Toni DiLeonardo for ensuring the quality of the MRI images for this study. Thank you to Emily Wiebenga for assistance with data collections. E. C. Brenneman Wilson was funded by a Canadian Graduate Scholarship from the Natural Sciences and Engineering Research Council of Canada (NSERC). A. A. Gatti was supported by an Ontario Graduate Scholarship and The Arthritis Society. M. R. Maly holds The Arthritis Society Stars Mid-Career Development Award funded by the Canadian Institutes of Health Research-Institute of Musculoskeletal Health and Arthritis.

Abstract

Object — When measuring changes in knee carilage thickness in vivo after loading, mean values may not reflect local changes. The objectives of this investigation were: 1) use statistical parametric mapping (SPM) to determine regional deformation patterns of tibiofemoral cartilage in response to running; 2) quantify regional differences in cartilage thickness between males and females; and 3) explore the influence of sex on deformation.

Materials and Methods — Asymptomatic males (n=15) and females (n=15) had MRI imaging of their right knee before and after 15-minutes of treadmill running. Medial and lateral tibial, and medial and lateral weight-bearing femoral cartilage were segmented. SPM was completed on cartilage thickness maps to test the main effects of Running and Sex, and their interaction. F-statistic maps were thresholded; clusters above this threshold indicated significant differences.

Results — Deformation was observed in all four compartments; the lateral tibia had the largest area of deformation ($p < 0.0001$). Thickness differences between sexes were observed in all four compartments, showing females have thinner cartilage ($p \leq 0.009$). The lateral tibia had small clusters indicating an interaction of sex on deformation ($p \leq 0.012$).

Discussion — SPM identified detailed spatial information on tibiofemoral cartilage thickness differences observed after Running, and between Sexes and their interaction.

Keywords: Cartilage, Articular; Running; Magnetic Resonance Imaging; Statistics

2.1 Introduction

Running causes deformation in knee articular cartilage to distribute and dissipate mechanical loads. Magnetic resonance imaging (MRI) has been used to quantify global changes in cartilage volume and thickness following an acute bout of running (Boocock et al. 2009; Kersting et al. 2005; Kessler et al. 2006; Mosher et al. 2005; Niehoff et al. 2011; Subburaj et al. 2012). After running, cartilage volume remains unchanged in the medial tibia, but decreases in the lateral tibia (-4.0% to -6.1%) (Boocock et al. 2009; Kersting et al. 2005; Niehoff et al. 2011), whole tibia (-2.6% to -3.6%) (Kersting et al. 2005; Kessler et al. 2006), and whole femur (-3.0% to -3.2%) (Kersting et al. 2005; Niehoff et al. 2011), independent of running distance and MRI scanner used. However, changes in cartilage thickness following running were less consistent. Decreases in tibial cartilage thickness following running have ranged from 2.2% to 13.6% (Mosher et al. 2005; Niehoff et al. 2011; Subburaj et al. 2012). This range could stem from methodological differences in the quantification of cartilage thickness. As well, it is likely that presenting the mean thickness change in whole cartilage regions (e.g., medial tibia), or cartilage sub-regions defined *a priori* based on anatomical location, may underestimate true changes in regional thickness. That is, it is likely these mean values from pre-defined regions "wash out" localized changes. While important in providing researchers a strategy to define regions of interest, loading and wear patterns do not fall explicitly within these anatomical definitions. A pixelwise (i.e., by-pixel) approach that can identify clusters that demonstrate significant deformation, without *a priori* identification of anatomically-defined cartilage regions, could be an ideal solution.

Statistical parametric mapping (SPM) may be a unique and useful alternative to subregional analyses of cartilage. This technique employs basic statistical tests such as z-scores, Student's t-tests, or F-statistics for every pixel (or voxel) of an image. Suprathreshold clusters, or clusters of pixels which reach a defined threshold are then identified from these maps of statistical tests. The minimum cluster size required for a cluster to be deemed statistical significant is then determined, often using Random Field Theory (Ashby 2011; Worsley et al. 1996) or Monte Carlo simulation (Nichols and Hayasaka 2003; Nichols 2012), which address the issue of multiple comparisons. SPM was first introduced in fMRI analysis (3D), and has since been adopted in biomechanics to evaluate 1-Dimensional (1D) continuous time-series (Li et al. 2016; Pataky 2010; Pataky et al. 2013). It has also been used to assess differences between populations in cartilage composition measured using MRI (T2 relaxation, T1ρ relaxation). For example, regional group differences in tibiofemoral and patellar cartilage T1ρ were quantified in ACL-injured patients and a separate cohort of patients with knee osteoarthritis (OA), each compared to age-matched controls (Pedoia et al. 2017).

Using the same technique, regional variations in hip cartilage composition were quantified between clinical hip OA patients and healthy controls (Pedoia et al. 2016). To our knowledge, this approach has not been adopted for cartilage deformation analyses. SPM could provide unique insight to specific regional changes in cartilage deformation due to running.

Knee OA, a degenerative joint disease characterized by cartilage loss, is both more prevalent (Srikanth et al. 2005) and severe in females than males (Hawker et al. 2000; Srikanth et al. 2005)[1]; yet relatively little work has explored sex-differences in the function of cartilage under mechanical loading, limiting our understanding of the underlying mechanisms of this disease. Studies have shown sex-differences in cartilage morphology, static knee alignment, and cartilage composition that may play a role in cartilage mechanics. First, females have thinner tibiofemoral cartilage (Cicuttini et al. 2002; Otterness and Eckstein 2007) and less tibiofemoral cartilage volume (Cicuttini et al. 1999; Ding et al. 2003) than males after multivariate adjustment for age, body size, and bone size. Second, females tend to have greater valgus knee alignment (Wise et al. 2012), and greater quadriceps angle (Horton and Hall 1989). Finally, in an OA population, females had greater T1ρ relaxation times in the lateral knee compartment compared to males suggestive of fewer proteoglycans (poorer cartilage quality) (Kumar et al. 2015). It is possible that a combination of these morphological and biomechanical factors could result in differing patterns of cartilage deformation when subjected to activity between females and males. Hudelmaier et al. (2001) showed a -4.5±1.3% and -6.2±2.1% decrease in patellar cartilage thickness in young females and males, respectively following 30 deep knee-bends; sex-differences were not explicitly tested in this study. Boocock et al. (2009) showed that tibial and femoral cartilage volume changes following approximately 30 minutes of running (5000 steps) were not different between sexes. However, the absence of sex differences in this study may be due to the use of a global approach, where differences were analyzed using means of the entire region-of-interest. Statistical Parametric Mapping may have the capacity to identify sex-differences in thickness, as well as deformational patterns, between males and females following running. This could imply differences in strain distributions across the tibiofemoral joint between sexes, and provide insight to mechanical factors contributing to the sex disparity in prevalent knee OA.

The purpose of this investigation was three-fold: 1) use statistical parametric mapping to quantify the specific, regional changes in tibial and weight-bearing femoral cartilage deformation following an acute bout of running in young healthy adults; 2) identify regional differences in tibiofemoral cartilage thickness between males and females; and 3) explore

---

[1] Unless gender (man, woman) was explicitly recorded, all previous studies that explored sex analyses were changed to sex-based language (male, female) for consistency.

the influence of biological sex on the deformational response of tibiofemoral cartilage. We hypothesized the following: 1) the lateral tibia (Boocock et al. 2009; Kersting et al. 2005; Niehoff et al. 2011) would contain the largest, statistically significant cluster of deformation following running; and 2) females would have thinner cartilage than males throughout the tibiofemoral compartment. The tertiary purpose was exploratory and therefore no a priori hypothesis was defined. To our knowledge, no study has quantified specific regional changes using F-statistic parametric mapping. This unique analysis approach will enable the visualization of regional changes in cartilage thickness following running. Further, no study has investigated sex-differences in acute changes in pixelwise tibiofemoral cartilage thickness. The findings will show whether cartilage deformation may be influenced by sex.

2.2 Methods

This is a prospective cohort study (Level II) which received clearance through the Hamilton Integrated Research Ethics Board. Participants provided written, informed consent.

2.2.1 Recruitment

All participants were recruited through poster advertisements and word-of-mouth. Young, recreationally active females (n=15) and males (n=15) who self-reported they were absent of musculoskeletal injuries that would hinder participation in a running activity were recruited. Further, participants were excluded if they had: prior orthopaedic surgery to the right lower limb (test knee); self-reported lower-limb pain within the last 3-months; symptomatic knee OA according to the American College of Rheumatology diagnostic criteria (Altman et al. 1986); a score on the Lower Extremity Function Scale (LEFS) of less than 74 (Wang et al. 2009); and, to be comfortably accommodated in the MRI scanner, a body mass of greater than 90 kg. All eligible participants were screened for contraindications to MRI by an experienced, trained MRI technician: presence of implants, cardiac or neural stents, aneurysm clip(s), and/or claustrophobia. Data from the men were collected in a previous study in our lab investigating T2 relaxation and volume changes in the tibiofemoral cartilage following running and bicycling (Gatti et al. 2017). Imaging data from the women were subsequently collected using the identical protocol.

2.2.2 Protocol

2.2.2.1 Magnetic Resonance Imaging

Participants were asked to attend one visit at the Imaging Research Centre at St. Joseph's Healthcare in Hamilton, Ontario, Canada. Prior-to and immediately following 15-minutes of treadmill running two sets of MR images were acquired on the right knee.

All imaging visits occurred at 8 am to prevent cumulative effects of daily activity on tibiofemoral cartilage (Gatti et al. 2017; Mosher et al. 2010). Participants were asked to minimize their physical activity prior to their visit and either drive to the IRC, or accept a complimentary taxicab ride to minimize the effects of weight-bearing activity on tissue outcomes. To mitigate loading effects, upon arrival participants rested supine for 30 minutes (Gatti et al. 2017; Okafor et al. 2014; Subburaj et al. 2012).

Following arrival and rest, each participant was brought into the scanner room via wheelchair. The participant was positioned on the MRI bed of a 3-Tesla MRI scanner (MR750 Discovery; GE Healthcare, Milwaukee, WI) with their right knee in an 8-channel transmit/receive radiofrequency lower-extremity coil (Invivo Corporation, Gainsville, FL). The participant's lower limb was marked with indelible ink to reduce repositioning effects for post-imaging. A 3D fat-saturated fast spoiled gradient recalled (3D-FSPGR) scan was collected pre- and post-activity (Gatti et al. 2017) and was used for subsequent cartilage segmentation. The scan parameters were as follows: TR = 17.368 ms; TE = 5.816 ms; FOV = 16 cm; Frequency = 127.780 MHz; Matrix Size = 512×512; Pixel Size = 0.3125×0.3125 mm; Slice Thickness = 1 mm; Echo Train Length = 1; Pixel Bandwidth = 122.070 Hz/px; NEX = 1; Flip Angle = 18^o.

2.2.2.2 Treadmill Running

Participants ran for 15-minutes on a commercial treadmill (5.1AT, Advanced Fitness Group, Cottage Grove, WI). Their instructions were to run at a speed of "moderate" effort that they could maintain comfortably for 15-minutes. Immediately following, participants were re-positioned in the MRI scanner for post-activity imaging. 3D-FSPGR images were obtained to capture the change in cartilage thickness and volume following running. Imaging occurred approximately 3-minutes following the cessation of exercise.

2.2.3 Image Analysis

Tibiofemoral cartilage was automatically segmented from the pre- and post-activity 3D-FSPGR volumes using a multi-stage convolutional neural network framework (Gatti and

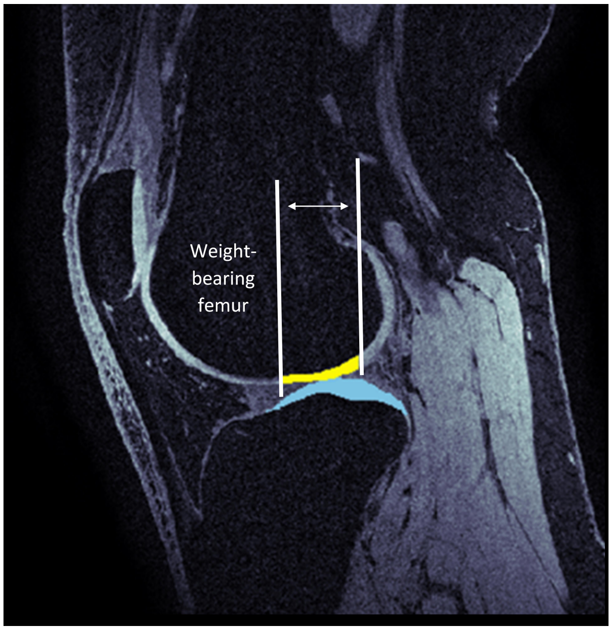

Figure 2.2.1: The weight-bearing femur was determined using methods described by Eckstein et al. (2006).

Maly 2019). Since manual segmentation is still considered the gold standard, all automatically-generated segmentations were manually checked in 3DSlicer software and adjusted if necessary. Only 1 out of 60 volumes (pre and post for n=30) required minor manual correction. As is standard in quantitative cartilage analysis, the anterior and posterior borders of the weight-bearing femoral cartilage were defined as the intercondylar notch and 60% of the distance from the intercondylar notch to the most posterior aspect of the femoral condyles, respectively (Eckstein et al. 2006; Eckstein and Wirth 2011; Schneider et al. 2012) (Fig 2.2.1). Separate medial and lateral weight-bearing femoral cartilage regions were identified. Medial and lateral tibial cartilage, and medial and lateral weight-bearing femoral cartilage were analyzed separately using custom code written in Python 2.7.

Two-dimensional cartilage thickness maps were created separately for each region of interest. First, in three-dimensions, for every voxel on the bone-cartilage interface, the minimum Euclidean distance to the articular surface was calculated in millimetres (mm). Second, to create two-dimensional maps, the three-dimensional maps were flattened along the inferior-superior axis by taking the maximum thickness value. Due to limited curvature of the tibial plateau and of the weight-bearing femoral cartilage region, this resulted in either one unique cartilage thickness value per pixel, or a value of 0 indicating no cartilage. To enable group analyses, all two-dimensional thickness maps were cropped to tightly bind the cartilage edges. Then, 2D Affine registration was used to register all maps to a reference thickness map. Cropping and registration was performed independently for each cartilage region. All analyses were performed on the registered maps.

2.2.4 Statistical Analysis

Descriptive statistics (means, standard deviations) for cartilage volume and mean cartilage thickness were reported. Sex differences pre- and post-activity were reported with independent samples t-tests using a Sidak correction for multiple comparisons. Percent change in cartilage volume and mean cartilage thickness between regions (medial and lateral tibia, and medial and lateral weight-bearing femur) were tested with a one-way analysis of variance (ANOVA). A Sidak correction was used to account for multiple comparisons.

To explore the reproducibility of the cartilage thickness maps, pixelwise Standard Error of Measurement (SEM) maps were generated for a subgroup of n=13 males. These participants had an additional set of baseline 3D-FSPGR images taken on a separate day within one week as required by participation in a different study in our lab (Gatti et al. 2017). The imaging protocol was identical to that presented in the current study. Final SEM maps are available in Supplementary Material 2.A showing acceptable reproducibility.

Statistical parametric mapping was completed using a custom Python code. First, maps were smoothed using a Gaussian kernel filter with a full-width half-maximum (FWHM) of 4 mm to impose spatial correlation between adjacent pixels. The FWHM is in the order of maximal cartilage thickness. Then, pixelwise F-statistic maps (F-maps) were calculated using a 2-way repeated measures ANOVA. The main effects of Running and Sex were investigated, as well as the interaction of Running and Sex (Running$\times$Sex) to investigate the influence of sex on changes in articular cartilage following running. Only pixels containing data from all participants were included in the analysis.

F-maps were initially thresholded at an F-statistic of 7.64 ($p = 0.01$). Then, a minimum significant cluster size was determined using 10,000 Monte Carlo simulations of the dataset *a posteriori*, a method adapted from Forman et al (1995). In each iteration, cartilage thickness maps were generated for each participant, at each time point, with individual pixel thickness values being randomly sampled from a normal distribution defined by the grand mean and standard deviation of the whole dataset. For each iteration, data were smoothed using the same Gaussian kernel (FWHM $= 4\ mm$), F-maps were generated, and pixels were thresholded at an F-statistic of 7.64. The number of contiguous pixels in each cluster was recorded, and the frequency of the largest cluster size over the 10,000 iterations was tabulated. A cumulative distribution function (CDF) was generated, and a minimum cluster size was chosen. The cluster size chosen corresponded to a cumulative probability of 0.95

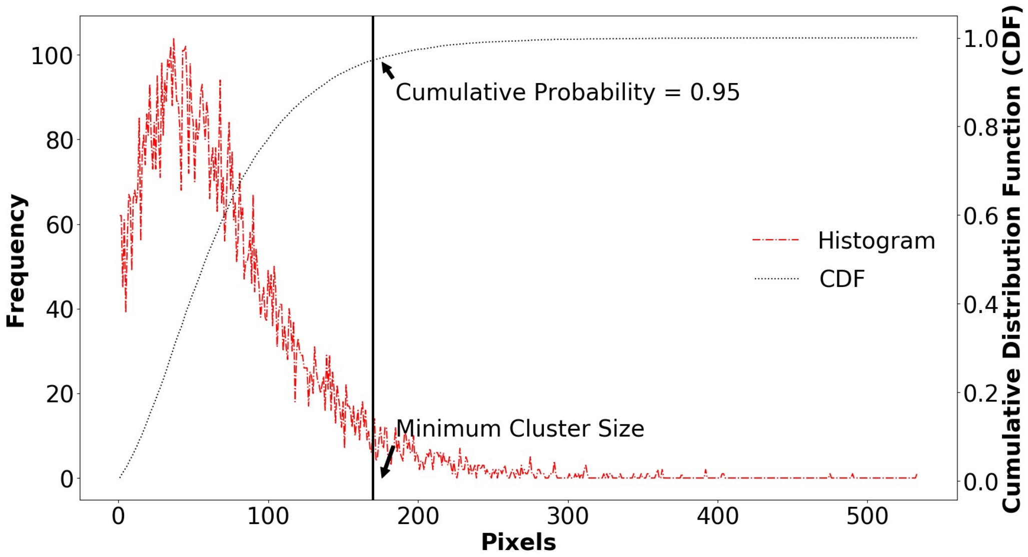

Figure 2.2.2: For each of the 10,000 Monte Carlo simulations, the frequency of cluster sizes (i.e., number of contiguous pixels in largest extracted cluster at each iteration) was recorded and represented as a histogram (left y-axis). From that data, a cumulative distribution function (CDF) was calculated (right y-axis). The threshold at which CDF > 0.95 (analogous to an alpha level of 0.05) determined the minimum number of contiguous pixels required to determine a significantly different change (solid vertical black line).

(or alpha of 0.05). An example of the cluster frequency and the CDF for the main effect of Sex is presented in Fig 2.2.2.

2.3 Results

Data from 30 participants were included (Females: $n = 15$; Males: $n = 15$). Demographic data are presented in Table 2.3.1. There were no differences in age, BMI, LEFS score, and running speed between men and women ($p > 0.386$).

Females had less cartilage volume at pre-activity and post-activity than males ($p < 0.001$, Table 2.3.2). Cartilage volume decreased following running in all tissues (Fig 2.3.1A). Compared to both the medial tibia ($p < 0.001$) and lateral weight-bearing femur ($p = 0.003$), the lateral tibia experienced the greatest percent change in volume (Females: -5.32%, Males: -5.21%; Fig 2.3.1A). Percent change of volume in the medial tibia was not significantly different from the other tissues.

Females had thinner mean medial tibial cartilage thickness at pre-activity ($p = 0.005$,

Table 2.3.1: Demographic data with p-values representing the difference between males and females (independent samples t-test).

	MALES		FEMALES		
	Mean	Range (Min-Max)	Mean	Range (Min-Max)	p
Age (y)	25.6 (4.1)	20-32	26.1 (3.4)	20-31	0.703
BMI (kg/m^2)	23.7 (2.7)	18.4-27.1	23.1 (3.1)	19.7-28.8	0.585
LEFS	79.8 (0.6)	78-80	79.5 (1.4)	75-80	0.386
Treadmill Speed (km/h)	9.9 (1.3)	7.9-13.1	9.8 (1.6)	7.9-12.9	0.864

BMI = Body Mass Index
LEFS = Lower Extremity Functional Score

Table 2.3.2); all other sex comparisons at pre- and post-activity were not significant at the Sidak-corrected p-value. Mean cartilage thickness also decreased in all tissues following running (Fig 2.3.1B). The lateral tibia observed the greatest relative decrease in cartilage thickness (Females: -4.14%, Males –3.72%; Fig 2.3.1B), deforming significantly more than the medial tibia ($p < 0.001$) and lateral weight-bearing femur ($p = 0.004$). The medial weight-bearing femur also deformed significantly more than the medial tibia ($p = 0.01$).

For raw thickness maps (i.e., before smoothing), the mean SEM for a region (e.g., medial tibia) was between 0.126 – 0.139 mm. Except for a small percentage of pixels on the periphery (medial tibia: 0.84%; lateral tibia: 0.71%; medial weight-bearing femur: 2.52%; lateral weight-bearing femur: 2.52%), all SEMs were less than in-plane pixel resolution (0.3125 mm). Once the Gaussian filter was applied, the mean SEM dropped to below 0.092 mm for each map (Supplementary Material 2.A), and no pixels exceeded the pixel resolution.

Monte Carlo simulations determined a minimum cluster size of 143 - 174 contiguous pixels, dependent on the tissue and F- statistic (Table 2.3.3). Running caused significant cartilage changes in all four compartments, but especially the lateral tibia (Fig 2.3.2A; $p < 0.0001$). For the main effect of Sex, significant clusters reflecting cartilage difference

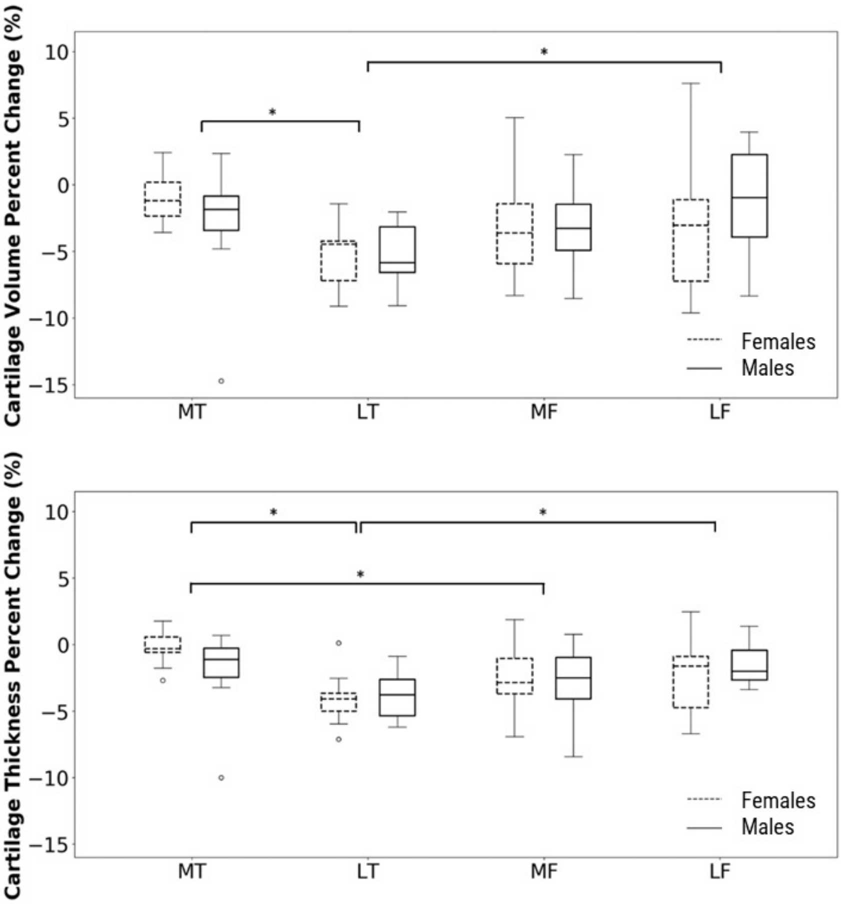

Figure 2.3.1: Top: Boxplots for percent change of the cartilage volume for males and females following running. Percent change of the medial tibia (MT) was significantly lower than the lateral tibia (LT), and the weight-bearing lateral femur (LF) was also significantly lower than the LT (asterisks). Medial weight-bearing femur (MF) was not significantly different. Bottom: Boxplots representing percent change of the cartilage thickness for both males and females following running. Similarly, percent change of the LT was significantly higher than the MT and LF.

Table 2.3.2: Means and standard deviations for volume (mm^3) and thickness (mm) measurements of the medial and lateral tibia, and medial and lateral weight-bearing femur. Statistical significance between males and females were assessed with a Sidak corrected p-value of $p < 0.006$. Bolded comparisons are significant.

		BEFORE RUNNING			**AFTER RUNNING**		
		Males	Females	p	Males	Females	p
CARTILAGE VOLUME (mm^3)	Medial Tibia	2605.96 (409.24)	1913.81 (256.33)	**<0.001**	2537.26 (402.76)	1896.46 (264.00)	**<0.001**
	Lateral Tibia	3443.91 (473.23)	2422.13 (388.65)	**<0.001**	3264.15 (450.59)	2294.43 (380.92)	**<0.001**
	Medial Femur	1511.62 (184.47)	1102.38 (138.21)	**<0.001**	1463.05 (201.28)	1068.82 (150.51)	**<0.001**
	Lateral Femur	1622.66 (196.47)	1131.90 (178.74)	**<0.001**	1600.59 (195.36)	1087.77 (168.15)	**<0.001**
MEAN CARTILAGE THICKNESS (mm)	Medial Tibia	2.25 (0.20)	2.08 (0.10)	**0.005**	2.21 (0.19)	2.07 (0.11)	0.021
	Lateral Tibia	2.74 (0.20)	2.56 (0.19)	0.016	2.64 (0.18)	2.45 (0.18)	0.008
	Medial Femur	2.40 (0.22)	2.21 (0.16)	0.014	2.33 (0.33)	2.15 (0.14)	0.019
	Lateral Femur	2.30 (0.19)	2.16 (0.17)	0.055	2.26 (0.19)	2.11 (0.15)	0.021

Table 2.3.3: Results for the Monte Carlo simulations.

	MAIN EFFECT: SEX					MAIN EFFECT: ACTIVITY					INTERACTION: SEX×ACTIVITY				
	Minimum Cluster Size (Pixels)	Area (mm^2)	Number of Sig. Clusters	Number of Pixels	p	Minimum Cluster Size (Pixels)	Area (mm^2)	Number of Sig. Clusters	Number of Pixels	p	Minimum Cluster Size (Pixels)	Area (mm^2)	Number of Sig. Clusters	Number of Pixels	p
Medial Tibia	170	16.60	1	2436	< 0.0001	171	16.70	1	302	0.004	173	16.89	0	-	-
Lateral Tibia	172	16.80	2	1351	< 0.0001	166	16.21	1	7274	< 0.0001	174	16.99	2	495	< 0.001
				383	< 0.001									244	0.012
Medial Femur	144	14.06	1	1618	< 0.0001	145	14.16	2	1885	< 0.0001	143	13.96	0	-	-
Lateral Femur	146	14.26	1	218	0.009	147	14.36	1	1500	< 0.0001	145	14.16	0	-	-

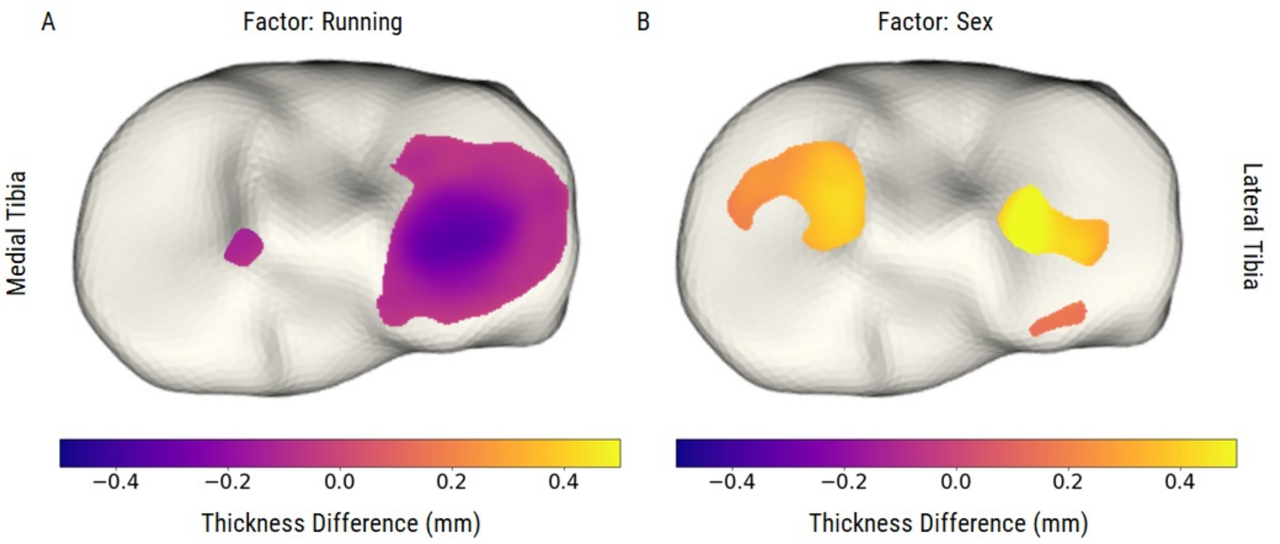

Figure 2.3.2: Thickness difference (mm) in medial and lateral tibial cartilage for A) the main effect of Running (post – pre) and B) the main effect of Sex (males – females) overlaid on a representative 3D render of a segmented FSPGR volume. Only areas depicted in colour were significant in the SPM analysis. Running caused a significant deformation in the lateral tibia ($p < 0.0001$), with smaller but significant regions identified in the other three compartments. There was a widespread difference in cartilage thickness between males and females that spanned the central and anterior regions of the medial tibia, and central region of the lateral tibia, where females had thinner cartilage.

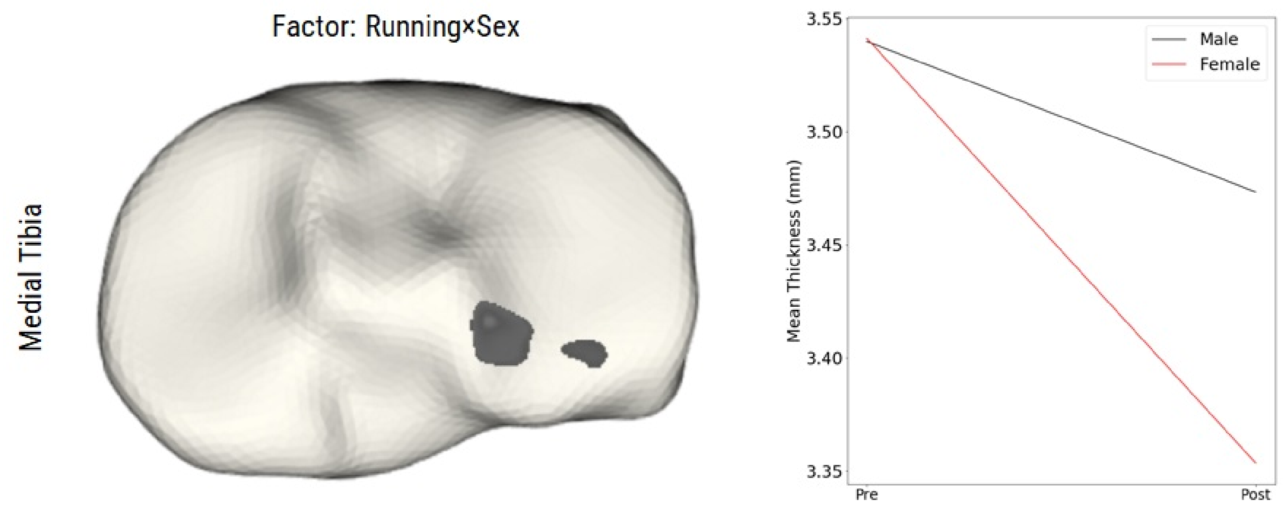

Figure 2.3.3: Left: Significant clusters on the posterior lateral tibia (grey) for the interaction of Running×Sex. Right: The interaction effect was graphed using mean thicknesses for both regions. Females had greater lateral tibial deformation in these regions than males. This may suggest males have stiffer cartilage in these regions.

were identified on all four tissues, with females associated with overall thinner cartilage (Fig 2.3.2B; $p \leq 0.009$). For the interaction of Running×Sex, two small significant clusters were identified on the lateral tibia (Fig 2.3.3; $p \leq 0.012$). These findings suggest females experience greater deformation than males in these explicit regions.

2.4 Discussion

Statistical parametric mapping proved a useful technique to identify and locate tibiofemoral cartilage deformations after exposure to weight-bearing activity, and to explore differences between sexes in cartilage morphology and deformation. SPM is an attractive alternative to global measurements of cartilage thickness change, or sub-regional analyses where the region of interest is defined by anatomical landmarks. Further, SPM enables an unconstrained, yet sensitive assessment of cartilage thickness differences using MRI. Our method was able to detect regions of significant difference in cartilage thickness between sexes that were not otherwise identified using mean thicknesses (Table 2.3.2). Running deformed cartilage, especially in the central region of the lateral tibia (i.e., became "thinner") in both asymptomatic young males and females. These findings support the hypothesis that the lateral tibia is well adapted to dissipate knee loads encountered during running because it contains the thickest region of cartilage (Lad et al. 2016; Li et al. 2005). This analysis also showed a small region on the lateral tibia where sex interacted with running, suggesting that females experienced greater deformation than males.

In asymptomatic, young females and males, mean cartilage thickness decreased in all four tibiofemoral compartments following running, suggesting a global deformation of the cartilage in the knee. There were, however, a few inconsistencies between our data and mean cartilage thickness changes presented by others that likely highlight methodological differences (e.g., imaging parameters, segmentation algorithm, cartilage boundary definition, treadmill/overground surface). First, while our baseline mean thickness measures were similar to those of an early study exploring cartilage response to running in seven healthy men (Mosher et al. 2005), our sample experienced greater tibiofemoral deformation despite running for half the time. In contrast, after 30-minutes of running and using the same imaging sequence as the current study, Subburaj et al. (2012) found -4.5% change in mean tibial thickness and -2.1% in mean femoral thickness in a cohort of 20 young healthy adults, though this was not statistically significant. Greater deformation, especially in the tibia (-4.5% versus -2.4%), likely reflects the longer duration of running compared to our study (30-minutes versus 15-minutes), or methodological differences in the calculation of cartilage thickness.

A 2D cartilage thickness mapping procedure, including group-wise registration, was introduced in this study to enable pixelwise statistical analyses. Tibiofemoral cartilage segmentation, and the subsequent generation of 2D thickness maps, were examined for repeatability. First, all tibiofemoral cartilage regions were automatically segmented with a validated convolutional neural network (training set: 166 MR volumes, testing set: 28 MR volumes) (Gatti and Maly 2019). Using this framework, segmentations of tibiofemoral cartilage from 3D-FSPGR volumes on healthy participants (12 volumes from 3 males) demonstrated accuracies of 0.92-0.96, measured using the Dice similarity coefficient (Gatti and Maly 2019). These accuracies are higher than manual inter-radiologist accuracies (0.88), the current gold standard in the field (Shim et al. 2009). Also, test-retest 3D-FSPGR volumes were collected on a different day with the same pre-scanning rest protocol for thirteen males from this study (Gatti et al. 2017). Medial tibia, lateral tibia, and whole femur cartilage segmentations (volume, mm^3) were repeatable, with intraclass correlation coefficients of 0.988, 0.987, and 0.996 respectively. These ICCs align with results from Cicuttini et al. (2000) demonstrating ICCs of 0.992, 0.990, and 0.992 for the tibial, femoral, and patellar cartilage respectively using manual segmentation. Repeatability of the thickness maps using the Affine transform registration technique were also investigated using pixelwise standard error of measurement (SEM) maps and intra-class correlation coefficient (ICC) maps (Supplementary Material 2.A). SEM maps revealed a small percentage of pixels on the periphery (0.71 – 2.52%) had error surpassing the pixel resolution; the Gaussian filter minimized this error. ICC maps showed overall good-to-excellent agreement, with only 3.88, 3.71, 7.32, and 12.80% of the pixels on the periphery in the medial tibia, lateral tibia, medial weight-bearing femur, and lateral weight-bearing femur maps showing ICC < 0.5. Once the Gaussian filter was applied, the percentage of pixels with ICC < 0.5 dropped to 0.05 - 3.96%. Overall, the cartilage segmentations and thickness maps presented in the current work showed excellent repeatability.

Our pixelwise analyses showed systematic cartilage deformation after running in all four compartments, with the greatest region identified on the lateral tibia. Other studies investigating cartilage deformation following running have also observed greater deformation in the lateral tibia than the medial tibia (Boocock et al. 2009; Kersting et al. 2005; Niehoff et al. 2011). The spatial location of the cluster in our analysis aligns with the thickest area of the lateral tibia, as shown in thickness maps generated by others (Lad et al. 2016; Li et al. 2005). Areas of thicker cartilage have been suggested to result in lower surface pressure and von Mises stresses (Li et al. 2001) – thus, this compilation of findings from the current and previous studies may suggest that the lateral tibia is an ideal location to deform in response to higher physiological loading observed in running. In addition, this cluster aligns with the modeled *in vivo* cartilage-to-cartilage articulation at the lateral tibiofemoral joint at 0–90^o of weight-bearing knee flexion (DeFrate et al. 2004; Li et al. 2005), a range that would fully encompass the knee flexion range of self-selected running.

Knee OA is more prevalent (Srikanth et al. 2005) and symptomatic (Hawker et al. 2000) in females. It is possible that increased risk for OA among females is associated with, at least in part, the smaller volume and thickness of cartilage within the knee compared to males. From MRI measures of mean thickness and mean volume, females have thinner cartilage and less volume of cartilage than males (Cicuttini et al. 2002; Lad et al. 2016; Otterness and Eckstein 2007). In fact, these findings remain when accounting for factors such as bone size, body mass, age, and physical activity (Cicuttini et al. 2002; Ding et al. 2003; Jones et al. 2000; Lad et al. 2016). The pixelwise analyses in the current study were able to determine the specific spatial location of consistent cartilage differences due to sex. Compared to males, females showed thinner cartilage in areas spanning the anterior and central regions of the medial tibia, central and posterior regions of the lateral tibia, centrally in the medial femoral condyle, and a small posterior region of the lateral femoral condyle. In those indicated regions, females had thinner cartilage in the medial tibia (12.7%), lateral tibia (11.4%), medial weight-bearing femur (13.7%), and lateral weight-bearing femur (12.3%) than males. Interestingly, our identified regions encompass the spatial locations of full-thickness cartilage lesions observed in patients undergoing total knee arthroplasty from advanced knee OA (Gulati et al. 2009). Future longitudinal work should explore whether these sex differences in regional cartilage thickness play a role in the sex-disparity in knee OA prevalence.

Reported sex differences in knee cartilage morphology (Ding et al. 2003; Otterness and Eckstein 2007), static knee alignment (Wise et al. 2012), and cartilage composition (Kumar et al. 2015) may reflect in different spatial patterns of cartilage deformation between males and females. A significant interaction effect of sex and pre-post running was observed in a small region of the posterior lateral tibia; no other compartment had an effect. This interaction suggested that females experience greater deformation than males in these regions. To our knowledge, this is the first study to identify explicit sex differences in cartilage deformation. Following adjustment for body mass, no significant relationships were observed between maximal compressive stress and cartilage volume change following running in healthy males and females (Boocock et al. 2009). Another study quantifying the *in vivo* deformational response of cartilage did not explicitly test for significant differences between sexes (Hudelmaier et al. 2001). Hudelmaier et al. (2001) compared mean thickness changes of the patellar cartilage in young males (n=12), young females (n=12), elderly males (n=11), and elderly females (n=12) following 30 deep knee bends. While there was a clear effect of age on the response of cartilage to the loading stimulus, inspection of the means and variances suggested no apparent effect of sex. In the current work, the significant regions identified include cartilage covered by the lateral meniscus. During the mechanical testing of tibial plateaus from female cadaveric donors, it was shown that cartilage covered by the posterior meniscus had lower tangent modulus than cartilage covered by the rest of the meniscus (Deneweth et al. 2013). It is possible that greater deformation in this region is reflective of lower stiffness in females. Further work is required to quantify cartilage composition differences between males and females, and how those relate to cartilage deformation mechanics.

While pixelwise analyses provide detailed spatial information, determining a minimum cluster size that defines a statistically significant difference is difficult. For example, there is no strict guideline for choosing an alpha level threshold. Furthermore, when each pixel of a statistical map is thresholded on an alpha level (e.g., $p < 0.01$), it is unknown how many contiguous pixels (cluster sizes) are required to suggest a meaningful change. A detailed approach for determining minimum cluster size for F-maps was formulated by Cao (1999). However, this approach has recently been criticized for producing high false positive rates (Eklund et al. 2016). We addressed this issue using a Monte Carlo simulation approach (Forman et al. 1995; Nichols and Hayasaka 2003). The simulations identified cluster sizes of 143 – 174 contiguous pixels as significant change at an alpha level of 0.05, dependent on the tissue investigated. Therefore, using this simulation approach, we are confident that any identified clusters are true differences.

The current analyses describe a method of determining pixelwise relationships of cartilage change with activity exposure and sex. These methods demonstrated small measurement error; SEM errors were smaller than in-plane resolution. Furthermore, these methods accurately depicted sex differences in cartilage thickness over the entire cartilage surface, without relying on individual summary statistics. These methods show promise for future investigations. For example, longitudinal studies quantifying changes in cartilage thickness could identify the rate of cartilage change at the individual pixel level. Findings from such an analysis could be used to re-define regions of interest to find regions that are most sensitive to change. Work by Iranpour-Boroujeni and colleagues utilized a manual technique to locate a region of interest by marking cartilage lesions on MRI scans (Iranpour-Boroujeni et al. 2011). Our current method improves this technique by automatically identifying regions of interest. Our method facilitates the inclusion of additional parameters like sex, BMI, or biomechanical parameters, which could identify specific regions that are sensitive to change. This method has the potential to improve sensitivity to change over time, and to improve our understanding of the relationship between individual characteristics and cartilage changes.

This study had limitations. First, we used a convenience sample of 15 females and 15 males. With small samples, the power to detect a significant interaction effect decreases. Therefore, caution is recommended in the interpretation of the significant lateral tibia clusters due to the interaction of Running×Sex. Second, with a pre-post imaging protocol, patient re-positioning errors may occur. This was mitigated by clearly marking coil position on the leg in the pre-imaging session, enabling better estimation of patient re-positioning after exercise. Third, this study was a secondary analysis. The original study design included an analysis of T2 relaxation. Immediately following exercise, T2 relaxation images were acquired first to capture changes in free water, meaning approximately 14-minutes elapsed between the cessation of running and the 3D-FSPGR images. This protocol is modeled after others (Mosher et al. 2010; Subburaj et al. 2012), and studies have suggested that 45-minutes is required for patellar cartilage to recover by 50% (Eckstein et al. 1999). Finally, for the clustering analyses, a thresholding value of $p = 0.01$ was used instead of $p = 0.05$ to minimize the potential for false-positives. In doing so, there is the potential to cause a Type II error by excluding more diffuse regions containing smaller magnitude of change.

This study was the first to our knowledge to use SPM to identify regional deformation changes in tibiofemoral cartilage following running in young asymptomatic adults, showing that the central region of the lateral tibia undergoes the most deformation after running. We also used SPM to specifically address the influence of biological sex on the tibiofemoral deformational response. Using robust pixelwise analyses to generate F-statistic maps, we found cartilage deformation occurred in all four compartments, with a greater region of change in the lateral tibia after running. As well, a small region in the posterior lateral tibia had a significant interaction of Running×Sex. Moving forward, we promote the use of the SPM technique to provide detailed spatial information in biomedical and biomechanical applications.

Authors' Contribution

Brenneman Wilson: study conception and design, acquisition of data, analysis and interpretation of data, drafting of manuscript, and critical revision; Gatti: study conception and design, acquisition of data, and critical revision; Maly: study conception and design, and critical revision.

Funding

This research was funded by an NSERC Discovery grant (MRM: 353715), the Canadian Foundation for Innovation Leaders Opportunity Fund, and the Ministry of Research and Innovation – Ontario Research Fund (MRM).

Compliance with Ethic Standards

Conflict of Interest: A. A Gatti is the founder of NeuralSeg, Ltd. There are no other conflicts of interest to disclose.

Ethical Approval: This research was approved via the Hamilton Integrated Research Ethics Board, and all participants gave written, informed consent.

2.5 References

Altman, R., Asch, E., Bloch, D., Bole, G., Borenstein, D., Brandt, K., ... Hochberg, M. et al. (1986). Development of criteria for the classification and reporting of osteoarthritis: Classification of osteoarthritis of the knee. *Arthritis & Rheumatology*, *29*(8), 1039–1049.

Ashby, F. G. (2011). *Statistical analysis of fMRI data*. MIT press.

Boocock, M., McNair, P., Cicuttini, F., Stuart, A., & Sinclair, T. (2009). The short-term effects of running on the deformation of knee articular cartilage and its relationship to biomechanical loads at the knee. *Osteoarthritis and Cartilage*, *17*(7), 883–890.

Cao, J. (1999). The size of the connected components of excursion sets of chi-squared, t and F fields. *Advances in Applied Probability*, *31*(3), 579–595.

Cicuttini, F., Forbes, A., Morris, K., Darling, S., Bailey, M., & Stuckey, S. (1999). Gender differences in knee cartilage volume as measured by magnetic resonance imaging. *Osteoarthritis and Cartilage*, *7*(3), 265–271.

Cicuttini, F., Forbes, A., Asbeutah, A., Morris, K., & Stuckey, S. (2000). Comparison and reproducibility of fast and conventional spoiled gradient-echo magnetic resonance sequences in the determination of knee cartilage volume. *Journal of Orthopaedic Research*, *18*(4), 580–584.

Cicuttini, F., Wluka, A., Wang, Y., Davis, S., Hankin, J., & Ebeling, P. (2002). Compartment differences in knee cartilage volume in healthy adults. *The Journal of Rheumatology*, *29*(3), 554–556.

DeFrate, L., Sun, H., Gill, T., Rubash, H., & Li, G. (2004). In vivo tibiofemoral contact analysis using 3D MRI-based knee models. *Journal of Biomechanics*, *37*(10), 1499–1504.

Deneweth, J. M., Newman, K. E., Sylvia, S. M., McLean, S. G., & Arruda, E. M. (2013). Heterogeneity of tibial plateau cartilage in response to a physiological compressive strain rate. *Journal of Orthopaedic Research*, *31*(3), 370–375.

Ding, C., Cicuttini, F., Scott, F., Glisson, M., & Jones, G. (2003). Sex differences in knee cartilage volume in adults: Role of body and bone size, age and physical activity. *Rheumatology*, *42*(11), 1317–1323.

Eckstein, F., Hudelmaier, M., Wirth, W., Kiefer, B., Jackson, R., Yu, J., ... Schneider, E. (2006). Double echo steady state magnetic resonance imaging of knee articular cartilage at 3 Tesla: A pilot study for the Osteoarthritis Initiative. *Annals of the Rheumatic Diseases*, *65*(4), 433–441.

Eckstein, F., Tieschky, M., Faber, S., Englmeier, K.-H., & Reiser, M. (1999). Functional analysis of articular cartilage deformation, recovery, and fluid flow following dynamic exercise in vivo. *Anatomy and Embryology*, *200*(4), 419–424.

Eckstein, F., & Wirth, W. (2011). Quantitative cartilage imaging in knee osteoarthritis. *Arthritis*, *2011*.

Eklund, A., Nichols, T., & Knutsson, H. (2016). Cluster failure: Why fMRI inferences for spatial extent have inflated false-positive rates. *Proceedings of the National Academy of Sciences*, *113*(28), 7900–7905.

Forman, S., Cohen, J., Fitzgerald, M., Eddy, W., Mintun, M., & Noll, D. (1995). Improved assessment of significant activation in functional magnetic resonance imaging (fMRI): Use of a cluster-size threshold. *Magnetic Resonance in Medicine*, *33*(5), 636–647.

Gatti, A., & Maly, M. (2019). Fully-automated cartilage segmentation using deep learning - Data from the Osteoarthritis Initiative. *2019 meeting of the International Society for Biomechanics*.

Gatti, A. A., Noseworthy, M. D., Stratford, P. W., Brenneman, E. C., Totterman, S., Tamez-Peña, J., & Maly, M. R. (2017). Acute changes in knee cartilage transverse relaxation time after running and bicycling. *Journal of Biomechanics*, *53*, 171–177.

Gulati, A., Chau, R., Beard, D., Price, A., Gill, H., & Murray, D. (2009). Localization of the full-thickness cartilage lesions in medial and lateral unicompartmental knee osteoarthritis. *Journal of Orthopaedic Research*, *27*(10), 1339–1346.

Hawker, G., Wright, J., Coyte, P., Williams, J., Harvey, B., Glazier, R., & Badley, E. (2000). Differences between men and women in the rate of use of hip and knee arthroplasty. *New England Journal of Medicine*, *342*(14), 1016–1022.

Horton, M. G., & Hall, T. L. (1989). Quadriceps femoris muscle angle: Normal values and relationships with gender and selected skeletal measures. *Physical therapy*, *69*(11), 897–901.

Hudelmaier, M., Glaser, C., Hohe, J., Englmeier, K.-H., Reiser, M., Putz, R., & Eckstein, F. (2001). Age-related changes in the morphology and deformational behavior of knee joint cartilage. *Arthritis & Rheumatism*, *44*(11), 2556–2561.

Iranpour-Boroujeni, T., Watanabe, A., Bashtar, R., Yoshioka, H., & Duryea, J. (2011). Quantification of cartilage loss in local regions of knee joints using semi-automated segmentation software: Analysis of longitudinal data from the Osteoarthritis Initiative (OAI). *Osteoarthritis and Cartilage*, *19*(3), 309–314.

Jones, G., Glisson, M., Hynes, K., & Cicuttini, F. (2000). Sex and site differences in cartilage development: A possible explanation for variations in knee osteoarthritis in later life. *Arthritis & Rheumatism*, *43*(11), 2543–2549.

Kersting, U., Stubendorff, J., Schmidt, M., & Brüggemann, G.-P. (2005). Changes in knee cartilage volume and serum COMP concentration after running exercise. *Osteoarthritis and Cartilage*, *13*(10), 925–934.

Kessler, M. A., Glaser, C., Tittel, S., Reiser, M., & Imhoff, A. B. (2006). Volume changes in the menisci and articular cartilage of runners: An in vivo investigation based on 3-d magnetic resonance imaging. *The American Journal of Sports Medicine*, *34*(5), 832–836.

Kumar, D., Souza, R., Subburaj, K., MacLeod, T., Singh, J., Calixto, N., … Lane, N. et al. (2015). Are there sex differences in knee cartilage composition and walking mechanics in healthy and osteoarthritis populations? *Clinical Orthopaedics and Related Research*, *473*(8), 2548–2558.

Lad, N., Liu, B., Ganapathy, P., Utturkar, G., Sutter, E., Moorman III, C., … DeFrate, L. (2016). Effect of normal gait on in vivo tibiofemoral cartilage strains. *Journal of Biomechanics*, *49*(13), 2870–2876.

Li, G., Lopez, O., & Rubash, H. (2001). Variability of a three-dimensional finite element model constructed using magnetic resonance images of a knee for joint contact stress analysis. *Journal of Biomechanical Engineering*, *123*(4), 341–346.

Li, G., Park, S., DeFrate, L., Schutzer, M., Ji, L., Gill, T., & Rubash, H. (2005). The cartilage thickness distribution in the tibiofemoral joint and its correlation with cartilage-to-cartilage contact. *Clinical Biomechanics*, *20*(7), 736–744.

Li, X., Santago II, A., Vidt, M., & Saul, K. (2016). Analysis of effects of loading and postural demands on upper limb reaching in older adults using statistical parametric mapping. *Journal of Biomechanics*, *49*(13), 2806–2816.

Mosher, T. J., Smith, H. E., Collins, C., Liu, Y., Hancy, J., Dardzinski, B. J., & Smith, M. B. (2005). Change in knee cartilage T2 at MR imaging after running: A feasibility study. *Radiology*, *234*(1), 245–249.

Mosher, T. J., Liu, Y., & Torok, C. M. (2010). Functional cartilage MRI T2 mapping: Evaluating the effect of age and training on knee cartilage response to running. *Osteoarthritis & Cartilage*, *18*(3), 358–364.

Nichols, T., & Hayasaka, S. (2003). Controlling the familywise error rate in functional neuroimaging: A comparative review. *Statistical Methods in Medical Research*, *12*(5), 419–446.

Nichols, T. (2012). Multiple testing corrections, nonparametric methods, and random field theory. *Neuroimage*, *62*(2), 811–815.

Niehoff, A., Müller, M., Brüggemann, L., Savage, T., Zaucke, F., Eckstein, F., … Brüggemann, G.-P. (2011). Deformational behaviour of knee cartilage and changes in serum cartilage oligomeric matrix protein (COMP) after running and drop landing. *Osteoarthritis and Cartilage*, *19*(8), 1003–1010.

Okafor, E., Utturkar, G., Widmyer, M., Abebe, E., Collins, A., Taylor, D., … DeFrate, L. (2014). The effects of femoral graft placement on cartilage thickness after anterior cruciate ligament reconstruction. *Journal of Biomechanics*, *47*(1), 96–101.

Otterness, I., & Eckstein, F. (2007). Women have thinner cartilage and smaller joint surfaces than men after adjustment for body height and weight. *Osteoarthritis and Cartilage*, *15*(6), 666–672.

Pataky, T. (2010). Generalized n-dimensional biomechanical field analysis using statistical parametric mapping. *Journal of Biomechanics*, *43*(10), 1976–1982.

Pataky, T., Robinson, M., & Vanrenterghem, J. (2013). Vector field statistical analysis of kinematic and force trajectories. *Journal of Biomechanics*, *46*(14), 2394–2401.

Pedoia, V., Gallo, M., Souza, R., & Majumdar, S. (2017). Longitudinal study using voxel-based relaxometry: Association between cartilage T1rho and T2 and patient reported outcome changes in hip osteoarthritis. *Journal of Magnetic Resonance Imaging*, *45*(5), 1523–1533.

Pedoia, V., Li, X., Su, F., Calixto, N., & Majumdar, S. (2016). Fully automatic analysis of the knee articular cartilage T1rho relaxation time using voxel-based relaxometry. *Journal of Magnetic Resonance Imaging*, *43*(4), 970–980.

Schneider, E., Nevitt, M., McCulloch, C., Cicuttini, F., Duryea, J., Eckstein, F., & Tamez-Pena, J. (2012). Equivalence and precision of knee cartilage morphometry between different segmentation teams, cartilage regions, and mr acquisitions. *Osteoarthritis and Cartilage*, *20*(8), 869–879.

Shim, H., Chang, S., Tao, C., Wang, J., Kwoh, C., & Bae, K. (2009). Knee cartilage: Efficient and reproducible segmentation on high-spatial-resolution MR images with the semiautomated graph-cut algorithm method. *Radiology*, *251*(2), 548–556.

Srikanth, V., Fryer, J., Zhai, G., Winzenberg, T., Hosmer, D., & Jones, G. (2005). A meta-analysis of sex differences prevalence, incidence and severity of osteoarthritis. *Osteoarthritis and Cartilage*, *13*(9), 769–781.

Subburaj, K., Kumar, D., Souza, R. B., Alizai, H., Li, X., Link, T. M., & Majumdar, S. (2012). The acute effect of running on knee articular cartilage and meniscus magnetic resonance relaxation times in young healthy adults. *The American Journal of Sports Medicine*, *40*(9), 2134–2141.

Wang, Y.-C., Hart, D. L., Stratford, P. W., & Mioduski, J. E. (2009). Clinical interpretation of a Lower-Extremity Functional Scale–derived computerized adaptive test. *Physical Therapy*, *89*(9), 957–968.

Wise, B. L., Niu, J., Yang, M., Lane, N. E., Harvey, W., Felson, D. T., ... Torner, J. et al. (2012). Patterns of compartment involvement in tibiofemoral osteoarthritis in men and women and in whites and african americans. *Arthritis care & research*, *64*(6), 847–852.

Worsley, K., Marrett, S., Neelin, P., Vandal, A., Friston, K., & Evans, A. (1996). A unified statistical approach for determining significant signals in images of cerebral activation. *Human Brain Mapping*, *4*(1), 58–73.

Supplementary Material for Chapter 2

2.A SEM Maps

We were interested in the reproducibility of our pixelwise thickness mapping technique. Our maps were generated by taking each voxel on the bone-cartilage interface of the tissue of interest and calculating the Euclidean distance to each voxel on the articular surface. From that array, the minimum Euclidean distance was extracted for each BCI voxel, creating a 2D map of thickness values in millimetres (mm).

To assess reproducibility, Standard Error of Measurement (SEM; Fig. 2.A.1), and intra-class correlation coefficient (ICC; Fig. 2.A.2) maps were generated. Thirteen of the fifteen men in the current study had a second, pre-activity 3D-FSPGR volume taken of their right knee as required by participation in a different study in our lab (Gatti et al. 2017). Those second images were acquired on a second day, and followed the identical protocol as this study, except they completed a bicycling activity instead of running. The two sets of scans were acquired within one week. Each volume (13 participants, 2 pre-activity time-points) was segmented (medial and lateral tibial cartilage and femoral cartilage) using a multi-stage convolutional neural network (Gatti and Maly 2019). Medial and lateral weight-bearing femur were calculated using previously established methods (Eckstein et al. 2006). Thickness maps were generated as described. All 2D thickness maps of the same tissue were registered to a common template using the 2D Affine transform implemented in SimpleITK.

SEM maps were generated between the two time points (13 samples per time point; Fig 2.A.1). Looking at raw thickness maps (i.e., before smoothing), the mean SEM was between 0.126 – 0.139 mm, below the pixel resolution of 0.3125 mm. Around the periphery of each map, some pixels surpassed the 0.3125 mm threshold (Table 2.A.1), which is likely due to known issues in cartilage segmentation at the periphery owing to partial volume effects (Koo et al. 2005). ICC maps were also generated (Fig. 2.A.2). A small percentage of peripheral pixels had ICCs below 0.5 (<12.80%).

When spatial correlation was introduced with the Gaussian kernel filter, as was performed in this study, the mean SEM drops to <0.092 mm. No pixel (in any SEM map) surpassed the 0.3125 mm error threshold. For ICC maps, Gaussian filtering improved the

Table 2.A.1: Percentage of pixels in the SEM maps that surpass the 0.3125 mm image resolution threshold.

	Number of Pixels with SEM > 0.3125 mm	Total Number of Pixels in Map	Percentage of Pixels with SEM > 0.3125 mm
Medial Tibia	107	12,706	0.84
Lateral Tibia	83	11,704	0.71
Medial Weight-Bearing Femur	142	5,641	2.52
Lateral Weight-Bearing Femur	163	6,478	2.52

percentage of pixels on the periphery containing poor agreement (ICC <0.5; <3.96%).

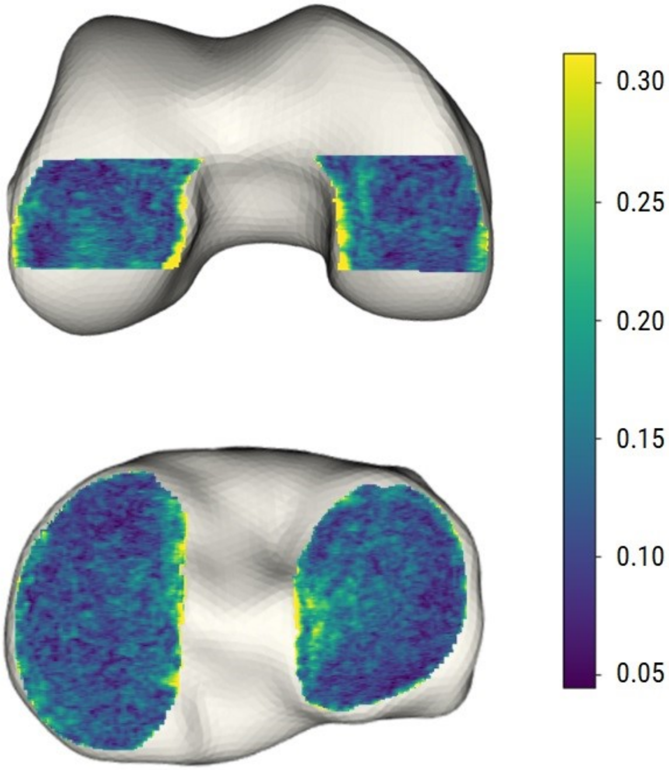

Figure 2.A.1: Standard error of measurement (SEM) maps representing reproducibility of pixelwise cartilage thickness maps (in millimetres). The above represents "raw" maps (i.e., before the application of a Gaussian kernel filter). All SEM values above the pixel resolution of 0.3125 mm are labeled in yellow.

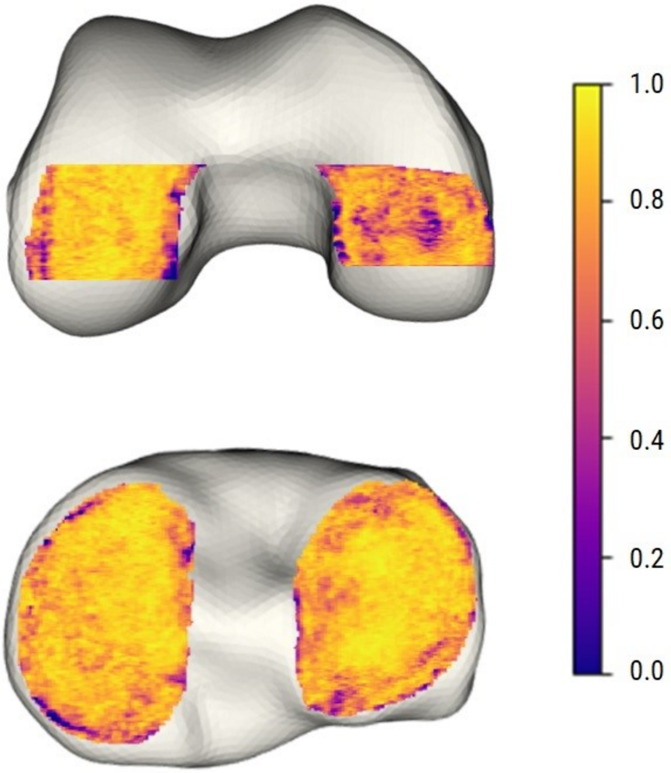

Figure 2.A.2: Intra-class correlation coefficient (ICC) maps representing reproducibility of pixelwise cartilage thickness maps. The above represents "raw" maps (i.e., before the application of a Gaussian kernel filter).

References

Eckstein, F., Hudelmaier, M., Wirth, W., Kiefer, B., Jackson, R., Yu, J., . . . Schneider, E. (2006). Double echo steady state magnetic resonance imaging of knee articular cartilage at 3 Tesla: A pilot study for the Osteoarthritis Initiative. *Annals of the Rheumatic Diseases*, *65*(4), 433–441.

Gatti, A., & Maly, M. (2019). Fully-automated cartilage segmentation using deep learning - Data from the Osteoarthritis Initiative. *2019 meeting of the International Society for Biomechanics*.

Gatti, A. A., Noseworthy, M. D., Stratford, P. W., Brenneman, E. C., Totterman, S., Tamez-Peña, J., & Maly, M. R. (2017). Acute changes in knee cartilage transverse relaxation time after running and bicycling. *Journal of Biomechanics*, *53*, 171–177.

Koo, S., Gold, G., & Andriacchi, T. (2005). Considerations in measuring cartilage thickness using mri: Factors influencing reproducibility and accuracy. *Osteoarthritis and cartilage*, *13*(9), 782–789.

3 — Physical Activity Levels and Tibiofemoral Cartilage Response to Loading

This paper was submitted to Gait & Posture on 2 July 2020 (Submission # GAIPOS-S-20-00953). This manuscript was transcribed to LaTeX and follows the formatting guidelines required by McMaster University's School of Graduate Studies.

Original Article

DAILY CUMULATIVE LOAD AND BODY MASS INDEX ALTER KNEE CARTILAGE RESPONSE TO RUNNING IN WOMEN

Elora C. Brenneman Wilson[a], Anthony A. Gatti[b,c], Peter J. Keir,[a], Monica R. Maly[a,c,d]*

[a]Department of Kinesiology, McMaster University, Hamilton, ON Canada
[b]NeuralSeg Ltd., Hamilton, ON Canada
[c]School of Rehabilitation Science, McMaster University, Hamilton, ON Canada
[d]Department of Kinesiology, University of Waterloo, Waterloo, ON Canada

*Corresponding Author:
Monica R. Maly
Burt Matthews Hall, Rm 1036
Department of Kinesiology
University of Waterloo
200 University Avenue West
Waterloo, ON N2L 3G1
Phone: (519) 888-4567 ext. 37916
E-mail: mrmaly@uwaterloo.ca

Acknowledgements

We would like to thank imaging technicians Julie Lecomte, Carol Awde, Cheryl Contant, and Toni DiLeonardo at the Imaging Research Centre at St. Joseph's Healthcare in Hamilton, Ontario for ensuring quality of the image volumes. Thank you to Emily Wiebenga for help with collections at the biomechanics visit. Elora Brenneman Wilson was supported by a Canadian Graduate Scholarship through the Natural Sciences and Engineering Research Council of Canada (NSERC). Anthony Gatti was supported by an Ontario Graduate Scholarship and The Arthritis Society. Monica Maly is supported by The Arthritis Society Stars Career Development Award, funded by the Canadian Institutes of Health Research-Institute of Musculoskeletal Health and Arthritis. This research was funded by an NSERC Discovery grant (Monica Maly: 353715) and the Canadian Foundation for Innovation Leaders Opportunity Fund (Peter Keir: 16194).

Abstract

Background: Cartilage requires load to facilitate healthy function. It is unknown whether a greater accumulation of knee joint load over a typical day is related to how cartilage responds to an acute boat of loading. This information may clarify the role of habitual activity on cartilage function.

Research Question: We sought to determine the relationship between change in tibial and femoral cartilage thickness, volume, and T2 relaxation following running with daily cumulative knee load in women. Secondarily, we examined the relationship between cartilage change following running with the interaction of body mass index (BMI) and daily steps.

Methods: Participants ($n = 15$) completed gait analyses and wore an accelerometer over a week. Daily cumulative knee load was the interaction between tibial compressive joint reaction force impulse (JRFI) with the average number of daily steps measured using accelerometry. Magnetic resonance imaging scans were acquired before and immediately after 15-minutes of treadmill running. Changes in tibial and femoral cartilage thickness, volume, and T2 relaxation were calculated. Multiple linear regressions tested the associations of cartilage change outcomes with: baseline (thickness, volume, T2), JRFI, steps, and the interaction of JRFI×steps. Secondarily, BMI was substituted for JRFI.

Results and Significance: Tibial volume change was explained by baseline volume, JRFI, steps, and JRFI×steps ($R^2 = 0.50$, $p = 0.013$). Additionally, tibial volume change was explained by baseline volume, BMI, steps, and BMI×steps ($R^2 = 0.43$, $p = 0.002$). Those who were more physically active with lower JRFI (or lower BMI) showed less change in tibial cartilage after a running exposure. This may suggest cartilage conditioning.

Keywords: Cartilage, Articular; Exercise; Biomechanical Phenomena; Magnetic Resonance Imaging

3.1 Introduction

Too little or too much loading degenerates articular cartilage. In patients with a complete spinal cord injury, knee cartilage thickness progressively decreased at 6 and 24 months post-injury (Vanwanseele et al. 2002); this rate was greater than that of normal aging (Cicuttini et al. 2005). The influence of large mechanical loads on cartilage, however, appears more complex. Those with knee osteoarthritis (OA) who experience greater medial knee loads have greater longitudinal cartilage loss (Brisson et al. 2017). Alternatively, habitual runners who experience high volumes of large magnitude forces are not at an increased risk of knee OA (Timmins et al. 2017). Cartilage likely experiences a conditioning effect whereby a mechanical remodeling occurs to withstand frequent or habitual loads (Seedhom 2005).

Biomechanical gait analyses and joint modeling enable estimation of joint reaction forces (JRF) incurred by soft tissues. JRF refers to the summation of internal joint forces that are unaccounted for in the underlying model. While force magnitude plays a role in cartilage response (Eckstein et al. 2005), other factors including loading rate, duration, and frequency need to be considered. Impulse can provide information on loading duration (Miller 2017). Despite walking fewer steps per day, and after accounting for differences in body mass, participants with knee OA had greater daily accumulation of knee load than healthy controls (Maly et al. 2013). It is possible the accumulation of joint load over an average day plays a role in conditioning cartilage to tolerate acute loads.

The *in vivo* relationship between physical activity history and cartilage response following acute loads (cartilage strain) is unclear. Neither age nor activity level were related to differences in T2 relaxation (free water) following 30 minutes of self-selected running (Mosher et al. 2010). Alternatively, healthy young men with higher levels of reported physical activity had smaller changes in T2 following activity (Gatti et al. 2017). This work is corroborated by longitudinal findings that showed cartilage glycosaminoglycan content improved in women who underwent a 10-week Start To Run program 2010. These reports highlight the benefit of physical activity on articular cartilage; however, to-date, no work has explored the influence of daily cumulative load exposure on cartilage response.

The purpose of this study was to determine the relationship of number of steps per day, JRF impulse (JRFI), and their interaction (i.e., daily cumulative knee load) on tibial and femoral thickness, volume, and T2 relaxation change following an acute bout of running in healthy women. Secondarily, we investigated the associations of BMI, steps per day, and their interaction on tibial and femoral thickness, volume, and T2 relaxation change. With strong relationships between cartilage strain and BMI (Collins et al. 2018), the investigation of a BMI×steps interaction could inform a potential role of BMI and daily activity in influencing cartilage response to loading. We hypothesized 1) a JRFI×steps interaction would relate to changes in tibial cartilage T2 relaxation, suggesting a role of habitual physical activity on cartilage composition (Gatti et al. 2017; Subburaj et al. 2012); and 2) BMI and a BMI×steps interaction would relate to cartilage thickness and volume changes (Collins et al. 2018).

3.2 Methods

3.2.1 Recruitment

A convenience sample of healthy women were recruited. All were screened for the following exclusion criteria: answering ”Yes” on any question on the Get Active Questionnaire, symptomatic knee osteoarthritis (Altman et al. 1986), prior orthopaedic surgery to the right lower limb (test knee), self-reported lower-limb pain in the previous 3-months, and a score of <74 on the Lower Extremity Function Scale (Wang et al. 2009). Participants were also screened for contraindications to MRI, including but not limited to implants, stents, aneurysm clips, and/or claustrophobia. All participants gave written, informed consent and this study was approved by the institutional ethics board.

3.2.2 Protocol

Participants were asked to attend two visits: one to the McMaster Occupational Biomechanics Laboratory at McMaster University for biomechanical gait analyses, and one to the Imaging Research Centre at St. Joseph’s Healthcare in Hamilton, Ontario, Canada.

3.2.2.1 Physical Activity Quantification

Physical activity was quantified using two methods. Participants completed the International Physical Activity Questionnaire for descriptive purposes. Second, participants were sent home with an accelerometer (GTX3, ActiGraph, Pensacola, FL, USA). Participants were asked to wear the accelerometer over the right hip during waking hours over a period of 7 consecutive days.

3.2.2.2 Gait Analysis

Biomechanical gait analyses were employed. Individual reflective markers were placed on specific anatomical landmarks on the pelvis and right lower limb using double-sided tape.

These landmarks included: left and right posterior superior iliac spines, left and right anterior superior iliac spines, left and right greater trochanters, medial and lateral femoral condyles, medial and lateral tibial condyles, tibial tuberosity, medial and lateral malleoli, heel, first and fifth metatarsal heads, and superior midfoot. In addition, rigid body marker clusters were placed on the approximate centre of mass of each segment (pelvis, thigh, shank, foot).

Participants walked barefoot across a 12-metre walkway equipped with a floor-embedded force platform (OR6-7, Advanced Mechanical Technology Inc., Watertown, MA). Kinematics were captured using 11 high-speed infrared cameras (Raptor-4, Motion Analysis Corporation, Santa Rosa, CA) using a sampling frequency of 100 Hz. Motion data was time-synchronized with force data sampled at 1000 Hz. Seven successful gait trials were collected in which heel strike and toe-off of the right foot occurred on the force platform.

3.2.2.3 Magnetic Resonance Imaging

At the imaging visit, sets of MR images on the right knee were acquired prior-to and immediately following 15-minutes of treadmill running at a self-selected pace (Gatti et al. 2017). Images were acquired using a 3-Tesla MR750 Discovery MRI scanner (GE Healthcare, Milwaukee, WI). All imaging visits occurred in the morning to prevent cumulative effects of daily activity on tibiofemoral cartilage (Gatti et al. 2017; Mosher et al. 2010). Further, participants were asked to drive or accept a complimentary taxicab ride to their appointment, and participants rested supine for 30 minutes upon arrival (Gatti et al. 2017; Subburaj et al. 2012).

Each participant was transported to the scanner room via wheelchair. The participant was positioned on the MRI bed with their right knee in an 8-channel transmit/receive radiofrequency lower extremity coil (Invivo Corporation, Gainsville, FL, USA). The researcher (ECBW) used indelible ink to mark the coil position for accurate re-positioning post-activity. Scans included: 1) 3D fat-saturated fast spoiled gradient recalled (3D-F-SPGR) image for segmentation (TR=17.488ms; TE=5.812ms; Matrix=512×512; Pixel spacing=0.312×0.312mm; Slice Thickness=1mm; Flip Angle=18^o); and 2) sagittal multi-echo spin-echo (MESE) images acquired with a CartiGram T2-mapping sequence (GE Healthcare) [10,16] for the calculation of T2 maps (TR=2600ms; TE=6.328, 12.656, 18.984, 25.312, 31.640, 37.968, 44.296, 50.624ms; Matrix=256×256; Pixel spacing=0.625×0.625mm; Slice Thickness=3mm; Flip Angle=90^o)

During post-activity imaging, the order of scan acquisition was reversed such that sagittal MESE scans were acquired immediately following activity to capture changes in T2 due to activity.

3.2.2.4 Treadmill

Following pre-activity imaging, participants ran on a treadmill (5.1AT, Advanced Fitness Group, Cottage Grove, WI) with zero incline for 15-minutes. Participants were asked to run at a perceived exertion of moderate to strong; treadmill speed was adjusted to reflect this range.

3.2.3 Data Analysis

3.2.3.1 Biomechanical Gait Analysis

Gait trials were digitized in Cortex Motion Capture software (Motion Analysis Corporation, Santa Rosa, CA). Marker and force plate data were post processed in Matlab R2018b (The MathWorks Inc., Natick, MA). Trials were trimmed to reflect stance phase on the force plate. Virtual markers were added to the pelvis, knee, and foot to facilitate model scaling.

Joint reaction analyses were completed using OpenSim 3.2 (simTK, Stanford, CA, USA). A refined generic lower-limb model was used (Lai et al. 2017). Mass and inertial actuators were added to the pelvis to account for the absence of a torso in the model. Inverse kinematics were calculated. The resulting kinematics and ground reaction forces were filtered with a dual-pass 6Hz Butterworth filter. Net joint external moments were calculated. Next, static optimization was performed using the simTK Synergy Optimization Tool which enables weighting of model actuators (Steele et al. 2012). The hamstrings and gastrocnemius were adjusted to a weight of 0.33 and 0.14 respectively, as these weightings produced the best match between experimental and modeled compressive tibiofemoral JRF (Steele et al. 2012). The compressive tibiofemoral JRF was calculated using individual muscle controls from static optimization, kinematics, and external ground reaction forces.

The impulse of the JRF was calculated using trapezoidal integration and expressed in Newton seconds (Ns). Mean impulse was calculated from the first 5 successful trials.

3.2.3.2 Accelerometry

Daily step data was extracted for all days with >10 hours of wear (Troiano et al. 2008). Mean number of daily steps was calculated.

3.2.3.3 Image Analysis

Tibial and femoral cartilage were segmented from pre- and post-activity 3D-FSPGR scans using a convolutional neural network (NeuralSeg Ltd, Hamilton, ON, Canada) (Gatti and Maly 2019). All segmentations were manually checked in 3DSlicer software. Of 30 scans (pre

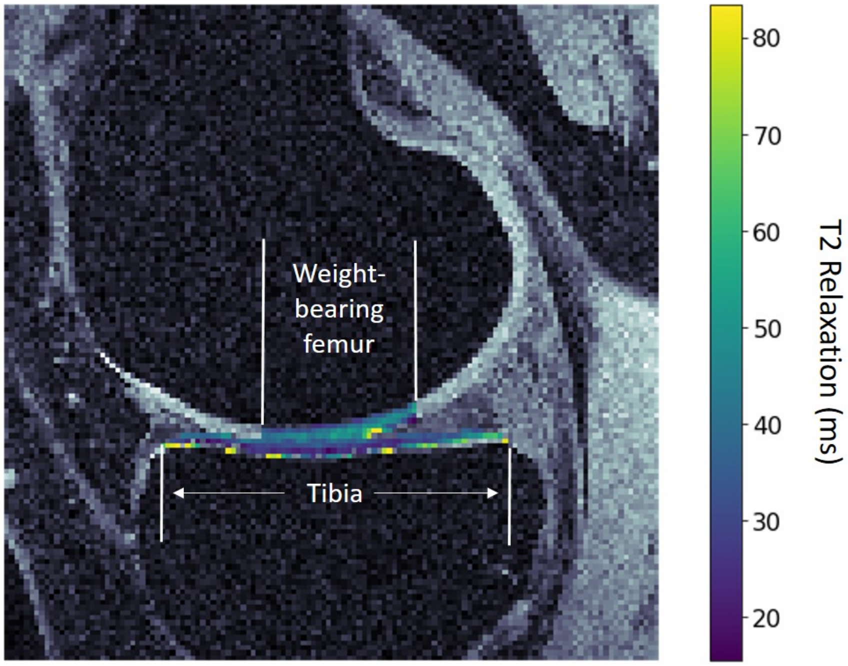

Figure 3.2.1: T2 relaxation (ms) values overlaid on a down-sampled 3D-FSPGR image. White lines on the femur indicate the weight-bearing femur as described by Eckstein 2006.

and post for 15 participants), one segmentation required minor manual adjustment. The medial tibia, lateral tibia, medial weight-bearing femur, and lateral weight-bearing femur were analyzed separately in custom Python software (version 2.7). Weight-bearing femoral cartilage was determined by finding the first coronal slice of the intercondylar notch in the 3D-FSPGR volume and calculating 60% of the distance to the posterior ends of the femoral cartilage (Eckstein et al. 2006) (Figure 3.2.1). Cartilage thickness (mm) was calculated by taking the minimum Euclidean distance from each voxel on the bone-cartilage interface to every voxel on the articular surface. Cartilage volume was represented in millimetres cubed (mm^3).

Calculation of T2 maps was completed in a custom Python program. The signal intensity of each voxel was transformed via a natural logarithm. Then, a least squares estimation approach was used to calculate T2 relaxation time (milliseconds; ms). T2 values greater than 100 ms or any T2 estimation with a $R^2 < 0.7$ were excluded from analysis (Gatti et al. 2017; Subburaj et al. 2012).

Alignment of segmentations and T2 maps were checked manually, and transformed if necessary using rigid registration in 3DSlicer. The segmentation volume was downsampled to match the slice thickness and spacing of the T2 map. Then, T2 values for each region were extracted for analysis.

3.2.4 Statistical Analyses

Means and standard deviations were provided for descriptive variables. Two-tailed paired t-tests were used to determine if cartilage thickness, cartilage volume, and T2 relaxation were significantly different from baseline following running. A Sidak-corrected p-value of 0.004 was used to account for multiple comparisons.

The influence of daily knee compressive cumulative load on 1) thickness change, 2) volume change, and 3) T2 relaxation change in the tibiofemoral cartilage after running was assessed using multiple linear regression in Stata (13.1, StataCorp, College Station, TX). Tibial cartilage and weight-bearing femoral cartilage were assessed separately. Baseline cartilage outcome (thickness, volume, or T2 relaxation), number of steps per day (right leg only), JRFI, and their interaction (JRFI×steps; daily cumulative compressive knee load) were used as independent variables. For the secondary analysis, BMI substituted JRFI in the multiple linear regressions. Standard errors and the regression variance-covariance matrix were adjusted using Stata's vce(cluster) command to account for multiple observations per participant. Models were tested for assumptions of multiple regression.

3.3 Results

Of 16 participants recruited, 15 completed both visits (Table 3.3.1). One participant was lost to follow-up due to an unrelated musculoskeletal injury between visits. One set of MESE volumes were lost due to movement artefact, therefore T2 relaxation changes were available for 14 participants. All participants had at least three valid days of accelerometer wear (median: 6 days, range 3-7 days).

Cartilage deformed following running (Table 3.3.2). Thickness decreased in the lateral tibia (-0.11 mm, -4.30% change from baseline, $p < 0.001$), medial weight-bearing femur (-0.06 mm, -2.71%, $p < 0.001$), and lateral weight-bearing femur (-0.05 mm, -2.31%, $p = 0.002$). Volume also decreased in the lateral tibia (-127.7 mm^3, -5.27%, $p < 0.001$), medial weight-bearing femur (-33.6 mm^3, -3.04%, $p = 0.004$), and lateral weight-bearing femur (-44.1 mm^3, -3.90%, $p = 0.003$). T2 relaxation increased in the medial tibia following running (2.6 ms, 6.23%, $p < 0.001$). Other regions did not significantly change (thickness, volume, or T2).

Table 3.3.1: Descriptive statistics including mean and standard deviations.

	Mean	SD
Age (y)	26.1	3.2
Height (m)	1.68	0.05
Weight (kg)	65.4	11.2
BMI (kg/m^2)	23.1	3.0
Daily Steps	9679.2	2350.4
Walking ($MET \cdot min/week$)	2076.4	1745.7
Moderate ($MET \cdot min/week$)	1802.2	2042.6
Vigourous ($MET \cdot min/week$)	2205.3	1688.0
Total ($MET \cdot min/week$)	6083.9	3592.9

MET = Metabolic Equivalent. Objective measure of the ratio of the rate one expends energy, compared to quiet sitting.

Daily cumulative knee load (JRFI×steps interaction) was related to tibial volume change after running [F(4, 14) = 4.68, $p = 0.013$, $R^2 = 0.50$; Table 3.3.3]. Visualization of the JRFI×steps interaction is shown in Figure 3.3.1. Linear predictions of tibial volume change are shown over the range of data observed for JRFI and daily steps. Those with a JRFI of 574 Ns show no effect of the interaction (i.e., no slope). Positive slope of the linear prediction for those with low JRFI (i.e., JRFI lower than 574 Ns) suggests that higher daily steps result in smaller changes in tibial volume (i.e., change closer to zero). A negative slope of the linear prediction for those with high JRFI (i.e., JRFI greater than 574 Ns) suggests that higher daily steps result in greater change (more negative) in tibial volume following running. Similar results were observed for our secondary analysis (Figure 3.3.2). Among those with low BMI (19.7 kg/m^2; minimum BMI in sample), increasing number of daily steps resulted in a smaller change in tibial volume following activity. Those with a BMI of 21.6 kg/m^2 show no effect of the interaction. For those with BMI above 21.6 kg/m^2, increasing number of daily steps resulted in a greater change in tibial volume following activity. No models predicting femoral cartilage change were significant.

The running bout was not standardized. To ensure self-selected running speed did not influence results, treadmill speed was added as an additional independent variable to the multiple linear regression analysis predicting tibial volume change from 1. baseline volume,

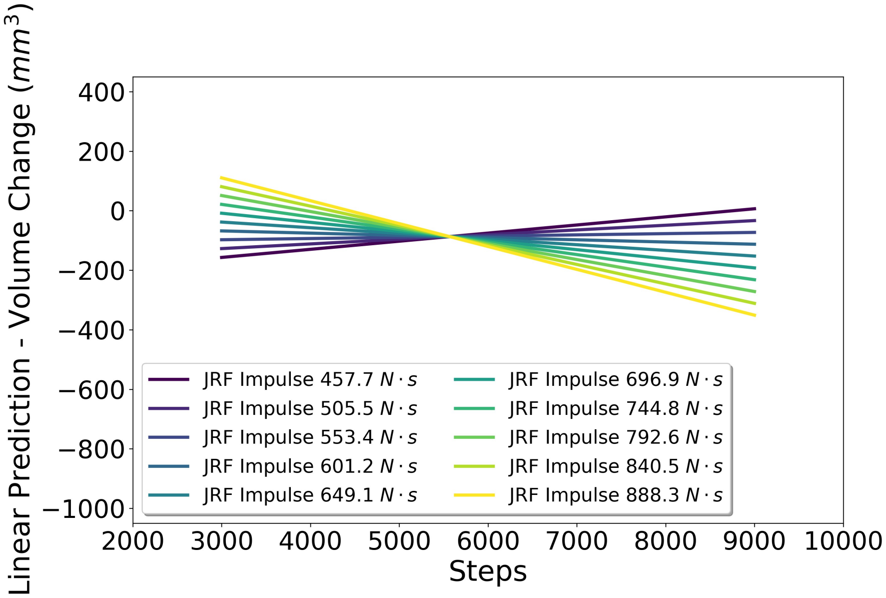

Figure 3.3.1: Linear predictions and standard errors for the significant interaction of JRFI×steps in the model that estimated tibial volume change from baseline volume, JRFI, steps per day, and the interaction of JRFI×steps (i.e., daily cumulative joint load). Steps taken by the right leg only are displayed on the x-axis and predictive margins for volume change are displayed on the y-axis. The interaction is plotted over the range of JRFI and step counts observed in this investigation. A JRFI of 574 Ns (teal region) suggests no effect of the interaction, or increasing daily steps does not change tibial response to load. Amongst those with a small JRFI (purple region; smaller than 574 Ns), increasing number of steps per day resulted in smaller changes following running. As JRFI increases beyond 574 Ns (green and yellow regions), greater daily step count resulted in greater volume change post-run.

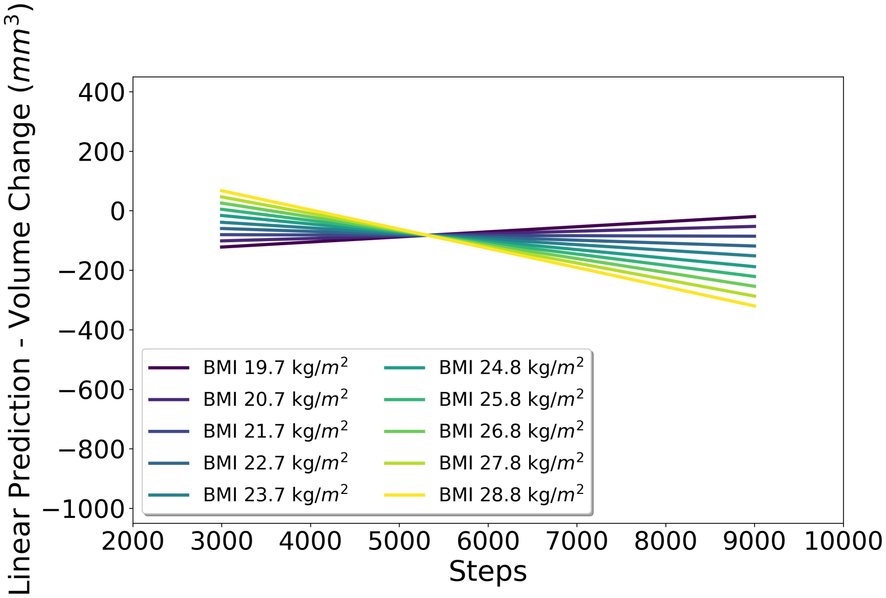

Figure 3.3.2: Linear predictions and standard errors for significant interaction of BMI×steps in the model that estimated tibial volume change from baseline volume, BMI, steps per day, and the interaction of BMI×steps. The x-axis is steps taken by the right leg only, and the y-axis is predictive margins for volume change. The interaction is plotted over the range of BMIs and step counts observed in this investigation. A BMI of 21.6 kg/m^2 (teal region) shows no effect of the interaction, or increasing daily steps does not affect tibial change following running. Similar to the results from the JRFI, amongst those with a lower BMI (purple region; lower than 21.6 kg/m^2), increasing number of steps per day resulted in less volume change following running. As BMI increased up to 28.8 kg/m^2 (green and yellow regions), greater daily step count resulted in greater volume change post-run.

Table 3.3.2: Pre and post running values for cartilage thickness (mm), cartilage volume (mm^3), and T2 relaxation (ms), along with their change. Paired t-tests were performed, and significance was determined at a Sidak corrected p-value of 0.004 to account for multiple comparisons. Changes significantly different from zero were indicated with an asterisk (*).

		Pre	Post	Post-Pre
THICKNESS (mm)	Med Tibia	2.077	2.074	-0.003
	Lat Tibia	2.559	2.452	-0.107*
	Med WB Femur	2.214	2.155	-0.059*
	Lat WB Femur	2.164	2.108	-0.057*
VOLUME (mm^3)	Med Tibia	1913.8	1896.5	-17.4
	Lat Tibia	2422.1	2294.4	-127.7*
	Med WB Femur	1102.4	1068.8	-33.6*
	Lat WB Femur	1087.8	1087.8	-44.1*
T2 RELAXATION (ms)	Med Tibia	41.9	44.5	2.6*
	Lat Tibia	38.1	38.6	0.5
	Med WB Femur	42.0	41.5	-0.5
	Lat WB Femur	41.9	40.1	-1.8

Table 3.3.3: Multiple linear regression results for the volume change models.

$F(4,14) = 4.68$
$p = 0.013$
$R^2 = 0.50$

Volume Change (Post-Pre)	Unstandardized β	Robust Standard Error	p	[95% CI]
Volume (pre)	-0.13167	0.03047	**0.001**	[-0.19603, -0.06531]
JRFI	1.34679	0.44261	**0.009**	[0.39749, 2.29610]
Steps	0.13797	0.04826	**0.013**	[0.03447, 0.24148]
JRFI×steps	-0.00024	0.00008	**0.013**	[-0.00042, -0.00006]
Constant	-571.841	213.202	**0.018**	[-1029.11, -114.567]

$F(4,14) = 7.60$
$p = 0.002$
$R^2 = 0.43$

Volume Change (Post-Pre)	Unstandardized β	Robust Standard Error	p	[95% CI]
Volume (pre)	-0.11254	0.02768	**0.001**	[-0.17190, -0.05318]
BMI	47.7202	21.8492	**0.046**	[0.85833, 92.5822]
Steps	0.19376	0.08553	**0.040**	[0.01031, 0.37722]
BMI×steps	-0.00897	0.00389	**0.037**	[-0.01731, -0.00063]
Constant	-869.453	455.718	**0.077**	[-1846.87, 107.964]

steps, JRFI, and JRFI×steps; and 2. baseline volume, steps, BMI, and BMI×steps. There was no effect of treadmill speed in either model ($p = 0.836$ and $p = 0.682$ respectively).

3.4 Discussion

Our study explored the relationship of daily cumulative knee joint load with knee cartilage volume, thickness, and compositional changes following an acute bout of running. Change in tibial cartilage volume was related to the interaction of JRFI and number of steps per day (i.e., daily cumulative joint load), where higher number of daily steps in those with lower JRFI resulted in lesser changes in tibial volume following 15 minutes of running. Also, a greater number of daily steps amongst those with lower BMI resulted in lesser changes in tibial volume following running. These models suggest that among those with lower JRFI (or lower BMI), greater levels of physical activity may show a cartilage conditioning effect in the tibia.

Advances in MRI have enabled the investigation of cartilage response to loading. While a number of MRI studies have used changes in volume (Boocock et al. 2009; Kersting et al. 2005; Kessler et al. 2006) and thickness (Mosher et al. 2010; Paranjape et al. 2019; Subburaj et al. 2012) as surrogates for cartilage strain, few studies have combined this data with biomechanical gait analysis to obtain additional information on knee joint loading (Boocock et al. 2009; Van Rossom et al. 2019). Maximum lateral compressive stress in the knee joint estimated by a 2D musculoskeletal model was related to percent change in lateral femoral cartilage volume following 30-minutes of running (Boocock et al. 2009). A subject-specific multi-body knee model (via MRI) combined with a lower-limb musculoskeletal model quantified relationships between the topographical variation in cartilage measurements (thickness, T2, T1ρ) and localized stresses (Van Rossom et al. 2019). We contribute a novel metric of daily cumulative joint load to explore the role of daily load exposure on cartilage response to loading.

There is a strong link between body mass and cartilage strain. In overweight participants ($25 - 31\ kg/m^2$), greater diurnal strains in tibial cartilage were observed compared to healthy BMI adults (Widmyer et al. 2013). When comparing healthy participants with normal ($n = 8$) versus overweight and obese BMIs ($n = 7$), tibial strain following a walking protocol was positively associated with BMI (Collins et al. 2018). Participants with a high BMI had less cartilage at baseline, and cartilage strains after activity nearly 4 times greater than those with healthy BMI (Collins et al. 2018). Further, high BMI ($>31\ kg/m^2$) participants with knee OA that accrued moderate (6,000-7,900) to high (>7,900) steps per day had an increased risk of worsening tibiofemoral damage (Voinier et al. 2020). These results corroborate the strong link between obesity and poor cartilage quality (Mezhov et al. 2014). In the current work, amongst those with higher BMI, higher levels of physical activity resulted in greater change in tibial cartilage volume following activity. Nonetheless, our results are not generalizable to obese populations, as our models only predicted up to a BMI of 28.8 kg/m^2. More work is needed to explore the role of habitual physical activity on cartilage response in obese individuals.

Contrary to our initial hypothesis, changes in tibial T2 relaxation did not have a relationship with daily cumulative knee load. This result was in contrast to previous results that found a relationship between tibial T2 relaxation change after running and an interaction of baseline T2 relaxation and self-reported physical activity in young healthy men (Gatti et al. 2017). However, our results did support a cross-sectional study, where age but not physical activity level affected change in cartilage T2 following acute activity (Mosher et al. 2010). We also had no relationship between changes in cartilage thickness and daily knee loads; this was not surprising. Physical activity level did not have an effect on thickness change outcomes, even when divided into smaller regions of interest (Mosher et al. 2010). Still, it is possible that reporting mean values from a large region underestimate true change.

Our results should be interpreted in light of a few limitations. It is not practical to measure *in vivo* joint loads in a young healthy sample. The model (Lai et al. 2017) and synergy-based static optimization (Steele et al. 2012) show excellent agreement with *in vivo* instrumented total knee replacement data. Next, due to the sensitivity of T2 relaxation measurements, MESE scans were obtained immediately after activity. Therefore, 3D-FSPGR scans used for segmentation were obtained approximately 14 minutes after cessation of exercise, creating a potential for cartilage recovery. Nonetheless, this imaging protocol was modeled after others (Gatti et al. 2017; Mosher et al. 2010; Subburaj et al. 2012). Further, Eckstein and colleagues (1999) determined that patellar cartilage recovered 50% 90-minutes after dynamic activity suggesting recovery in 14-minutes is likely not substantial.

This was the first study to our knowledge to explore a relationship between daily cumulative knee load (JRFI×steps interaction) and cartilage response following activity. Secondarily, we were interested in the effect of BMI×steps on cartilage response. Our results suggest that a higher number of daily steps in those with lower JRFI (or lower BMI) results in reduced tibial cartilage volume change following a run. Alternatively, increasing number of daily steps amongst those with higher JRFI (or higher BMI) increased tibial cartilage volume change following exercise. These results suggest a potential cartilage conditioning effect in the tibial cartilage in those of a healthy BMI only. More work is required to explore the influence of daily load exposure on cartilage response in clinical and obese samples.

Conflict of Interest Statement

The authors wish to disclose that co-author Anthony A. Gatti is the founder of NeuralSeg, Ltd, the company that provided cartilage segmentations. There are no other conflicts of interest to disclose.

3.5 References

Altman, R., Asch, E., Bloch, D., Bole, G., Borenstein, D., Brandt, K., … Hochberg, M. et al. (1986). Development of criteria for the classification and reporting of osteoarthritis: Classification of osteoarthritis of the knee. *Arthritis & Rheumatology*, *29*(8), 1039–1049.

Boocock, M., McNair, P., Cicuttini, F., Stuart, A., & Sinclair, T. (2009). The short-term effects of running on the deformation of knee articular cartilage and its relationship to biomechanical loads at the knee. *Osteoarthritis and Cartilage*, *17*(7), 883–890.

Brisson, N. M., Wiebenga, E. G., Stratford, P. W., Beattie, K. A., Totterman, S., Tamez-Peña, J. G., … Maly, M. R. (2017). Baseline knee adduction moment interacts with body mass index to predict loss of medial tibial cartilage volume over 2.5 years in knee osteoarthritis. *Journal of Orthopaedic Research*.

Cicuttini, F., Ding, C., Wluka, A., Davis, S., Ebeling, P. R., & Jones, G. (2005). Association of cartilage defects with loss of knee cartilage in healthy, middle-age adults: A prospective study. *Arthritis & Rheumatism*, *52*(7), 2033–2039.

Collins, A. T., Kulvaranon, M. L., Cutcliffe, H. C., Utturkar, G. M., Smith, W. A., Spritzer, C. E., … DeFrate, L. E. (2018). Obesity alters the in vivo mechanical response and biochemical properties of cartilage as measured by MRI. *Arthritis Research & Therapy*, *20*(1), 232.

Eckstein, F., Hudelmaier, M., Wirth, W., Kiefer, B., Jackson, R., Yu, J., … Schneider, E. (2006). Double echo steady state magnetic resonance imaging of knee articular cartilage at 3 Tesla: A pilot study for the Osteoarthritis Initiative. *Annals of the Rheumatic Diseases*, *65*(4), 433–441.

Eckstein, F., Lemberger, B., Gratzke, C., Hudelmaier, M., Glaser, C., Englmeier, K., & Reiser, M. (2005). In vivo cartilage deformation after different types of activity and its dependence on physical training status. *Annals of the rheumatic diseases*, *64*(2), 291–295.

Eckstein, F., Tieschky, M., Faber, S., Englmeier, K.-H., & Reiser, M. (1999). Functional analysis of articular cartilage deformation, recovery, and fluid flow following dynamic exercise in vivo. *Anatomy and Embryology*, *200*(4), 419–424.

Gatti, A., & Maly, M. (2019). Fully-automated cartilage segmentation using deep learning - Data from the Osteoarthritis Initiative. *2019 meeting of the International Society for Biomechanics.*

Gatti, A. A., Noseworthy, M. D., Stratford, P. W., Brenneman, E. C., Totterman, S., Tamez-Peña, J., & Maly, M. R. (2017). Acute changes in knee cartilage transverse relaxation time after running and bicycling. *Journal of Biomechanics*, *53*, 171–177.

Kersting, U., Stubendorff, J., Schmidt, M., & Brüggemann, G.-P. (2005). Changes in knee cartilage volume and serum COMP concentration after running exercise. *Osteoarthritis and Cartilage*, *13*(10), 925–934.

Kessler, M. A., Glaser, C., Tittel, S., Reiser, M., & Imhoff, A. B. (2006). Volume changes in the menisci and articular cartilage of runners: An in vivo investigation based on 3-d magnetic resonance imaging. *The American Journal of Sports Medicine*, *34*(5), 832–836.

Lai, A., Arnold, A., & Wakeling, J. (2017). Why are antagonist muscles co-activated in my simulation? A musculoskeletal model for analysing human locomotor tasks. *Annals of Biomedical Engineering*, *45*(12), 2762–2774.

Maly, M. R., Robbins, S. M., Stratford, P. W., Birmingham, T. B., & Callaghan, J. P. (2013). Cumulative knee adductor load distinguishes between healthy and osteoarthritic knees–A proof of principle study. *Gait & Posture*, *37*(3), 397–401.

Mezhov, V., Ciccutini, F. M., Hanna, F. S., Brennan, S. L., Wang, Y., Urquhart, D. M., & Wluka, A. E. (2014). Does obesity affect knee cartilage? A systematic review of magnetic resonance imaging data. *Obesity Reviews*, *15*(2), 143–157.

Miller, R. H. (2017). Joint loading in runners does not initiate knee osteoarthritis. *Exercise and Sport Sciences Reviews*, *45*(2), 87–95.

Mosher, T. J., Liu, Y., & Torok, C. M. (2010). Functional cartilage MRI T2 mapping: Evaluating the effect of age and training on knee cartilage response to running. *Osteoarthritis & Cartilage*, *18*(3), 358–364.

Paranjape, C., Cutcliffe, H., Grambow, S., Utturkar, G., Collins, A., Garrett, W., ... DeFrate, L. (2019). A new stress test for knee joint cartilage. *Scientific Reports*, *9*(1), 2283.

Seedhom, B. (2005). Conditioning of cartilage during normal activities is an important factor in the development of osteoarthritis. *Rheumatology*, *45*(2), 146–149.

Steele, K., DeMers, M., Schwartz, M., & Delp, S. (2012). Compressive tibiofemoral force during crouch gait. *Gait & Posture*, *35*(4), 556–560.

Subburaj, K., Kumar, D., Souza, R. B., Alizai, H., Li, X., Link, T. M., & Majumdar, S. (2012). The acute effect of running on knee articular cartilage and meniscus magnetic resonance relaxation times in young healthy adults. *The American Journal of Sports Medicine*, *40*(9), 2134–2141.

Timmins, K. A., Leech, R. D., Batt, M. E., & Edwards, K. L. (2017). Running and knee osteoarthritis: A systematic review and meta-analysis. *The American Journal of Sports Medicine*, *45*(6), 1447–1457.

Troiano, R. P., Berrigan, D., Dodd, K. W., Masse, L. C., Tilert, T., & McDowell, M. (2008). Physical activity in the United States measured by accelerometer. *Medicine & Science in Sports & Exercise*, *40*(1), 181–188.

Van Ginckel, A., Baelde, N., Almqvist, K., Roosen, P., McNair, P., & Witvrouw, E. (2010). Functional adaptation of knee cartilage in asymptomatic female novice runners compared to sedentary controls. A longitudinal analysis using delayed gadolinium enhanced magnetic resonance imaging of cartilage (dGEMRIC). *Osteoarthritis and Cartilage*, *18*(12), 1564–1569.

Van Rossom, S., Wesseling, M., Van Assche, D., & Jonkers, I. (2019). Topographical variation of human femoral articular cartilage thickness, T1rho and T2 relaxation times is related to local loading during walking. *Cartilage*, *10*(2), 229–237.

Vanwanseele, B., Eckstein, F., Knecht, H., Stüssi, E., & Spaepen, A. (2002). Knee cartilage of spinal cord-injured patients displays progressive thinning in the absence of normal joint loading and movement: Progressive thinning of knee cartilage after spinal cord injury. *Arthritis & Rheumatism*, *46*(8), 2073–2078.

Voinier, D., Neogi, T., Stefanik, J., Guermazi, A., Roemer, F., Thoma, L., … Torner, J. et al. (2020). Using cumulative load to explain how body mass index and daily walking relate to worsening knee cartilage damage over two years: The MOST Study. *Arthritis & Rheumatology*, *72*(6), 957–965.

Wang, Y.-C., Hart, D. L., Stratford, P. W., & Mioduski, J. E. (2009). Clinical interpretation of a Lower-Extremity Functional Scale–derived computerized adaptive test. *Physical Therapy*, *89*(9), 957–968.

Widmyer, M. R., Utturkar, G. M., Leddy, H. A., Coleman, J. L., Spritzer, C. E., Moorman III, C. T., … Guilak, F. (2013). High body mass index is associated with increased diurnal strains in the articular cartilage of the knee. *Arthritis & Rheumatism*, *65*(10), 2615–2622.

4 — Build of a 3D Voxelwise Statistical Map Examining the Relationship Between Femoral Cartilage Response to Loading and Mechanical Properties

This paper was submitted to Annals of Biomedical Engineering on 7 October 2020 (Submission # ABME-D-20-01025). Due to word limits provided by the journal, the manuscript version presented in this chapter includes some additional information in the methods and cited literature. This manuscript was transcribed to LaTeX and follows the formatting guidelines required by McMaster University's School of Graduate Studies.

Refer to the following Appendices for further information on specific elements presented in this manuscript:

Appendix A	MRI-Compatible Loading Apparatus
Appendix B	Static Loading Components
Appendix C	Equations from Hayes et al.
Appendix D	Linear Fit of T2 Decay
Appendix E	Groupwise Registration

INTEGRATING MR IMAGING WITH FULL SURFACE INDENTATION MAPPING OF FEMORAL CARTILAGE IN AN EX VIVO PORCINE STIFLE

Elora C. Brenneman Wilson, Cheryl E. Quenneville, Monica R. Maly

Abstract

No studies to date have explored the potential of MRI to predict cartilage mechanical properties across an entire cartilage surface in an *ex vivo* model. The purpose of this study was to integrate MR imaging with full-surface indentation mapping to determine the relationship between femoral cartilage thickness and T2 relaxation change following loading, and cartilage mechanical properties in an *ex vivo* porcine stifle model. Matched-pairs of stifle joints from the same pig were randomized into either 1) an imaging protocol where stifles were imaged at baseline and after 35 minutes of static axial loading; and 2) full surface mapping of the instantaneous modulus (IM) and electromechanical properties, named quantitative parameter (QP). The femur and femoral cartilage were segmented from baseline and post-loading scans, then meshes were generated. Coordinate locations of the indentation mapping points were rigidly registered to the femur. Multiple linear regressions were performed at each voxel testing the relationship between cartilage outcomes (thickness change, T2 change) and mechanical properties (IM, QP) after accounting for covariates. Statistical Parametric Mapping was used to determine significance of clusters. No significant clusters were identified; however, this integrative method shows promise for future work in *ex vivo* modeling by identifying spatial relationships between variables.

Index Terms: Cartilage, Articular; Magnetic Resonance Imaging; Statistics; Elastic Modulus.

E. C. Brenneman Wilson was funded by a Canadian Graduate Scholarship from the Natural Sciences and Engineering Research Council of Canada (NSERC). M. R. Maly holds The Arthritis Society Stars Mid-Career Development Award funded by the Canadian Institutes of Health Research-Institute of Musculoskeletal Health and Arthritis. This research was funded by an NSERC Discovery grant (MRM: 353715) and a McMaster University Interdisciplinary Fund (CEQ).

E. C. Brenneman Wilson is a doctoral student with the Department of Kinesiology, McMaster University, Hamilton, Canada (e-mail: brennema@mcmaster.ca).

C. E. Quenneville is an associate professor with the Department of Mechanical Engineering and an Associate Member of the School of Biomedical Engineering, McMaster University, Hamilton, Canada (email: quennev@mcmaster.ca).

M. R. Maly is an associate professor with the Department of Kinesiology, University of Waterloo, Waterloo, Canada. She is also an adjunct professor in the School of Rehabilitation Science, and Department of Kinesiology at McMaster University, Hamilton, Canada (email: mrmaly@uwaterloo.ca).

4.1 Introduction

Magnetic resonance imaging (MRI) is a non-invasive imaging modality capable of providing insightful information on biological tissues. Articular cartilage morphology (thickness, volume) and composition (e.g., T2 relaxation [free water]) are common outcomes, and have been used extensively to describe healthy cartilage mechanics (Eckstein et al. 2005; Paranjape et al. 2019; Subburaj et al. 2012), detect early signs of cartilage disruption due to osteoarthritis (OA) (Chang et al. 2016), and track disease progression (Brisson et al. 2017; Carballido-Gamio et al. 2009; Chang et al. 2015). Using MRI to estimate mechanical properties of cartilage to help in the detection and monitoring of disease is a useful application of this non-invasive modality. Many studies to date that explored the relationship between MRI cartilage outcomes and mechanical properties of articular cartilage have used explants (Hatcher et al. 2017; Juras et al. 2009; Kurkijärvi et al. 2004; Lammentausta et al. 2006; Nebelung et al. 2018; Nebelung et al. 2017b; Nieminen et al. 2004; Nissi et al. 2007; Nissi et al. 2004; Rautiainen et al. 2015; Wheaton et al. 2005). Samosky et al. 2005 was one of the first to complete indentation tests at pre-defined locations across the tibial surface of excised tibial plateaus from total knee arthroplasty patients, and register those locations with dGEMRIC scans. They were able to determine site-specific estimates of glycosaminoglycan concentration, and their relationship to cartilage stiffness at corresponding sites (Samosky et al. 2005). The ability to explore spatial relationships between cartilage imaging measures and mechanical properties will expand research capacity to explore cartilage responses to loading.

The use of *ex vivo* joint models is attractive as it can mimic an *in situ* loading environment. Loaded *ex vivo* tibiofemoral joints have been imaged using MRI (Chan et al. 2009; Herberhold et al. 1999; Nebelung et al. 2017a; Shiomi et al. 2010). For example, in a pair of studies, human femoro-patellar joints were imaged before and after loading to approximately 150% body mass in an MRI-compatible static loading device to evaluate cartilage thickness changes (Herberhold et al. 1999; Herberhold et al. 1998). Chan et al. 2009 used a simultaneous imaging and cyclic loading protocol to measure tibiofemoral strain in an intact porcine joint; that technique has since been used to evaluate cartilage strain *in vivo* (Chan et al. 2016). Nebelung et al.2017 assessed imaging and biomechanical parameters in cartilage explants that were placed within silicon bone molds of a femur and tibia from a human cadaver. The mold was then loaded within an MRI-compatible quasi-static loading device to obtain thickness and T2 relaxation measurements at 3 displacement positions, and finally subjected to unconfined compression tests to obtain measures of Young's Modulus

(Nebelung et al. 2017a). This combination of loading and cartilage indentation biomechanics enabled the estimation of mechanical properties following loading in an *in situ* loading environment. To our knowledge, an integration of external loading and cartilage indentation mechanics in an intact *ex vivo* porcine stifle model to localize regions where MRI cartilage outcomes can predict cartilage mechanical properties has not been explored in the literature.

Mapping mechanical properties across the surface of a joint provides information on topographical variations in cartilage function. The automated indentation procedure developed by Biomomentum, Inc. (Laval, QC) enables estimations of the instantaneous modulus (IM) at pre-determined grid locations across a joint surface (Sim et al. 2017a). Electromechanical properties measured via the Quantitative Parameter (QP) can also be estimated. QP was negatively associated with fibril modulus (r = -0.76), matrix modulus (r = -0.69), the natural logarithm of permeability (r = 0.72), and polarized light microscopy score (r = -0.70) (Sim et al. 2014) suggesting that higher values of QP were related to poor cartilage quality. Topographical variations in IM and QP measures over the cartilage surface (Sim et al. 2017a; Sim et al. 2014) align with findings from others observing significant variation in cartilage thickness (Lad et al. 2016; Van Rossom et al. 2019) and cartilage T2 relaxation (Kurkijärvi et al. 2004) measured via MRI. To-date, however, no work has explored the associations of MRI cartilage outcomes with measures reflecting tissue mechanics in an intact porcine stifle model.

The capacity to infer mechanical tissue properties from MRI scans would enable brand new perspectives to predicting the load-bearing capacity of knee cartilage, assessing disease status, and predicting disease progression. Statistical parametric mapping (SPM) can enable studies associating features captured from MRI with mechanical tissue properties. SPM can identify spatial extent of clusters that indicate significant change, while taking multiple comparisons into account (Nichols 2012). Exploring statistical relationships over every voxel over a region of interest (e.g., femoral condyle) runs the risk for Type I error. Therefore, methods for identifying clusters of significant models while simultaneously correcting for the familywise error rate are imperative. A Monte Carlo technique (random permutation) can then be used to determine the minimum cluster size required to determine cluster-based inference (Cox et al. 2017). SPM is commonly used in fMRI imaging, and has transitioned into a useful tool for musculoskeletal imaging to identify location of significant clusters that reject the null hypothesis (Pedoia et al. 2017; Pedoia et al. 2016).

We used a novel method to integrate femoral meshes derived from MRI scans with mechanical properties from surface indentation mapping. The purpose of this study was to determine the relationship between femoral cartilage response (thickness and T2 relaxation change) following static loading and cartilage mechanical properties (IM, QP) in a whole-joint porcine stifle model. A voxelwise approach, SPM, was used to investigate these relationships. The few explant studies that have explicitly studied relationships between T2 and mechanical properties (Young's modulus, dynamic modulus, aggregate modulus, IM) have observed low-to-moderate correlations (Juras et al. 2009; Kurkijärvi et al. 2004; Lammentausta et al. 2006; Nieminen et al. 2004; Nissi et al. 2007; Nissi et al. 2004; Rautiainen et al. 2015). As well, relationships between changes in T2 in response to loading and instantaneous Young's modulus showed moderate correlations (Nebelung et al. 2017b). We hypothesized that the SPM approach in our work would be able to specifically identify and localized regions of significant relationships across the femoral condyle surfaces, if present.

4.2 Methods

4.2.1 Study Design

Matched pairs of porcine stifle specimens were randomized into one of two protocols: 1) a loading and imaging protocol, or 2) a full-surface indentation mapping to quantify articular cartilage mechanical properties. Of those in the loading and imaging protocol, stifles were further randomized into one of two loading groups: 1) low load (LL); or 2) high load (HL). A schematic of the study design is displayed in Figure 4.2.1.

4.2.2 Specimen Preparation

Twenty-four matched pairs of porcine stifle joints were purchased from a local abattoir (Highland Meat Packers, Stoney Creek, ON). Stifles were required to be intact, with no compromise of the joint capsule or encapsulated tissues. Pairs were immediately frozen for at least 24 hours. Then, pairs were removed and thawed at room temperature for 18 hours before dissection. Pairs were closely inspected to ensure no cuts were made into the joint capsule during the butchering process. The stifle randomized to imaging was then removed of excess muscle tissue using a scalpel, careful not to cut into the joint capsule. The whole, intact joint was then labelled and re-frozen.

The stifle randomized to indentation was prepared for surface mapping of the femoral condyles. The capsule was carefully cut by first removing the patella on a plane parallel to the articular surface. The medial and lateral collateral ligaments were then cut, ensuring that the scalpel did not compromise the underlying articular cartilage. Then, the anterior and posterior cruciate ligaments were excised. Once the femur and tibia were separated,

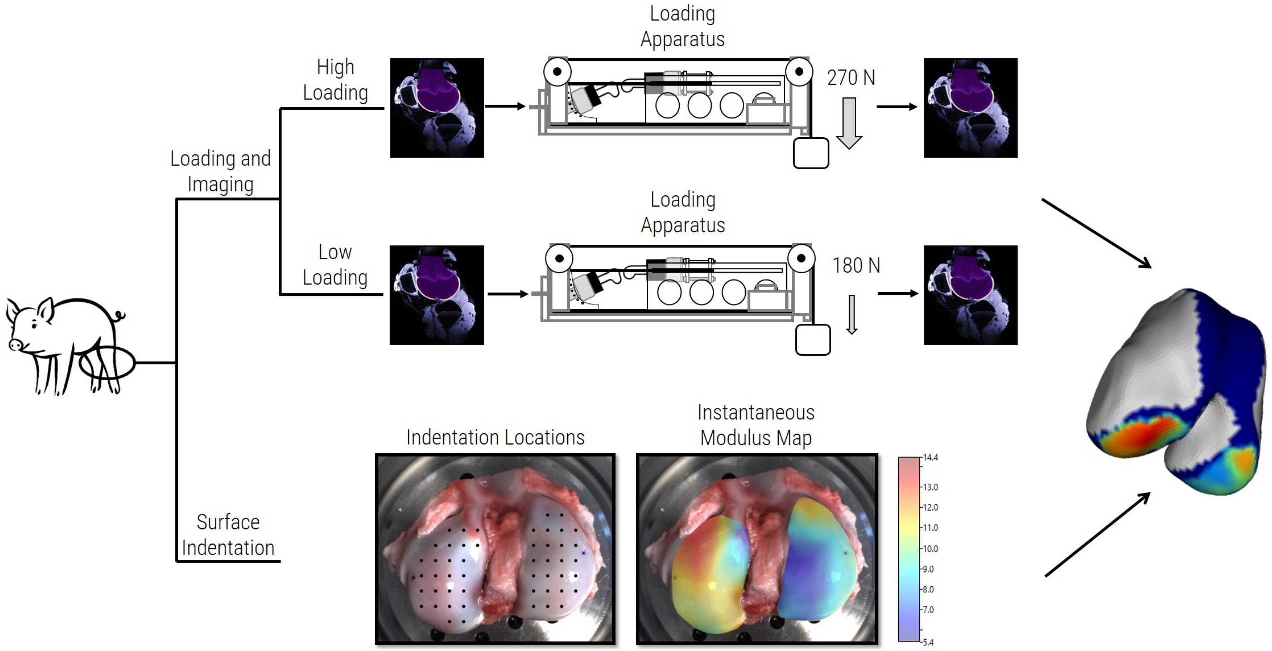

Figure 4.2.1: Schematic diagram of the study design. Left and right stifle joints of the same pig were randomized into one of two protocols: a loading and imaging protocol (top) or an indentation mapping protocol (bottom). Stifles in the loading and imaging group were randomized into either a high-loading (HL) or low-loading (LL) group, where the static load exposure was varied (270 N or 180 N for 35 minutes). Stifles in the indentation group were dissected and underwent an automated indentation mapping protocol using a Mach-1 v500csst mechanical tester (Biomomentum, Inc., Laval, QC). These two datasets (MRI scans, mechanical properties at specified locations) were combined using custom code in Python (version 3.6) to complete voxelwise statistical mapping to predict mechanical properties from MRI metrics (right).

the trochlear notch (on the femur) was removed with a hand saw and miter box on a plane parallel to the most anterior points of the medial and lateral notch. Then, the femoral condyles were removed on a plane parallel to the most inferior points of the medial and lateral articulating surfaces. During the preparation of the femoral condyle specimen, exposed cartilage was sprayed with a 0.9% saline solution to retain moisture in the tissue. Prepared and imaged specimens were placed in a labelled plastic bag with a saline-soaked paper towel and re-frozen.

Both stifles, independent of randomization, underwent two freeze-thaw cycles. It has been shown that up to 3 freeze-thaw cycles have no significant effect on cartilage mechanical properties (Peters et al. 2017).

4.2.3 Estimation of Cartilage Mechanical Properties

4.2.3.1 Electromechanical Properties - 'Quantitative Parameter'

Each specimen was thawed in a 4^oC refrigerator, then mounted in a 3" tall sample chamber using standard screws. Using a 2D camera registration system, the specimen was placed in view of the camera. In proprietary software (Analysis-MAP, Biomomentum, Laval, QC), boundaries were drawn around each the medial and lateral condyles. Within the boundaries, testing points were labelled in a grid pattern (4.5×4.5 mm) on each surface. Approximately 30 testing points were labelled for each the medial and lateral condyles. The sample was then covered and allowed to equilibrate in phosphate-buffered saline (PBS) solution for 5 minutes. Using the camera registration system as a guide, the cartilage surface was contacted with the Arthro-BST^{TM} probe at each indentation site, and the QP was recorded.

The handheld Arthro-BST^{TM} probe is a tool that uses 37 micro-electrodes on the surface of a 6.36 mm indenter to measure surface streaming potential (Sim et al. 2014). As electrodes come in contact with the surface, the overall summation of the streaming potential increases; the number of electrodes in contact with the surface when the streaming potential hits 100 mV is reflective of the probe output (Quantitative Parameter [QP]; unitless).

4.2.3.2 Cartilage Indentation

Following quantification of the electromechanical properties, the specimen chamber was loaded onto the Mach-1 v500csst mechanical testing system (Biomomentum, Laval, QC). A 1 mm diameter porous Ruby spherical indenter was attached to a multi-axis load cell (70 N range, 350 mN resolution. The x (left/right) and y (front/back) coordinates of the indentation points were calibrated to the mechanical testing system using two reference points marked on each condyle with indelible ink. Next, the following indentation parameters were set for a stress-relaxation response: contact velocity – 0.5 m/s, contact criteria – 0.0175 N, stage limit – 20 mm, scanning grid – 0.5 mm, indentation amplitude – 0.2 mm, indentation velocity – 0.2 m/s, relaxation time – 5 s, load limit – 30 N. At each location, the indenter contacted the surface. Then, in four corners surrounding the indentation site, the surface was contacted again. These four points were used to create a plane of the surface, and the absolute surface angle was calculated. Using this information, the stage would then time the contact of the surface at the indentation location with the indenter tip such that the contact was normal to the surface. All raw data for time, position, and force were recorded at each location.

After the indentation process, the spherical indenter was replaced with a 26G 3/8" PrecisionGlide intradermal bevel needle (BD, Franklin Lakes, NJ). At each indentation location the needle penetrated the cartilage until bone was reached. Time-varying force and displacement data were recorded at each location.

4.2.3.3 Data Analysis

Raw data from each indentation location were imported into proprietary software (Automated Indentation and Thickness Batch Analysis, Biomomentum, Inc., Laval, QC). Manual identification of the bone-cartilage interface was completed to calculate normal cartilage thickness. Using the calculated surface angle, the normal thickness was calculated as:

$$h = cos\theta \cdot d \tag{1}$$

where θ is the absolute surface angle and d is the horizontal displacement from the articular surface to the bone-cartilage interface. Then, the calculated cartilage thickness was input to Hayes equation for the indentation mechanics of an infinite elastic layer bonded to a rigid half-space (Hayes et al. 1972). The instantaneous modulus (IM; MPa) was determined by:

$$IM = \frac{P}{H} \cdot \left(\frac{1 - v^2}{2\alpha\kappa(\frac{a}{h}, v)} \right) \tag{2}$$

where P is the normal load measured by the indenter; H is the normal position of the indenter; v is Poisson's ratio; a is the radius of the contact region between the indenter and the cartilage surface; and κ is a dimensionless correction factor calculated based on the aspect ratio (a/h; where h is the cartilage thickness) and v (Sim et al. 2017a). IM was determined at the instant displacement was 0.15 mm (Sim et al. 2017a).

4.2.4 Imaging

4.2.4.1 Specimen Preparation

The day before the imaging protocol, specimens were removed from the standing freezer. Specimens were potted while frozen. The femur was potted in 3” of dental stone within an 8” long piece of 4”-diameter PVC pipe. Once the femur was set, the tibia was then potted in a 3” long piece of 3”-diameter PVC pipe. Then, potted specimens were labeled and placed in a sink to thaw at room temperature overnight.

4.2.4.2 Loading Protocol

Specimens were loaded into a custom-built static loading MRI-compatible apparatus (Figure 4.2.2). All specimens, independent of loading condition, were subjected to a static pre-load of 180 N for 15-minutes to counteract swelling in the tissue from the freeze-thaw cycle (Milicevic 2016). Next, baseline imaging was completed. Then, specimens underwent their respective loading condition. Specifically, those randomized to the LL condition were subjected to an axial load equivalent to quiet stance experienced by the stifle in an average adult pig (180 N) for 35 minutes. Those randomized to the HL condition were subjected to a hyper-physiologic static axial load equivalent to 1.5 times that experienced by the stifle in an average adult pig during stance (270 N) for 35 minutes. Finally, the specimen was placed back in the scanner for post-loading imaging.

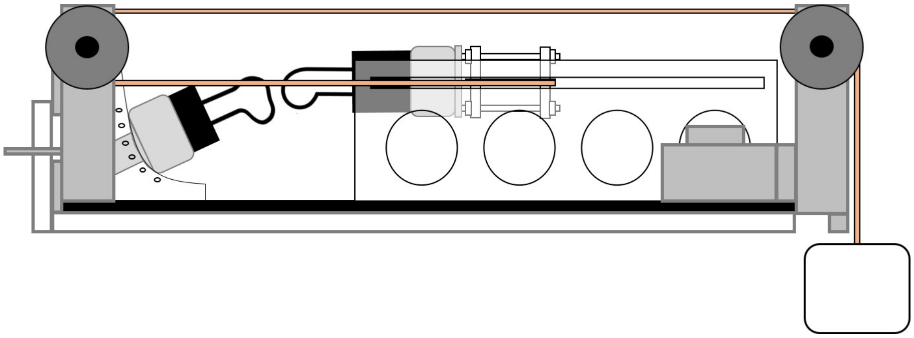

Figure 4.2.2: A) Schematic diagram of the MRI-compatible apparatus that applied static load to porcine specimens. B) Picture of the apparatus during laboratory testing. Custom designed plastic components housed a prepared specimen mounted in dental stone within pieces of PVC piping. A pulley system made of wood components and 3D-printed PLA plastic pulleys facilitated axial compressive force at the stifle joint.

Table 4.2.1: Imaging parameters for baseline and post-loading scans.

	3D Fast Spoiled Gradient Recalled (3D-FSPGR)	Multi-Echo Spin Echo (MESE)
Series Duration ($mm : ss$)	7:19	11:01
TR (ms)	17.5	2400
TE (ms)	5.804	6.264, 12.528, 18.792, 25.056, 31.32, 37.584, 43.848, 50.112
FOV (mm)	160	160
Frequency (MHz)	127.779	127.779
Matrix Size	512×512	256×256
Pixel Spacing (mm)	0.313×0.312	0.625×0.625
Slice Thickness (mm)	1	3
Slice Spacing (mm)	0	0.6
NEX	1	1
ETL	1	1
Flip Angle (^{o})	18	90

TR - Relaxation Time, TE - Echo Time, FOV - Field of View, NEX - Number of Excitations, ETL - Echo Train Length

4.2.4.3 Imaging Protocol

Specimens were scanned in a 3.0T MR750 Discovery MRI scanner (GE Healthcare, Milwaukee, WI) using an 8-channel transmit/receive radiofrequency knee array coil (Invivo Corporation, Gainsville, FL). Two sets of scans were acquired at each the baseline and post-loading time points: 1) 3D fat-saturated fast spoiled gradient recalled (3D-FSPGR) for bone and cartilage segmentation; and 2) sagittal multi-echo spin-echo (MESE) for the calculation of T2 relaxation maps. The sagittal MESE scan was acquired using the CartiGram T2-mapping sequence (GE Healthcare, Milwaukee, WI) designed for the calculation of T2 relaxation of cartilage tissue (Bining et al. 2009; Dautry et al. 2014; Gatti et al. 2017). Imaging parameters for the two sequences are shown in Table 4.2.1.

4.2.4.4 Image Segmentation

The femur and femoral cartilage were manually segmented by one rater (ECBW) from the 3D-FSPGR scans using 3DSlicer software (http://www.slicer.org). Only femoral cartilage was studied as it is thicker, enabling better delineation of tissues (Shiomi et al. 2010).

4.2.4.5 Cartilage Thickness Calculation

All image post-processing was completed with custom Python code (Python 3.6). First, meshes were generated for each the femur and femoral articular cartilage using the visualization toolkit (VTK) implementation of the Marching Contour filter. Meshes were resampled (Valette et al. 2008; Valette and Chassery 2004), then cartilage thickness was calculated using a ray casting method. Briefly, on the femoral mesh, vectors were rendered normal to the surface at each mesh centroid. If the vector intersected the cartilage mesh twice (the first intersection representing the bone-cartilage interface, and the second intersection representing the articular surface), the locations of those intersections were recorded. Then, the Euclidean distance was calculated representing cartilage thickness at that location.

4.2.4.6 T2 Relaxation Mapping

T2 relaxation maps (T2 maps) were calculated using a least squares estimation approach:

$$b = (X^T X)^{-1} X^T Y \tag{3}$$

where b is a 2-by-n matrix where the first column contains data to calculate the intercept (PD) and the second column is used to calculate T2 relaxation; X is an 8-by-2 matrix with the first column containing ones and the second column containing the 8 echo times (see Table 4.2.1); and Y is an n-by-8 matrix of the natural logarithm of the signal intensities (flattened matrix) at each of the 8 echo times. T2 values greater than 100 ms were excluded from analysis (Gatti et al. 2017; Kumar et al. 2014; Souza et al. 2014; Subburaj et al. 2012). Additionally, any T2 estimation an $R^2 < 0.7$ was excluded from analysis (Gatti et al. 2017; Wirth et al. 2014).

To extract T2 values corresponding to the femoral cartilage, T2 map and FSPGR volumes were aligned using a rigid translation. Cartilage T2 maps were generated, also using the ray casting method. Rays generated from the femoral mesh centroids that intersected the femoral cartilage mesh were used to calculate the T2 map. The Bresenham line algorithm was used to record all intersected voxels from the T2 volume. Corresponding T2 values were averaged along those vectors to create a voxelwise map of T2.

4.2.4.7 Within-Specimen Image Registration

Data was processed at baseline and post-loading. Initial, rough within-specimen registration of meshes was completed using the VTK implementation of the Iterative Closest Point (ICP) algorithm.

Baseline femur segmentations were registered to the location of cartilage indentations using a rigid Coherent Point Drift (CPD) method (Myronenko and Song 2010). Then, post-loading segmentations were registered to the same space using the output parameters of the registration algorithm:

$$YT = sYR + t \tag{4}$$

where YT is the transformed point set; s is a scaling factor; Y is the original point set; R is a 3-by-3 rotation matrix; and t is a 1-by-3 translation vector. IM and QP values were upsampled and interpolated over the femoral mesh using a Gaussian kernel filter with a sigma of 1.0.

4.2.4.8 Groupwise Image Registration

To compute groupwise statistics, baseline and post-loading specimen data were registered to a common template. To choose the common template, each baseline femur was registered to each other using the ICP algorithm. Then, the root mean squared error (RMSE) of the registration was computed. The specimen with the lowest RMSE across all registrations was chosen as the template (1.77 mm).

Every femur segmentation was registered to the template in two steps. First, the affine implementation of the CPD algorithm was used to provide an initial, rough registration of the two bones. Then, the deformable implementation of the CPD algorithm was used to align the two bones. Corresponding cartilage thickness (baseline and post-loading), T2 relaxation (baseline and post-loading), IM, and QP data were simultaneously filtered and registered to the template using a Gaussian kernel filter with a sigma of 1.0.

4.2.5 Statistical Analyses

Descriptive statistics (means and standard deviations) were provided for indentation and MRI measurements. Differences in IM and QP between loading group and condyle were determined using two-factor analyses of variance (ANOVA). General differences in cartilage thickness and T2 relaxation variables between loading groups, condyles, and time points (baseline, post-loading) were explored using three-way repeated measures ANOVAs.

The prediction of mechanical properties (IM, QP) from MR variables (cartilage thickness change, T2 relaxation change) was estimated at each indentation location using multiple linear regressions. Voxels containing data for at least 16 of 18 specimens were used for analysis. Missing data was filled using the group mean. The dependent variable was either 1) IM, or 2) QP. Predictors in the models were: thickness change (or T2 relaxation change), baseline thickness (or baseline T2 relaxation), and loading group (LL or HL; coded as dummy variables). Significant models were thresholded at $p < 0.05$.

To resolve issues of multiple comparisons, a random permutation method was used to compute the minimum cluster size required to determine significance at an alpha of $p < 0.05$. Random permutations of the dependent variable (Y; modulus or QP) from the regression models were computed at each voxel, and model parameters were re-calculated. The number, size (in voxels), and area (mm^2) of clusters of statistically significant models were recorded at each permutation. The minimum cluster size requirement was then determined using a Cumulative Distribution Function of the largest cluster from each permutation.

4.3 Results

A total of 24 matched pairs were acquired for testing. All 24 femoral specimens were probed and indented at Biomomentum., Inc. For the matched pair undergoing loading and imaging, 19 specimens were tested. Facility closures due to the COVID-19 pandemic precluded testing of the remaining 5 specimens. One loaded specimen was removed from analysis due to issues with post-loading image reconstruction, therefore 18 specimens were used in the final analysis. Of the final sample, 10 specimens were in the LL group and 8 specimens were in the HL group.

Descriptive statistics are provided in Table 4.3.1. Mean maps for cartilage thickness and T2 relaxation measurements, and IM and QP are shown in Figures 4.3.1 and 4.3.2 respectively. Medial condyles had higher values of IM than the lateral side ($p = 0.047$). Alternatively, QP was higher in the medial versus lateral compartment ($p = 0.005$). Medial femoral condyle cartilage thickness was greater than the lateral compartment across both time points ($p = 0.001$). There was a significant interaction of loading group and time points ($p = 0.002$), where thickness change magnitudes between baseline and post-loading were driven by the LL group [-0.21 mm (-7.42%) and -0.15 mm (-6.28%) versus -0.01 mm (-0.39%) and -0.02 mm (-0.86%)]. T2 relaxation was greater in the medial versus lateral compartment ($p = 0.002$). There was a main effect of loading group, where the LL group had greater T2 relaxation times ($p = 0.042$). There was no interaction effect of loading group and time points for T2 ($p = 0.142$).

The largest cluster of significant models from voxelwise analyses were extracted (Figure 4.3.3). These models looked at the association of mechanical properties (IM or QP) and cartilage outcomes from MRI (thickness, T2). When compared to the results of the random permutation analysis, clusters of significant tests extracted from the dataset were not significant at an alpha of 0.05 (Table 4.3.2). A visualization of the size of cluster required to be considered significant is shown in Figure 4.3.3.

Table 4.3.1: Summary statistics (mean (SD)) of baseline and post-loading measurements at lateral and medial condyle regions of interest.

			Cartilage Thickness (mm)	T2 Relaxation (ms)	Instantaneous Modulus (MPa)	QP
Low Loading	Medial	Baseline	2.83 (0.46)	66.5 (7.46)	7.33 (2.29)	7.29 (1.58)
		Post-Loading	2.62 (0.41)	65.2 (8.40)	-	-
	Lateral	Baseline	2.39 (0.36)	60.3 (7.98)	7.68 (2.31)	6.83 (1.59)
		Post-Loading	2.24 (0.32)	59.0 (8.77)	-	-
High Loading	Medial	Baseline	2.54 (0.53)	61.4 (12.7)	7.05 (1.88)	7.35 (1.52)
		Post-Loading	2.53 (0.55)	61.9 (13.0)	-	-
	Lateral	Baseline	2.32 (0.36)	56.6 (10.4)	8.34 (2.23)	6.50 (1.24)
		Post-Loading	2.30 (0.37)	57.8 (11.2)	-	-

Table 4.3.2: Number of cells and area (mm^3) of clusters size thresholds for determining significance at alpha < 0.05. All clusters from the dataset were not significant.

		Permutation Results		Largest Cluster from Dataset	
		Cells in Cluster	Area of Cluster	Area of Cluster	p-value
Thickness	IM	75	49.13	0.12	0.713
	QP	57	33.17	7.37	0.377
T2 Relaxation	IM	62	37.21	1.10	0.609
	QP	48	26.20	1.62	0.650

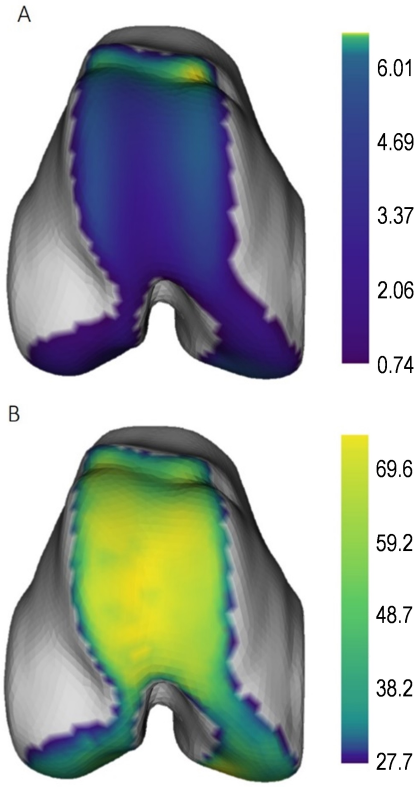

Figure 4.3.1: A) Mean thickness map (mm); and B) mean T2 relaxation map (ms) for the entire sample.

4.4 Discussion

Exploring the utility of MRI, a non-invasive imaging modality, to estimate mechanical properties of articular cartilage is critical to advance our ability to quantify tissue tolerances and monitor joint disease. To-date, many studies that have quantified relationships between cartilage mechanical properties and MRI have used cartilage explants (Hatcher et al. 2017; Juras et al. 2009; Kurkijärvi et al. 2004; Lammentausta et al. 2006; Nebelung et al. 2018; Nebelung et al. 2017b; Nieminen et al. 2004; Nissi et al. 2007; Nissi et al. 2004; Rautiainen et al. 2015; Wheaton et al. 2005).. While these studies provide an important foundation for characterizing the theoretical mechanical behaviour of cartilage, explants do not mimic the physiological loading environment (Herberhold et al. 1999). We proposed a novel integration of full-surface cartilage indentation mapping data with cartilage outcomes derived from MRI in an *ex vivo* porcine stifle model. SPM with a random permutation procedure to

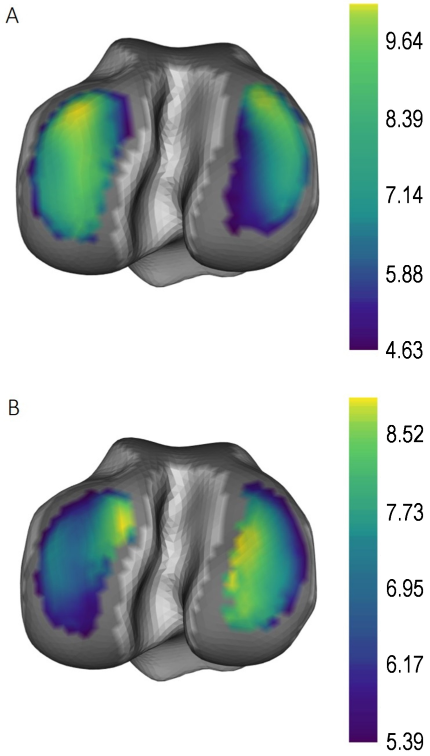

Figure 4.3.2: Mean map for A) Instantaneous Modulus (IM; measured in MPa), and B) Quantitative Parameter (QP; unitless). Grey indicates articular cartilage that was not testing during indentation. The lateral condyle is on the left and the medial condyle is on the right.

determine cluster-wise inference was used to create a 3D voxel-wise statistical map exploring the relationship between cartilage mechanical properties (IM, QP) and cartilage outcomes (thickness, T2 relaxation change following loading). In the current sample, no significant relationships were found. However, the integration of imaging and biomechanical datasets, along with voxel-wise statistical mapping, introduces a novel method for the exploration of relationships between mechanical properties and cartilage outcomes from MRI.

The loading protocol resulted in changes in cartilage thickness in the porcine *ex vivo* model. Interestingly, a significant interaction of loading group and time point suggests that this change was driven by the LL group. Intuitively, it would be expected that the group who experiences greater static loads (HL group) would experience greater change. The LL group had greater baseline cartilage thickness than the HL group, especially in the medial tibia (2.83 vs. 2.54 mm, $p = 0.053$). Potentially, having greater thickness at baseline allows

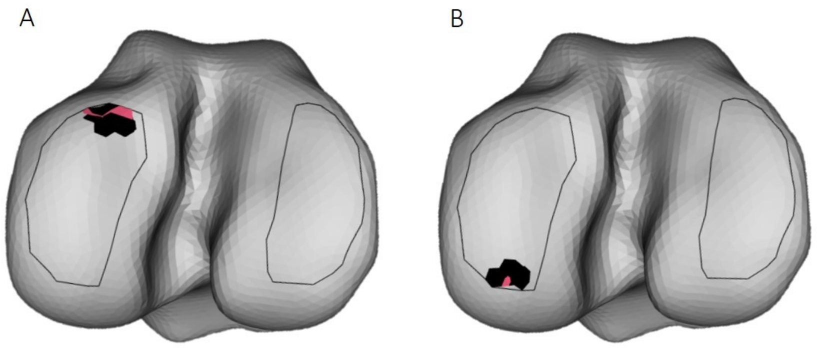

Figure 4.3.3: Largest clusters pulled from the models predicting A) QP from cartilage thickness change; and B) QP from T2 relaxation change following static loading. The black outline shows the spatial location of all voxels included in the statistical mapping. The black cluster shows the cluster area required to determine significant relationships at alpha < 0.05 (determined from 10,000 random permutations of the dataset). Overimposed in red is the largest cluster area extracted from the current dataset, which had p-values of 0.377 and 0.650 for the cartilage thickness (A) and T2 relaxation (B) models respectively.

for greater deformation. In a cross-sectional study investigating age-related differences in patellar deformation following 30 deep knee bends, older participants had less baseline cartilage and less deformation (Hudelmaier et al. 2001). Alternatively, it was shown that despite having thinner tibial cartilage at baseline, high BMI participants experienced nearly 4 times greater strains than those with healthy BMI following walking (Collins et al. 2018); femoral cartilage strain was also greater in high BMI participants despite no baseline differences in thickness. Obvious differences between the work from Collins et al. 2018 and our work is the use of an *ex vivo* model. It should be re-iterated that in our models, baseline cartilage thickness was included as a covariate. Nonetheless, it appears 180 N of compression for 35-minutes was sufficient to show measurable change in the femoral cartilage using 3D-FSPGR scans in a 3.0 T scanner.

Full surface indentation mapping allows for the quantification of topographical differences in properties over an entire cartilage surface. In this study, QP measured using the handheld Arthro-BST^{TM} probe and IM measured via the automated indentation technique were primary outcomes. QP was found to have a moderate negative correlation with fibre modulus ($r = -0.69$) and Young's modulus ($r = -0.30$), and a moderate positive correlation with permeability ($r = 0.56$) modeled from unconfined compression tests on cartilage explants (Sim et al. 2017a). In general, higher QP values are suggestive of poor cartilage quality (Sim et al. 2017b). Alternatively, IM showed a moderate positive correlation with fibre modulus ($r = 0.70$) and Young's modulus ($r = 0.49$), and a moderate negative correlation with permeability ($r = -0.47$) (Sim et al. 2017a). Our results showed higher IM and lower QP in the lateral condyle, suggesting stiffer cartilage in the lateral femoral compartment. Though not significant, cartilage deformed less in the lateral compartment (in the LL group, which drove the significant interaction of loading group and time point). This likely suggests stiffer cartilage is more tolerable to static loads in this *ex vivo* model.

A validated rigid point cloud registration technique (coherent point drift [CPD]) (Myronenko and Song 2010) successfully registered IM and QP data to the femoral mesh. CPD solves a probability density estimation problem between two point sets, one of which is modeled as centroids in a Gaussian mixture model (GMM) (Myronenko and Song 2010). CPD can appropriately handle outliers by assigning lower probabilities to specific points. Also, CPD allows for the registration of point clouds with different lengths (e.g., 1,200 up-sampled surface mapping points, and 5,000 mesh points), making it an appropriate alternative to other rigid registration algorithms (Besl and McKay 1992; Myronenko and Song 2010).

Computing voxelwise statistical analyses and subsequent clustering techniques results in the spatial localization of significant regions (or clusters) that reject the null hypothesis. In functional MRI, this has been done using SPM and Random field theory (RFT) (Worsley et al. 1992). Following the calculation of a test-statistic at each voxel in an MRI volume, SPM uses a Gaussian kernel filter to model a Gaussian smooth random field. This mimics spatial correlation present in biological data (Worsley et al. 1992). In the current study, a Gaussian kernel filter with a sigma of 1.0 was used to transfer data from each registered mesh (thickness, T2, IM, QP) onto the groupwise template. This not only filtered specimen data to introduce spatial correlation, but it also ensured correspondence between the registered mesh and the template mesh. Then following voxelwise multiple linear regressions, a Monte Carlo technique (random permutation) was employed to determine the minimum cluster size required to determine cluster-based inference (Cox et al. 2017). The random permutation method preserves the smoothness of the data field (Cox et al. 2017), and does not require estimation of RFT assumptions (Nichols 2012). Using this technique, no significant clusters were identified in this dataset. Nonetheless, this novel technique shows promise in evaluating cartilage by combining the benefits of full-surface mapping of material properties, 3D image registration, and SPM. We believe our technique has a wide range of applications in *ex vivo* joint modeling.

This results of this study should be interpreted in light of a few limitations. First, the specific age, sex, and mass of the specimens at time of slaughter was not known. All estimates for static loads were based on a mass of 80 *kg*, which is within the range reported by Thorup and colleagues with their work in pig gait biomechanics (Thorup et al. 2007). Second, to capture immediate changes in cartilage free water content, T2 relaxation was imaged immediately following loading. Therefore, the second 3D-FSPGR scan was captured approximately 14 minutes following the cessation of static loading, leaving room for the possibility of cartilage recovery. Nonetheless, this imaging procedure was modeled after others who studied cartilage T2 changes following acute loading *in vivo* (Souza et al. 2014; Subburaj et al. 2012). Cartilage recovery has been studied. A period of 45 minutes was needed for *in vivo* patellar cartilage thickness to recover 50% following deep knee bends(Eckstein et al. 1999). The characteristic recovery time of tibial cartilage modeled using a Kelvin-Voigt viscoelastic two-parameter exponential model was determined to be 25.6 minutes following 30 minutes of walking (Cutcliffe et al. 2020). Future work in *ex vivo* loading studies should consider cartilage recovery time with the timing and order of scans post-loading. Finally, using a matched-pair design assumes mechanical properties and cartilage outcomes are comparable between stifles.

4.5 Conclusions

Voxel-wise statistical tests (multiple linear regression) were computed to explore relationships between mechanical properties of articular cartilage (IM, QP) and cartilage outcomes measured via MRI (thickness, T2 relaxation) in an ex vivo stifle model. The methods introduced in this study to integrate MRI and indentation datasets, along with the use of SPM to test specific research questions, introduces a novel analysis method for *ex vivo* knee joint modeling. Future work should aim to build statistical models for use *in vivo* to quantify tissue mechanical properties, and monitor disease progression in OA.

Acknowledgements

Thank you to Imaging Research Centre director Norm Konyer for your help with imaging. Thank you to Guillaume Hesketh, Kevin Perera, Jeff Rice, and Cooper Gluek for their help with the MRI-compatible loading apparatus. We would also like to extend thanks to Dr. Eric Quenneville and Dr. Sotcheadt Sim at Biomomentum, Inc (Laval, QC) for their assistance in indentation mapping.

4.6 References

Besl, P. J., & McKay, N. D. (1992). Method for registration of 3-D shapes. In *Sensor fusion iv: Control paradigms and data structures* (Vol. 1611, pp. 586–606). International Society for Optics and Photonics.

Bining, H. J., Santos, R., Andrews, G., & Forster, B. B. (2009). Can T2 relaxation values and color maps be used to detect chondral damage utilizing subchondral bone marrow edema as a marker? *Skeletal Radiology*, *38*(5), 459–465.

Brisson, N. M., Wiebenga, E. G., Stratford, P. W., Beattie, K. A., Totterman, S., Tamez-Peña, J. G., ... Maly, M. R. (2017). Baseline knee adduction moment interacts with body mass index to predict loss of medial tibial cartilage volume over 2.5 years in knee osteoarthritis. *Journal of Orthopaedic Research*.

Carballido-Gamio, J., Stahl, R., Blumenkrantz, G., Romero, A., Majumdar, S., & Link, T. (2009). Spatial analysis of magnetic resonance T1rho and T2 relaxation times improves classification between subjects with and without osteoarthritis: Spatial analysis of cartilage MRI T1rho and T2. *Medical Physics*, *36*(9Part1), 4059–4067.

Chan, D., Neu, C., & Hull, M. (2009). In situ deformation of cartilage in cyclically loaded tibiofemoral joints by displacement-encoded MRI. *Osteoarthritis & Cartilage*, *17*(11), 1461–1468.

Chan, D. D., Cai, L., Butz, K. D., Trippel, S. B., Nauman, E. A., & Neu, C. P. (2016). In vivo articular cartilage deformation: Noninvasive quantification of intratissue strain during joint contact in the human knee. *Scientific Reports*, *6*, 19220.

Chang, A., Moisio, K., Chmiel, J., Eckstein, F., Guermazi, A., Prasad, P., ... Sharma, L. (2015). External knee adduction and flexion moments during gait and medial tibiofemoral disease progression in knee osteoarthritis. *Osteoarthritis & Cartilage*, *23*(7), 1099–1106.

Chang, E. Y., Ma, Y., & Du, J. (2016). MR parametric mapping as a biomarker of early joint degeneration. *Sports Health*, *8*(5), 405–411.

Collins, A. T., Kulvaranon, M. L., Cutcliffe, H. C., Utturkar, G. M., Smith, W. A., Spritzer, C. E., ... DeFrate, L. E. (2018). Obesity alters the in vivo mechanical response and biochemical properties of cartilage as measured by MRI. *Arthritis Research & Therapy*, *20*(1), 232.

Cox, R. W., Chen, G., Glen, D. R., Reynolds, R. C., & Taylor, P. A. (2017). FMRI clustering in AFNI: False-positive rates redux. *Brain Connectivity*, *7*(3), 152–171.

Cutcliffe, H. C., Davis, K. M., Spritzer, C. E., & DeFrate, L. (2020). The characteristic recovery time as a novel, noninvasive metric for assessing in vivo cartilage mechanical function. *Annals of Biomedical Engineering*, 1–10.

Dautry, R., Bousson, V., Manelfe, J., Perozziello, A., Boyer, P., Loriaut, P., … Laredo, J. et al. (2014). Correlation of MRI T2 mapping sequence with knee pain location in young patients with normal standard MRI. *Journal of the Belgian Society of Radiology*, *97*(1).

Eckstein, F., Lemberger, B., Gratzke, C., Hudelmaier, M., Glaser, C., Englmeier, K., & Reiser, M. (2005). In vivo cartilage deformation after different types of activity and its dependence on physical training status. *Annals of the rheumatic diseases*, *64*(2), 291–295.

Eckstein, F., Tieschky, M., Faber, S., Englmeier, K.-H., & Reiser, M. (1999). Functional analysis of articular cartilage deformation, recovery, and fluid flow following dynamic exercise in vivo. *Anatomy and Embryology*, *200*(4), 419–424.

Gatti, A. A., Noseworthy, M. D., Stratford, P. W., Brenneman, E. C., Totterman, S., Tamez-Peña, J., & Maly, M. R. (2017). Acute changes in knee cartilage transverse relaxation time after running and bicycling. *Journal of Biomechanics*, *53*, 171–177.

Hatcher, C. C., Collins, A. T., Kim, S. Y., Michel, L. C., Mostertz, W. C., Ziemian, S. N., … McNulty, A. L. (2017). Relationship between T1rho magnetic resonance imaging, synovial fluid biomarkers, and the biochemical and biomechanical properties of cartilage. *Journal of Biomechanics*, *55*, 18–26.

Hayes, W., Keer, L., Herrmann, G., & Mockros, L. (1972). A mathematical analysis for indentation tests of articular cartilage. *Journal of Biomechanics*, *5*(5), 541–551.

Herberhold, C., Faber, S., Stammberger, T., Steinlechner, M., Putz, R., Englmeier, K. H., … Eckstein, F. (1999). In situ measurement of articular cartilage deformation in intact femoropatellar joints under static loading. *Journal of Biomechanics*, *32*(12), 1287–1295. Retrieved October 3, 2016, from http://www.sciencedirect.com/science/article/pii/S002192909900130X

Herberhold, C., Stammberger, T., Faber, S., Putz, R., Englmeier, K.-H., Reiser, M., & Eckstein, F. (1998). An MR-based technique for quantifying the deformation of articular cartilage during mechanical loading in an intact cadaver joint. *Magnetic Resonance in Medicine*, *39*(5), 843–850. Retrieved October 3, 2016, from http://onlinelibrary.wiley.com/doi/10.1002/mrm.1910390522/abstract

Hudelmaier, M., Glaser, C., Hohe, J., Englmeier, K.-H., Reiser, M., Putz, R., & Eckstein, F. (2001). Age-related changes in the morphology and deformational behavior of knee joint cartilage. *Arthritis & Rheumatism*, *44*(11), 2556–2561.

Juras, V., Bittsansky, M., Majdisova, Z., Szomolanyi, P., Sulzbacher, I., Gäbler, S., … Trattnig, S. (2009). In vitro determination of biomechanical properties of human articular cartilage in osteoarthritis using multi-parametric MRI. *Journal of Magnetic Resonance*, *197*(1), 40–47.

Kumar, D., Souza, R. B., Singh, J., Calixto, N. E., Nardo, L., Link, T. M., … Majumdar, S. (2014). Physical activity and spatial differences in medial knee T1rho and T2 relaxation times in knee osteoarthritis. *Journal of Orthopaedic & Sports Physical Therapy*, *44*(12), 964–972.

Kurkijärvi, J., Nissi, M., Kiviranta, I., Jurvelin, J., & Nieminen, M. (2004). Delayed gadolinium-enhanced MRI of cartilage (dGEMRIC) and T2 characteristics of human knee articular cartilage: Topographical variation and relationships to mechanical properties: dGEMRIC and T2 of human cartilage. *Magnetic Resonance in Medicine*, *52*(1), 41–46.

Lad, N., Liu, B., Ganapathy, P., Utturkar, G., Sutter, E., Moorman III, C., … DeFrate, L. (2016). Effect of normal gait on in vivo tibiofemoral cartilage strains. *Journal of Biomechanics*, *49*(13), 2870–2876.

Lammentausta, E., Kiviranta, P., Nissi, M., Laasanen, M., Kiviranta, I., Nieminen, M., & Jurvelin, J. (2006). T2 relaxation time and delayed gadolinium-enhanced mri of cartilage (dGEMRIC) of human patellar cartilage at 1.5 T and 9.4 T: Relationships with tissue mechanical properties. *Journal of Orthopaedic Research*, *24*(3), 366–374.

Milicevic, D. (2016). *The effect of altered work-rest ratios on porcine stifles* (MSc, McMaster University).

Myronenko, A., & Song, X. (2010). Point set registration: Coherent point drift. *IEEE Transactions on Pattern Analysis and Machine Intelligence*, *32*(12), 2262–2275.

Nebelung, S., Sondern, B., Jahr, H., Tingart, M., Knobe, M., Thüring, J., … Truhn, D. (2018). Non-invasive T1rho mapping of the human cartilage response to loading and unloading. *Osteoarthritis and Cartilage*, *26*(2), 236–244.

Nebelung, S., Post, M., Raith, S., Fischer, H., Knobe, M., Braun, B., … Bruners, P. et al. (2017a). Functional in situ assessment of human articular cartilage using MRI: A whole-knee joint loading device. *Biomechanics and Modeling in Mechanobiology*, *16*(6), 1971–1986.

Nebelung, S., Sondern, B., Oehrl, S., Tingart, M., Rath, B., Pufe, T., … Jahr, H. et al. (2017b). Functional MR imaging mapping of human articular cartilage response to loading. *Radiology*, *282*(2), 464–474.

Nichols, T. (2012). Multiple testing corrections, nonparametric methods, and random field theory. *Neuroimage*, *62*(2), 811–815.

Nieminen, M., Töyräs, J., Laasanen, M., Silvennoinen, J., Helminen, H., & Jurvelin, J. (2004). Prediction of biomechanical properties of articular cartilage with quantitative magnetic resonance imaging. *Journal of Biomechanics*, *37*(3), 321–328.

Nissi, M., Rieppo, J., Töyräs, J., Laasanen, M., Kiviranta, I., Nieminen, M., & Jurvelin, J. (2007). Estimation of mechanical properties of articular cartilage with MRI – dGEMRIC, T2 and T1 imaging in different species with variable stages of maturation. *Osteoarthritis & Cartilage*, *15*(10), 1141–1148.

Nissi, M., Töyräs, J., Laasanen, M., Rieppo, J., Saarakkala, S., Lappalainen, R., … Nieminen, M. (2004). Proteoglycan and collagen sensitive MRI evaluation of normal and degenerated articular cartilage. *Journal of Orthopaedic Research*, *22*(3), 557–564.

Paranjape, C., Cutcliffe, H., Grambow, S., Utturkar, G., Collins, A., Garrett, W., … DeFrate, L. (2019). A new stress test for knee joint cartilage. *Scientific Reports*, *9*(1), 2283.

Pedoia, V., Gallo, M., Souza, R., & Majumdar, S. (2017). Longitudinal study using voxel-based relaxometry: Association between cartilage T1rho and T2 and patient reported outcome changes in hip osteoarthritis. *Journal of Magnetic Resonance Imaging*, *45*(5), 1523–1533.

Pedoia, V., Li, X., Su, F., Calixto, N., & Majumdar, S. (2016). Fully automatic analysis of the knee articular cartilage T1rho relaxation time using voxel-based relaxometry. *Journal of Magnetic Resonance Imaging*, *43*(4), 970–980.

Peters, A. E., Comerford, E. J., Macaulay, S., Bates, K. T., & Akhtar, R. (2017). Micromechanical properties of canine femoral articular cartilage following multiple freeze-thaw cycles. *Journal of the Mechanical Behavior of Biomedical Materials*, *71*, 114–121.

Rautiainen, J., Nissi, M. J., Salo, E.-N., Tiitu, V., Finnilä, M. A., Aho, O.-M., … Nieminen, M. T. (2015). Multiparametric MRI assessment of human articular cartilage degeneration: Correlation with quantitative histology and mechanical properties. *Magnetic Resonance in Medicine*, *74*(1), 249–259.

Samosky, J. T., Burstein, D., Grimson, W. E., Howe, R., Martin, S., & Gray, M. L. (2005). Spatially-localized correlation of dGEMRIC-measured GAG distribution and mechanical stiffness in the human tibial plateau. *Journal of Orthopaedic Research*, *23*(1), 93–101.

Shiomi, T., Nishii, T., Tanaka, H., Yamazaki, Y., Murase, K., Myoui, A., … Sugano, N. (2010). Loading and knee alignment have significant influence on cartilage MRI T2 in porcine knee joints. *Osteoarthritis and Cartilage*, *18*(7), 902–908.

Sim, S., Chevrier, A., Garon, M., Quenneville, E., Lavigne, P., Yaroshinsky, A., … Buschmann, M. (2017a). Electromechanical probe and automated indentation maps are sensitive techniques in assessing early degenerated human articular cartilage. *Journal of Orthopaedic Research*, *35*(4), 858–867.

Sim, S., Chevrier, A., Garon, M., Quenneville, E., Yaroshinsky, A., Hoemann, C., & Buschmann, M. (2014). Non-destructive electromechanical assessment (Arthro-BST) of human articular cartilage correlates with histological scores and biomechanical properties. *Osteoarthritis and Cartilage*, *22*(11), 1926–1935.

Sim, S., Hadjab, I., Garon, M., Quenneville, E., Lavigne, P., & Buschmann, M. D. (2017b). Development of an electromechanical grade to assess human knee articular cartilage quality. *Annals of Biomedical Engineering*, *45*(10), 2410–2421.

Souza, R., Kumar, D., Calixto, N., Singh, J., Schooler, J., Subburaj, K., … Majumdar, S. (2014). Response of knee cartilage T1rho and T2 relaxation times to in vivo mechanical loading in individuals with and without knee osteoarthritis. *Osteoarthritis & Cartilage*, *22*(10), 1367–1376.

Subburaj, K., Kumar, D., Souza, R. B., Alizai, H., Li, X., Link, T. M., & Majumdar, S. (2012). The acute effect of running on knee articular cartilage and meniscus magnetic resonance relaxation times in young healthy adults. *The American Journal of Sports Medicine*, *40*(9), 2134–2141.

Thorup, V. M., Tøgersen, F. A., Jørgensen, B., & Jensen, B. R. (2007). Biomechanical gait analysis of pigs walking on solid concrete floor. *Animal*, *1*(5), 708–715.

Valette, S., Chassery, J. M., & Prost, R. (2008). Generic remeshing of 3D triangular meshes with metric-dependent discrete Voronoi diagrams. *IEEE Transactions on Visualization and Computer Graphics*, *14*(2), 369–381.

Valette, S., & Chassery, J.-M. (2004). Approximated centroidal voronoi diagrams for uniform polygonal mesh coarsening. In *Computer graphics forum* (Vol. 23, *3*, pp. 381–389). Wiley Online Library.

Van Rossom, S., Wesseling, M., Van Assche, D., & Jonkers, I. (2019). Topographical variation of human femoral articular cartilage thickness, T1rho and T2 relaxation times is related to local loading during walking. *Cartilage*, *10*(2), 229–237.

Wheaton, A., Dodge, G., Elliott, D., Nicoll, S., & Reddy, R. (2005). Quantification of cartilage biomechanical and biochemical properties via T1 rho magnetic resonance imaging. *Magnetic Resonance in Medicine*, *54*(5), 1087–1093.

Wirth, W., Eckstein, F., Boeth, H., Diederichs, G., Hudelmaier, M., & Duda, G. (2014). Longitudinal analysis of mr spin–spin relaxation times (T2) in medial femorotibial cartilage of adolescent vs mature athletes: Dependence of deep and superficial zone properties on sex and age. *Osteoarthritis and Cartilage*, *22*(10), 1554–1558.

Worsley, K. J., Evans, A. C., Marrett, S., & Neelin, P. (1992). A three-dimensional statistical analysis for CBF activation studies in human brain. *Journal of Cerebral Blood Flow & Metabolism*, *12*(6), 900–918.

5 — Discussion

Magnetic resonance imaging (MRI) allows for the non-invasive investigation of articular cartilage. Specifically, MRI scans of articular cartilage before and immediately following a bout of loading (e.g., running, static load) provide information on cartilage morphological (thickness, volume) and compositional (T2 relaxation) response to external loads. Ideally, quantifying this cartilage response to load would provide critical information on cartilage mechanical properties, from which we can infer the quality of cartilage.

This thesis used a multi-disciplinary approach to explore tibial and femoral cartilage response to loading. Elements of engineering (MRI-compatible loading apparatus, cartilage indentation mapping), biomechanics (joint modeling, tissue mechanics), and imaging (MRI) were integrated into this thesis. Two *in vivo* studies were documented, which 1) employed Statistical Parametric Mapping to quantify regional differences in tibiofemoral cartilage deformation following running, and whether this deformation was influenced by biological sex (Chapter 2); and 2) explored the role of daily cumulative knee joint compressive load and body mass index in cartilage conditioning following running in healthy young women[1] (Chapter 3). The next manuscript outlined the integration of MR imaging and full-surface cartilage indentation mapping to complete 3D voxel-by-voxel statistics on the relationship between MRI-derived metrics and mechanical properties in porcine femoral cartilage (Chapter 4).

Two common threads were present in this thesis, and are discussed in detail below. Studies 1 and 3 (Chapters 2 and 4) used a form of SPM to investigate spatial changes in cartilage outcomes from MRI. Studies 2 and 3 (Chapters 3 and 4) integrated imaging and biomechanics to provide insight into the impact of the local loading environment on the tissues within the knee joint. A schematic diagram of the common threads, and how these studies integrated to answer the central theme of the thesis is shown in Figure 5.1.1.

---

[1] Any reference to Study 1 (Chapter 2) uses sex-based language (male, female) as the main purpose of that study was based on quantifying sex-differences in cartilage thickness maps. Alternatively, any reference to Study 2 (Chapter 3) — along with cited studies used for providing background information — uses gender-based language (women, men) as is common in the literature.

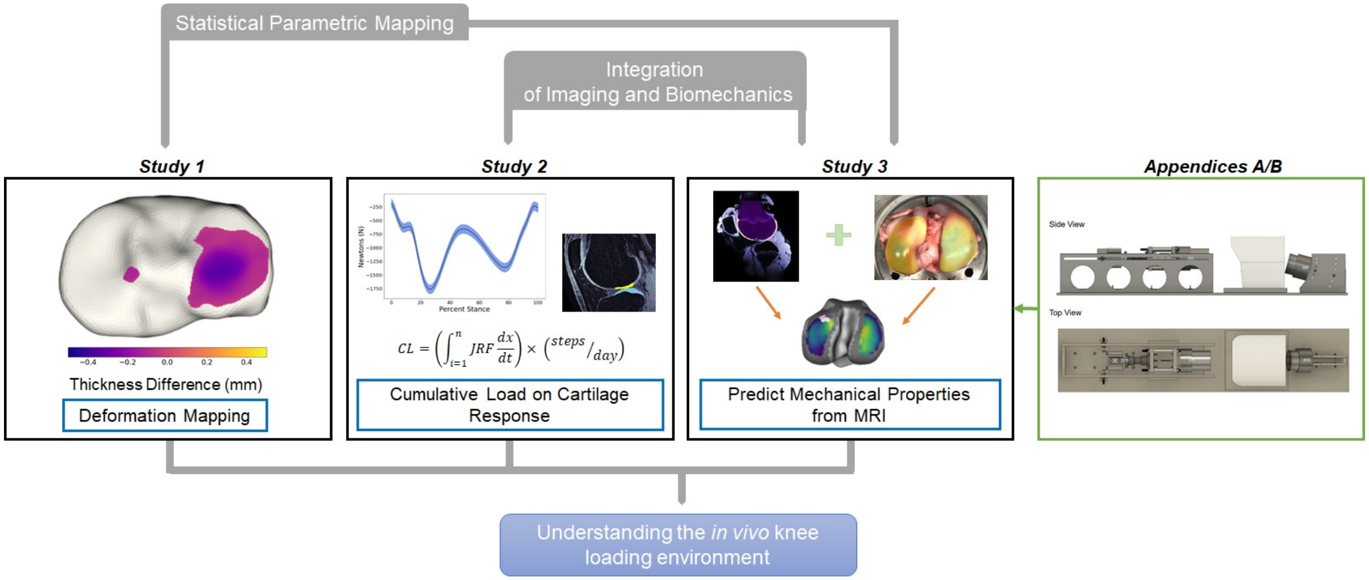

Figure 5.1.1: Schematic of the common threads present throughout this thesis (light grey boxes), namely, Statistical Parametric Mapping and the integration of imaging with biomechanical measurements. These manuscripts answered the central theme of this thesis (blue box), which was to quantify cartilage response to load in a whole-joint model.

5.1 Statistical Parametric Mapping

Statistical Parametric Mapping (SPM) is a technique that was developed to solve the multiplicity problem in functional MRI (brain imaging) (Worsley et al. 1996). SPM allows for the application of statistical tests at each voxel in a dataset. Then, either 1) adjusts the significant p-value required to determine voxel-based inference; or 2) adjusts the threshold of the test statistic (Student's t-tests, F-statistics, χ^2) to identify significant clusters of contiguous pixels in the dataset (Nichols 2012). The former is a familywise error rate (FWER)-corrected p-value that determines whether the null hypothesis can be rejected at each voxel, while the latter is an FWER-corrected threshold that controls FWER at a chosen alpha (e.g., $p = 0.05$) (Nichols and Hayasaka 2003). *This thesis contributed two novel applications of SPM to the literature: the assessment of cartilage deformation maps, and voxel-based 3D modeling of articular cartilage mechanical properties from MRI.*

5.1.1 Novel Assessment of *In Vivo* Cartilage Deformation using SPM

A novel implementation of SPM for the assessment of 2D tibial and femoral cartilage thickness maps was implemented in this thesis (Chapter 2). Specifically, two-way ANOVAs were computed at each pixel (representing a cartilage measurement (mm) from the bone-cartilage interface to the articular surface) to test the main effects of running (objective 1), sex (objective 2), and their interaction (objective 3) on cartilage thickness in young healthy males and females following 15 minutes of self-selected running. This technique successfully identified the spatial location of significant clusters on the tibial plateau and weight-bearing femur. The main effect of running showed a large cluster of thinner cartilage in the central lateral tibia, matching results from others (Boocock et al. 2009; Kersting et al. 2005; Niehoff et al. 2011). Widespread differences in thickness from the main effect of sex was present on all four of the medial and lateral tibia, and medial and lateral weight-bearing femur. These results corroborate findings that show sex-differences in cartilage thickness, even after adjusting for common covariates (Cicuttini et al. 2002; Ding et al. 2003; Jones et al. 2000; Lad et al. 2016). There was an interaction effect of Sex×Running on the posterior lateral tibia, suggesting females have greater cartilage deformation than males in this region.

Presenting the mean thickness change in cartilage sub-regions based on meniscal coverage (Liu et al. 2017); landmarked anterior, central, and posterior regions (Mosher et al. 2010; Sutter et al. 2015); or principal axes of rotation of the subchondral plate (Wirth and Eckstein 2008) have been used to infer regional differences in cartilage deformation. However, significant clusters of thickness changes may span multiple of these previously defined regions, underestimating true changes in regional thickness. That is, while calculating means for a given region of interest has been useful for quantifying general changes occurring in cartilage, it is very likely these mean values "wash out" localized changes reflecting cartilage regions that may be of interest. SPM and the spatial identification of significant clusters eradicate the need for *a priori* identification of regions of interest. This advantage was highlighted by the fact that while clusters of significant difference in thickness due to the main effect of sex were identified in all four compartments ($p \leq 0.009$), mean thickness differences between sexes, following correction for multiple comparisons, were not statistically significant except for baseline medial tibia thickness (Chapter 2, Table 2.3.2). Therefore, this novel implementation of SPM provided specific spatial information on cartilage thickness changes.

The original proposal of SPM in imaging used Random Field Theory (RFT) to identify clusters of contiguous voxels containing statistically significant test statistics (Worsley et al. 1996). RFT uses the Euler characteristic[2] to threshold all voxels, leaving clusters contained at local maxima (Worsley et al. 1992). In this thesis, a Monte Carlo method was used as a clustering method instead of the Euler characteristic (Nichols 2012). For Study 1 (Chapter 2) specifically, using F-statistics complicated the RFT approximations (Cao 1999). Therefore, the Monte Carlo method to determine a minimum cluster size required to determine significance at $p < 0.05$ is not only simple, but it does not rely on the accuracy of RFT assumptions (Nichols 2012).

5.1.2 SPM for the Creation of a 3D Voxelwise Statistical Model in an *Ex Vivo* Model

Another implementation of SPM was described in this thesis (Chapter 4): a novel quantification of the relationship between MRI cartilage outcomes (thickness, T2 relaxation) and articular cartilage mechanical properties (IM, QP) in a whole-joint *ex vivo* porcine stifle model. A matched-pair design saw one stifle undergo cartilage indentation testing and the matched stifle undergo static loading and MR imaging. Multiple linear regressions were

---

[2] The Euler characteristic (EC), or Euler number, is a topological invariant. For a random Gaussian field, the EC is calculated based on the following equation from Worsley et al. (1992):

$$EC = R(4log_e 2)(2\pi^{-3/2})ze^{-1/2z^2} \tag{1}$$

where R is the number of resolution units, or number of "independent" samples after accounting for spatial correlation; and z is the test-statistic threshold (in this case, a Z-score). As EC approaches zero, it approximates the probability that one or more clusters occur. Therefore, at the Z threshold where EC = 0.05, it is an approximation of the FWER-corrected threshold that controls FWER at EC = α = 0.05 (Ashby 2011; Worsley et al. 1992; Worsley et al. 1996).

computed at each voxel of the femoral condyle, with either 1) IM; or 2) QP as the dependent variable, and 1) cartilage change (thickness, T2); 2) baseline cartilage outcome (thickness, T2); or 3) loading group as independent predictors. No significant clusters were identified using this technique. Nonetheless, the novel implementation of SPM in this study enabled the development of a statistical model capable of exploring relationships between cartilage outcomes acquired from magnetic resonance imaging and mechanical properties of the tissue.

A second clustering technique was used in Study 3 (Chapter) to determine the FWER-corrected threshold. While still under the umbrella of Monte Carlo, a random permutation technique was used to sample the current dataset, instead of simulating new datasets based on the Gaussian distribution about the grand mean. The random permutation approach offers advantages. First, one of the assumptions of the RFT approach is uniform spatial smoothness with a Gaussian distribution (Worsley et al. 1992). Work by Eklund et al. (2016) in fMRI, and further updated by Cox et al. (2017), showed spatial smoothness is more aligned with a 'long-tail' distribution; these long tails demonstrated a significant effect on cluster-based inference using the RFT approach. It has been suggested a Monte Carlo method (Nichols 2012), or a non-parametric alternative in random permutation (Cox et al. 2017) can better adjust for FWER by maintaining the inherent smoothness structure in the dataset.

The central assumption of permutation is exchangeability under the null hypothesis. Permutations of the statistical models used in Study 3 (Chapter 4) were based on the work of Anderson (2001). The multiple linear regressions assumed the following model:

$$Y = \beta_0 + X_1\beta_1 + X_2\beta_2 + X_3\beta_3 + \epsilon \tag{2}$$

where β_0 is the intercept; X_1, X_2, and X_3 are the independent variables (cartilage change, baseline cartilage, loading group); β_1, β_2, and β_3 are the associated β coefficients; and ϵ are the errors. Testing for the relationship of Y versus all independent variables together, the null hypothesis is:

$$H0 : \beta_1 = \beta_2 = \beta_3 = 0 \tag{3}$$

If $H0$ is true, the model in Eq 2 becomes $Y = \beta_0 + \epsilon$, and Y is exchangeable under the null hypothesis (Anderson 2001). Therefore, this thesis used 10,000 random permutations of the dependent variable Y with fixed independent variables X_1, X_2, and X_3 at each voxel. Then, the largest contiguous cluster was recorded at each iteration, and the cluster size at $p = 0.05$ was determined using a cumulative distribution function. This last step was consistent across both Studies 1 and 3.

The simplicity of the SPM implementation in this thesis will ideally invite others in the biomechanics community to adopt this technique, especially for 2D and 3D analyses. Pataky (2010) first described the utility of SPM to process n-dimensional biomechanical fields. This resulted in publicly available packages in both Python and Matlab for 1D SPM analysis of time-varying biomechanical feeds (Pataky 2012; Python: spm1d, Matlab: spm1dmatlab). Since, SPM has been implemented in the field of biomechanics, mainly to process 1D fields. For example, Li et al. (2016) identified differences at movement initiation and termination in shoulder elevation kinematics during a reaching task in young versus older adults. Smale et al. (2016) used SPM to compare ankle, knee, and hip moments in pre-fatigued and post-fatigued states during a standardized squatting task. This thesis introduced an alternative way to identify significant clusters in 2D and 3D SPM, an element that is not available in the current spm1d implementations (see specific documentation on 2D analyses: http://spm1d.org/doc/).

SPM enables benefits over traditional corrections for multiple comparisons by accounting for spatial correlation and controlling the FWER. Importantly, SPM can facilitate the integration of imaging with biomechanics to quantify localized, significant clusters in a 3D model.

5.2 Integration of Imaging and Biomechanics

Imaging provides insight into tissue morphology and composition. Further, studies have quantified changes in cartilage volume (Boocock et al. 2009; Kersting et al. 2005; Kessler et al. 2006; Niehoff et al. 2011) and thickness (Mosher et al. 2005; Mosher et al. 2010; Niehoff et al. 2011; Paranjape et al. 2019; Subburaj et al. 2012) as estimates of cartilage strain. Few studies to date have combined imaging and biomechanical modeling to advance our understanding of load-bearing on knee tissues. *This thesis contributed two novel studies that integrated datasets related to 1) cartilage response to load; and 2) local cartilage loading via musculoskeletal modeling [in vivo, Study 2 (Chapter 3)] or cartilage indentation [in vitro, Study 3 (Chapter 4)].*

5.2.1 Cumulative Load Affects Tibial Response to Running

Articular cartilage requires optimal loading to maintain homeostasis. In patients with complete spinal cord injury — a scenario where knee cartilage would receive 'too little' loading — cartilage thickness progressively decreased at 6 and 24 months post-injury (Vanwanseele et al. 2002) at a rate greater than normal aging (Cicuttini et al. 2005; Wluka 2004). The influence of large mechanical loads, or 'too much' loading, appears more complex. Those with knee OA who experience greater medial knee loads have greater cartilage loss over 1-5 years (Bennell et al. 2011; Brisson et al. 2017; Chang et al. 2015; Chehab et al. 2014). Alternatively, habitual runners who experience high volumes of large magnitude forces are not at an increased risk of knee OA (Miller 2017; Timmins et al. 2017). Therefore, it is reasonable to assume that factors that influence the loading environment including loading rate, duration, and frequency need to be considered. From this, Study 2 (Chapter 3) explored the relationship of daily cumulative knee joint load (measured via the impulse of the axial compressive tibiofemoral joint reaction force during the stance phase of walking) with knee cartilage volume, thickness, and compositional changes following an acute bout of running in women. This analysis demonstrated that change in tibial volume was related to daily cumulative joint load, where those with lower joint reaction force impulse (JRFI) and a higher daily step count had lesser changes in tibial volume following running. A secondary analysis using BMI in place of JRFI showed similar results, in that a higher step count in combination with a lower BMI related to lesser changes in tibial volume post-run.

Healthy articular cartilage undergoes mechanically-driven modeling to acclimate to loads (Seedhom 2005). This theory of cartilage conditioning helps explain why the areas within an articulating joint that handle the greatest magnitude of surface stresses have greater compressive modulus (Yao and Seedhom 1993) and cartilage thickness (Li et al. 2001; Li et al. 2005) than areas that undergo less stress. Findings from this thesis suggest that among those with lower JRFI (or lower BMI), greater levels of physical activity may show a cartilage conditioning effect in the tibia. Previous work has shown inconsistent results regarding the relationship between loading and cartilage morphology and composition. For Study 2 (Chapter 3), only tibial volume change was explained by daily cumulative knee load. T2 relaxation change had no relationship. In a secondary analysis of 10 women and 10 men, participants were stratified by self-reported physical activity level as measured by the International Physical Activity Questionnaire (IPAQ) into low versus high physical activity (Subburaj et al. 2012). The low IPAQ group had greater (but insignificant) changes in T1ρ and T2 relaxation in the articular cartilage following 30 minutes of running (Subburaj et al. 2012). Others have identified significant relationships between physical activity and cartilage composition (Gatti et al. 2017; Van Ginckel et al. 2010). Knee cartilage GAG content as measured by dGEMRIC imaging improved in women who underwent a 10-week Start-to-Run program compared to sedentary controls (Van Ginckel et al. 2010). In a secondary analysis of young healthy men, those with higher levels of reported physical activity as measured by the IPAQ had smaller changes in T2 relaxation following running and bicycling activities (Gatti et al. 2017). Because Chapter 3 steps beyond activity frequency to account for knee joint loads, our results add novel data to the literature to suggest the importance of physical activity on cartilage health.

Alternatively, the significant interactions also suggest higher daily step counts in women with greater BMI (up to 28.8 kg/m^2) result in greater tibial volume change following running. A recent longitudinal assessment in those with knee OA showed that high BMI ($< 31kg/m^2$) coupled with moderate (6,000 - 7,900) or high (>7,900) steps per day increased relative risk of medial tibiofemoral joint worsening via MRI (Voinier et al. 2020). In overweight but otherwise healthy (i.e., no diagnosed OA) participants, greater diurnal strains in tibial cartilage were observed compared to healthy BMI controls (Widmyer et al. 2013). Following a walking protocol, tibial strain was highly correlated to BMI (Collins et al. 2018). In addition, participants with high BMI had less tibial cartilage at baseline, and had strains nearly 4 times greater than those with healthy BMI (Collins et al. 2018). These results corroborate the strong link between obesity and poor cartilage quality (Mezhov et al. 2014), and highlight the role of obesity in osteoarthritis. In a large knee OA cohort, those who lost >10% of body mass at 4-year follow-up (Gersing et al. 2016) and >5% at 8-year follow-up (Gersing et al. 2019) had lower increases in cartilage T2 relaxation compared to those whose weight remained stable. These studies suggested slowed cartilage degeneration in those who lost weight (Gersing et al. 2019; Gersing et al. 2016). It is possible that our findings offer minor support for weight management strategies in adjunct with physical activity to promote joint health.

The combination of MR imaging and biomechanical modeling can improve our understanding of the *in vivo* loading environment in the knee joint. Few studies have modeled JRF to understand its relationship to MRI cartilage outcomes. Boocock et al. (2009) improved preceding running/imaging studies (e.g., Kersting et al. 2005; Kessler et al. 2006; Mosher et al. 2005) by assessing the relationship between cartilage volume change and biomechanical parameters estimated from 2D musculoskeletal modeling of running trials. Only one significant finding was reported, where maximum lateral compressive stress was moderately correlated with lateral femoral cartilage volume change following a standardized run of 5,000 steps. Recently, MRI volumes of the knee were segmented and incorporated into a subject-specific multi-body knee model combined with a lower-limb musculoskeletal model in SIMM (Van Rossom et al. 2019). Cartilage-to-cartilage contact was modeled using a collision detection algorithm (Smith et al. 2018)[3], and localized cartilage stresses were estimated via an

---

[3] Interestingly, the collision detection algorithm developed by Smith et al. (2018) is very similar to the cartilage thickness mapping technique described in Study 3 (Chapter 4). A hierarchical, top-down oriented bounding box (OBB) was constructed from the femoral cartilage mesh. Then, rays were cast from the centroid of each the tibial and patellar meshes. If a ray intersected the OBB,

elastic foundation contact model and an implementation of the Concurrent Optimization of Muscle Activations and Kinematics (COMAK) algorithm (Smith et al. 2019; Smith et al. 2016). This technique quantified relationships between cartilage outcomes (thickness, T2, T1ρ) and localized stresses during walking (Van Rossom et al. 2019). This thesis expanded the current literature by contributing a novel quantification of daily cumulative knee load and its relation to acute cartilage response following running. This work adds a rigourous, biomechanical analysis of cumulative joint loading, which is an improvement over studies that estimate activity level or loading via self-report measures or step count alone (Subburaj et al. 2012; Voinier et al. 2020). Both JRFI and daily step count may play a synergistic role in this response, and prompts future work in exploring clinical and obese populations.

5.2.2 Predicting Articular Cartilage Mechanical Properties from MRI

Changes in articular cartilage structure and function are evident with OA. Many of these changes are observed at a macroscopic level, and include 1) altered chondrocyte activity (Aigner et al. 2007); 2) breakdown and disorganization of the collagen structural matrix (Panula et al. 1998; Saarakkala et al. 2010); 3) reduced number of PGs (Bi et al. 2006); and 4) increased in tissue hydration (Armstrong and Mow 1982; Guilak et al. 1994). In fact, many of these early osteoarthritic changes are evident with MRI before radiographic presentation of disease, which is the current gold standard. In several small sample studies, it was demonstrated that healthy (asymptomatic) participants had evidence of cartilage defects (11.4 - 35.7%) (Beattie et al. 2005; Wu et al. 2007), osteophyte formation (17.9 - 27.3%) (Beattie et al. 2005; Wu et al. 2007), or signs of meniscal abnormalities (24.1 - 97.7%) (Beattie et al. 2005; Boden et al. 1992; LaPrade et al. 1994; Wu et al. 2007). The presence of MRI-defined abnormalities in the absence of diagnosed radiographic OA was confirmed in a large-scale study (N=710) by Guermazi et al. (2012), showing that 89% of participants had at least one type of cartilage abnormality.

Concerning composition, cartilage T2 has been shown to discriminate healthy versus OA cartilage (Mosher and Dardzinski 2004). Bovine patellar explants exposed to either no treatment (0 Hour - control), incubation without enzyme (44 Hour - control), incubation

---

the depth of penetration was calculated. Contact pressure could then be calculated on an individual triangular mesh element:

$$p = -\frac{(1-v)E}{(1+v)(1-2v)} \ln\left(1-\frac{d}{h}\right) \tag{4}$$

where E is the cartilage elastic modulus, v is the Poisson's ratio, d is the local overlap depth, and h is the local cartilage thickness (Bei and Fregly 2004).

with Type VII collagenase (collagen depletion), or incubation with chondroitinase ABC (PG depletion) showed differences in superficial zone T2, suggesting enzymatically-induced OA increased tissue hydration (Nieminen et al. 2000). In addition, a study using human articular cartilage explants from the femoral head confirmed the hypothesis that interstitial fluid content increases in OA (Mankin and Thrasher 1975); an increase in cartilage water content has been shown to increase T2 (Liess et al. 2002). These results demonstrate the potential for MRI to identify elements of cartilage function, health, and biomechanics.

While morphology and composition provide useful information about cartilage status, detailed information on cartilage mechanical properties can dramatically advance OA detection and monitor disease progression; model and predict tissue loading tolerances; and track response to interventions. Currently, many of the studies predicting cartilage mechanical properties from MRI use cartilage explants (see Table 1.5.1 in Chapter 1). The novel outcome of Study 3 (Chapter 4), and a large contribution of this thesis, was the development of a 3D voxelwise statistical mapping technique to predict cartilage mechanical properties from MRI in an *ex vivo* porcine stifle model. This comprehensive study involved the integration of data obtained from an automated cartilage indentation procedure (Sim et al. 2017a) and MRI volumes. Two other thesis projects to my knowledge have utilized full surface mapping of indentation in a porcine model. Zheng (2017) recreated a porcine stifle joint from CT scans. Cartilage plates along with their mechanical properties (IM) were calculated using the automated indentation mapping procedure (Sim et al. 2017a). Topographical variations in IM, and estimated values for Young's modulus, were used in a fibril-reinforced model to quantify contact mechanics (displacement, JRF, contact pressure, pore pressure) in an FE model (Zheng 2017). A recent thesis from Zare (2020)[4] determined the effect of topographical variation in mechanical properties via automated indentation testing on the poromechanical response of a porcine stifle model derived from MRI data. *My thesis took a novel approach to explore the relationship between mechanical properties and cartilage outcomes from MRI.* The loading scenario enabled measurement of cartilage thickness and T2 changes while talking into account the natural articulation of all joint structures. This work contributes necessary knowledge for the development of *in vivo* tools for the assessment of articular cartilage health.

---

[4] The thesis by Zare was published on Prism (University of Calgary thesis repository) in June 2020, and is not yet available for download. The information summarized here is from the thesis abstract, therefore specific information on the methods could not be determined.

5.2.2.1 Loading in the MRI Environment

To perform external loading on an *ex vivo* porcine stifle joint, an MRI-compatible loading apparatus was required (Appendix A). This apparatus needed to be composed of plastic and wood components wherever possible. Any metal components were required to be non-ferrous (e.g., brass, austenitic stainless steel) and be situated as far from the iso-centre of the MRI as possible. Porcine stifle joints have a natural degree of flexion (Milicevic 2016; Proffen et al. 2012), therefore a fixed component able to house the tibia in discrete flexion angles was required. The apparatus was initially designed to be a pneumatically-controlled cyclic loading apparatus, with pressure regulators and the control system housed in the control room adjacent to the scanner (contains ferromagnetic metal components). However, issues in the pneumatic control system implementation required a timeline extending past this thesis. Additional modular components were constructed from wood, wood glue, brass screws, and custom 3D printed plastic pulleys to convert the apparatus into a static loading system (Appendix B). This testing setup enabled static loading replicating axial compression at the stifle joint. Figure 5.2.1 shows a schematic of the static loading system used in this thesis.

There are a few considerations when replicating a loading scenario in an *ex vivo* model. First and foremost, additional joint forces (e.g., cartilage-to-cartilage contact, ligament forces) should be considered when planning for the magnitude of force to use in experimentation. For this project, a compressive force of 180 N was used as the physiologic (LL) compressive load, which equates to 23% of the vertical ground reaction force during quiet stance of an 80 kg pig (Thorup et al. 2007). The assumption that vertical ground reaction force is equal to joint reaction force (JRF) in a quadruped model is a limitation; however, it is likely a close estimate. Thorup et al. (2008) estimated that peak stifle JRF during gait was 4.29 N/kg, or 343 N for an 80 kg pig (this equates to 0.44× body mass). JRF for quiet stance in pigs, to my knowledge, has not been reported. For contrast, humans (bipeds) experience peak vertical ground reaction forces of 0.5× body mass for quiet stance (based on a simplified static equilibrium model), and approximately 1.15-1.62× body mass for walking, dependent on gait speed (Keller et al. 1996). JRF is approximately 1× body mass for quiet stance (Miller et al. 2015) and 3× body mass for walking (Bergmann et al. 2014; Miller et al. 2015). Muscular co-contraction in bipedal locomotion results in higher estimated JRF in comparison to quadrupeds. Therefore, an axial compression equal to vertical ground reaction force during stance was chosen as a reasonable estimate of JRF for this model.

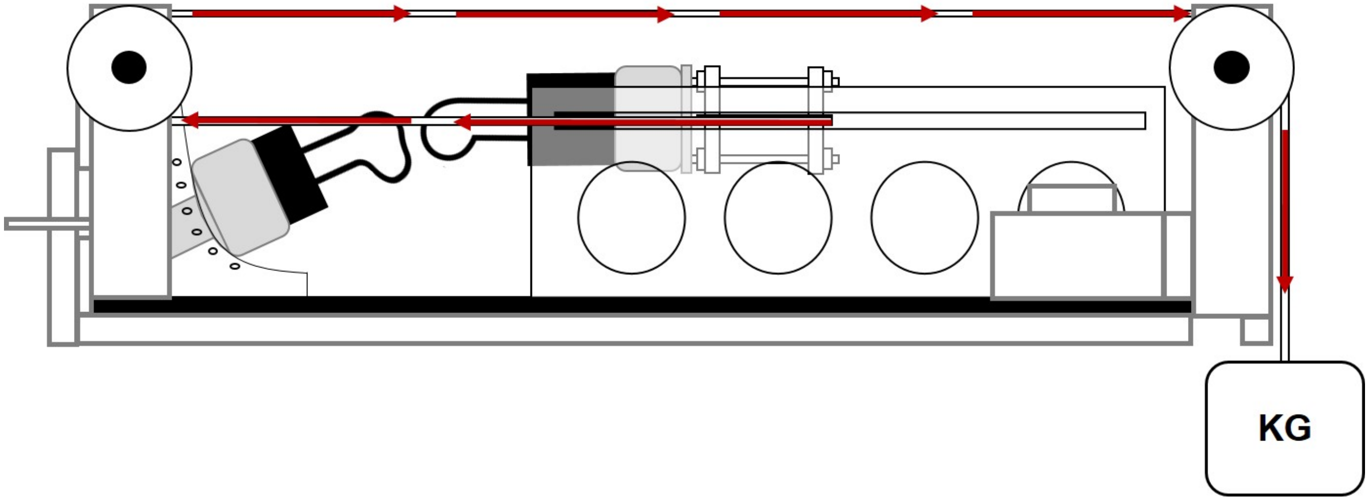

Figure 5.2.1: Schematic diagram of the MRI-compatible static loading apparatus. The specimen was potted in dental stone within pieces of PVC pipe. The tibia was affixed in the angle mount (left); this was fixed in place on the apparatus. The femur was loaded into a sliding mount (right), which had 4 *mm* static rope attached to the far end. The rope ran in line with the femur, wrapped around pulleys at the angle mount, and double-backed across the apparatus (maroon lines indicate direction of force). A mass was hung from the far end (sliding mount), resulting in axial compression at the stifle joint. Note: Adapted from Figure 4.2.1A in Chapter 4.

5.2.2.2 Surface Mapping of Mechanical Properties

The automated indentation mapping procedure from Biomomentum, Inc. can quantify topographical variation in IM over the entire cartilage surface. Indentation locations (X, Y coordinates) were chosen using a 2D calibrated camera registration system. Then, indentations were completed, followed by thickness measurements. In their proprietary software, IM was calculated, and standard 2D linear interpolation was used to map IM values across the entire surface (projected onto a 2D image). For this thesis, the Z (up/down) position was also recorded from the Mach-1 v500csst mechanical testing system (Biomomentum, Inc., Laval, QC) to get 3D coordinates of each indentation location (Figure 5.2.2A). These points were then up-sampled to approximately match that of the femoral mesh (Figure 5.2.2B). QP was also measured at each location using the handheld Arthro-BST^{TM} probe. The 2D camera registration system was used to guide probing locations. Values were recorded at each location, and up-sampled.

QP and IM have reciprocal relationships to specific electromechanical properties. QP was found to have a moderate negative correlation with fibre modulus and Young's modulus, and a moderate positive correlation with permeability (Sim et al. 2017a). In addition, QP showed a positive linear relationship to International Cartilage Repair Scores (ICRS) in human cartilage until ICRS Grade III (Sim et al. 2017b). A sharp decline in QP values for cartilage ICRS Grade IV was suggestive of denuded areas with no electromechanical activity (Sim et al. 2017b). IM, however, showed moderate positive relationships with fibre and Young's moduli, and a moderate positive correlation with permeability (Sim et al. 2017a). The results in this thesis showed higher IM and lower QP present within the same compartment (lateral). This suggested that the lateral femoral compartment of the porcine stifle model was stiffer. It is difficult to interpret the range of IM and QP values presented in this thesis, as there are few published studies on the automated indentation technique in porcine cartilage. A Master's thesis by Zheng (2017) presented IM values for a single porcine specimen much lower than what was reported here (lateral femoral condyle = 2.20 MPa; medial femoral condyle = 2.29 MPa). In fact, the mean values presented by Zheng (2017) are lower than the mean values presented for any specimen in this thesis. Two points worth noting are 1) the age of the obtained specimen was not reported; and 2) besides the indenter and load cell used (which were consistent with the current work), the experimental parameters were not reported. It is possible that differences in indentation parameters and/or modeling parameters would result in drastic differences in outcomes.

5.2.2.3 Registration of Two Datasets

The up-sampled 3D co-ordinates of the IM and QP data required registration to the femoral mesh. Coherent point drift (CPD) was chosen to register these two point clouds (Myronenko and Song 2010). CPD has advantages to other, more widely utilized rigid registration techniques such as the iterative closest point algorithm (Besl and McKay 1992). First, CPD allows for the two points clouds to have a different number of points, which was a requirement in this thesis. Second, CPD can appropriately handle outliers. Instead of minimizing the least-squares estimation between the two datasets (Besl and McKay 1992; Myronenko and Song 2010), CPD solves a probability density estimation problem between two point sets. Therefore, CPD can assign lower probabilities to specific points, and even remove outliers to obtain the best matching solution (Myronenko and Song 2010).

The Python implementation of the CPD algorithm was not perfect for all specimens. In approximately half of the specimens (8 of 18), registration completed without issue. In the remaining 10 specimens, the final registration would come out rotated or upside down. To remedy this, applying pre-rotations to the point set changed the initialization state, and would result in correct registration. To streamline this process in the future, more attention is required to implement data pipeline strategies that will automatically ingest these data and output correct registrations.

5.3 Conclusions and Future Directions

The analysis technique in Study 1 (Chapter 2) outlines a novel application of SPM and shows sensitivity in spatially localizing significant regions of interest in articular cartilage. Future studies could look to adopt this method in place of *a priori* identification of arbitrary regions of interest, or manual *a posteriori* identification of specific areas (e.g., denuded cartilage). The reported technique could automate this detection process, and provide a rigourous, quantitative alternative to manual localization.

This thesis has expanded research capacity for understanding the interactions of joint loads and cartilage tissue change. The combination of imaging with biomechanical gait analysis used in Study 2 (Chapter 3) showed the effect of daily cumulative knee load on the tibiofemoral response to load. Recent advancements in musculoskeletal modeling present an exciting opportunity for this type of dataset. The COMAK algorithm (Smith et al. 2019; Smith et al. 2016) is now available in OpenSim 4.1 (Feb 2020) through the OpenSim JAM release (Github: https://github.com/clnsmith/opensim-jam). This open-sourced method to rigorously integrate imaging and musculoskeletal modeling is a huge step for biomechanics. Future work could look to quantify localized stresses during walking and combine these data

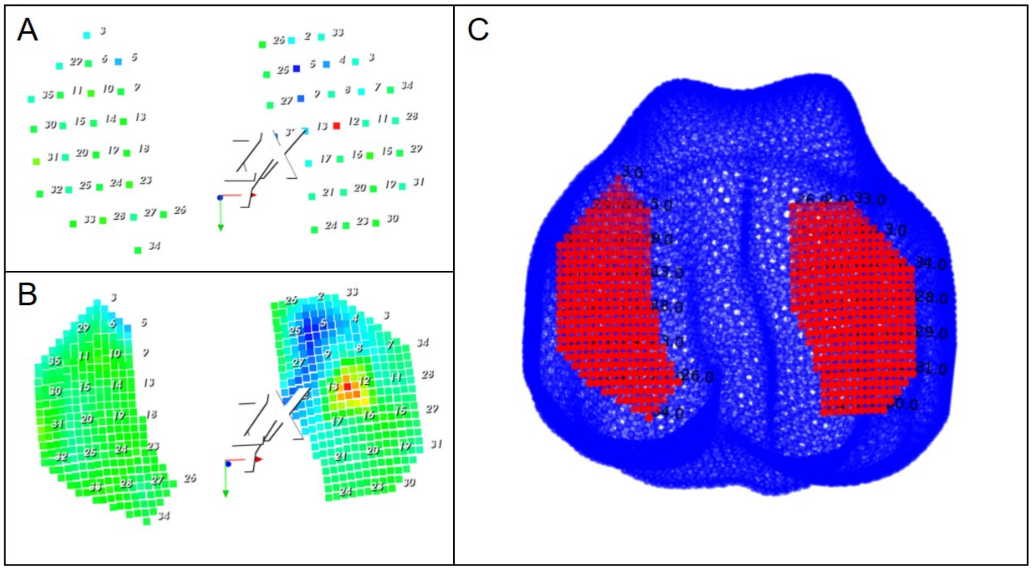

Figure 5.2.2: A) 3D locations of the indentation mapping. Each point is labeled by a unique identifier, and colour-coded based on the scalar value of the IM at that point (blue is low IM, red is high IM). B) Indentation points were up-sampled to approximately match the point resolution of the femoral mesh. C) Rigid registration of the indentation point set (red) onto the femur (mesh element centroids).

with accelerometry to obtain a cumulative stress map in tibiofemoral cartilage. Comparing this map to changes observed in cartilage morphology or composition following a specific task (e.g., walking, running, bicycling) would provide detailed insight into cartilage mechanics.

Imaging and biomechanical datasets were also integrated in Study 3 (Chapter 4), but in an *ex vivo* porcine stifle model. *Ex vivo* modeling offers advantages by incorporating the interaction of intact joint structures with external loading. The novel methods proposed in this thesis are flexible to allow different loading scenarios (type, duration, magnitude), imaging parameters (morphological, parametric), and statistical models (random permutations exchangeable under the null hypothesis). Future work should aim to expand sample sizes and testing scenarios to build appropriate statistical models able to identify relationships between imaging and mechanics.

The work presented in this thesis improves our understanding of cartilage deformation patterns following loading, and how this deformation relates to mechanical properties of the cartilage tissue. This will directly impact our ability to estimate cartilage quality from non-invasive imaging techniques. Specifically, this work builds a critical foundation for the development of tools (e.g., statistical model) for the clinical monitoring of cartilage health, a foundational step in joint disease management.

References

These references are for Chapters 1 (Literature Review) and 5 (Discussion).

Aigner, T., Söder, S., Gebhard, P. M., McAlinden, A., & Haag, J. (2007). Mechanisms of disease: Role of chondrocytes in the pathogenesis of osteoarthritis—Structure, chaos and senescence. *Nature Clinical Practice Rheumatology*, *3*(7), 391–399.

Akella, S. V., Reddy Regatte, R., Gougoutas, A. J., Borthakur, A., Shapiro, E. M., Kneeland, J. B., ... Reddy, R. (2001). Proteoglycan-induced changes in T1rho-relaxation of articular cartilage at 4T. *Magnetic Resonance in Medicine*, *46*(3), 419–423.

Aletras, A. H., Ding, S., Balaban, R. S., & Wen, H. (1999). DENSE: Displacement encoding with stimulated echoes in cardiac functional MRI. *Journal of Magnetic Resonance*, *137*(1), 247–252.

Alexopoulos, L. G., Haider, M. A., Vail, T. P., & Guilak, F. (2003). Alterations in the mechanical properties of the human chondrocyte pericellular matrix with osteoarthritis. *Journal of Biomechanical Engineering*, *125*(3), 323–333.

Alexopoulos, L. G., Williams, G. M., Upton, M. L., Setton, L. A., & Guilak, F. (2005). Osteoarthritic changes in the biphasic mechanical properties of the chondrocyte pericellular matrix in articular cartilage. *Journal of Biomechanics*, *38*(3), 509–517.

Anderson, M. J. (2001). Permutation tests for univariate or multivariate analysis of variance and regression. *Canadian Journal of Fisheries and Aquatic Sciences*, *58*(3), 626–639.

Andriacchi, T. P., Koo, S., & Scanlan, S. F. (2009). Gait mechanics influence healthy cartilage morphology and osteoarthritis of the knee. *The Journal of Bone and Joint Surgery. American volume.*, *91*(Suppl 1), 95.

Armstrong, C. G., & Mow, V. C. (1982). Variations in the intrinsic mechanical properties of human articular cartilage with age, degeneration, and water content. *Journal of Bone and Joint Surgery American*, *64*(1), 88–94.

Armstrong, C., Lai, W., & Mow, V. (1984). An analysis of the unconfined compression of articular cartilage. *Journal of biomechanical engineering*, *106*(2), 165–173.

Ashby, F. G. (2011). *Statistical analysis of fMRI data*. MIT press.

Ateshian, G. A., Lai, W. M., Zhu, W. B., & Mow, V. C. (1994). An asymptotic solution for the contact of two biphasic cartilage layers. *Journal of Biomechanics*, *27*(11), 1347–1360.

Athanasiou, K. A., Rosenwasser, M. P., Buckwalter, J. A., Malinin, T. I., & Mow, V. C. (1991). Interspecies comparisons of in situ intrinsic mechanical properties of distal femoral cartilage. *Journal of Orthopaedic Research*, *9*(3), 330–340.

Beattie, K., Boulos, P., Pui, M., O'Neill, J., Inglis, D., Webber, C., & Adachi, J. (2005). Abnormalities identified in the knees of asymptomatic volunteers using peripheral magnetic resonance imaging. *Osteoarthritis & Cartilage*, *13*(3), 181–186.

Bei, Y., & Fregly, B. J. (2004). Multibody dynamic simulation of knee contact mechanics. *Medical Engineering & Physics*, *26*(9), 777–789.

Bennell, K. L., Egerton, T., Wrigley, T. V., Hodges, P. W., Hunt, M., Roos, E. M., … Ageberg, E. et al. (2011). Comparison of neuromuscular and quadriceps strengthening exercise in the treatment of varus malaligned knees with medial knee osteoarthritis: A randomised controlled trial protocol. *BMC Musculoskeletal Disorders*, *12*(1), 276.

Bergmann, G., Bender, A., Graichen, F., Dymke, J., Rohlmann, A., Trepczynski, A., … Kutzner, I. (2014). Standardized loads acting in knee implants. *PLoS ONE*, *9*(1), e86035.

Besl, P. J., & McKay, N. D. (1992). Method for registration of 3-D shapes. In *Sensor fusion iv: Control paradigms and data structures* (Vol. 1611, pp. 586–606). International Society for Optics and Photonics.

Bi, X., Yang, X., Bostrom, M. P., & Camacho, N. P. (2006). Fourier transform infrared imaging spectroscopy investigations in the pathogenesis and repair of cartilage. *Biochimica et Biophysica Acta (BBA) - Biomembranes*, *1758*(7), 934–941.

Blumenkrantz, G., & Majumdar, S. (2007). Quantitative magnetic resonance imaging of articular cartilage in osteoarthritis. *European Cells & Materials*, *13*(7). Retrieved October 3, 2016, from http://www.ecmjournal.org/journal/papers/vol013/pdf/v013a08.pdf

Boden, S. D., Davis, D. O., Dina, T. S., Stoller, D. W., Brown, S. D., Vailas, J. C., & Labropoulos, P. A. (1992). A prospective and blinded investigation of magnetic resonance imaging of the knee: Abnormal findings in asymptomatic subjects. *Clinical Orthopaedics and Related Research*, *282*, 177–185.

Bombardier, C., Hawker, G., & Mosher, D. (2011). The impact of arthritis in Canada: Today and over the next 30 years. *Arthritis Alliance of Canada*, 1–52.

Boocock, M., McNair, P., Cicuttini, F., Stuart, A., & Sinclair, T. (2009). The short-term effects of running on the deformation of knee articular cartilage and its relationship to biomechanical loads at the knee. *Osteoarthritis and Cartilage*, *17*(7), 883–890.

Boschetti, F., & Peretti, G. M. (2008). Tensile and compressive properties of healthy and osteoarthritic human articular cartilage. *Biorheology*, *45*(3-4), 337–344. Retrieved from http://content.iospress.com/articles/biorheology/bir479

Brisson, N. M., Wiebenga, E. G., Stratford, P. W., Beattie, K. A., Totterman, S., Tamez-Peña, J. G., … Maly, M. R. (2017). Baseline knee adduction moment interacts with body mass index to predict loss of medial tibial cartilage volume over 2.5 years in knee osteoarthritis. *Journal of Orthopaedic Research*.

Buckwalter, J. A., & Mankin, H. J. (1997). Instructional course lectures, The American Academy of Orthopaedic Surgeons - Articular cartilage. Part I: Tissue design and chondrocyte - matrix interactions. *Journal of Bone and Joint Surgery American*, *79*(4), 600–11.

Buckwalter, J. A., Mankin, H. J., & Grodzinsky, A. J. (2005). Articular cartilage and osteoarthritis. *Instructional Course Lectures-American Academy of Orthopaedic Surgeons*, *54*, 465.

Burstein, D., Velyvis, J., Scott, K. T., Stock, K. W., Kim, Y.-J., Jaramillo, D., … Gray, M. L. (2001). Protocol issues for delayed Gd (DTPA) 2—enhanced MRI (dGEMRIC) for clinical evaluation of articular cartilage. *Magnetic Resonance in Medicine*, *45*(1), 36–41.

Butz, K. D., Chan, D. D., Nauman, E. A., & Neu, C. P. (2011). Stress distributions and material properties determined in articular cartilage from MRI-based finite strains. *Journal of Biomechanics*, *44*(15), 2667–2672.

Cao, J. (1999). The size of the connected components of excursion sets of chi-squared, t and F fields. *Advances in Applied Probability*, *31*(3), 579–595.

Carballido-Gamio, J., Stahl, R., Blumenkrantz, G., Romero, A., Majumdar, S., & Link, T. (2009). Spatial analysis of magnetic resonance T1rho and T2 relaxation times improves classification between subjects with and without osteoarthritis: Spatial analysis of cartilage MRI T1rho and T2. *Medical Physics*, *36*(9Part1), 4059–4067.

Chalkias, S. M., Pozzi-Mucelli, R. S., Pozzi-Mucelli, M., Frezza, F., & Longo, R. (1994). Hyaline articular cartilage: Relaxation times, pulse-sequence parameters and MR appearance at 1.5 T. *European Radiology*, *4*(4), 353–359. Retrieved July 6, 2017, from http://www.springerlink.com/index/X047116JR0N3LH53.pdf

Chan, D., Neu, C., & Hull, M. (2009a). In situ deformation of cartilage in cyclically loaded tibiofemoral joints by displacement-encoded MRI. *Osteoarthritis & Cartilage*, *17*(11), 1461–1468.

Chan, D. D., Cai, L., Butz, K. D., Trippel, S. B., Nauman, E. A., & Neu, C. P. (2016). In vivo articular cartilage deformation: Noninvasive quantification of intratissue strain during joint contact in the human knee. *Scientific Reports*, *6*, 19220.

Chan, D. D., Neu, C. P., & Hull, M. L. (2009b). Articular cartilage deformation determined in an intact tibiofemoral joint by displacement-encoded imaging. *Magnetic Resonance in Medicine*, *61*(4), 989–993.

Chang, A., Moisio, K., Chmiel, J., Eckstein, F., Guermazi, A., Prasad, P., . . . Sharma, L. (2015). External knee adduction and flexion moments during gait and medial tibiofemoral disease progression in knee osteoarthritis. *Osteoarthritis & Cartilage*, *23*(7), 1099–1106.

Chehab, E., Favre, J., Erhart-Hledik, J., & Andriacchi, T. (2014). Baseline knee adduction and flexion moments during walking are both associated with 5 year cartilage changes in patients with medial knee osteoarthritis. *Osteoarthritis & Cartilage*, *22*(11), 1833–1839.

Cicuttini, F., Forbes, A., Morris, K., Darling, S., Bailey, M., & Stuckey, S. (1999). Gender differences in knee cartilage volume as measured by magnetic resonance imaging. *Osteoarthritis and Cartilage*, *7*(3), 265–271.

Cicuttini, F., Ding, C., Wluka, A., Davis, S., Ebeling, P. R., & Jones, G. (2005). Association of cartilage defects with loss of knee cartilage in healthy, middle-age adults: A prospective study. *Arthritis & Rheumatism*, *52*(7), 2033–2039.

Cicuttini, F., Wluka, A., Wang, Y., Davis, S., Hankin, J., & Ebeling, P. (2002). Compartment differences in knee cartilage volume in healthy adults. *The Journal of Rheumatology*, *29*(3), 554–556.

Cohen, N. P., Foster, R. J., & Mow, V. C. (1998). Composition and dynamics of articular cartilage: Structure, function, and maintaining healthy state. *Journal of Orthopaedic & Sports Physical Therapy*, *28*(4), 203–215.

Coleman, J., Widmyer, M., Leddy, H., Utturkar, G., Spritzer, C., Moorman III, C., … DeFrate, L. (2013). Diurnal variations in articular cartilage thickness and strain in the human knee. *Journal of Biomechanics*, *46*(3), 541–547.

Collins, A. T., Kulvaranon, M. L., Cutcliffe, H. C., Utturkar, G. M., Smith, W. A., Spritzer, C. E., … DeFrate, L. E. (2018). Obesity alters the in vivo mechanical response and biochemical properties of cartilage as measured by MRI. *Arthritis Research & Therapy*, *20*(1), 232.

Cotofana, S., Eckstein, F., Wirth, W., Souza, R. B., Li, X., Wyman, B., … Majumdar, S. (2011). In vivo measures of cartilage deformation: Patterns in healthy and osteoarthritic female knees using 3T MR imaging. *European Radiology*, *21*(6), 1127–1135.

Cox, R. W., Chen, G., Glen, D. R., Reynolds, R. C., & Taylor, P. A. (2017). FMRI clustering in AFNI: False-positive rates redux. *Brain Connectivity*, *7*(3), 152–171.

Crema, M., Roemer, F., Marra, M., Burstein, D., Gold, G., Eckstein, F., … Guermazi, A. (2011). Articular cartilage in the knee: Current MR imaging techniques and applications in clinical practice and research. *Radiographics*, *31*(1), 37–61.

Dardzinski, B. J., Mosher, T. J., Li, S., Van Slyke, M. A., & Smith, M. B. (1997). Spatial variation of T2 in human articular cartilage. *Radiology*, *205*(2), 546–550.

Ding, C., Cicuttini, F., Scott, F., Glisson, M., & Jones, G. (2003). Sex differences in knee cartilage volume in adults: Role of body and bone size, age and physical activity. *Rheumatology*, *42*(11), 1317–1323.

Dunn, T., Lu, Y., Jin, H., Ries, M., & Majumdar, S. (2004). T2 relaxation time of cartilage at MR imaging: Comparison with severity of knee osteoarthritis. *Radiology*, *232*(2), 592–598.

Duvvuri, U., Reddy, R., Patel, S. D., Kaufman, J. H., Kneeland, J. B., & Leigh, J. S. (1997). T1rho -relaxation in articular cartilage: Effects of enzymatic degradation. *Magnetic Resonance in Medicine*, *38*(6), 863–867. Retrieved July 7, 2017, from http://onlinelibrary.wiley.com/doi/10.1002/mrm.1910380602/full

Eckstein, F., Lemberger, B., Stammberger, T., Englmeier, K. H., & Reiser, M. (2000). Patellar cartilage deformation in vivo after static versus dynamic loading. *Journal of Biomechanics*, *33*(7), 819–825.

Eckstein, F., Lemberger, B., Gratzke, C., Hudelmaier, M., Glaser, C., Englmeier, K., & Reiser, M. (2005). In vivo cartilage deformation after different types of activity and its dependence on physical training status. *Annals of the rheumatic diseases*, *64*(2), 291–295.

Eklund, A., Nichols, T., & Knutsson, H. (2016). Cluster failure: Why fMRI inferences for spatial extent have inflated false-positive rates. *Proceedings of the National Academy of Sciences*, *113*(28), 7900–7905.

Farrokhi, S., Colletti, P., & Powers, C. (2011). Differences in patellar cartilage thickness, transverse relaxation time, and deformational behavior: A comparison of young women with and without patellofemoral pain. *The American Journal of Sports Medicine*, *39*(2), 384–391.

Felson, D. T., Zhang, Y., Hannan, M. T., Naimark, A., Weissman, B. N., Aliabadi, P., & Levy, D. (1995). The incidence and natural history of knee osteoarthritis in the elderly, the Framingham osteoarthritis study. *Arthritis & Rheumatism*, *38*(10), 1500–1505.

Gatti, A. A., Noseworthy, M. D., Stratford, P. W., Brenneman, E. C., Totterman, S., Tamez-Peña, J., & Maly, M. R. (2017). Acute changes in knee cartilage transverse relaxation time after running and bicycling. *Journal of Biomechanics*, *53*, 171–177.

Gersing, A. S., Schwaiger, B., Nevitt, M., Zarnowski, J., Joseph, G., Feuerriegel, G., … McCulloch, C. et al. (2019). Weight loss regimen in obese and overweight individuals is associated with reduced cartilage degeneration: 96-month data from the Osteoarthritis Initiative. *Osteoarthritis and Cartilage*, *27*(6), 863–870.

Gersing, A. S., Solka, M., Joseph, G. B., Schwaiger, B. J., Heilmeier, U., Feuerriegel, G., … Link, T. M. (2016). Progression of cartilage degeneration and clinical symptoms in obese and overweight individuals is dependent on the amount of weight loss: 48-month data from the Osteoarthritis Initiative. *Osteoarthritis and Cartilage*, *24*(7), 1126–1134.

Goldring, M. B., & Marcu, K. B. (2009). Cartilage homeostasis in health and rheumatic diseases. *Arthritis research & therapy*, *11*(3), 1–16.

Guccione, A. A. (1994). Arthritis and the process of disablement. *Physical Therapy*, *74*(5), 408–414.

Guermazi, A., Niu, J., Hayashi, D., Roemer, F. W., Englund, M., Neogi, T., … Felson, D. T. (2012). Prevalence of abnormalities in knees detected by MRI in adults without knee osteoarthritis: Population based observational study (Framingham Osteoarthritis Study). *BMJ*, *345*(aug29 1), e5339–e5339.

Guermazi, A., Hayashi, D., Eckstein, F., Hunter, D. J., Duryea, J., & Roemer, F. W. (2013). Imaging of osteoarthritis. *Rheumatic Disease Clinics of North America*, *39*(1), 67–105.

Guilak, F., Ratcliffe, A., Lane, N., Rosenwasser, M. P., & Mow, V. C. (1994). Mechanical and biochemical changes in the superficial zone of articular cartilage in canine experimental osteoarthritis. *Journal of Orthopaedic Research*, *12*(4), 474–484.

Hahn, E. L. (1950). Spin echoes. *Physical Review*, *80*(4), 580.

Hatcher, C. C., Collins, A. T., Kim, S. Y., Michel, L. C., Mostertz, W. C., Ziemian, S. N., … McNulty, A. L. (2017). Relationship between T1rho magnetic resonance imaging, synovial fluid biomarkers, and the biochemical and biomechanical properties of cartilage. *Journal of Biomechanics*, *55*, 18–26.

Hawker, G., Wright, J., Coyte, P., Williams, J., Harvey, B., Glazier, R., & Badley, E. (2000). Differences between men and women in the rate of use of hip and knee arthroplasty. *New England Journal of Medicine*, *342*(14), 1016–1022.

Hayes, W., Keer, L., Herrmann, G., & Mockros, L. (1972). A mathematical analysis for indentation tests of articular cartilage. *Journal of Biomechanics*, *5*(5), 541–551.

Henkelman, R. M., Stanisz, G. J., Kim, J. K., & Bronskill, M. J. (1994). Anisotropy of NMR properties of tissues. *Magnetic Resonance in Medicine*, *32*(5), 592–601.

Herberhold, C., Faber, S., Stammberger, T., Steinlechner, M., Putz, R., Englmeier, K. H., … Eckstein, F. (1999). In situ measurement of articular cartilage deformation in intact femoropatellar joints under static loading. *Journal of Biomechanics*, *32*(12), 1287–1295. Retrieved October 3, 2016, from http://www.sciencedirect.com/science/article/pii/S002192909900130X

Herberhold, C., Stammberger, T., Faber, S., Putz, R., Englmeier, K.-H., Reiser, M., & Eckstein, F. (1998). An MR-based technique for quantifying the deformation of articular cartilage during mechanical loading in an intact cadaver joint. *Magnetic Resonance in Medicine*, *39*(5), 843–850. Retrieved October 3, 2016, from http://onlinelibrary.wiley.com/doi/10.1002/mrm.1910390522/abstract

Horton, M. G., & Hall, T. L. (1989). Quadriceps femoris muscle angle: Normal values and relationships with gender and selected skeletal measures. *Physical therapy*, *69*(11), 897–901.

Houard, X., Goldring, M. B., & Berenbaum, F. (2013). Homeostatic mechanisms in articular cartilage and role of inflammation in osteoarthritis. *Current Rheumatology Reports*, *15*(11).

Hudelmaier, M., Glaser, C., Hohe, J., Englmeier, K.-H., Reiser, M., Putz, R., & Eckstein, F. (2001). Age-related changes in the morphology and deformational behavior of knee joint cartilage. *Arthritis & Rheumatism*, *44*(11), 2556–2561.

Jones, G., Glisson, M., Hynes, K., & Cicuttini, F. (2000). Sex and site differences in cartilage development: A possible explanation for variations in knee osteoarthritis in later life. *Arthritis & Rheumatism*, *43*(11), 2543–2549.

Jordan, C. D., Saranathan, M., Bangerter, N. K., Hargreaves, B. A., & Gold, G. E. (2013). Musculoskeletal MRI at 3.0T and 7.0T: A comparison of relaxation times and image contrast. *European Journal of Radiology*, *82*(5), 734–739.

Juras, V., Bittsansky, M., Majdisova, Z., Szomolanyi, P., Sulzbacher, I., Gäbler, S., … Trattnig, S. (2009). In vitro determination of biomechanical properties of human articular cartilage in osteoarthritis using multi-parametric MRI. *Journal of Magnetic Resonance*, *197*(1), 40–47.

Keenan, K., Besier, T., Pauly, J., Smith, R. L., Delp, S., Beaupre, G., & Gold, G. (2015). T1rho dispersion in articular cartilage: Relationship to material properties and macromolecular content. *Cartilage*, *6*(2), 113–122.

Keenan, K., Kourtis, L., Besier, T., Lindsey, D., Gold, G., Delp, S., & Beaupre, G. (2009). New resource for the computation of cartilage biphasic material properties with the interpolant response surface method. *Computer Methods in Biomechanics and Biomedical Engineering*, *12*(4), 415–422.

Keller, T. S., Weisberger, A., Ray, J., Hasan, S., Shiavi, R., & Spengler, D. (1996). Relationship between vertical ground reaction force and speed during walking, slow jogging, and running. *Clinical Biomechanics*, *11*(5), 253–259.

Kersting, U., Stubendorff, J., Schmidt, M., & Brüggemann, G.-P. (2005). Changes in knee cartilage volume and serum COMP concentration after running exercise. *Osteoarthritis and Cartilage*, *13*(10), 925–934.

Kessler, M. A., Glaser, C., Tittel, S., Reiser, M., & Imhoff, A. B. (2006). Volume changes in the menisci and articular cartilage of runners: An in vivo investigation based on 3-d magnetic resonance imaging. *The American Journal of Sports Medicine*, *34*(5), 832–836.

Koff, M. F., Amrami, K. K., Felmlee, J. P., & Kaufman, K. R. (2008). Bias of cartilage T2 values related to method of calculation. *Magnetic Resonance Imaging*, *26*(9), 1236–1243.

Kopec, J. A., Rahman, M. M., Berthelot, J.-M., Le Petit, C., Aghajanian, J., Sayre, E. C., … Badley, E. M. (2007). Descriptive epidemiology of osteoarthritis in British Columbia, Canada. *The Journal of Rheumatology*, *34*(2), 386–393.

Kopec, J. A., Rahman, M. M., Sayre, E. C., Cibere, J., Flanagan, W. M., Aghajanian, J., … Badley, E. M. (2008). Trends in physician-diagnosed osteoarthritis incidence in an administrative database in British Columbia, Canada, 1996–1997 through 2003–2004. *Arthritis & Rheumatism*, *59*, 929–934.

Korhonen, R., Laasanen, M., Töyräs, J., Rieppo, J., Hirvonen, J., Helminen, H., & Jurvelin, J. (2002). Comparison of the equilibrium response of articular cartilage in unconfined compression, confined compression and indentation. *Journal of biomechanics*, *35*(7), 903–909.

Kumar, D., Souza, R., Subburaj, K., MacLeod, T., Singh, J., Calixto, N., … Lane, N. et al. (2015). Are there sex differences in knee cartilage composition and walking mechanics in healthy and osteoarthritis populations? *Clinical Orthopaedics and Related Research*, *473*(8), 2548–2558.

Kurkijärvi, J., Nissi, M., Kiviranta, I., Jurvelin, J., & Nieminen, M. (2004). Delayed gadolinium-enhanced MRI of cartilage (dGEMRIC) and T2 characteristics of human knee articular cartilage: Topographical variation and relationships to mechanical properties: dGEMRIC and T2 of human cartilage. *Magnetic Resonance in Medicine*, *52*(1), 41–46.

Lad, N., Liu, B., Ganapathy, P., Utturkar, G., Sutter, E., Moorman III, C., … DeFrate, L. (2016). Effect of normal gait on in vivo tibiofemoral cartilage strains. *Journal of Biomechanics*, *49*(13), 2870–2876.

Lammentausta, E., Kiviranta, P., Nissi, M., Laasanen, M., Kiviranta, I., Nieminen, M., & Jurvelin, J. (2006). T2 relaxation time and delayed gadolinium-enhanced mri of cartilage (dGEMRIC) of human patellar cartilage at 1.5 T and 9.4 T: Relationships with tissue mechanical properties. *Journal of Orthopaedic Research*, *24*(3), 366–374.

LaPrade, R. F., Burnett, Q. M., Veenstra, M. A., & Hodgman, C. G. (1994). The prevalence of abnormal magnetic resonance imaging findings in asymptomatic knees: With correlation of magnetic resonance imaging to arthroscopic findings in symptomatic knees. *The American Journal of Sports Medicine*, *22*(6), 739–745.

Li, G., Lopez, O., & Rubash, H. (2001). Variability of a three-dimensional finite element model constructed using magnetic resonance images of a knee for joint contact stress analysis. *Journal of Biomechanical Engineering*, *123*(4), 341–346.

Li, G., Park, S., DeFrate, L., Schutzer, M., Ji, L., Gill, T., & Rubash, H. (2005). The cartilage thickness distribution in the tibiofemoral joint and its correlation with cartilage-to-cartilage contact. *Clinical Biomechanics*, *20*(7), 736–744.

Li, L., Cheung, J., & Herzog, W. (2009). Three-dimensional fibril-reinforced finite element model of articular cartilage. *Medical & Biological Engineering & Computing*, *47*(6), 607.

Li, Q., Amano, K., Link, T. M., & Ma, C. B. (2016a). Advanced imaging in osteoarthritis. *Sports Health: A Multidisciplinary Approach*, 1941738116663922. Retrieved June 20, 2017, from http://sph.sagepub.com/content/early/2016/08/09/1941738116663922.abstract

Li, X., Santago II, A., Vidt, M., & Saul, K. (2016b). Analysis of effects of loading and postural demands on upper limb reaching in older adults using statistical parametric mapping. *Journal of Biomechanics*, *49*(13), 2806–2816.

Liess, C., Lüsse, S., Karger, N., Heller, M., & Glüer, C.-C. (2002). Detection of changes in cartilage water content using MRI T2-mapping in vivo. *Osteoarthritis & Cartilage*, *10*(12), 907–913.

Liu, B., Lad, N., Collins, A., Ganapathy, P., Utturkar, G., McNulty, A., ... Garrett, W. et al. (2017). In vivo tibial cartilage strains in regions of cartilage-to-cartilage contact and cartilage-to-meniscus contact in response to walking. *The American Journal of Sports Medicine*, *45*(12), 2817–2823.

Lu, X., & Mow, V. (2008). Biomechanics of articular cartilage and determination of material properties. *Medicine+ Science in Sports+ Exercise*, *40*(2), 193.

Lüssea, S., Claassen, H., Gehrke, T., Hassenpflug, J., Schünke, M., Heller, M., & Glüer, C.-C. (2000). Evaluation of water content by spatially resolved transverse relaxation times of human articular cartilage. *Magnetic Resonance Imaging*, *18*(4), 423–430. Retrieved July 6, 2017, from http://www.sciencedirect.com/science/article/pii/S0730725X99001447

Mak, A. F., Lai, W. M., & Mow, V. C. (1987). Biphasic indentation of articular cartilage—I. Theoretical analysis. *Journal of Biomechanics*, *20*(7), 703–714.

Maly, M. R., Robbins, S. M., Stratford, P. W., Birmingham, T. B., & Callaghan, J. P. (2013). Cumulative knee adductor load distinguishes between healthy and osteoarthritic knees–A proof of principle study. *Gait & Posture*, *37*(3), 397–401.

Mankin, H. J., & Thrasher, A. (1975). Water content and binding in normal and osteoarthritic human cartilage. *Journal of Bone and Joint Surgery American*, *57*(1), 76–80.

Manzano, S., Armengol, M., J. Price, A., A. Hulley, P., S. Gill, H., Doblaré, M., & Hamdy Doweidar, M. (2016). Inhomogeneous response of articular cartilage: A three-dimensional multiphasic heterogeneous study. *PLoS ONE*, *11*(6), e0157967.

Maroudas, A. (1976). Balance between swelling pressure and collagen tension in normal and degenerate cartilage. *Nature*, *260*(5554), 808–809.

Martin, K. J., Neu, C. P., & Hull, M. L. (2009). Quasi-steady-state displacement response of whole human cadaveric knees in a MRI scanner. *Journal of Biomechanical Engineering*, *131*(8), 081004.

Mazor, M., Best, T. M., Cesaro, A., Lespessailles, E., & Toumi, H. (2019). Osteoarthritis biomarker responses and cartilage adaptation to exercise: A review of animal and human models. *Scandinavian journal of medicine & science in sports*, *29*(8), 1072–1082.

McCormack, T., & Mansour, J. M. (1997). Reduction in tensile strength of cartilage precedes surface damage under repeated compressive loading in vitro. *Journal of Biomechanics*, *31*(1), 55–61.

McLure, S. W. D., Fisher, J., Conaghan, P. G., & Williams, S. (2012). Regional cartilage properties of three quadruped tibiofemoral joints used in musculoskeletal research studies. *Proceedings of the Institution of Mechanical Engineers, Part H: Journal of Engineering in Medicine*, *226*(8), 652–656.

Mezhov, V., Ciccutini, F. M., Hanna, F. S., Brennan, S. L., Wang, Y., Urquhart, D. M., & Wluka, A. E. (2014). Does obesity affect knee cartilage? A systematic review of magnetic resonance imaging data. *Obesity Reviews*, *15*(2), 143–157.

Milford, D., Rosbach, N., Bendszus, M., & Heiland, S. (2015). Mono-exponential fitting in T2-relaxometry: Relevance of offset and first echo. *PLoS ONE*, *10*(12).

Milicevic, D. (2016). *The effect of altered work-rest ratios on porcine stifles* (MSc, McMaster University).

Miller, R., Edwards, W., & Deluzio, K. (2015). Energy expended and knee joint load accumulated when walking, running, or standing for the same amount of time. *Gait & Posture*, *41*(1), 326–328.

Miller, R. H. (2017). Joint loading in runners does not initiate knee osteoarthritis. *Exercise and Sport Sciences Reviews*, *45*(2), 87–95.

Miller, R. H., Edwards, W. B., Brandon, S. C. E., Morton, A. M., & Deluzio, K. J. (2014). Why don't most runners get knee osteoarthritis? A case for per-unit-distance loads. *Medicine & Science in Sports & Exercise*, *46*(3), 572–579.

Miller, R. H., & Krupenevich, R. L. (2020). Medial knee cartilage is unlikely to withstand a lifetime of running without positive adaptation: A theoretical biomechanical model of failure phenomena. *PeerJ*, *8*, e9676.

Minns, R. J., & Steven, F. S. (1977). The collagen fibril organization in human articular cartilage. *Journal of Anatomy*, *123*(Pt 2), 437–457.

Miyazaki, T., Wada, M., Kawahara, H., Sato, M., Baba, H., & Shimada, S. (2002). Dynamic load at baseline can predict radiographic disease progression in medial compartment knee osteoarthritis. *Annals of the Rheumatic Diseases*, *61*(7), 617–622.

Mlynárik, V., Degrassi, A., Toffanin, R., Vittur, F., Cova, M., & Pozzi-Mucelli, R. S. (1996). Investigation of laminar appearance of articular cartilage by means of magnetic resonance microscopy. *Magnetic Resonance Imaging*, *14*(4), 435–442.

Mononen, M. E., Tanska, P., Isaksson, H., & Korhonen, R. K. (2016). A novel method to simulate the progression of collagen degeneration of cartilage in the knee: Data from the osteoarthritis initiative. *Scientific reports*, *6*, 21415.

Mosher, T. J., & Dardzinski, B. J. (2004). Cartilage MRI T2 relaxation time mapping: Overview and applications. In *Seminars in musculoskeletal radiology* (Vol. 8, pp. 355–368). Thieme Medical Publishers, Inc., New York, NY.

Mosher, T. J., Dardzinski, B. J., & Smith, M. B. (2000). Human articular cartilage: Influence of aging and early symptomatic degeneration on the spatial variation of T2 - preliminary findings at 3 T. *Radiology*, *214*(1), 259–266.

Mosher, T. J., Smith, H. E., Collins, C., Liu, Y., Hancy, J., Dardzinski, B. J., & Smith, M. B. (2005). Change in knee cartilage T2 at MR imaging after running: A feasibility study. *Radiology*, *234*(1), 245–249.

Mosher, T. J., Liu, Y., & Torok, C. M. (2010). Functional cartilage MRI T2 mapping: Evaluating the effect of age and training on knee cartilage response to running. *Osteoarthritis & Cartilage*, *18*(3), 358–364.

Mosher, T., Collins, C., Smith, H., Moser, L., Sivarajah, R., Dardzinski, B., & Smith, M. (2004). Effect of gender on in vivo cartilage magnetic resonance imaging T2 mapping. *Journal of Magnetic Resonance Imaging*, *19*(3), 323–328.

Mow, V. C., Holmes, M. H., & Michael Lai, W. (1984). Fluid transport and mechanical properties of articular cartilage: A review. *Journal of Biomechanics*, *17*(5), 377–394.

Mow, V. C., Kuei, S. C., Lai, W. M., & Armstrong, C. G. (1980). Biphasic creep and stress relaxation of articular cartilage in compression: Theory and experiments. *Journal of Biomechanical Engineering*, *102*(1), 73–84.

Muir, H. (1978). Proteoglycans of cartilage. *Journal of Clinical Pathology. Supplement (Royal College of Pathologists).*, *12*, 67.

Muir, H. (1995). The chondrocyte, architect of cartilage. Biomechanics, structure, function and molecular biology of cartilage matrix macromolecules. *Bioessays*, *17*(12), 1039–1048.

Muir, H., Bullough, P., & Maroudas, A. (1970). The distribution of collagen in human articular cartilage with some of its physiological implications. *Bone & Joint Journal*, *52*(3), 554–563.

Murphy, J. M., Dixon, K., Beck, S., Fabian, D., Feldman, A., & Barry, F. (2002). Reduced chondrogenic and adipogenic activity of mesenchymal stem cells from patients with advanced osteoarthritis. *Arthritis & Rheumatism*, *46*(3), 704–713.

Myronenko, A., & Song, X. (2010). Point set registration: Coherent point drift. *IEEE Transactions on Pattern Analysis and Machine Intelligence*, *32*(12), 2262–2275.

Narmoneva, D. A., Wang, J. Y., & Setton, L. A. (1999). Nonuniform swelling-induced residual strains in articular cartilage. *Journal of Biomechanics*, *32*(4), 401–408. Retrieved October 11, 2016, from http://www.sciencedirect.com/science/article/pii/S0021929098001845

Nebelung, S., Sondern, B., Jahr, H., Tingart, M., Knobe, M., Thüring, J., … Truhn, D. (2018). Non-invasive T1rho mapping of the human cartilage response to loading and unloading. *Osteoarthritis and Cartilage*, *26*(2), 236–244.

Nebelung, S., Post, M., Knobe, M., Tingart, M., Emans, P., Thüring, J., … Truhn, D. (2019). Detection of early-stage degeneration in human articular cartilage by multiparametric MR imaging mapping of tissue functionality. *Scientific Reports*, *9*(1), 1–11.

Nebelung, S., Post, M., Raith, S., Fischer, H., Knobe, M., Braun, B., … Bruners, P. et al. (2017a). Functional in situ assessment of human articular cartilage using MRI: A whole-knee joint loading device. *Biomechanics and Modeling in Mechanobiology*, *16*(6), 1971–1986.

Nebelung, S., Sondern, B., Oehrl, S., Tingart, M., Rath, B., Pufe, T., … Jahr, H. et al. (2017b). Functional MR imaging mapping of human articular cartilage response to loading. *Radiology*, *282*(2), 464–474.

Neu, C. P., & Hull, M. L. (2003). Toward an MRI-based method to measure non-uniform cartilage deformation: An MRI-cyclic loading apparatus system and steady-state cyclic displacement of articular cartilage under compressive loading. *Journal of Biomechanical Engineering*, *125*(2), 180.

Neu, C., Hull, M., & Walton, J. (2005). Heterogeneous three-dimensional strain fields during unconfined cyclic compression in bovine articular cartilage explants. *Journal of Orthopaedic Research*, *23*(6), 1390–1398.

Neu, C. P., & Walton, J. H. (2008). Displacement encoding for the measurement of cartilage deformation. *Magnetic Resonance in Medicine*, *59*(1), 149–155.

Nichols, T., & Hayasaka, S. (2003). Controlling the familywise error rate in functional neuroimaging: A comparative review. *Statistical Methods in Medical Research*, *12*(5), 419–446.

Nichols, T. (2012). Multiple testing corrections, nonparametric methods, and random field theory. *Neuroimage*, *62*(2), 811–815.

Niehoff, A., Müller, M., Brüggemann, L., Savage, T., Zaucke, F., Eckstein, F., … Brüggemann, G.-P. (2011). Deformational behaviour of knee cartilage and changes in serum cartilage oligomeric matrix protein (COMP) after running and drop landing. *Osteoarthritis and Cartilage*, *19*(8), 1003–1010.

Nieminen, M. T., Töyräs, J., Rieppo, J., Hakumäki, J. M., Silvennoinen, J., Helminen, H. J., & Jurvelin, J. S. (2000). Quantitative MR microscopy of enzymatically degraded articular cartilage. *Magnetic Resonance in Medicine*, *43*(5), 676–681.

Nieminen, M., Töyräs, J., Laasanen, M., Silvennoinen, J., Helminen, H., & Jurvelin, J. (2004). Prediction of biomechanical properties of articular cartilage with quantitative magnetic resonance imaging. *Journal of Biomechanics*, *37*(3), 321–328.

Nissi, M., Rieppo, J., Töyräs, J., Laasanen, M., Kiviranta, I., Jurvelin, J., & Nieminen, M. (2006). T2 relaxation time mapping reveals age- and species-related diversity of collagen network architecture in articular cartilage. *Osteoarthritis & Cartilage*, *14*(12), 1265–1271.

Nissi, M., Rieppo, J., Töyräs, J., Laasanen, M., Kiviranta, I., Nieminen, M., & Jurvelin, J. (2007). Estimation of mechanical properties of articular cartilage with MRI – dGEMRIC, T2 and T1 imaging in different species with variable stages of maturation. *Osteoarthritis & Cartilage*, *15*(10), 1141–1148.

Nissi, M., Töyräs, J., Laasanen, M., Rieppo, J., Saarakkala, S., Lappalainen, R., … Nieminen, M. (2004). Proteoglycan and collagen sensitive MRI evaluation of normal and degenerated articular cartilage. *Journal of Orthopaedic Research*, *22*(3), 557–564.

Otterness, I., & Eckstein, F. (2007). Women have thinner cartilage and smaller joint surfaces than men after adjustment for body height and weight. *Osteoarthritis and Cartilage*, *15*(6), 666–672.

Panula, H. E., Hyttinen, M. M., Arokoski, J. P., L\a angsjö, T. K., Pelttari, A., Kiviranta, I., & Helminen, H. J. (1998). Articular cartilage superficial zone collagen birefringence reduced and cartilage thickness increased before surface fibrillation in experimental osteoarthritis. *Annals of the Rheumatic Diseases*, *57*(4), 237–245.

Paranjape, C., Cutcliffe, H., Grambow, S., Utturkar, G., Collins, A., Garrett, W., … DeFrate, L. (2019). A new stress test for knee joint cartilage. *Scientific Reports*, *9*(1), 2283.

Pataky, T. (2010). Generalized n-dimensional biomechanical field analysis using statistical parametric mapping. *Journal of Biomechanics*, *43*(10), 1976–1982.

Pataky, T. C. (2012). One-dimensional statistical parametric mapping in Python. *Computer Methods in Biomechanics and Biomedical Engineering*, *15*(3), 295–301.

Patel, J. M., Wise, B. C., Bonnevie, E. D., & Mauck, R. L. (2019). A systematic review and guide to mechanical testing for articular cartilage tissue engineering. *Tissue Engineering Part C: Methods*, *25*(10), 593–608.

Proffen, B. L., McElfresh, M., Fleming, B. C., & Murray, M. M. (2012). A comparative anatomical study of the human knee and six animal species. *The Knee*, *19*(4), 493–499.

Racunica, T. L., Teichtahl, A. J., Wang, Y., Wluka, A. E., English, D. R., Giles, G. G., … Cicuttini, F. M. (2007). Effect of physical activity on articular knee joint structures in community-based adults. *Arthritis Care & Research*, *57*(7), 1261–1268.

Rautiainen, J., Nissi, M. J., Salo, E.-N., Tiitu, V., Finnilä, M. A., Aho, O.-M., … Nieminen, M. T. (2015). Multiparametric MRI assessment of human articular cartilage degeneration: Correlation with quantitative histology and mechanical properties. *Magnetic Resonance in Medicine*, *74*(1), 249–259.

Ridgway, J. (2015). Gradient echo versus spin echo. In *Cardiovascular mr manual* (pp. 91–95). Springer.

Rieppo, J., Hyttinen, M., Halmesmaki, E., Ruotsalainen, H., Vasara, A., Kiviranta, I., … Helminen, H. (2009). Changes in spatial collagen content and collagen network architecture in porcine articular cartilage during growth and maturation. *Osteoarthritis & Cartilage*, *17*(4), 448–455.

Robinson, D. L., Kersh, M. E., Walsh, N. C., Ackland, D. C., de Steiger, R. N., & Pandy, M. G. (2016). Mechanical properties of normal and osteoarthritic human articular cartilage. *Journal of the Mechanical Behavior of Biomedical Materials*, *61*, 96–109.

Roemer, F. W., Eckstein, F., Hayashi, D., & Guermazi, A. (2014). The role of imaging in osteoarthritis. *Best Practice & Research Clinical Rheumatology*, *28*(1), 31–60.

Roughley, P. J., & Lee, E. R. (1994). Cartilage proteoglycans: Structure and potential functions. *Microscopy Research and Technique*, *28*(5), 385–397.

Saarakkala, S., Julkunen, P., Kiviranta, P., Mäkitalo, J., Jurvelin, J., & Korhonen, R. (2010). Depth-wise progression of osteoarthritis in human articular cartilage: Investigation of composition, structure and biomechanics. *Osteoarthritis & Cartilage*, *18*(1), 73–81.

Samosky, J. T., Burstein, D., Grimson, W. E., Howe, R., Martin, S., & Gray, M. L. (2005). Spatially-localized correlation of dGEMRIC-measured GAG distribution and mechanical stiffness in the human tibial plateau. *Journal of Orthopaedic Research*, *23*(1), 93–101.

Schinagl, R. M., Gurskis, D., Chen, A. C., & Sah, R. L. (1997). Depth-dependent confined compression modulus of full-thickness bovine articular cartilage. *Journal of Orthopaedic Research*, *15*(4), 499–506. Retrieved October 3, 2016, from http://onlinelibrary.wiley.com/doi/10.1002/jor.1100150404/full

Schinagl, R. M., Ting, M. K., Price, J. H., & Sah, R. L. (1996). Video microscopy to quantitate the inhomogeneous equilibrium strain within articular cartilage during confined compression. *Annals of Biomedical Engineering*, *24*(4), 500–512. Retrieved October 11, 2016, from http://link.springer.com/article/10.1007/BF02648112

Schulze-Tanzil, G., Müller, R. D., Kohl, B., Schneider, N., Ertel, W., Ipaktchi, K., ... John, T. (2009). Differing in vitro biology of equine, ovine, porcine and human articular chondrocytes derived from the knee joint: An immunomorphological study. *Histochemistry and Cell Biology*, *131*(2), 219–229.

Seedhom, B. (2005). Conditioning of cartilage during normal activities is an important factor in the development of osteoarthritis. *Rheumatology*, *45*(2), 146–149.

Sim, S., Chevrier, A., Garon, M., Quenneville, E., Lavigne, P., Yaroshinsky, A., ... Buschmann, M. (2017a). Electromechanical probe and automated indentation maps are sensitive techniques in assessing early degenerated human articular cartilage. *Journal of Orthopaedic Research*, *35*(4), 858–867.

Sim, S., Chevrier, A., Garon, M., Quenneville, E., Yaroshinsky, A., Hoemann, C., & Buschmann, M. (2014). Non-destructive electromechanical assessment (Arthro-BST) of human articular cartilage correlates with histological scores and biomechanical properties. *Osteoarthritis and Cartilage*, *22*(11), 1926–1935.

Sim, S., Hadjab, I., Garon, M., Quenneville, E., Lavigne, P., & Buschmann, M. D. (2017b). Development of an electromechanical grade to assess human knee articular cartilage quality. *Annals of Biomedical Engineering*, *45*(10), 2410–2421.

Smale, K. B., Shourijeh, M. S., & Benoit, D. L. (2016). Use of muscle synergies and wavelet transforms to identify fatigue during squatting. *Journal of Electromyography and Kinesiology*, *28*, 158–166.

Smith, C. R., Choi, K. W., Negrut, D., & Thelen, D. G. (2018). Efficient computation of cartilage contact pressures within dynamic simulations of movement. *Computer Methods in Biomechanics and Biomedical Engineering: Imaging & Visualization*, *6*(5), 491–498.

Smith, C. R., Brandon, S. C., & Thelen, D. G. (2019). Can altered neuromuscular coordination restore soft tissue loading patterns in anterior cruciate ligament and menisci deficient knees during walking? *Journal of Biomechanics*, *82*, 124–133.

Smith, C. R., Lenhart, R. L., Kaiser, J., Vignos, M. F., & Thelen, D. G. (2016). Influence of ligament properties on tibiofemoral mechanics in walking. *The Journal of Knee Surgery*, *29*(02), 099–106.

Soltz, M. A., & Ateshian, G. A. (1998). Experimental verification and theoretical prediction of cartilage interstitial fluid pressurization at an impermeable contact interface in confined compression. *Journal of biomechanics*, *31*(10), 927–934.

Souza, R., Kumar, D., Calixto, N., Singh, J., Schooler, J., Subburaj, K., … Majumdar, S. (2014). Response of knee cartilage T1rho and T2 relaxation times to in vivo mechanical loading in individuals with and without knee osteoarthritis. *Osteoarthritis & Cartilage*, *22*(10), 1367–1376.

Souza, R. B., Baum, T., Wu, S., Feeley, B. T., Kadel, N., Li, X., … Majumdar, S. (2012). Effects of unloading on knee articular cartilage T1rho and T2 magnetic resonance imaging relaxation times: A case series. *Journal of Orthopaedic & Sports Physical Therapy*, *42*(6), 511–520.

Srikanth, V., Fryer, J., Zhai, G., Winzenberg, T., Hosmer, D., & Jones, G. (2005). A meta-analysis of sex differences prevalence, incidence and severity of osteoarthritis. *Osteoarthritis and Cartilage*, *13*(9), 769–781.

Standardization of Osteoarthritis Definitions. (2015). Retrieved from https://www.oarsi.org/research/standardization-osteoarthritis-definitions

Subburaj, K., Kumar, D., Souza, R. B., Alizai, H., Li, X., Link, T. M., & Majumdar, S. (2012). The acute effect of running on knee articular cartilage and meniscus magnetic resonance relaxation times in young healthy adults. *The American Journal of Sports Medicine*, *40*(9), 2134–2141.

Sutter, E., Widmyer, M., Utturkar, G., Spritzer, C., Garrett Jr, W., & DeFrate, L. (2015). In vivo measurement of localized tibiofemoral cartilage strains in response to dynamic activity. *The American Journal of Sports Medicine*, *43*(2), 370–376.

Tantisricharoenkul, G., Linde-Rosen, M., Araujo, P., Zhou, J., Smolinski, P., & Fu, F. H. (2014). Anterior cruciate ligament: An anatomical exploration in humans and in a selection of animal species. *Knee Surgery, Sports Traumatology, Arthroscopy*, *22*(5), 961–971.

Thorup, V. M., Laursen, B., & Jensen, B. R. (2008). Net joint kinetics in the limbs of pigs walking on concrete floor in dry and contaminated conditions. *Journal of Animal Science*, *86*(4), 992–998.

Thorup, V. M., Tøgersen, F. A., Jørgensen, B., & Jensen, B. R. (2007). Biomechanical gait analysis of pigs walking on solid concrete floor. *Animal*, *1*(5), 708–715.

Tiderius, C., Hori, M., Williams, A., Sharma, L., Prasad, P., Finnell, M., … Burstein, D. (2006). dGEMRIC as a function of BMI. *Osteoarthritis & Cartilage*, *14*(11), 1091–1097.

Timmins, K. A., Leech, R. D., Batt, M. E., & Edwards, K. L. (2017). Running and knee osteoarthritis: A systematic review and meta-analysis. *The American Journal of Sports Medicine*, *45*(6), 1447–1457.

Torzilli, P. A., Deng, X., & Warren, R. F. (1994). The effect of joint-compressive load and quadriceps muscle force on knee motion in the intact and anterior cruciate ligament-sectioned knee. *The American Journal of Sports Medicine*, *22*(1), 105–112.

Van Ginckel, A., Baelde, N., Almqvist, K., Roosen, P., McNair, P., & Witvrouw, E. (2010). Functional adaptation of knee cartilage in asymptomatic female novice runners compared to sedentary controls. A longitudinal analysis using delayed gadolinium enhanced magnetic resonance imaging of cartilage (dGEMRIC). *Osteoarthritis and Cartilage*, *18*(12), 1564–1569.

Van Rossom, S., Wesseling, M., Van Assche, D., & Jonkers, I. (2019). Topographical variation of human femoral articular cartilage thickness, T1rho and T2 relaxation times is related to local loading during walking. *Cartilage*, *10*(2), 229–237.

Vanwanseele, B., Eckstein, F., Knecht, H., Stüssi, E., & Spaepen, A. (2002). Knee cartilage of spinal cord-injured patients displays progressive thinning in the absence of normal joint loading and movement: Progressive thinning of knee cartilage after spinal cord injury. *Arthritis & Rheumatism*, *46*(8), 2073–2078.

Voinier, D., Neogi, T., Stefanik, J., Guermazi, A., Roemer, F., Thoma, L., … Torner, J. et al. (2020). Using cumulative load to explain how body mass index and daily walking relate to worsening knee cartilage damage over two years: The MOST Study. *Arthritis & Rheumatology*, *72*(6), 957–965.

Von der Mark, K. (1999). *Structure, biosynthesis and gene regulation of collagens in cartilage and bone*. Academic Press, Orlando.

Wheaton, A., Dodge, G., Elliott, D., Nicoll, S., & Reddy, R. (2005). Quantification of cartilage biomechanical and biochemical properties via T1 rho magnetic resonance imaging. *Magnetic Resonance in Medicine*, *54*(5), 1087–1093.

Wheaton, A. J., Casey, F. L., Gougoutas, A. J., Dodge, G. R., Borthakur, A., Lonner, J. H., … Reddy, R. (2004). Correlation of T1rho with fixed charge density in cartilage. *Journal of Magnetic Resonance Imaging*, *20*(3), 519–525.

Widmyer, M. R., Utturkar, G. M., Leddy, H. A., Coleman, J. L., Spritzer, C. E., Moorman III, C. T., … Guilak, F. (2013). High body mass index is associated with increased diurnal strains in the articular cartilage of the knee. *Arthritis & Rheumatism*, *65*(10), 2615–2622.

Williamson, A. K., Chen, A. C., Masuda, K., Thonar, E. J. M. A., & Sah, R. L. (2003). Tensile mechanical properties of bovine articular cartilage: Variations with growth and relationships to collagen network components. *Journal of Orthopaedic Research*, *21*(5), 872–880.

Wirth, W., Eckstein, F., Boeth, H., Diederichs, G., Hudelmaier, M., & Duda, G. (2014). Longitudinal analysis of mr spin–spin relaxation times (T2) in medial femorotibial cartilage of adolescent vs mature athletes: Dependence of deep and superficial zone properties on sex and age. *Osteoarthritis and Cartilage*, *22*(10), 1554–1558.

Wirth, W., Maschek, S., & Eckstein, F. (2017). Sex-and age-dependence of region-and layer-specific knee cartilage composition (spin–spin–relaxation time) in healthy reference subjects. *Annals of Anatomy-Anatomischer Anzeiger*, *210*, 1–8.

Wirth, W., & Eckstein, F. (2008). A technique for regional analysis of femorotibial cartilage thickness based on quantitative magnetic resonance imaging. *IEEE Transactions on Medical Imaging*, *27*(6), 737–744.

Wise, B. L., Niu, J., Yang, M., Lane, N. E., Harvey, W., Felson, D. T., . . . Torner, J. et al. (2012). Patterns of compartment involvement in tibiofemoral osteoarthritis in men and women and in whites and african americans. *Arthritis care & research*, *64*(6), 847–852.

Wluka, A. E. (2004). Tibial cartilage volume change in healthy postmenopausal women: A longitudinal study. *Annals of the Rheumatic Diseases*, *63*(4), 444–449.

Worsley, K. J., Evans, A. C., Marrett, S., & Neelin, P. (1992). A three-dimensional statistical analysis for CBF activation studies in human brain. *Journal of Cerebral Blood Flow & Metabolism*, *12*(6), 900–918.

Worsley, K., Marrett, S., Neelin, P., Vandal, A., Friston, K., & Evans, A. (1996). A unified statistical approach for determining significant signals in images of cerebral activation. *Human Brain Mapping*, *4*(1), 58–73.

Wu, H., Webber, C., Fuentes, C. O., & Bensen, R. (2007). Prevalence of knee abnormalities in patients with osteoarthritis and anterior cruciate ligament injury identified with peripheral magnetic resonance imaging: A pilot study. *Canadian Association of Radiologists Journal*, *58*(3), 167.

Xerogeanes, J. W., Fox, R. J., Takeda, Y., Kim, H.-S., Ishibashi, Y., Carlin, G. J., & Woo, S. L. (1998). A functional comparison of animal anterior cruciate ligament models to the human anterior cruciate ligament. *Annals of Biomedical Engineering*, *26*(3), 345–352. Retrieved July 11, 2017, from http://www.springerlink.com/index/lh876t25284un671.pdf

Yao, J., & Seedhom, B. (1993). Mechanical conditioning of articular cartilage to prevalent stresses. *Rheumatology*, *32*(11), 956–965.

Young, A. A., Stanwell, P., Williams, A., Rohrsheim, J. A., Parker, D. A., Giuffre, B., & Ellis, A. M. (2005). Glycosaminoglycan content of knee cartilage following posterior cruciate ligament rupture demonstrated by delayed gadolinium-enhanced magnetic resonance imaging of cartilage (dGEMRIC). *Journal of Bone and Joint Surgery American*, *87*(12), 2763–2767. Retrieved October 17, 2016, from http://jbjs.org/content/87/12/2763.extract

Zare, M. (2020). *Poromechanical modeling of porcine knee joint considering site-dependent material properties of articular cartilage from indentation testing* (PhD, Schulich School of Engineering, University of Calgary).

Zheng, X. (2017). *Geometry reconstruction and finite element modelling of porcine knee joint* (MASc, University of Calgary).

Appendices

Appendix A — MRI-Compatible Loading Device

A.1 Brief Overview

The proposed objective of this apparatus was to perform cyclic compression on an intact whole-stifle joint of a porcine specimen inside a knee array coil (Invivo Corporation, Gainsville, FL) within a research-dedicated Discovery MR750 3T MRI scanner (GE Healthcare, Milwaukee, WI). Proposed parameters for the cyclic loading task were: 0.85 Hz frequency to mimic the approximate walking speed of an adult pig (Thorup et al. 2007); 343 N magnitude to approximate peak joint reaction loads in the stifle joint during gait of an 80 kg pig (Thorup et al. 2008)[1]; and a loading duration of 30 minutes.

A.2 Architecture

A.2.1 System Architecture Overview

The proposed cyclic apparatus will contain multiple systems integrated with a control program in LabVIEW computing software. Elements of the pneumatic system, the load cell, along with physical components (slide rail, cylinder mount, extension piece, angle mount) will operate in the MR scanner. Therefore, those components have been constructed of plywood, plastics, and non-ferrous metals to not interfere with the external magnetic field. The remaining components of the pneumatic system (regulators, air compressor) as well as data acquisition and computing components will operate in the control room adjacent to the scanner. The control components will connect to the main apparatus via plastic tubing (pneumatic system) and shielded wiring (force control feedback) through a copper conduit between rooms. All cyclic loading parameters will be user-defined in a custom GUI designed in LabVIEW. A CAD model of the whole apparatus is included in Figure A.2.1, and a block diagram of the whole system is included in Figure A.2.2. Engineering drawings of the slide rail, piston mount, load cell, extension piece, potting cup, and angle mount[2] are included in Sub-Appendix A1.

---

[1] While 0.85 Hz and 343 N were suggested as a ballpark targets for frequency and magnitude of loading in this project, it was agreed upon by the project team to enable flexibility within the build. This would enable the apparatus to be tuned for future projects looking at human loading scenarios (e.g., walking speed of 1.45-1.5 m/s (Miller et al. 2015; Paranjape et al. 2019), and higher magnitude joint reaction forces observed in humans during gait (e.g., approximately 3× body mass for walking (Bergmann et al. 2014)).

[2] An engineering drawing for the specimen potting fixture is not available at this time.

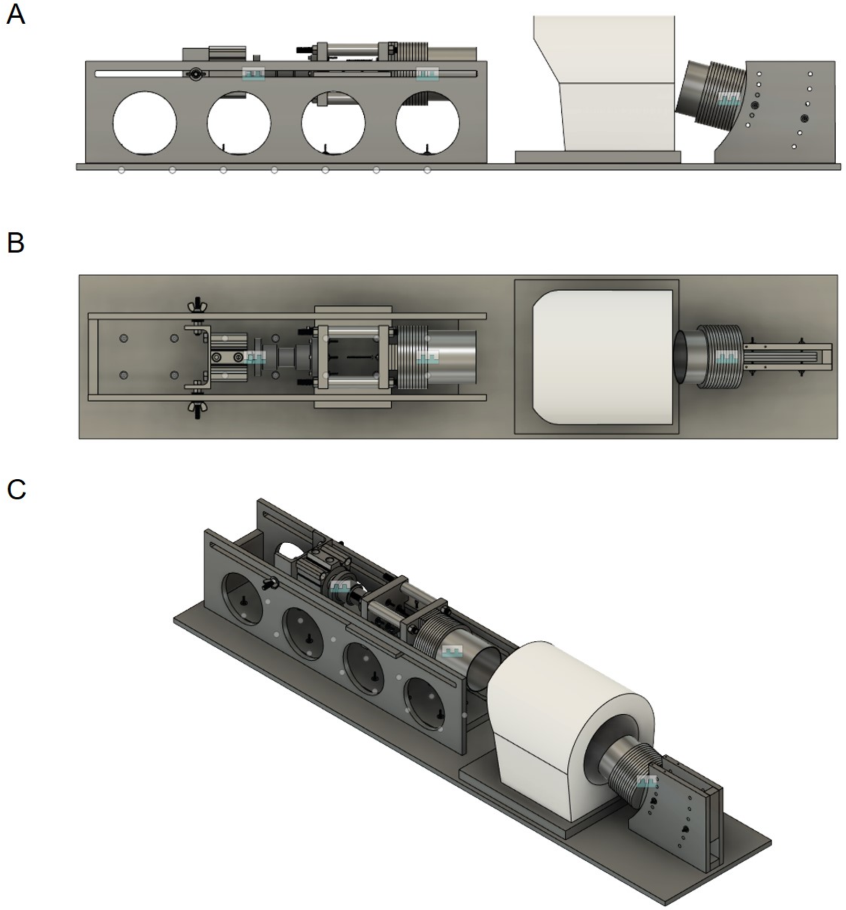

Figure A.2.1: A) Side, B) top, and C) angle view of the entire apparatus.

A.2.2 Constructed Components

A.2.2.1 Base

The base of the apparatus was constructed from 1/2" thick cedar plywood (13" × 60" dimensions). A thin 0.01" polycarbonate film covered the top surface of the plywood base to enable easy cleaning. Clearance fit countersink holes (size 7, 0.2010") were drilled into the underside of the base to affix apparatus components with nylon $10 - 32 \times 2$" screws, No. 10 nylon washers, and $10 - 32$ nylon hex nuts.

A.2.2.2 Slide Rail

The slide rail was designed to attach pneumatic and specimen potting components in series, and allow for low-friction sliding in ±X (ant/post) of the custom load cell, extension piece, and potting cup controlled via a pneumatic double-acting cylinder. The rail was composed of 1/2" thick polycarbonate plastic and 3/4" thick nylon. Two identical slabs of polycarbonate (13" × $31\frac{5}{8}$") with four equidistant circular cut-outs (reduce overall mass of the apparatus) and a 1/2" × $30\frac{1}{8}$" slot runner were separated by 6" wide pieces of nylon plastic. The entire construction was epoxied, and reinforced with 1/4"$-20 \times 1\frac{1}{2}$" nylon pan head slotted screws. A CAD model of the slide rail is displayed in Figure A.2.3.

A.2.2.3 Piston Mount

The piston mount was fabricated from stainless steel. Four holes aligning with the rear threaded holes in the cylinder were drilled in the back plate to allow clearance fit for 1/2" $-$ $13 \times 1\frac{1}{2}$" UNC brass bolts (size 17/32, 0.5312"). A hole in each side face of the mount allowed clearance fit of a 3/8" -16 brass threaded rod. Two 6" pieces of the 3/8" -16 brass threaded rod affixed the cylinder mount into each runner on the slide rail. Flat nylon washers, brass nuts (3/8" $-$ 16), and brass wing nuts (3/8" $-$ 16) allowed for manual tightening of the component. A CAD model of the piston mount is shown in Figure A.2.4.

A.2.2.4 Load Cell

The load cell body was designed using a custom dumbbell shape that facilitates axial (compressive) external forces. The load cell was constructed from Ultem plastic, a stiff plastic with high yield strength. A singular 5/8" $-$ 18 × 1" threaded hole was tapped to fit the piston rod of the cylinder. The other end of the load cell contained four holes drilled at 0, 90, 180, and 270^o to enable secure fastening to the extension piece with $10 - 32 \times 2$" nylon

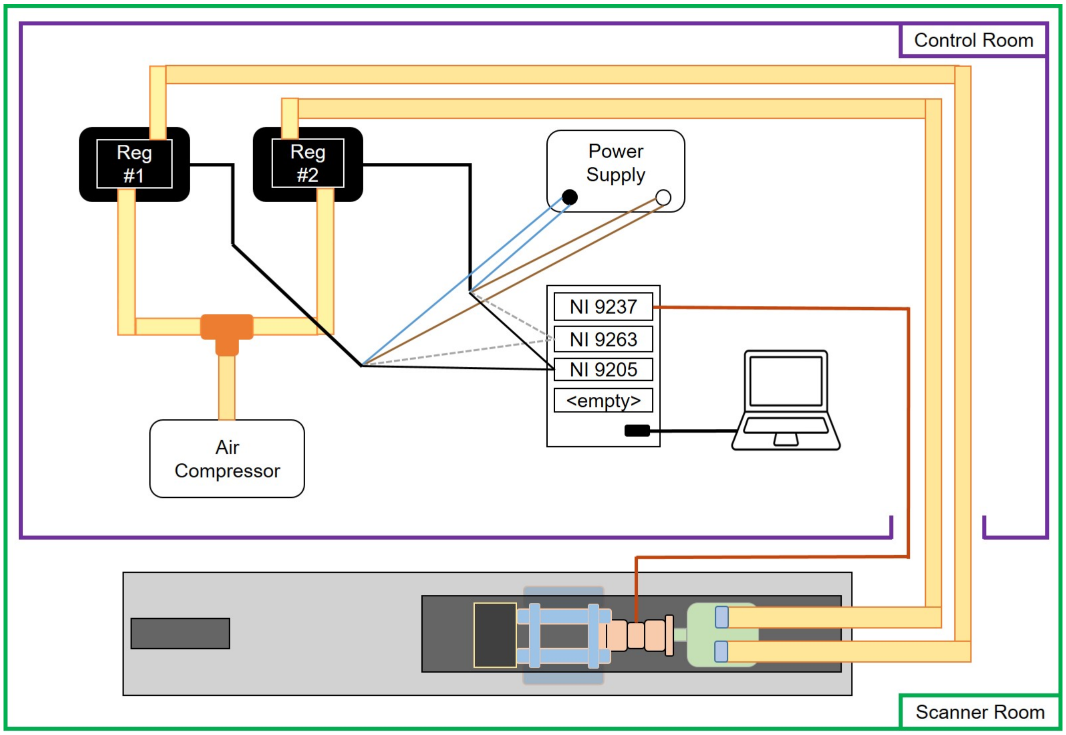

Figure A.2.2: Block diagram of the apparatus components, in the proposed configuration. A LabVIEW GUI will control two pneumatic regulators via the analog output signals of each regulator (cDAQ module NI 9163; controlled in a custom LabVIEW program). Pressure feedback will be read by an analog input signal (cDAQ module NI 9205). An air compressor will supply air through plastic tubing (controlled by the regulators) to each channel of the double-acting pneumatic cylinder in the MRI room (light green). A custom load cell will provide feedback back to the CPU to control the pneumatic output (cDAQ module NI 9237; load cell in light orange).

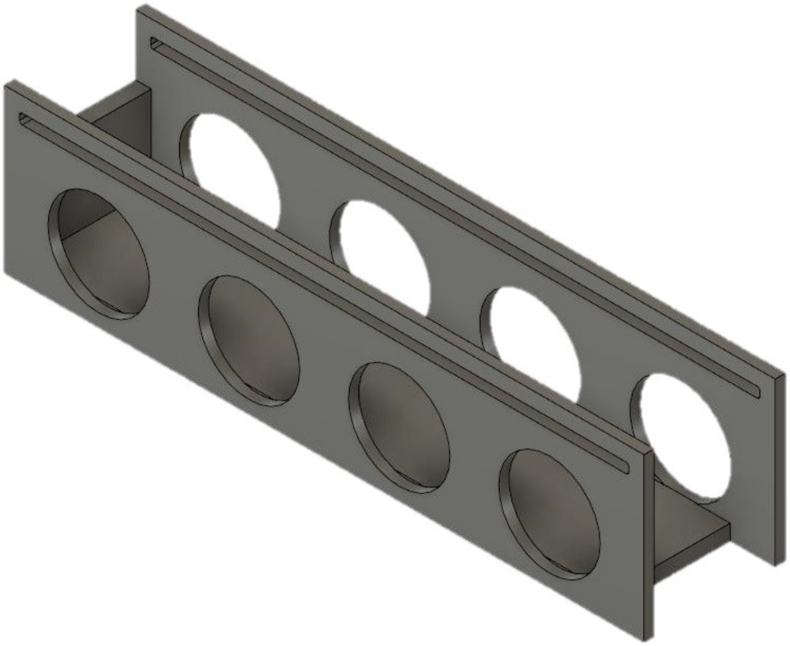

Figure A.2.3: Angle view of the slide rail, built using polycarbonate and nylon plastics. The side slabs contained circular cut-outs to reduce overall mass, and running slots that house the pneumatic cylinder, custom load cell, extension piece, and potting cup.

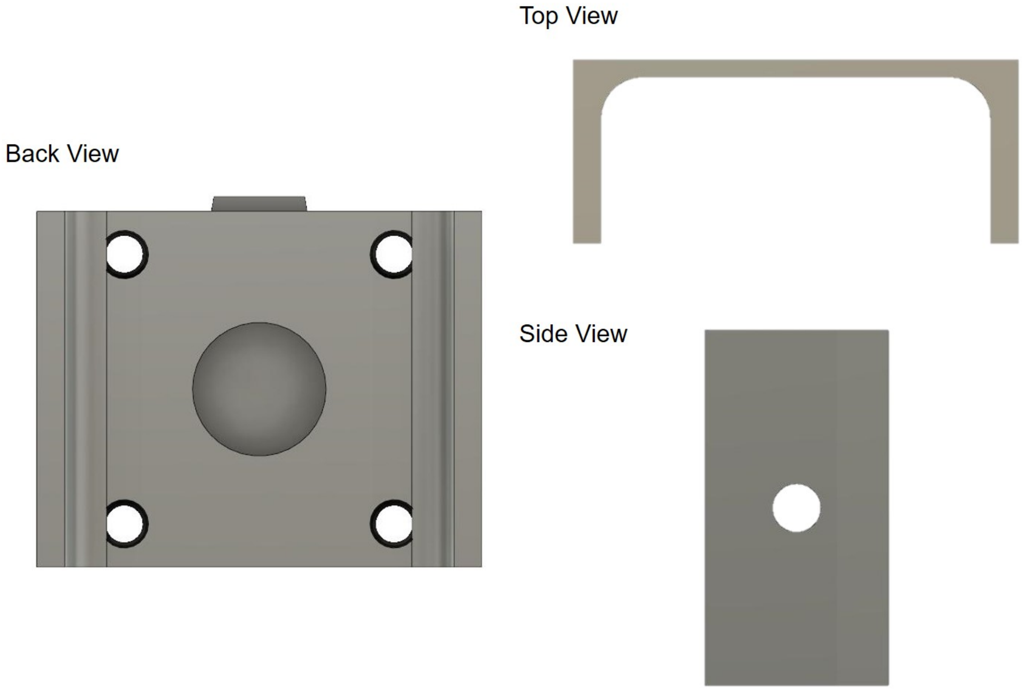

Figure A.2.4: Back view, top view, and side view of the cylinder mount. The mount attached to the cylinder using $1/2" - 13 \times 1\frac{1}{2}"$ brass bolts. The fixture fit through the runner of the sliding mount using two six-inch pieces of $3/8" - 16$ brass threaded rod, nylon washers, and $3/8" - 16$ brass wing nuts.

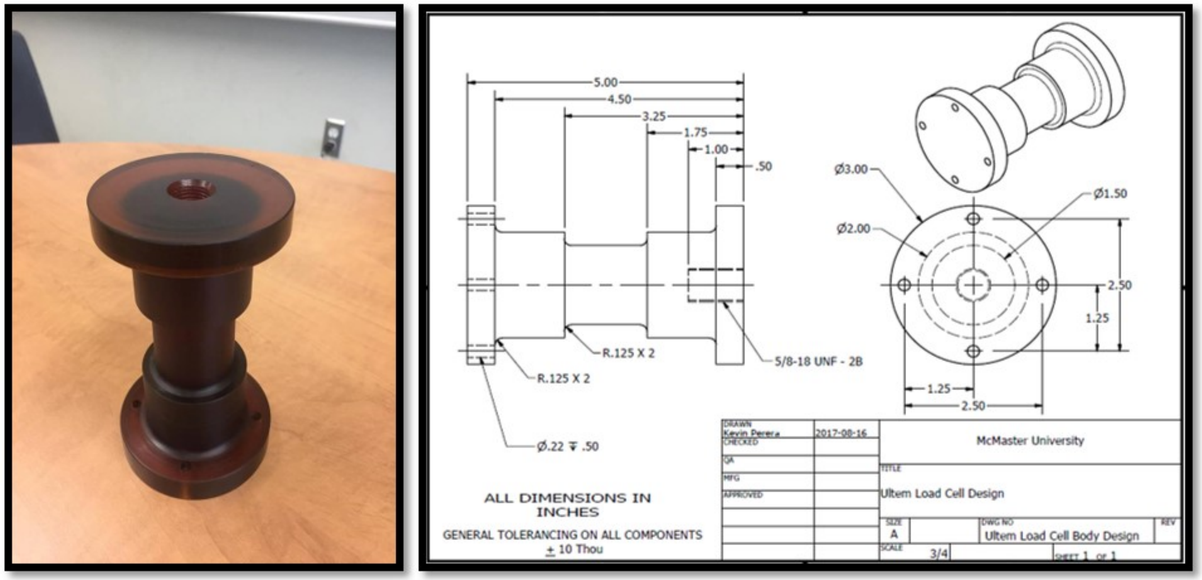

Figure A.2.5: Load cell body (left) and engineering drawing (right). Thank you to Kevin Perera for generating the drawing and milling the load cell from Ultem plastic.

socket head cap screws, No. 10 nylon washers, and $10-32$ nylon hex nuts. The load cell body and CAD drawing is provided in Figure A.2.5.

A.2.2.5 Extension Piece

The extension piece was designed to increase the distance between the metal components on the load cell and pneumatic double-acting cylinder, and the iso-centre of the magnet (joint centre of the specimen). Two 5" × 5" squares of 3/4" nylon plastic were separated by four 4" UHMW plastic tubes (1" OD 1/2" ID), one in each corner. Tubes were affixed to the nylon squares by 1/2" $-$ 13 nylon threaded rod, and accompanying 1/2" $-$ 13 nylon hex nuts.

To enable sliding of the extension piece in the slot runners, 3/8" Teflon ($\sim$ 2" × 6" dimensions) was engineered to fit into 3/8"[3] notches on the side edges of the nylon squares. To prevent the Teflon from shifting in place, a 3/4" × 4" piece of Teflon fit between the Nylon faces and was screwed into place with $10-32\times$ 2" nylon socket head cap screws[4]. To facilitate this, a size 21 tap drill (0.1590") created threaded holes for the $10-32$ screws. In the Nylon, a clearance fit (size 9, 0.1960") was used. A CAD model of the full extension piece with the engineered Teflon runners is shown in Figure A.2.6.

A.2.2.6 Potting Cup

The potting up was made from custom cut 1/4" thick sheets of clear acrylic plastic glued together by epoxy. This method was cheap, and facilitated complex shapes. Nine hollow "rings" (5" OD, $4\frac{1}{4}$" ID) and one full acrylic circle (5" OD) were laser-cut from the acrylic and stacked vertically to create a singular hollow cavity. This construction was able to clearance fit a $4\frac{1}{4}$" diameter PVC pipe. Three rectangular 5" × $2\frac{1}{8}$" acrylic sheets created a base to enable fixation to the extension component. Countersink clearance holes (size 7, 0.2010") through the potting cup base and nylon face of the extension piece enabled fixation using nylon $10-32\times$ 2" screws, No. 10 nylon washers, and $10-32$ nylon hex nuts.

---

[3] The notch was just over 3/8" to allow for a tight clearance fit of the Teflon piece into the nylon face.

[4] A shorter screw would have been appropriate here, however there were a lot of leftover socket head cap screws and flat head screws from the McMaster-CARR order.

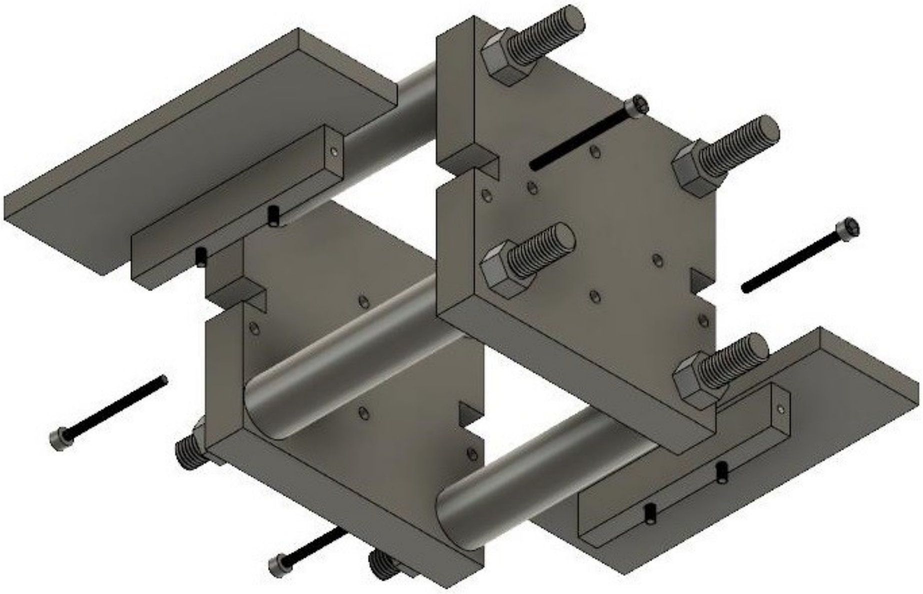

Figure A.2.6: Angle view of the extension piece with added slot runner guides exploded to visualize fittings. Thank you to Jeff Rice for the idea and construction of the extension piece, and to Cooper Gluek for fabricating the runners.

A.2.2.7 Angle Mount

The angle mount was designed to accommodate the natural degree of flexion (increase in relative angle between the tibia and femur) in the porcine stifle specimen. Two slabs of polycarbonate cut into cove designs[5] were separated by $1\frac{1}{8}$" wide pieces of 3/4" thick nylon plastic affixed together using epoxy. Along the curvature, close fit clearance holes (size 18, 0.1695") allow for positioning of the specimen potting fixture (below) in 5 discrete flexion angles [from 0^o (full extension) to 20^o]. The angle mount is shown in Figure A.2.7.

---

[5] A cove design is a popular cut in woodworking. It involves three square corners and one concave corner.

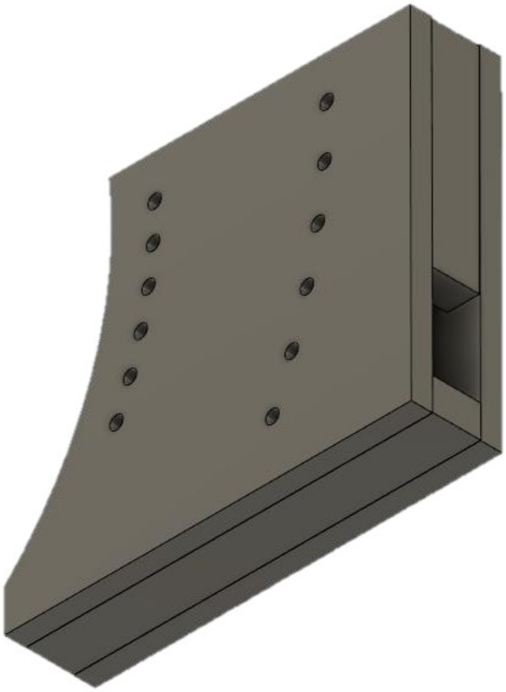

Figure A.2.7: The angle mount was constructed with polycarbonate and nylon materials. The cove design and strategically placed close fit clearance holes in the polycarbonate facilitated a range of natural, discrete flexion angles (0^o to 20^o).

A.2.2.8 Specimen Potting Fixture

The specimen potting fixture was made from 1/4" thick pieces of acrylic plastic, as described above. Nine hollow "rings" (5" OD, $4\frac{1}{4}$" ID) and three full acrylic circles (5" OD) were stacked vertically to create a singular hollow cavity to clearance fit a $4\frac{1}{4}$" diameter PVC pipe. Three rectangular sections with close fit clearance holes (size 18, 0.1695") spaced 4" apart were epoxied to the bottom of the fixture. This piece fit between the two slabs of the polycarbonate on the angle mount. The holes on the rectangular pieces aligned with the holes on the angle mount. Finally, three acrylic pieces on either side of the rectangular extender, attached to the bottom of the specimen potting fixture, allowed for a close, comfortable fit of the specimen potting fixture to the curvature of the angle mount. The position of the specimen potting fixture was manually adjusted and fastened through the clearance holes using a $8-32$ brass threaded rod, No. 8 flat nylon washer, and $8-32$ brass nuts. The angle mount with the specimen potting fixture is shown in Figure A.2.8.

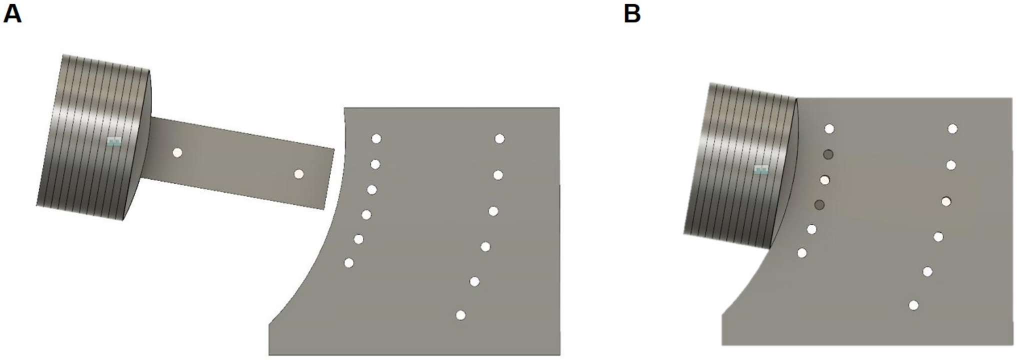

Figure A.2.8: A) Separate and B) completed views of the angle mount and specimen potting fixture. The specimen potting fixture was created from epoxying laser-cut 1/4" piece of acrylic plastic. The hollow rings allowed for a hollow cavity to clearance fit a 4" OD piece of PVC pipe (used for specimen mounting). The bottom piece, rectangular extender, and curved fit pieces enabled the fixture to sit comfortably on the cove design of the angle mount. The strategically-placed clearance fit holes allowed for manual placement of the specimen in one of five discrete flexion postures: 0, 5, 10, 15, and 20^o.

A.3 Control System and Electronics

The control system is still being implemented and tested. Below describes the proposed system. There will be three main components:

1. Transducers, including the pressure regulators and custom load cell;
2. National Instruments data acquisition hardware (National Instruments Compact DAQ) and other electronic hardware
    - NI 9237 with DSUB C-series Strain/Bridge Input module (4 AI, ± 25 mV/V, 24-bit, 50 kS/s/ch Simultaneous)
    - NI 9263 C-Series 4-channel analog output (AO) module (± 10 V, 16-bit, 100 kS/s/ch Simultaneous)
    - NI 9205 C-Series 32-channel single-ended (16-channel differential) analog input (AI) module (± 10 V, 16-bit, 250 kS/s)

3. LabVIEW control program

A.3.1 Pneumatic Components

A.3.1.1 Double-Acting Pneumatic Cylinder

External axial force on the specimen will be applied via a pneumatic double-acting cylinder (BIMBA EF-8030-3CEFMT, University Park, IL; Figure A.3.1). Aluminum and stainless steel materials construct the cylinder body; both are non-ferrous metals. The piston rod has a single-ended 5/8" $-$ 20 UNF male thread for easy attachment to external components. The cylinder has a 30 millimetre (mm) stroke length and 80 mm bore. Two 1/4" NPT full-flow orifices will control air flow to cylinder chambers.

Based on estimates provided, the piston was estimated to generate 3,000 N of force at 120 psi (maximum pressure output of the air compressor). However, using a standard equation of force for the outstroke phase of a pneumatic piston, the expected force at 120 psi is:

$$\begin{aligned} F(lbs) &= P(psi) \times ((bore(in)/2)^2 \times \pi) \\ &= 120 \times ((3.149/2)^2 \times \pi) \\ &\approx 467lbs \end{aligned} \tag{1}$$

where $((bore(in)/2) \times \pi)^2$ is equivalent to the area of the piston. For reference, 467 lbs is approximately 2,084 N. Considering the maximum range required for this project is 800 N, this pneumatic cylinder is well within the specifications to complete the loading task.

A.3.1.2 Electronic Pressure Regulators

Two electronic pressure regulators (TR-025-g10-s, Enfield Technologies, Shelton, CT) will be used to control air pressure to the double-acting cylinder. These linear, proportional regulators convert a current or voltage (voltage used in this setup) input into a pressure output. The solenoid valves allow for ramped pressure application, and deliver smooth, accurate air pressure control. Choice specifications are included in Sub-Appendix A2 for quick reference. More detailed information is available online at the following link: https://www.enfieldtech.com/site/Product-Documentation/TR-Electronic-Pressure-Regulator-Datasheet.pdf.

A.3.1.3 Regulator Wiring

M8 4-pole female flying leads will be used to wire the regulators. The brown lead is the Power, and will be connected to the positive terminal of a DC Power Supply (GQ-A305D,

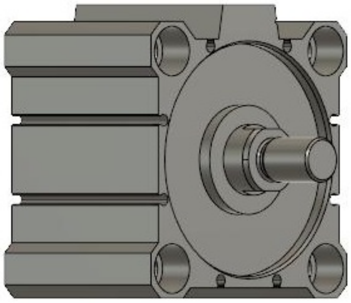

Figure A.3.1: Angle view of the BIMBA EF-8030-3CEFMT pneumatic double-acting cylinder. This 3D CAD model was generated from https://www.bimba.com/Products-and-Cad/Actuators/Inch/Compact/Square-Extruded-Body/Extruded-Flat-EF-One on 29 August 2019.

GQ Electronics LLC, Seattle, WA). The blue lead is the Common Ground and will be connected to the negative terminal of the power supply. The white lead is the Command input and will be wired into a NI 9263 C-Series 4-channel analog output (AO) module (± 10 V, 16-bit, 100 kS/s/ch Simultaneous; Figure A.3.2). The white Command input wires will be screwed into the AO0 (0) and AO1 (2) pins, one for each regulator. Each channel will be grounded (COM; pins 1 and 3) with standard copper wiring that terminate on the DC Common ground of the Power Supply. Finally, the black lead is the Monitor output (regulator feedback) and will be wired into an NI 9205 C-Series 32-channel single-ended (16-channel differential) analog input (AI) module (± 10 V, 16-bit, 250 kS/s; Figure A.3.3). The black Monitor output wires will be screwed into the AI0 (1) and AI1 (2) pins, one for each regulator. The regulators will be wired in a differential configuration, so standard copper wires will be inserted into channels AI8 (20) and AI9 (21) to complete the differential pairs (AI0+/AI8-; AI1+/AI9-). Another copper wire will be inserted into the isolated ground reference of the system (COM (29)). Figure A.3.4 shows an example of the proposed wiring setup.

A.3.1.4 Connection of Tubing

A 3.2 HP twin stack air compressor (Power Fist, Model: 8260705; max. psi 125, tank volume 4.3 gal.) will supply air to the regulators via plastic poly tubing (1/4” ID, 3/8” OD). A brass 3/8” NPT female tee-fitting (Swagelok B-600-3-6TTF) will split the compressor connector

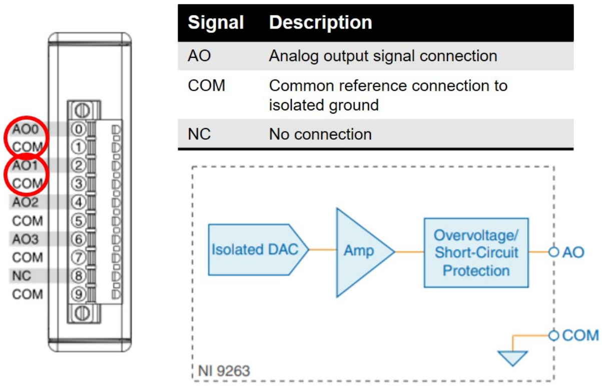

Signal	Description
AO	Analog output signal connection
COM	Common reference connection to isolated ground
NC	No connection

Figure A.3.2: Pin-out diagram (left), signal descriptions (top right), and wiring schematic (bottom right) of the NI 9263 C-Series module. Images and table information from the online manual found at: http://www.ni.com/pdf/manuals/373781b_02.pdf.

hose into two streams, one to each regulator (Figure A.3.5A). Brass 3/8” NPT male tube fittings (Swagelok B-600-1-4) will connect each tube to their respective input ports of the electronic pressure regulator (Figure A.3.5B). Brass fittings will connect tubing from the regulator output ports that then pass into the scanner room via the copper-plated conduit. On the apparatus, the output tubing will be connected to the cylinder via 3/8” NPT straight male ABS plastic fittings (Figure A.3.5C).

A.3.2 Load Cell

At the centre of the load cell (smallest inner diameter), two Aluminum Ribbon lead strain gauges (SGT 3S/350-TY13, OMEGA, Stamford, CT) were arranged 180^o apart. The strain gauges were wired into a NI 9237 with DSUB C-series Strain/Bridge Input module (4 AI, ± 25 mV/V, 24-bit, 50 kS/s/ch Simultaneous) in a half-bridge whetstone bridge configuration. *However, it is likely that additional strain gauges will be affixed to enable a full-bridge configuration.*

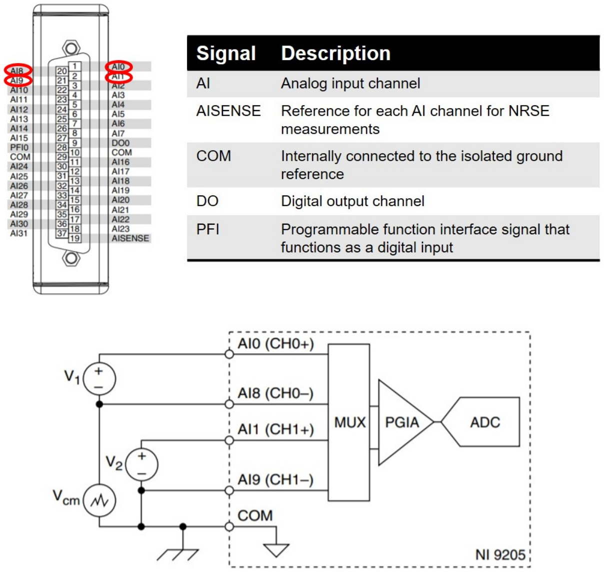

Signal	Description
AI	Analog input channel
AISENSE	Reference for each AI channel for NRSE measurements
COM	Internally connected to the isolated ground reference
DO	Digital output channel
PFI	Programmable function interface signal that functions as a digital input

Figure A.3.3: Pin-out diagram (left), signal descriptions (right), and wiring schematic (bottom) of the NI 9205 C-Series module. Images and table information are from the online manual found at the following link: http://www.ni.com/pdf/manuals/374188a_02.pdf.

A.4 Testing and Troubleshooting

A.4.1 Calibration of the Load Cell

A few standardized tests in an Instron mechanical tester (6800 series) were completed to create a calibration equation for strain to force, which would be required for the apparatus. This work was completed by Ariana Fraschetti as a 4th-year undergraduate project. Briefly, plans were generated to complete load-controlled (mimic the apparatus environment) and displacement-controlled (safer for the Instron!) tests for 500 cycles at $5mm/min$, $10mm/min$, $15mm/min$, $20mm/min$, and $25mm/min$ strain rates. Issues with some noise in the strain data itself, and a lab move (rendering the Instron unusable for a few months) put this project on hold.

The few tests that were run showed some drift in the system, suggesting that either: 1) a cyclic pre-load would be required to obtain a quasi-static state; or 2) a statistical model incorporating cycle number may be required to account for drift. A few figures are shown from a load-controlled trial at $5mm/min$ strain rate, for 500 cycles. Figure A.4.1 plots microstrain versus force (N) at each cycle peak, coloured by cycle number (purple -

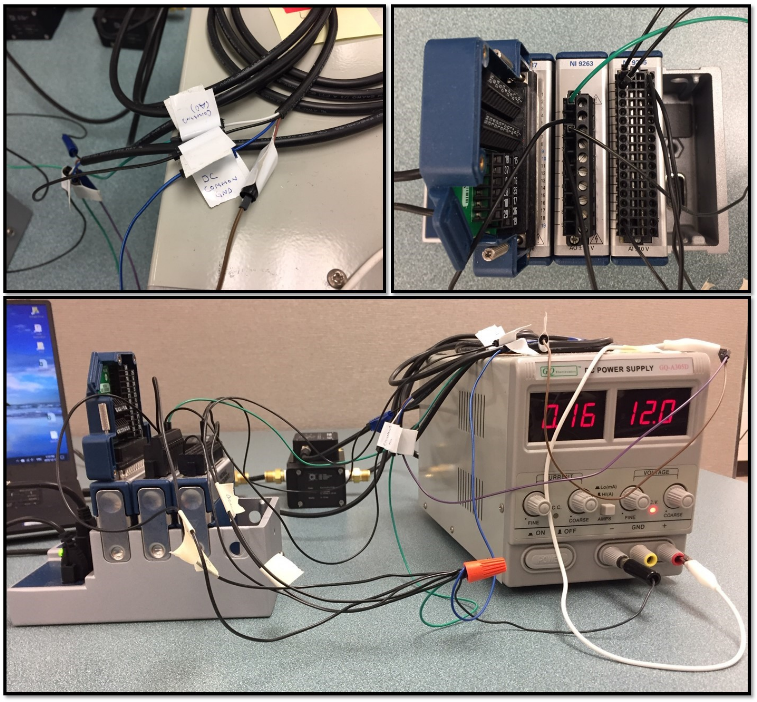

Figure A.3.4: A) Labeled M8 4-pole flying lead wires. B) Connected AO and AI wires for signal generation and regulator feedback. C) Wiring setup with the regulators (background).

1, yellow - 500). Overlaid in red is every 25th cycle. Visually, approximately half of the drift in strain measurement occurs over the first 150 cycles. Figure A.4.2 plots force (N) versus microstrain for the last 250 cycles, with colour transitioning from purple (cycle 251) to yellow (cycle 500). Here, the strain continues to drift, but not to the extent of the first few cycles. Finally, Figure A.4.3 shows the decrement in strain over the 500 cycle test, with the Levenberg-Marquardt non-linear fit in red.

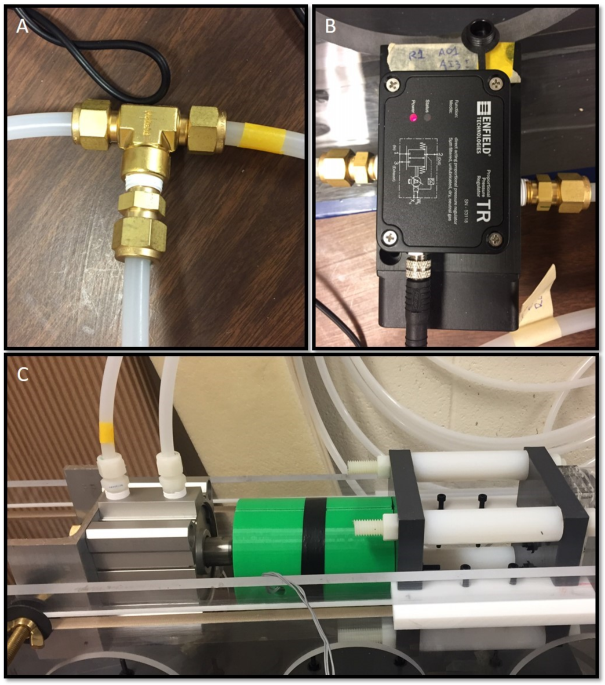

Figure A.3.5: A) Brass T-Fitting that will split the hose from the air compressor to each regulator. B) Input (left), output (right) and exhaust (not shown) of one regulator. C) Tubing into each orifice of the duble-acting pneumatic cylinder using ABS plastic tube fittings from Swagelok.

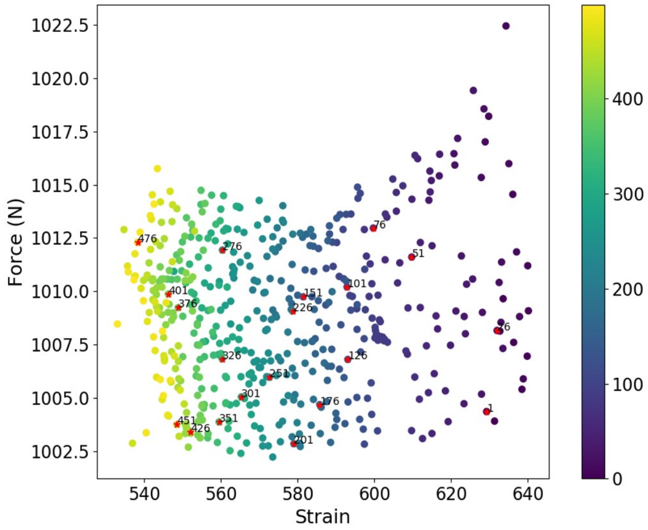

Figure A.4.1: Microstrain versus force (N) at each cycle peak, coloured by cycle number.

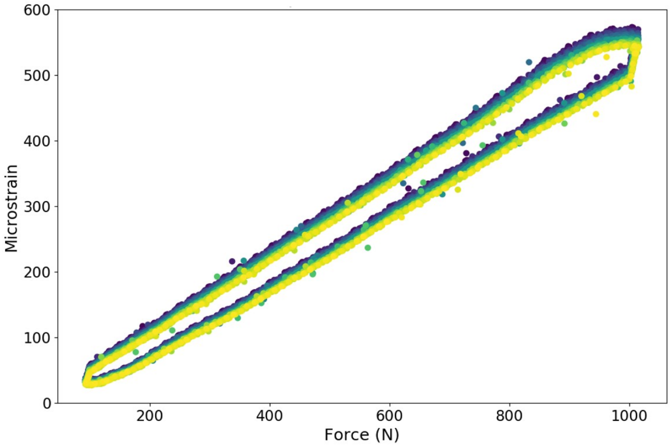

Figure A.4.2: Scatter plot of force (N) versus microstrain during $5mm/min$ load-controlled cycling test of the Delrin load cell for the last 250 cycles. The colour (purple - yellow) is normalized to cycle number, suggesting drift of the microstrain measurements with increasing cycle number.

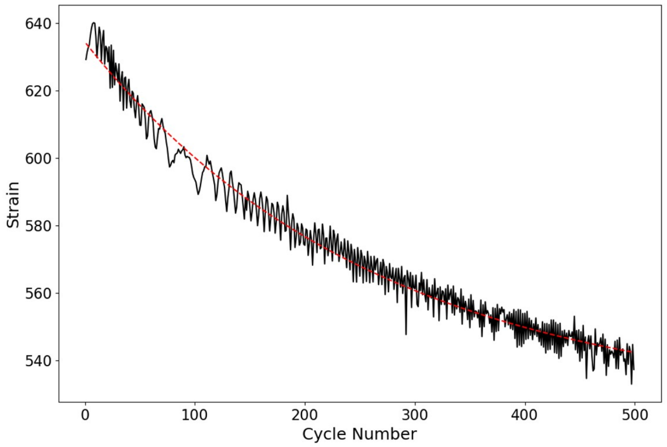

Figure A.4.3: Decrement of peak microstrain with increasing cycle number (black). The Levenberg-Marquardt model fit is overlaid in red.

A.4.2 Piston Feedback Loop

When the air hose was connected and the LabVIEW program started, there was no movement of the cylinder piston. It is likely due to no integration of position (or force via the strain gauge) at the time. To ensure the other components were working as expected, a number of steps were taken.

A.4.2.1 Check Analog Output Signals

With the waveform generator, two 0-10 V sinusoid waveforms 90 degrees out of phase were expected. To test these signals, an oscilloscope was used. The oscilloscope showed the waveforms being sent to the regulators were as expected.

A.4.2.2 Check Line Pressure

Using an old pressure gauge and extra pipe fitting found in the Kinesiology workshop, a device to measure the pressure output at the end of a tube was constructed (Figure A.4.4). Two spots along the chain for were checked for pressure: 1) at the input port of a regulator (i.e., is the correct pressure reaching the regulator?); and 2) at the output port of a regulator (i.e., is the pressure leaving the regulator ramping up and down in accordance with the sinosoidal voltage input to the regulator?). Setting the line pressure to 90 psi, the pressure reaching the regulator was 90 psi, indicating that the correct pressure was entering the input valve of the regulator. When connecting the pressure gauge to the opposite port (output), a slow, linear increase in pressure was observed instead of the anticipated sinusoidal function. This slow linear increase in pressure was confirmed via the Analog input (regulator feedback) signal in LabVIEW, as well as the TR Enfield software. Further work with the load cell, or the use of an MR-compatible linear optical encoder for external control of the piston are required.

A.4.3 Retaining Ring of Cylinder

The inner retaining ring of the pneumatic cylinder is ferromagnetic. The cylinder was custom-built to contain non-ferromagnetic metals. However, the retaining ring was either: 1) made with the wrong grade of stainless steel; or 2) the machining process changed the crystalline structure of the metal[6] Therefore, this needs to be outsourced, or created in-house

---

[6] Specific temperatures and/or plastic deformation of an austenitic stainless steel can induce martensite structure, which is ferromagnetic.

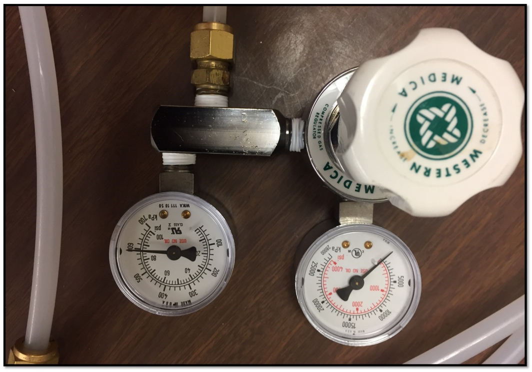

Figure A.4.4: Pressure gauge fixture.

to continue with the cyclic control via the pneumatic cylinder.

References

Bergmann, G., Bender, A., Graichen, F., Dymke, J., Rohlmann, A., Trepczynski, A., . . . Kutzner, I. (2014). Standardized loads acting in knee implants. *PLoS ONE*, *9*(1), e86035.

Miller, R., Edwards, W., & Deluzio, K. (2015). Energy expended and knee joint load accumulated when walking, running, or standing for the same amount of time. *Gait & Posture*, *41*(1), 326–328.

Paranjape, C., Cutcliffe, H., Grambow, S., Utturkar, G., Collins, A., Garrett, W., . . . DeFrate, L. (2019). A new stress test for knee joint cartilage. *Scientific Reports*, *9*(1), 2283.

Thorup, V. M., Laursen, B., & Jensen, B. R. (2008). Net joint kinetics in the limbs of pigs walking on concrete floor in dry and contaminated conditions. *Journal of Animal Science*, *86*(4), 992–998.

Thorup, V. M., Tøgersen, F. A., Jørgensen, B., & Jensen, B. R. (2007). Biomechanical gait analysis of pigs walking on solid concrete floor. *Animal*, *1*(5), 708–715.

Sub-Appendix A1 - Technical Drawings

This supplementary section includes technical drawings generated in Autodesk Fusion 360 of the slide rail, cylinder mount, custom Ultem load cell, extension piece, potting cup, angle mount, and specimen potting fixture.

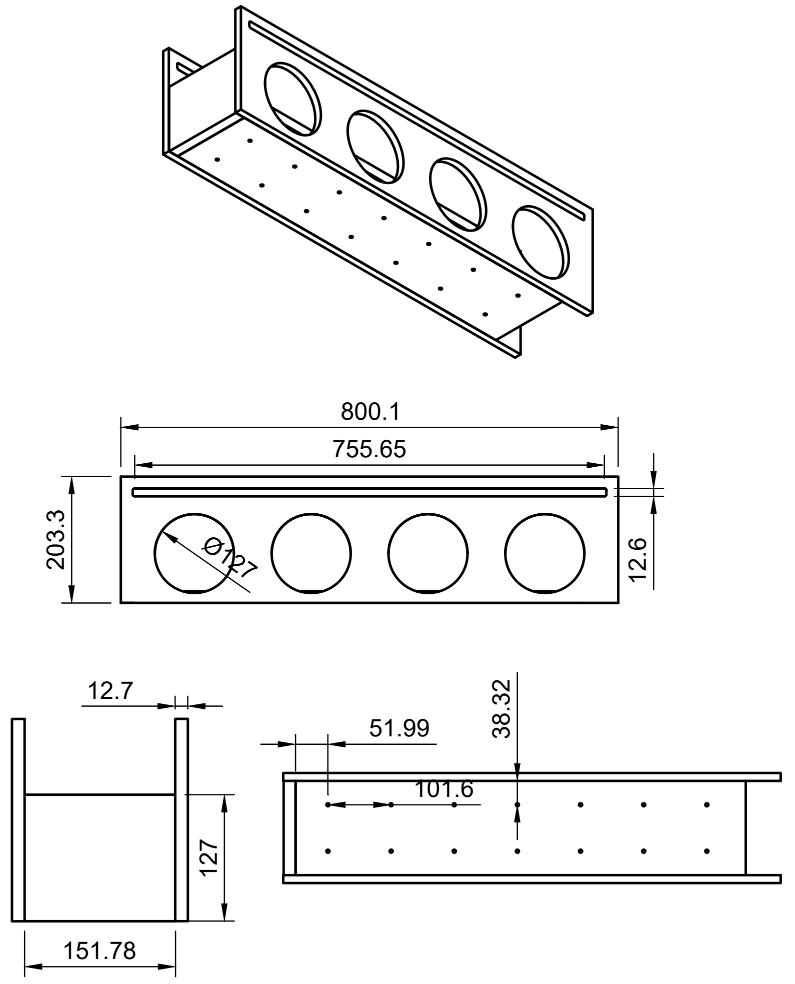

Dept.	Technical reference	Created by Elora Brenneman 2019-09-18	Approved by
		Document type	Document status
		Title SlideRail	DWG No.
			Rev. / Date of issue / Sheet 1/1

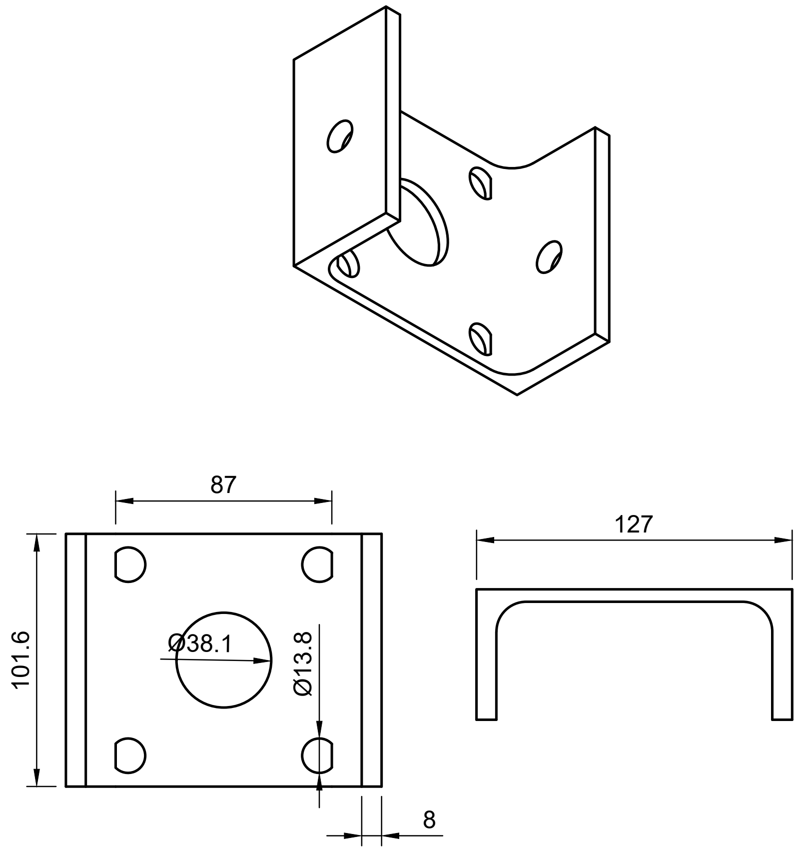

Dept.	Technical reference	Created by Elora Brenneman 2019-09-12	Approved by
		Document type	Document status
		Title CylinderMount	DWG No.
			Rev. Date of issue Sheet 1/1

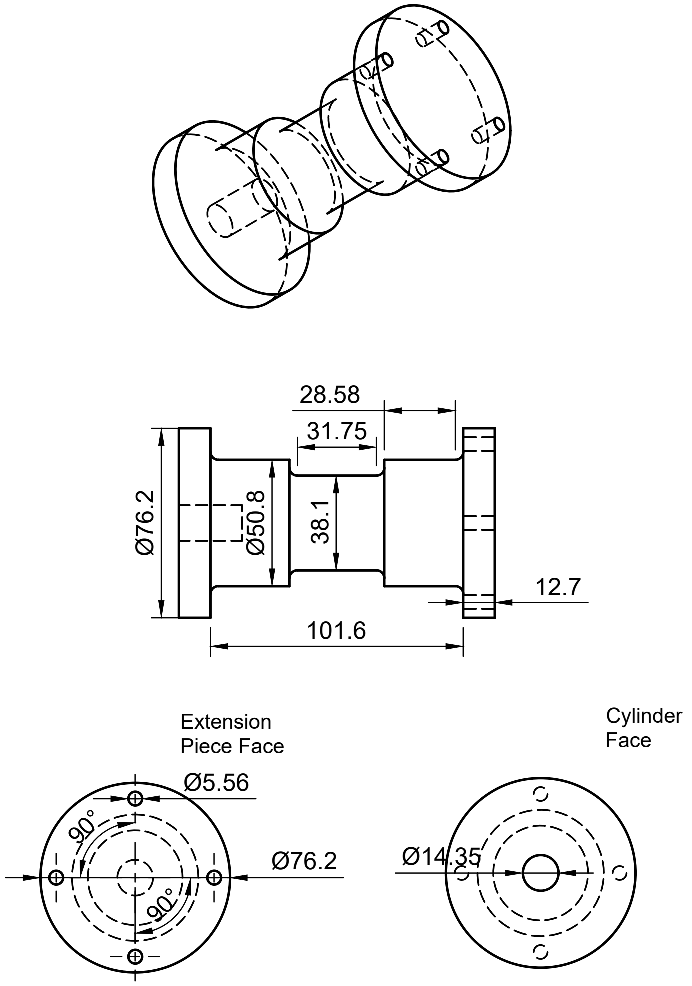

Dept.	Technical reference	Created by Elora Brenneman 2019-09-12	Approved by
		Document type	Document status
		Title UltemLoadCell	DWG No.
			Rev. Date of issue Sheet 1/1

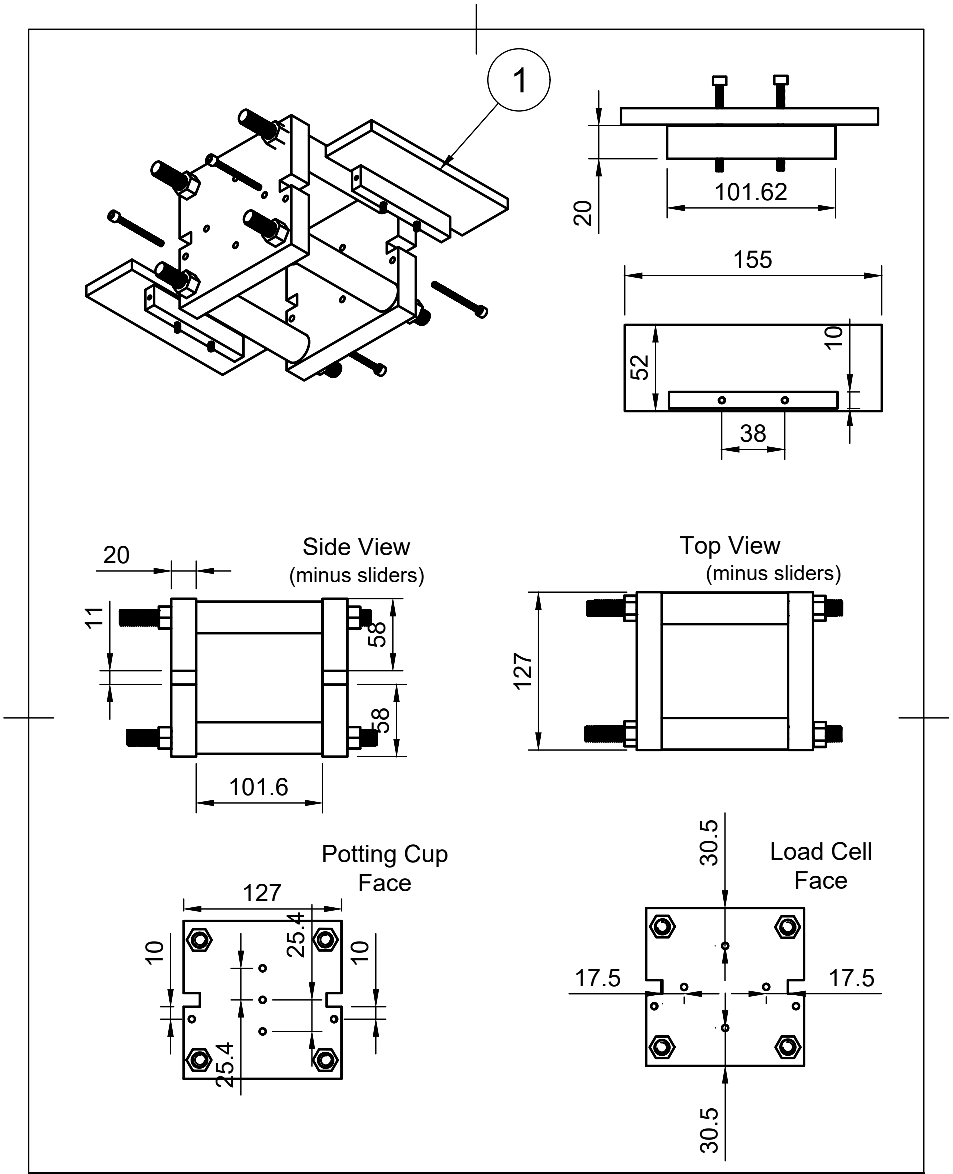

Dept.	Technical reference	Created by Elora Brenneman 2019-09-11	Approved by
		Document type	Document status
		Title ExtensionPiece	DWG No.
			Rev. Date of issue Sheet 1/1

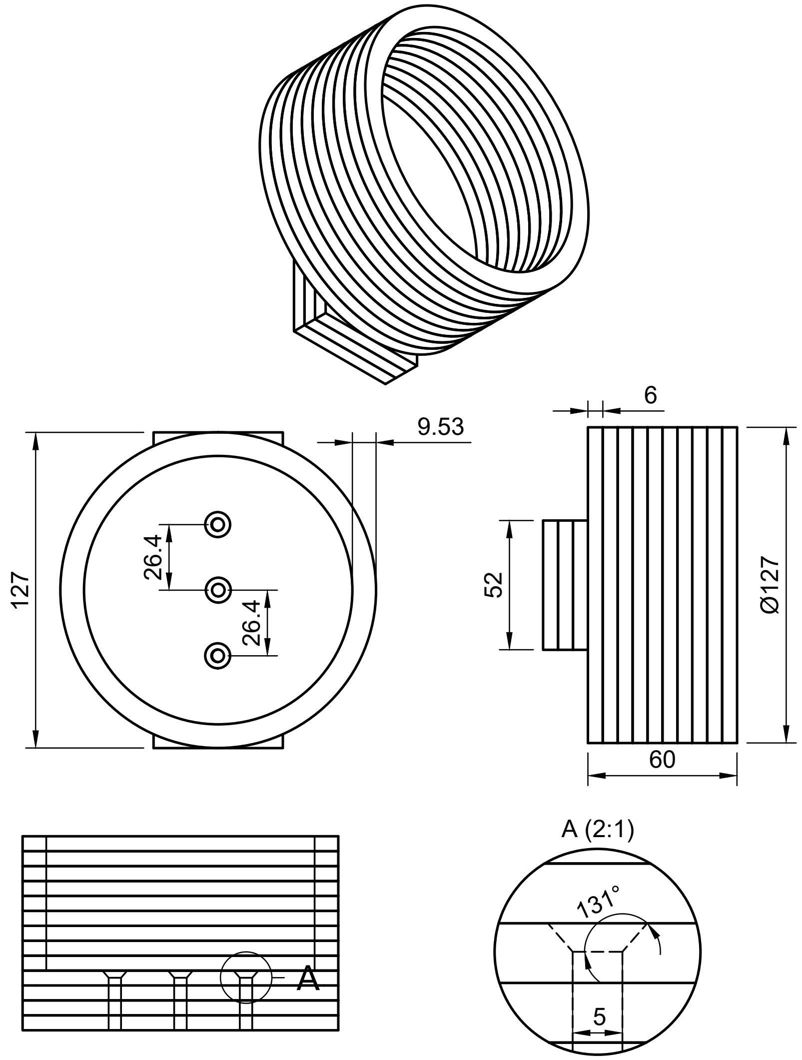

Dept.	Technical reference	Created by Elora Brenneman 2019-09-12	Approved by
		Document type	Document status
		Title PottingCup	DWG No.
			Rev. / Date of issue / Sheet 1/1

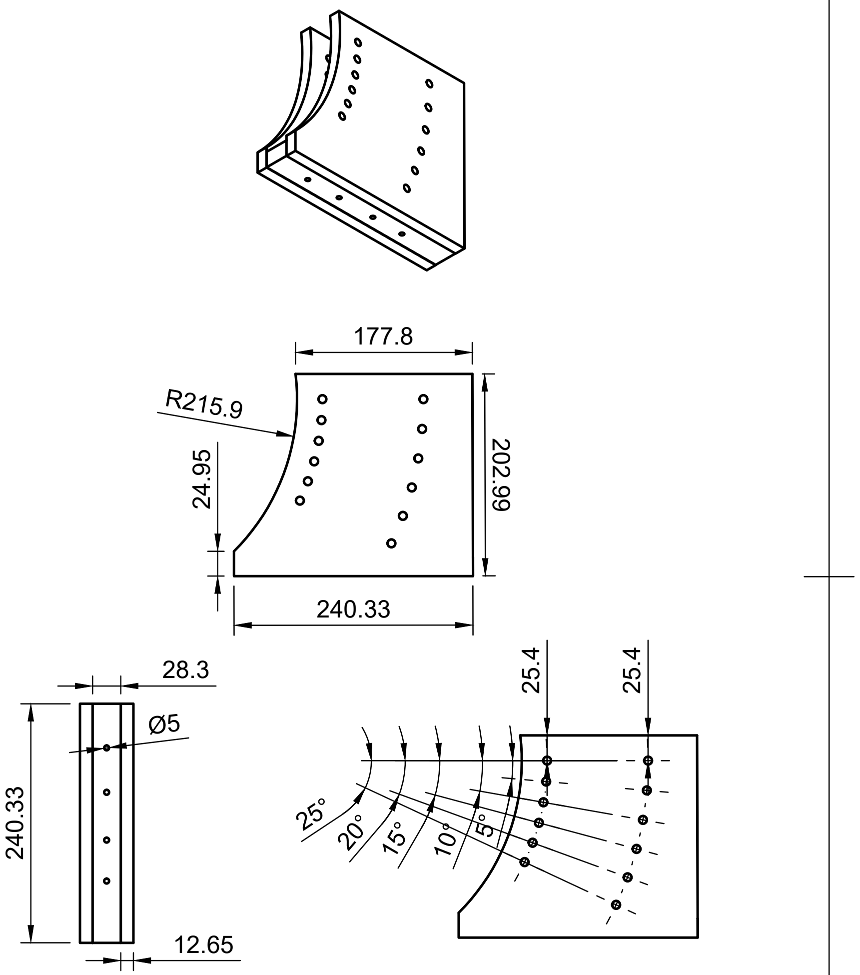

Dept.	Technical reference	Created by Elora Brenneman 2019-09-18	Approved by
		Document type	Document status
		Title AngleMount	DWG No.
			Rev. Date of issue Sheet 1/1

Sub-Appendix A2 - Regulator Specifications

The following specifications for the regulators were summarized from the TR Electronic Pressure Regulator Datasheet.

Mechanical Specifications	
Pressure Range	0-10 bar
	0-145 psi
Ports	1/4” NPTF
Operating Temperature	0-40^{o}C

Electrical Specifications	
Power Requirement	12 ± 2 VDC
	24 ± 4 VDC @ 20W
Command Input	Configurable 0-10VDC
	Configurable 4-20mA
Command Input Impedance	0-10VDC: 100k
	4-20mA: 210
Monitor Output	0-10VDC

Performance Specifications	
Minimum Volume	100 mL (6.1 in^3) preferred
Flow	1300 SLPM 5.5 → 0 bar
	46 SCFM 80 → 0 psi
Leak Rate	SLPM 10 → 0 bar
	12 SCFM 150 → 0 psi

Regulator Performance	
Resolution	± 0.1% Full Scale
Linearity	± 0.1% Full Scale
Hysteresis	± 0.1% Full Scale
Sensor Accuracy	± 1.5% Full Scale
Controller Accuracy	± 0.1% Full Scale

Appendix B — Designs and Testing for Static Loading of MRI-compatible Loading Apparatus

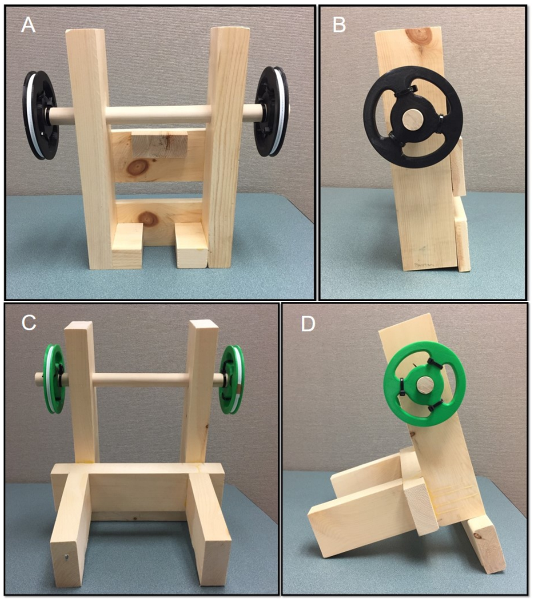

Figure B.1.1: A) Front and B) side view of the angle mount pulley assembly, and C) front and D) side view of the sliding mount pulley assembly. Pulleys were 3D printed from PLA plastic, and designed to facilitate $4mm$ diameter static Nylon utility rope. Two 14” pieces of 2” × 4” were separated by a 1” diameter wood dowling. Pieces of 1” × 4” and 2” × 4” lumber were cut and glued for support and fit around the angle mount.

B.1 Design

Wood, carpenters wood glue, and 3D printed plastic were used for the construction of external assembly components for the apparatus. First, to reinforce the plywood base, two $5'$ pieces of 2” × 4” lumber were cut and glued to the bottom of the plywood as ‘runners’ the length of the apparatus. These were glued using PLA Premium, a very strong wood adhesive. Then, a pulley system was constructed. Two ropes ($4mm$ diameter static rope, MEC), one on each side of the extension piece, translate the extension piece in along the sliding mount, resulting in an axial force applied to the specimen. The ropes continue around pulleys attached to the angle mount, loop back along the length of the whole apparatus, and around a second set of pulleys on the sliding mount end. Weights are then attached at the end of the rope hanging from the sliding mount pulley system.

For the angle mount pulley attachment (Figure B.1.1A and B), two 14” pieces of 2”x4” were cut. One inch holes were bore from each 2”x4” using a hole saw attached to a drill press. A 1" diameter dowling was pushed through the bored holes, and two 1"x4" pieces were glued to the back side for support. Small pieces of 2"x4" were glued in place to enable a clearance fit around the angle mount. Finally, pulleys were custom designed in Autodesk and 3D printed with PLA plastic.

Similarly, a pulley attachment was constructed for the sliding mount end (Figure B.1.1C and D). Two 14" pieces of 2"x4" lumber were cut and separated by 1" dowling. A 'U'-shape was glued and attached to the 14" pieces of lumber which fit around the end of the sliding mount. A final piece of 2"x4" was glued below the bottom edges of the 14" 2"x4" pieces of lumber for additional support. To further mitigate any torque that may be present from the hanging mass, a piece of 2"x4" was cut to fit through the end holes of the sliding mount and over the ends of the 'U' lumber piece.

B.2 Testing of the Pulley System

To test the pulley system, and quantify energy losses in the system, known masses were hung from a milk crate attached to the pulley system (Figure 5.2.3B from Chapter 5). An AMTI force cube (MC3A-500) was used to quantify forces observed at the approximate knee joint centre of a specimen. A straight cut piece of 2" × 4" was used in the extension piece to mimic the femur. Five different pieces of 2" × 4" were cut with angled edges to complement the 5 discrete angles that the angle mount can facilitate (Figure B.2.1). First, loading and unloading tests were completed where in 2-minute increments, known masses were added to the basket (up to 286 N [29 kg]), then removed in similar fashion. Three tests were completed at each discrete angle setting for a total of 15 loading/unloading tests (randomized). Figures B.2.2 and B.2.3 show examples of loading and unloading results from 3 tests at the 10 degree angle. Using these tests, it was determined that masses of 24 kg and 36 kg would be required to simulate 180 N and 270 N of axial compression force respectively.

As a final test, 24 kg and 36 kg masses were suspended in separate trials for 30-minutes to test the amount of drift in the system. Over the time period, 2-3% drift was calculated, suggesting negligible losses over time.

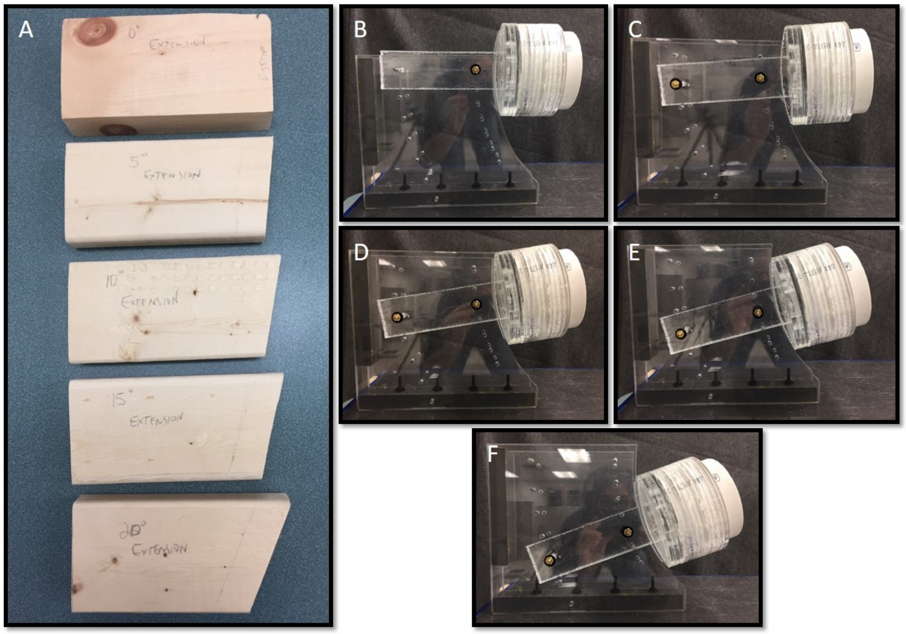

Figure B.2.1: Angled 2” × 4” pieces to test the loading apparatus as discrete positions.

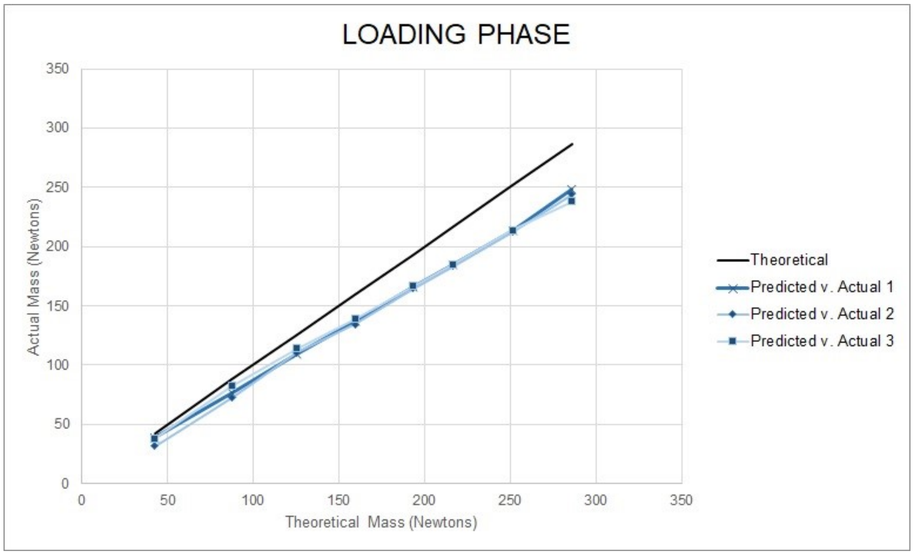

Figure B.2.2: Predicted v. Actual mass measured by the force cube during the loading protocol. Approaching 280 *N* (about twice that experienced by a porcine stifle joint physiologically), approximately 15% of the actual mass is deflected throughout the system.

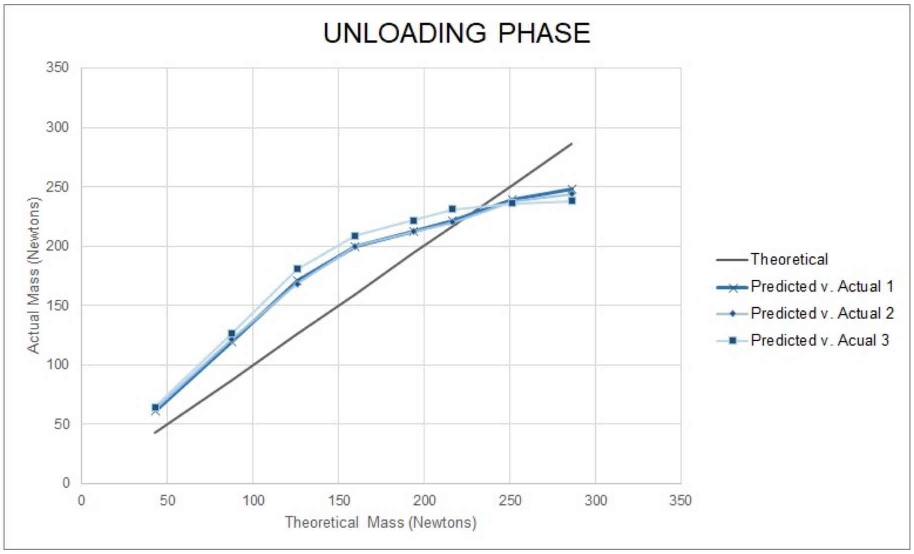

Figure B.2.3: Predicted v. Actual mass measured by the force cube during the unloading protocol.

Appendix C — Hayes Solution for Indentation Mechanics of Cartilage

Hayes et al (1972) formulated a mathematical solution for the indentation mechanics of articular cartilage, modeled as an infinite elastic layer bonded to a rigid half space. For a spherical indenter, the following dimensionless parameters are calculated to quantify the instantaneous modulus as presented in Sim et al (2017):

$$\chi = \left(\frac{a^2}{\omega_0 R}\right) \tag{Eq. 29}$$

$$\kappa = \frac{P(1-v)}{4aG\omega_0}\int_0^1 \omega_1(\tau)d\tau \tag{Eq. 30}$$

where a is the radius of the contact region; ω_0 is the normal displacement of the cartilage; R is the radius of the spherical indenter; p is the normal indenter load; v is Poisson's ratio; G is the elastic shear modulus; and numerical values from the term $\int_0^1 \omega_1(\tau)d\tau$ allow for the computation of κ at given values of the contact area to height of specimen ratio (aspect ratio, a/h) and v. The computations start with solving the following Fredholm integral equation of the second kind with symmetric kernel:

$$\omega(\xi) = 1 + \frac{1}{\pi}\int_0^1 \omega(\tau)[K(\tau+\xi) + K(\tau-\xi)]d\tau - \chi\xi^2 \tag{Eq. 26}$$

or:

$$\omega(\xi) = \omega_1(\xi) + \chi\omega_2(\xi) \tag{Eq. 27}$$

where:

$$\omega_1(\xi) = 1 - \frac{1}{\pi}\int_0^1 \omega_1(\tau)[K(\tau+\xi) + K(\tau-\xi)]d\tau, \tag{Eq. 23}$$

$$\omega_2(\xi) = -\xi^2 + \frac{1}{\pi}\int_0^1 \omega_2(\tau)[K(\tau+\xi) + K(\tau-\xi)]d\tau \tag{Eq. 28}$$

and function $K(u)$ is a symmetric kernel defined by:

$$\begin{aligned} K(u) &= \frac{a}{h}\int_0^\infty \left\{\frac{(3-4v)\sinh\alpha e^{-\alpha} - [\alpha(1+\alpha) + 4(1-v)^2]}{[(\alpha)^2 + 4(1-v)^2] + (3-4v)\sinh^2\alpha}\right\} \\ &\quad \times \cos[\alpha\left(\frac{a}{h}\right)u]d\alpha \qquad \text{(Eq. 24)} \\ &= \frac{a}{h}\int_0^\infty \left\{\frac{(3-4v)(\frac{-e^{-2\alpha}}{2} - \alpha - \alpha^2 - 4(1-v)^2}{[(\alpha)^2 + 4(1-v)^2] + (3-4v)(\frac{(e^{\alpha}+e^{-\alpha}-2)}{4})}\right\} \\ &\quad \times \cos[\alpha\left(\frac{a}{h}\right)u]d\alpha \end{aligned}$$

Providing values for a/h and v, the function $K(u)$ is calculated over the interval $0 \leq$

$u \leq 2$, and the determination of ω is reduced to the solution of a system of linear equations.

An excerpt of a Python Notebook is included below that takes defined values of a/h and v to compute the dimensionless variables χ and κ. The Python code was adapted from Matlab code available online from Chen et al (2016).

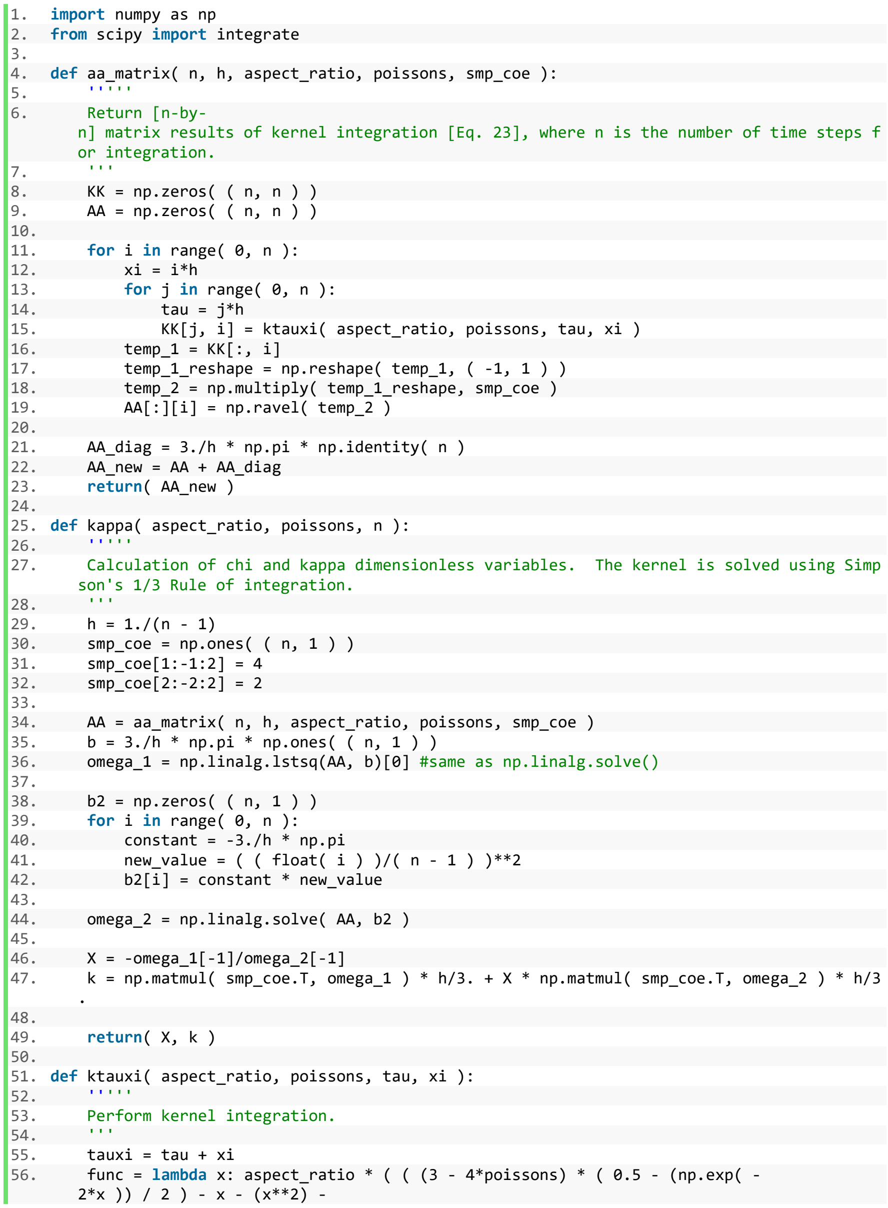

```
import numpy as np
from scipy import integrate

def aa_matrix( n, h, aspect_ratio, poissons, smp_coe ):
    '''''
    Return [n-by-n] matrix results of kernel integration [Eq. 23], where n is the number of time steps for integration.
    '''
    KK = np.zeros( ( n, n ) )
    AA = np.zeros( ( n, n ) )

    for i in range( 0, n ):
        xi = i*h
        for j in range( 0, n ):
            tau = j*h
            KK[j, i] = ktauxi( aspect_ratio, poissons, tau, xi )
        temp_1 = KK[:, i]
        temp_1_reshape = np.reshape( temp_1, ( -1, 1 ) )
        temp_2 = np.multiply( temp_1_reshape, smp_coe )
        AA[:][i] = np.ravel( temp_2 )

    AA_diag = 3./h * np.pi * np.identity( n )
    AA_new = AA + AA_diag
    return( AA_new )

def kappa( aspect_ratio, poissons, n ):
    '''''
    Calculation of chi and kappa dimensionless variables.  The kernel is solved using Simpson's 1/3 Rule of integration.
    '''
    h = 1./(n - 1)
    smp_coe = np.ones( ( n, 1 ) )
    smp_coe[1:-1:2] = 4
    smp_coe[2:-2:2] = 2

    AA = aa_matrix( n, h, aspect_ratio, poissons, smp_coe )
    b = 3./h * np.pi * np.ones( ( n, 1 ) )
    omega_1 = np.linalg.lstsq(AA, b)[0] #same as np.linalg.solve()

    b2 = np.zeros( ( n, 1 ) )
    for i in range( 0, n ):
        constant = -3./h * np.pi
        new_value = ( ( float( i ) )/( n - 1 ) )**2
        b2[i] = constant * new_value

    omega_2 = np.linalg.solve( AA, b2 )

    X = -omega_1[-1]/omega_2[-1]
    k = np.matmul( smp_coe.T, omega_1 ) * h/3. + X * np.matmul( smp_coe.T, omega_2 ) * h/3.

    return( X, k )

def ktauxi( aspect_ratio, poissons, tau, xi ):
    '''''
    Perform kernel integration.
    '''
    tauxi = tau + xi
    func = lambda x: aspect_ratio * ( ( (3 - 4*poissons) * ( 0.5 - (np.exp( -2*x )) / 2 ) - x - (x**2) -
```

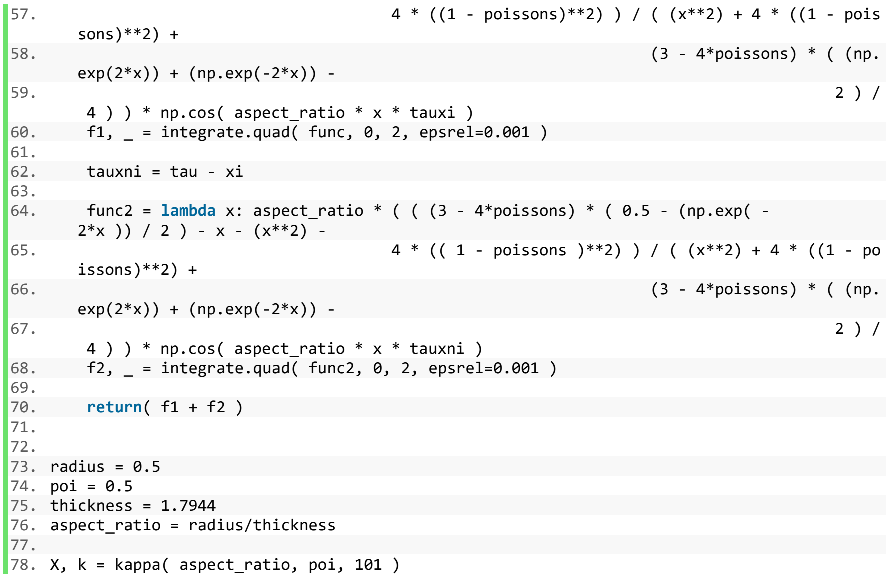

```
                                     4 * ((1 - poissons)**2) ) / ( (x**2) + 4 * ((1 - pois
   sons)**2) +
                                                                 (3 - 4*poissons) * ( (np.
   exp(2*x)) + (np.exp(-2*x)) -
                                                                                     2 ) /
    4 ) ) * np.cos( aspect_ratio * x * tauxi )
    f1, _ = integrate.quad( func, 0, 2, epsrel=0.001 )

    tauxni = tau - xi

    func2 = lambda x: aspect_ratio * ( ( (3 - 4*poissons) * ( 0.5 - (np.exp( -
   2*x )) / 2 ) - x - (x**2) -
                                     4 * (( 1 - poissons )**2) ) / ( (x**2) + 4 * ((1 - po
   issons)**2) +
                                                                 (3 - 4*poissons) * ( (np.
   exp(2*x)) + (np.exp(-2*x)) -
                                                                                     2 ) /
    4 ) ) * np.cos( aspect_ratio * x * tauxni )
    f2, _ = integrate.quad( func2, 0, 2, epsrel=0.001 )

    return( f1 + f2 )


radius = 0.5
poi = 0.5
thickness = 1.7944
aspect_ratio = radius/thickness

X, k = kappa( aspect_ratio, poi, 101 )
```

References

Chen, X., Zhou, Y., Wang, L., Santare, M. H., Wan, L. Q., & Lu, X. L. (2016). Determining tension–compression nonlinear mechanical properties of articular cartilage from indentation testing. *Annals of Biomedical Engineering*, *44*(4), 1148–1158.

Hayes, W., Keer, L., Herrmann, G., & Mockros, L. (1972). A mathematical analysis for indentation tests of articular cartilage. *Journal of Biomechanics*, *5*(5), 541–551.

Sim, S., Chevrier, A., Garon, M., Quenneville, E., Lavigne, P., Yaroshinsky, A., ... Buschmann, M. (2017). Electromechanical probe and automated indentation maps are sensitive techniques in assessing early degenerated human articular cartilage. *Journal of Orthopaedic Research*, *35*(4), 858–867.

Appendix D — Linear Fit of T2 Decay

This section describes the T2 mapping values for the porcine sample. The two conditions for inclusion of T2 values were: 1) Values between 0-100 *ms* (Gatti et al. 2017; Kumar et al. 2014; Souza et al. 2014; Subburaj et al. 2012); and 2) The fit of T2 decay was $R^2 > 0.7$ (Gatti et al. 2017; Wirth et al. 2014). For each specimen, signal intensities were extracted at each voxel within the femoral cartilage segmentation, for all 8 echo times. The natural logarithm of the intensites were calculated, then modeled using a linear least squares estimation.

The total number of cartilage voxels, number of voxels removed due to high T2 values (> 100 *ms*), and additional voxels removed due to poor fit ($R^2 < 0.7$) are shown in Table D.0.1. The number of voxels removed ranged from 3.2 – 12.6%[1]. Additional voxels lost in the analysis due to poor linear fit were minimal. In fact, only 9 voxels across all specimens and imaging times (pre-post loading) were removed due to issues with fit. An example of the linear fit from two voxels are shown in Figure D.0.1.

---

[1] The entire femoral cartilage was assessed, including areas not included in the statistical mapping analysis with the data from Biomomentum. It is likely that these high values are near cartilage edges, and are a result of partial voluming effects.

Table D.0.1: Investigation of T2 relaxation voxels from the femoral cartilage region.

Specimen Number	Time	Number of Cartilage Voxels	Number of Voxels $> 100\ ms$	Percentage of Total	Additional Voxels with $R^2 < 0.7$
1	Pre	4067	329	8.1	0
1	Post	4110	351	8.5	0
2	Pre	4763	452	9.5	1
2	Post	4509	323	7.2	0
3	Pre	4780	389	8.1	0
3	Post	4174	261	6.3	1
4	Pre	3322	233	7.0	1
4	Post	3642	247	6.8	0
5	Pre	3930	166	4.2	0
5	Post	3797	121	3.2	1
6	Pre	3994	257	6.4	1
6	Post	3773	156	4.1	0
7	Pre	5797	730	12.6	0
7	Post	5445	262	4.8	0
8	Pre	5119	644	12.6	0
8	Post	5058	412	8.1	0
9	Pre	5419	656	12.1	0
9	Post	4754	571	12.0	0
10	Pre	5969	715	12.0	0
10	Post	4877	442	9.1	1
11	Pre	3856	235	6.1	0
11	Post	3961	179	4.5	1
12	Pre	4828	428	8.9	0
12	Post	4726	277	5.9	0
13	Pre	4145	502	12.1	0
13	Post	3958	230	5.8	0
14	Pre	5453	435	8.0	0
14	Post	5638	432	7.7	0
15	Pre	4830	589	12.2	1
15	Post	5050	288	5.7	2
16	Pre	6157	645	10.5	0
16	Post	5614	569	10.1	0
17	Pre	3852	281	7.3	0
17	Post	3770	324	8.6	0
18	Pre	4746	410	8.6	0
18	Post	4191	323	7.7	0

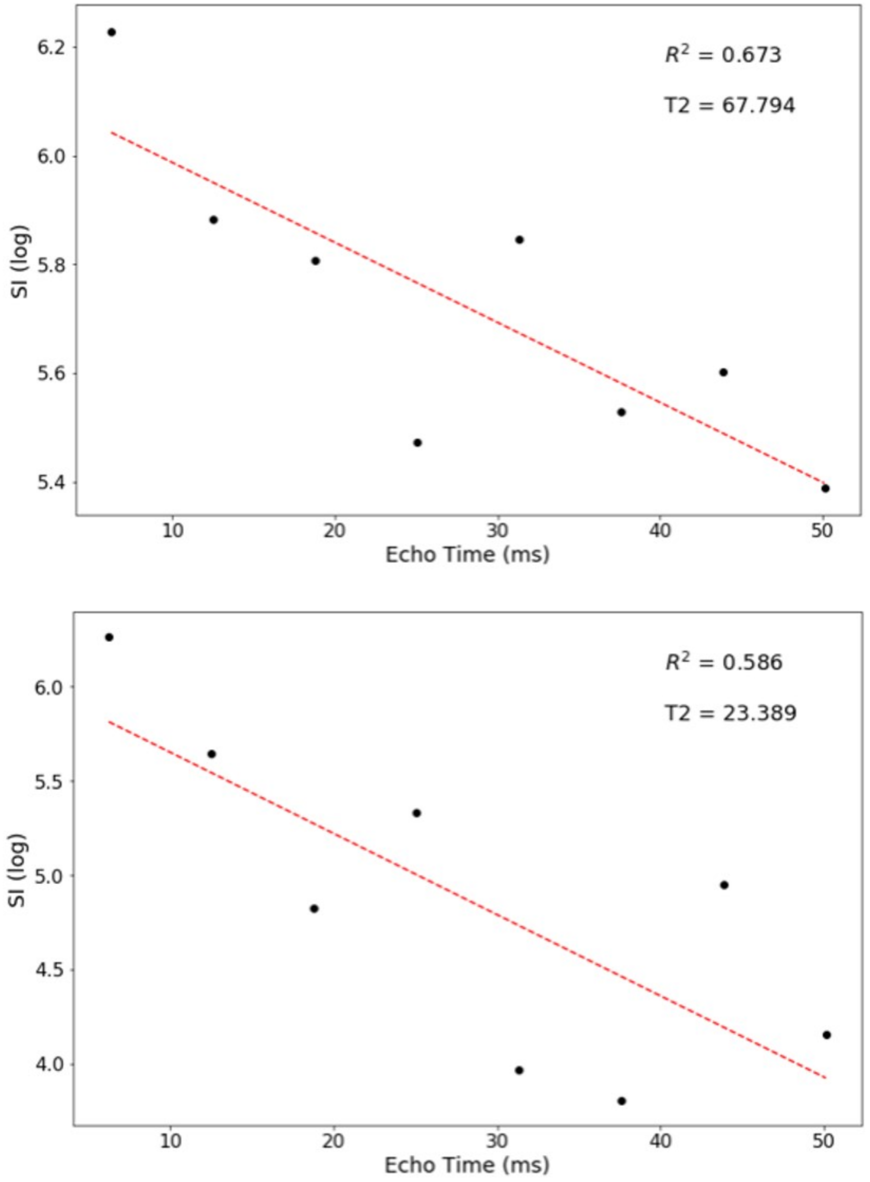

Figure D.0.1: Example of two voxels with a poor linear fit, and therefore were removed from analysis. The natural logarithm of the signal intensities over the 8 echo times allow for a least-squares estimation of the fit.

References

Gatti, A. A., Noseworthy, M. D., Stratford, P. W., Brenneman, E. C., Totterman, S., Tamez-Peña, J., & Maly, M. R. (2017). Acute changes in knee cartilage transverse relaxation time after running and bicycling. *Journal of Biomechanics*, *53*, 171–177.

Kumar, D., Souza, R. B., Singh, J., Calixto, N. E., Nardo, L., Link, T. M., . . . Majumdar, S. (2014). Physical activity and spatial differences in medial knee T1rho and T2 relaxation times in knee osteoarthritis. *Journal of Orthopaedic & Sports Physical Therapy*, *44*(12), 964–972.

Souza, R., Kumar, D., Calixto, N., Singh, J., Schooler, J., Subburaj, K., . . . Majumdar, S. (2014). Response of knee cartilage T1rho and T2 relaxation times to in vivo mechanical loading in individuals with and without knee osteoarthritis. *Osteoarthritis & Cartilage*, *22*(10), 1367–1376.

Subburaj, K., Kumar, D., Souza, R. B., Alizai, H., Li, X., Link, T. M., & Majumdar, S. (2012). The acute effect of running on knee articular cartilage and meniscus magnetic resonance relaxation times in young healthy adults. *The American Journal of Sports Medicine*, *40*(9), 2134–2141.

Wirth, W., Eckstein, F., Boeth, H., Diederichs, G., Hudelmaier, M., & Duda, G. (2014). Longitudinal analysis of mr spin–spin relaxation times (T2) in medial femorotibial cartilage of adolescent vs mature athletes: Dependence of deep and superficial zone properties on sex and age. *Osteoarthritis and Cartilage*, *22*(10), 1554–1558.

Appendix E — Groupwise Registration Template

Table E.0.1: Results from the iterative closest point algorithm to determine the groupwise registration.

		COMPARE																	
		S01	S02	S03	S04	S05	S06	S07	S08	S09	S10	S11	S12	S13	S14	S15	S16	S17	S18	MEAN
TEMPLATE	S01	X	1.25	1.51	2.53	4.47	2.37	1.72	1.56	2.40	3.37	4.81	1.67	1.41	1.82	1.72	2.87	4.36	3.64	2.557
	S02	1.24	X	1.49	2.68	4.86	2.47	2.03	1.67	2.52	3.40	5.10	1.74	1.45	1.43	1.87	2.87	4.40	3.76	2.647
	S03	1.46	1.47	X	1.84	3.71	1.73	1.52	1.37	1.74	2.53	4.19	1.16	1.13	1.36	1.34	2.06	3.48	2.82	2.053
	S04	2.40	2.58	1.74	X	2.37	1.19	1.84	1.80	0.99	1.14	2.64	1.43	1.78	2.04	1.40	1.32	2.20	1.52	1.787
	S05	3.97	4.11	3.31	2.15	X	2.55	3.15	3.27	2.36	2.00	1.67	3.00	3.40	3.53	2.96	2.30	1.68	1.63	2.767
	S06	2.28	2.35	1.67	1.26	2.98	X	2.17	1.62	1.43	2.02	3.14	1.31	1.64	1.87	1.36	1.42	2.86	2.12	1.971
	S07	1.64	1.91	1.44	1.90	3.62	2.17	X	1.83	1.85	2.33	4.22	1.62	1.55	1.93	1.67	2.37	3.28	2.75	2.240
	S08	1.58	1.65	1.46	1.97	4.08	1.85	1.99	X	1.71	2.37	4.74	1.23	1.36	1.57	1.46	2.36	3.78	2.98	2.243
	S09	2.21	2.33	1.61	1.06	2.65	1.34	1.71	1.60	X	1.19	2.91	1.31	1.61	1.92	1.35	1.49	2.37	1.71	1.786
	S10	2.94	3.07	2.32	1.16	2.40	1.71	2.19	2.19	1.13	X	2.39	1.93	2.26	2.54	1.91	1.71	1.82	1.17	2.049
	S11	4.49	4.66	3.82	2.46	1.66	2.77	3.66	3.70	2.68	2.03	X	3.41	3.78	4.01	3.36	2.52	1.50	1.54	3.062
	S12	1.64	1.71	1.16	1.48	3.69	1.38	1.69	1.20	1.35	2.03	3.95	X	1.18	1.40	1.08	1.81	3.36	2.50	1.917
	S13	1.37	1.45	1.14	1.82	3.72	1.67	1.59	1.25	1.71	2.37	4.04	1.18	X	1.39	1.24	2.17	3.45	2.79	2.021
	S14	1.90	1.42	1.41	2.16	4.03	2.01	2.21	1.57	2.06	2.75	4.41	1.44	1.60	X	1.62	2.16	4.01	3.24	2.353
	S15	1.69	1.82	1.34	1.47	3.42	1.37	1.70	1.39	1.45	2.07	3.62	1.05	1.24	1.51	X	1.75	3.21	2.38	1.911
	S16	2.80	2.78	2.04	1.37	2.57	1.37	2.36	2.08	1.43	1.91	2.79	1.69	2.14	2.02	1.70	X	2.55	1.69	2.077
	S17	3.95	4.06	3.19	2.02	1.62	2.41	3.01	3.22	2.16	1.66	1.58	2.92	3.21	3.47	2.89	2.20	X	1.27	2.637
	S18	3.44	3.58	2.67	1.47	1.74	1.83	2.62	2.68	1.64	1.11	1.66	2.33	2.69	2.92	2.29	1.54	1.35	X	2.210